Time-lapse seismic and electrical resistivity tomography combined for monitoring of the CO_2 storage site, Ketzin, Germany

Dissertation
zur Erlangung des Doktorgrades
der Mathematisch-Naturwissenschaftlichen Fakultät
der Christian-Albrechts-Universität zu Kiel

vorgelegt von
Peter Bergmann

Potsdam, 2012

GFZ
Helmholtz-Zentrum
POTSDAM

Referent: Prof. Dr. Wolfgang Rabbel (Universität Kiel)
Koreferent: Prof. Dr. Christopher Juhlin (Universität Uppsala)
Tag der mündlichen Prüfung: 20.12.2012
Zum Druck genehmigt: 20.12.2012

Der Dekan

Abstract

Imaging of subsurface fluid migration is a longstanding geophysical research task, in which CO_2 storage monitoring is a relatively recent application. It is well known that such monitoring can benefit from a combination of different geophysical methods, which complement each other with regard to imaging characteristics and sensitivity to variable saturation of CO_2.

At the Ketzin site, Germany, pilot-scale CO_2 injection is performed with then aim to improve the understanding of in-situ physical, chemical and biological processes, and to provide practical and operational experience for future geological storage of CO_2. This thesis addresses the geophysical monitoring of the CO_2 that was injected at the Ketzin site. Therefore, time-lapse analyses are carried out on the basis of repeated seismic experiments and electrical resistivity tomographies (ERT), both of which are presented separately in the first place. Finally, a methodical combination of these methods is proposed and applied to image the injected CO_2. The thesis gathers these investigations as follows:

First, a synthetic modelling of crosshole ERT and surface seismic experiments is performed. This study is carried out in order to identify key sensitivities of the time-lapse images from the Ketzin site and to provide assistance for the subsequent processing of real data. Therefore, a static reservoir model is derived from well logs and the structural interpretation of the baseline 3D seismic data. Further, multiphase flow simulations are used to establish dynamic CO_2 distributions in this model. The study indicates that a CO_2 quantification may not be possible on the basis of the seismic amplitude information only, since the thicknesses of the CO_2 distributions do not exceed the seismic resolution limit with regard to typical wavelengths that are provided by surface seismic data.

Secondly, the time-lapse processing of the baseline and first repeat 2D seismic surveys from the Ketzin site is presented. The first survey was performed before the start of the injection in 2005 and the second survey in 2009, after approximately 22 kilotons of CO_2 had been injected. Although the datasets show a good repeatability, near-surface velocity changes are found to have a degrading impact on the quality of the time-lapse images. As these changes could only be imperfectly resolved by refraction static corrections, a pre-stack static correction is proposed, which decomposes the timing delays of baseline and repeat traces in a surface-consistent manner. Together with a test of a post-stack static correction, this pre-stack static correction is shown to improve the quality of the time-lapse images considerably. In the subsequent interpretation of the time-lapse images, this provided evidence that in 2009 no CO_2 related amplitude change is observable where the 2D lines allow for monitoring of the reservoir. This finding is further confirmed by an AVO analysis and a comparison with the corresponding 3D surveys.

Thirdly, large-scale ERT surveys are presented, which have been carried out repeatedly during the site startup and the first year of CO_2 injection. The experimental setup of these surveys combines surface measurements with downhole measurements by utilizing a permanent electrode array which has been deployed in the three Ketzin wells. One baseline and three repeat experiments are presented, which show a resistivity increase over time at the CO_2 injector and indicate a preferential CO_2 migration towards the northwest. Using an experimental resistivity-saturation relationship, CO_2 saturations of up to 70% are mapped near the injection well, which is consistent with CO_2 saturations obtained from pulsed neutron-gamma logging.

Finally, a combination of seismic and geoelectric investigations is presented using a structurally constrained inversion approach. For this purpose, lithostructural constraints are interpreted from the seismic reflection data and implemented in the geoelectric inversion by means of a local regularization technique. Consequently, seismics and constrained resistivity inversion are arranged in a sequential workflow which is based on a structural similarity of seismic parameters and electric resistivity. In other words, a change in elastic impedance is expected to occur together with a change in resistivity and vice versa. Prior to an application to the Ketzin datasets, this approach was tested through a synthetic data example. In consistency, both the synthetic and the real data example demonstrated that the constrained inversion allows for an enhanced resistivity imaging along the caprock-reservoir boundary than a conventional ERT inversion.

The practical demonstration for the Ketzin datasets shows, that the approach has a potential for an integrated geophysical monitoring of CO_2 storages and is also significant for imaging of other subsurface processes, which trigger changes in elastic parameters and electric resistivity.

Zusammenfassung

Die Abbildung unterirdischer Fluidmigration stellt ein langjähriges Forschungsgebiet innerhalb der angewandten Geophysik dar, in welchem das Monitoring von CO_2-Speichern eine relativ neue Fragestellung bildet. Es ist bekannt, dass ein solches Monitoring von der Kombination verschiedener Methoden profitieren kann, welche sich im Bezug auf Abbildungseigenschaften und Sensitivität gegenüber CO_2 ergänzen.

Am Pilotstandort Ketzin (Deutschland) wird CO_2 in den Untergrund injiziert, um das Verständnis von in-situ physikalischen, chemischen und biologischen Prozessen zu verbessern sowie praktische Erfahrung für künftige CO_2-Speicher zu schaffen. Die vorliegende Dissertation befasst sich mit dem geophysikalischen Monitoring des am Standort Ketzin injizierten CO_2 mittels wiederholter seismischer und geoelektrischer (engl. Electrical Resistivity Tomography – ERT) Messungen. Darüber hinaus wird eine Kombination beider Methoden vorgestellt und zur Abbildung des injizierten CO_2 angewendet. In der Dissertation werden diese Untersuchungen wie folgt präsentiert:

Im ersten Abschnitt werden synthetische Modellierungen zu Crosshole-ERT und Oberflächen-Seismik vorgestellt. In Vorbereitung der folgenden Auswertungen realer Felddaten, werden diese Studien zur Erfassung der hauptsächlichen Einflussfaktoren der zeitabhängigen (time-lapse) Abbildungen durchgeführt. Hierfür wurde ein statisches Reservoirmodell aus Bohrlochmessungen und der Strukturinterpretation der 3D seismischen Basismessung abgeleitet. Weitergehend wurden Ergebnisse von Mehrphasenfluss-Modellierungen berücksichtigt um dynamische CO_2-Verteilungen in diesem Modell zu realisieren. Da die Mächtigkeiten dieser CO_2-Verteilungen im Vergleich zu dem in der Oberflächenseismik typischerweise erreichbaren Auflösungsvermögen gering sind, konnte gezeigt werden, dass eine ausschließlich auf Amplitudeninformation basierende CO_2 Quantifizerung problematisch ist.

Im zweiten Abschnitt der Disseration wird die Bearbeitung der 2D seismischen Basismessung und der ersten Wiederholungsmessung am Standort Ketzin vorgestellt. Die Basismessung wurde im Jahr 2005, vor Beginn der CO_2-Injektion, durchgeführt. Die erste Widerholungsmessung wurde im Jahr 2009, nach der Injektion von ungefähr 22 000 Tonnen CO_2, durchgeführt. Obwohl beide Datensätze eine gute Reproduzierbarkeit aufweisen, wurde eine Beeinträchtigung der zeitabhängigen Abbildungsqualität aufgrund oberflächennaher Geschwindigkeitsänderungen festgestellt. Da diese Geschwindigkeitsänderungen mittels refraktionsstatischer Korrekturen nicht vollständig beseitigt werden konnten, wird eine pre-stack statische Korrektur vorgeschlagen, welche die Zeitverzögerungen von Basis- und Wiederholungsspuren oberflächen-konsistent zerlegt. In einem Test mit einer post-stack statischen Korrektur wird gezeigt, dass diese pre-stack statische Korrektur zu einer deutlichen Verbesserung der zeitabhängigen Abbildungen führt. In der anschließenden Interpretation wird festgestellt, dass im Jahr 2009 entlang der 2D seismischen Linien keine CO_2-verursachte Amplitudenänderung vorliegt. Diese Feststellung wurde weitergehend durch eine AVO-Analyse und einen Vergleich mit den korrespondierenden 3D seismischen Daten, welche eine Reflektivitätsänderung um die Injektionsbohrung abbilden, bestätigt.

Im dritten Abschnitt werden groß-skalige ERT Messungen untersucht, welche vor Injektionbeginn und während des ersten Jahres der CO_2-Injektion durchgeführt wurden. Die Akquisitionsgeometrie dieser Messungen verbindet Stromeinspeisungen an der Oberfläche mit bohrloch-gestützten Messungen elektrischer Spannungen. Letztere werden mittels einer permanenten Elektrodenin-

stallation in den drei Bohrungen am Standort Ketzin durchgeführt. Eine Basismessung und drei Wiederholungsmessungen werden analysiert, welche im zeitlichen Verlauf eine Erhöhung des elektrischen Widerstands am CO_2-Injektor abbilden und auf eine nordwestliche Vorzugsrichtung der CO_2-Ausbreitung hindeuten. Auf Grundlage einer experimentellen Beziehung zwischen elektrischem Widerstand und CO_2-Sättigung wurden im Bereich der Injektionsbohrung CO_2-Sättigungen von bis zu 70% ermittelt, wofür sich eine gute Übereinstimmung mit den aus Neutron-Gamma Bohrlochmessungen abgeleiten CO_2-Sättigungen finden lässt.

Im letzten Abschnitt wird die Kombination von seismischen und geoelektrischen Messungen anhand einer strukturbasierten "Constrained" Inversion abgeleitet. Zu diesem Zweck werden aus den reflexionsseismischen Daten lithologisch relevante Schichtgrenzen interpretiert und mittels einer lokalen Regularisierungstechnik in die geoelektrische Inversion überführt. Die Bearbeitungen der Seismik und ERT werden folglich in einem sequentiellen Arbeitsablauf zusammengefasst, welcher auf einer angenommenen Strukturähnlichkeit seismischer und geoelektrischer Parameter beruht. Genauer gesagt wird vorausgesetzt, dass eine Änderung in den elastischen Parametern mit einer Änderung des elektrischen Widerstands einhergeht und umgekehrt. Vor der Anwendung auf die Ketzin-Datensätze, d.h. die Wiederholungsmessungen zur 3D-Seismik und zur großskaligen ERT, wurde der Ansatz anhand eines synthetischen Modells überprüft. Diese Anwendungen auf synthetische und reale Daten zeigen übereinstimmend, dass die "Constrained" Inversion im Vergleich zu einer konventionellen Inversion zu einer verbesserten Widerstandsabbildung entlang der Reservoir-Deckgebirgsgrenze führt.

Anhand der praktischen Anwendung auf die Ketzin-Datensätze wird gezeigt, dass sich dieser Ansatz für ein integriertes geophysikalisches Monitoring von CO_2 Speichern eignet und darüber hinaus auch für die Abbildung weiterer Untergrundprozesse, durch welche eine Änderung elastischer Parameter und elektrischer Widerstände hervorgerufen wird, von Bedeutung ist.

Contents

1

Introduction

The main objective of any applied geophysical method is the imaging of structures and processes in the subsurface. The subsurface itself is often characterized by complicated lithology and dynamic processes, such as fluid migration. In principle, geophysical investigation of these systems is performed through the imaging of their physical properties, e.g. seismic wave velocities, electrical conductivity, density. Interpretation of these properties is then carried out to differentiate and characterize lithological units and ongoing processes. However, physical properties can vary considerably within a single lithological unit, and their ranges overlap often for different lithologies. Since this can make an interpretation difficult, it is important to combine different physical properties within a geophysical investigation.

The research carried out in this thesis is addressing a combination of seismic and geoelectric imaging by means of common structural constraints. The motivation for it is not only met by the general objective of improving geophysical techniques, but also by a particular demand of integrating geophysical methods for monitoring of geologically stored carbon dioxide (CO_2).

1.1 Geological storage of CO_2

The global atmospheric concentration of CO_2 has increased from a pre-industrial value of about 280 ppm to 379 ppm in 2005, being the most important driver for climate change (IPCC, 2007). It is widely accepted that man-made CO_2 emission is a major contributor to this increase (IPCC, 2007). There is also a consensus to limit global temperature increase to 2°C to avoid severe disruptions in the earth's climate, which would cause e.g. sea level rise, excessive desertification, and the loss of sensitive ecosystems. In its effort to mitigate climate change, the European Council (EC) adopted the 2°C target in 1996 and reconfirmed it in 2005 (EC, 1996, 2005). At the present stage of knowledge, it seems likely that the 2°C target can be achieved by a reduction of global CO_2 emissions of at least 50% by 2050 with regard to 2000 (IPCC, 2007). Possible ways to be seen for this are reduced energy consumption, increased energy efficiency, increased use of renewable energy, and geological storage of CO_2 (IPCC, 2005).

Fossil-fuelled point sources, such as power plants and industrial facilities, account for approximately 60% of the EU's CO_2 emissions (Figure 1.1). Industrial emissions, as in the case of metal processing or cement production, are mostly related to combustion of coal. Since for these types of emissions a

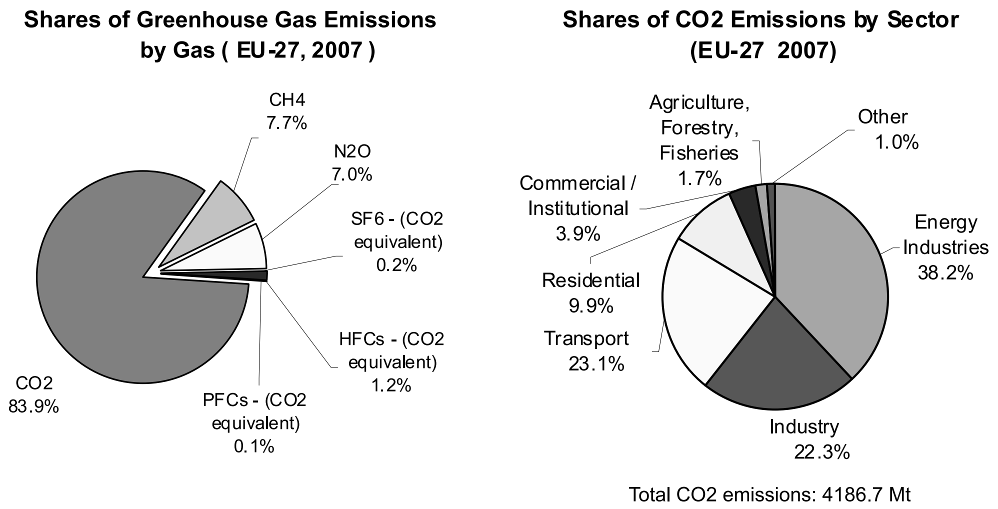

Figure 1.1: Shares of EU greenhouse gas (GHG) emissions by gas (left) and CO_2 emissions by source (right) in 2007. Shown greenhouse gases are carbon dioxide (CO_2), methane (CH_4), nitrous oxide (N_2O), sulfur hexafluoride (SF_6), hydrofluorocarbons (HFC), and perfluorocarbons (PFC). Emissions due to changed land use are not included. Source: EEA (2009).

substitution for renewable energy is difficult, geological storage of CO_2 is a particular option (IPCC, 2005). By means a consequent implementation geological CO_2 storage could contribute with up to 19% to the reductions required to meet the 2°C target (IEA, 2010a).

With the emissions in 1990 as baseline level, the EU committed itself to a reduction of greenhouse gas emission by 20% in 2020 and a further reduction to 80-95% in 2050 (EC, 2009a). Honoring a potential contribution from geological CO_2 storage, it released a directive in 2009 in order to trigger national law making in the EU member states (EC, 2009b). Some of those states, however, face severe delays in defining national regulations, as the issue continues to be subject of parliamentary and public debates. A main reason for these debates is some disagreement about the usefulness and risks of geological CO_2 storage (e.g. Greenpeace, 2008). In this context, Haszeldine (2009) ascertains a temporal lack in the transition from research projects to demonstration scale projects, which delays a potential deployment of Carbon Capture and Storage (CCS) technology on a climate-relevant scale. Aside from public perception and a demand for regulatory frameworks, he identifies a further reason for this lack in missing financial incentives for emission reduction.

Regarding this fact, the EC launched a European Union Emissions Trading Scheme (EU ETS) already in 2005 as a basis for certification and trading of emission allowances. In a broader context, CCS had also been embedded in the Clean Development Mechanism (CDM) in 2011, which facilitates the purchase of emission allowances between member states of the Kyoto Protocol. This is of particular relevance, since economic predictions see an increase in global primary energy consumption within the coming decades with fossil fuels remaining in a dominant position (e.g. OECD, 1999; IEA, 2010b). Against this backdrop, it appears necessary to consider geological storage of CO_2 as an option for mitigating climate change. Considering the early stage of this technology, it deserves scientific attention in order to quantify its potentials and risks before CCS can be implemented broadly. One of the key objectives herein is the ability to monitor the CO_2 that is injected into the underground. This is not only important for the accountability of emission allowances, but also what is more: it is an imperative aspect of storage safety.

1.2 Geophysical CO_2 storage monitoring

As geophysical methods allow for imaging of physical subsurface properties, they provide an opportunity for the monitoring of geological CO_2 storage. The objective of any geophysical site monitoring is the development of a baseline model and a description of its spatiotemporal changes. Comprehensive site models contain information about present geometrical structures and materials, such as rock types and fluid compositions. Since these models are always simplified representations of the reality, they ideally also convey quantities about the inherent uncertainties.

In order to correctly describe ongoing processes with these models, they persistently need to integrate elementary models, which are deduced from individual survey techniques. This implies the combination of different geophysical methods as a prerequisite for achieving a monitoring of different properties at a (as broad as possible) range of scales. Consequently, monitoring of geological CO_2 storage requires integrated multi-method concepts to allow for comprehensive site descriptions.

A vast number of reported studies underlines the capabilities of geophysical methods for subsurface monitoring. Although most of these studies have been carried out for near-surface hydrogeological purposes or hydrocarbon production, they are of great relevance for CO_2 storage monitoring since many of their methodical and practical aspects are similar. In addition, there is also a number of studies which address CO_2 storage monitoring in particular. The majority of these studies are based on ongoing CO_2 storage projects, such as those located in Norway (Sleipner), Canada (Weyburn), USA (Frio), Australia (Otway), Japan (Nagaoka), and Algeria (In Salah) and Germany (Ketzin).

These projects cover a wide range of characteristics, e.g. storage depth, reservoir system, reservoir use, pressure and temperature conditions. This variability also reflects the fact that different combinations of geophysical methods are used, which mostly include seismics and borehole logging, but also electromagnetics or gravity surveying (e.g. Michael et al., 2010). All of these methods provide resolutions and sensitivities within certain ranges, which underlines the importance of combination. There are also cases where geophysical methods do not deliver sufficient information or even fail. Therefore, several research initiatives were constituted (e.g. SACS, CO_2STORE, IEA-GHG Monitoring Network, CASTOR, CO_2GeoNet, CO_2ReMoVe, CO_2 Capture Project) in order to condense the gained experiences into best-practice guidelines and to support the definition of regulatory frameworks. Interestingly, these initiatives consistently agree in the fact that monitoring is indeed site-specific but always has to comprise multi-method geophysical programs.

1.3 CO_2 storage at the Ketzin pilot site

In this context, the Ketzin project comprises the longest-operating on-shore geological CO_2 storage in Europe. Located near Berlin, it provides a research-scale field laboratory for CO_2 storage in a saline aquifer in the Northeast German Basin (Schilling et al., 2009; Würdemann et al., 2010; Martens et al., 2011). Investigations at the Ketzin site were initiated within the framework of the EU project CO_2SINK (CO_2 Storage by Injection into a Natural saline aquifer at Ketzin) in

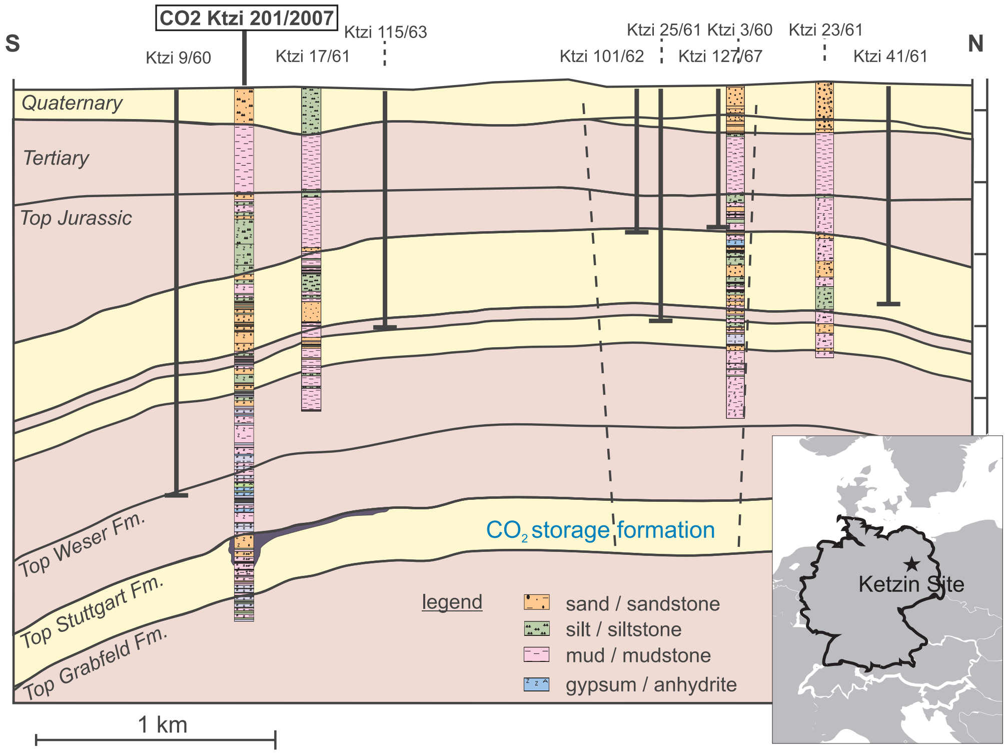

Figure 1.2: Simplified geology of the Ketzin anticline with aquifer (light yellow) and aquitard (pink) units after Förster et al. (2009). Detailed lithology is shown for selected boreholes including the CO_2 Ktzi 201/2007 injection well. The location of major faults is indicated by dashed lines. One scenario of CO_2 extension after 2.5 years of injection of 60,000 t CO_2 is shown in dark blue.

2004. The CO_2SINK project received support from a consortium of 18 partners from research institutes, universities, and industry from nine European countries and had been coordinated by the GFZ German Research Centre for Geosciences, Potsdam. Alongside with additional funding from national projects, CO_2SINK provided baseline surveys and characterization (Förster et al., 2006), the drilling and instrumentation of three wells (Prevedel et al., 2009), the set-up of the injection facility, and a multidisciplinary monitoring concept (Giese et al., 2009; Martens et al., 2011). In June 2008, injection of CO_2 into the sandstone units of the Upper Triassic Stuttgart Formation at 630 to 650 m depth began (Figure 1.2; Table 1.1). By the end of the CO_2SINK project (March 2010), approximately 40 000 tons of CO_2 had been injected. A continuation of the activities at the Ketzin site was realized within the nationally funded CO_2MAN (CO_2 Reservoir Management) project which is designated to terminate in August 2013.

Objectives of the investigations at the Ketzin site are an improved understanding of in-situ processes and the provision of practical experience for future geological storage of CO_2 (Giese et al., 2009). Testing and adaption of geophysical methods for monitoring are key aspects for this. In consequence, a wide range of geophysical activities have been realized in the framework of the Ketzin project.

Table 1.1: Selected activities and events at the Ketzin pilot site. The abbreviation SD-ERT stands for surface-downhole Electrical Resistivity Tomography, which is the type of geoelectric surveying addressed throughout this thesis.

Table of activities		
Apr 2004	Begin of CO_2SINK	
Fall 2005	1st Repeat 2D/3D seismic	
Summer/Fall 2006	Drilling of wells (Ktzi200, Ktzi201, and Ktzi202)	
Oct 2007	1st Baseline SD-ERT	
Apr 2008	2nd Baseline SD-ERT	
Summer 2008	Start of CO_2 injection through Ktzi201	CO_2 injected:
	Arrival of CO_2 at Ktzi200	530 t
Jun 2008	1st Repeat SD-ERT	600 t
Nov 2008	2nd Repeat SD-ERT	4.5 kt
March 2009	Arrival of CO_2 at Ktzi202	11 kt
Apr 2009	3rd Repeat SD-ERT	13.7 kt
Fall 2009	1st Repeat 2D/3D seismic	22 kt

Aside from well logging, both seismic methods and electrical resistivity tomography (ERT) play herein leading roles. Recognizing the demand for multi-method monitoring, the Ketzin project also addresses the evaluation of different geophysical methods within integrated monitoring procedures (Giese et al., 2009). This provides the impulse for this PhD project with an objective to combine seismics and ERT for monitoring of the CO_2 storage Ketzin. In fact, the combination of both methods belongs to a longstanding geophysical research field, as will be shown below.

1.4 Geophysical inversion of combined data sets

In recent decades, combined processing of different geophysical data has evolved into a broad research field. Early work dates back to Vozoff and Jupp (1975), who demonstrated a joint inversion of resistivity and magnetotelluric data. Lines et al. (1988) sequentially processed seismic reflection and gravity measurements by cooperative inversion, while Haber and Oldenburg (1997) proposed a joint inversion scheme for seismic tomography and gravity data based on common structure. Gallardo and Meju (2004, 2007) introduced the cross-gradient approach, in which a joint inversion exchanges gradient information between models obtained from DC resistivity and seismic traveltimes. Using the same methods, Wisen and Christiansen (2005) presented an alternative approach by a mutually and laterally constrained inversion, in which layered models are connected by cross-constraints. Christiansen et al. (2007) extended this approach to the combination of vertical electric soundings and transient electromagnetics. In many cases it is useful to continue the combined processing within a joint interpretation of the multi-parameter models. Such interpretative approaches can range from rather qualitative cross-comparisons to algorithmic procedures that use statistical or cluster-based methods (e.g. Paasche et al., 2006, 2010; Muñoz et al., 2010).

The above mentioned publications only reflect a subset of the literature that covers the combination of different geophysical data, however, they clearly indicate that there is no unified approach. Each implementation depends on diverse factors, such as the methods to be combined, available inversion routines, and also computational resources. Based on the reviewed literature, a classification by means of two items is feasible:

1) Composition of target parameters

- Inversion for a **single** parameter
- Inversion for **different** parameters sharing a physical/empirical relation
- Inversion for **unconnected** parameters

2) Inversion type

- **Separate** inversion (with joint interpretation)
- **Sequential** inversion
- **Joint** inversion

The inversion type describes the temporal conduct, whereas the composition of target parameters takes the imaged physical parameters into consideration. Both items assist in categorizing the wide range of available literature. For instance, the investigations of Vozoff and Jupp (1975) and Christiansen et al. (2007) could then be classified together as joint inversions for a single parameter, since the combined methods aim for the same physical property (electrical resistivity) within a simultaneous procedure.

It is worth mentioning that the majority of the reported studies, which include a seismic component, are restricted to the traveltime information of the first arrivals. In this case the Eikonal equation constitutes a forward operator, which compares to the role that Ohm's law has in resistivity inversion. However, this is unsatisfactory for the requirements of this thesis since we deal with reflection seismic data that contains the relevant time-lapse signal in the wave coda of later-arrival reflections. Such a case would ideally be addressed by Full Waveform Inversion (FWI), which is based on wave-equation operations. As examples for CO_2 monitoring, Gosselet and Singh (2008) and Zhang et al. (2012) reported successful applications of 2D acoustic FWI. However, 4D fluid tracking by means of FWI is still a future challenge (Virieux and Operto, 2009), which is mainly due to the massiveness of the involved forward computations. Furthermore, it is questionable for the objectives of this thesis, whether a joint inversion of FWI and ERT would be an optimum inversion type. This is conditioned by the different resolutions both methods provide as well as the often unknown and/or inexistant connection of elastic and electric parameters. Both issues deserve particular consideration and will therefore be discussed briefly before making a final choice for an inversion type.

1.5 Links between reflection seismics and geoelectrics

Images obtained from seismic reflection and geoelectric investigations are generally of different visual appearance. This observation is caused by the different characteristics of both methods which mainly stand out in the following three domains:

- **The physical domain:** Seismics is based on elastic waves, whereas geoelectrics is based on diffusive electric currents. Applicability of wave theory for the first and potential theory for the latter poses different implications in terms of model resolution and ambiguity.

- **The petrophysical domain:** In first order, seismic wave propagation is determined by the velocities in the subsurface, whereas electric current flow is determined by the resistivity distribution. Since seismic velocity is mainly sensitive to the rock-matrix and electric resistivity is mainly sensitive to the pore-fill, both methods emphasize complementary subsurface properties.
- **The imaging domain:** In the physical domain elastic parameters and electric resistivity constitute analogues, which determine seismic wave propagation and electric current flow, respectively. In this context, it is a clear difference that ERT is focused on imaging of the resistivity, whereas reflection seismics actually images the discontinuities in the distributions of elastic parameters.

Due to these disparities, it appears reasonable to combine both methods in order to get a broader image of the subsurface. These considerations, however, also indicate that not all types of inversion are favourable. For instance, an inversion for different parameters sharing a physical/empirical relation can lead to misinterpretation, as the required relation is usually uncertain or simply inexistent. Although several case studies report relations between seismic velocity and electric resistivity to exist (e.g. Meju et al., 2003; Han et al., 2011; Mukerji et al., 2009; Carcione et al., 2007), such relations are only valid for very specific geological conditions. Generally, in situations where no such prior knowledge about a relation is given, both properties should be assumed to be largely independent. The geology at the Ketzin site comprises various geological formations, partly of high complexity, which are relevant for the storage reservoir and its caprock barriers. Moreover, in the following chapters it will be shown that variable saturation of CO_2 has a different impact on seismic velocity and electric resistivity. In case of homogeneous mixing of brine and CO_2, the change in electric resistivity occurs most notably for large saturations, whereas seismic velocity shows significant changes only for small saturations. For a rock exposed to increasing CO_2 saturation, this indicates that a resistivity response can be lagging behind the seismic response. Taking this into account, any inversion approach which exchanges gradient information between seismic and geoelectric models can potentially become problematic. Consequently, the inversion approach of this thesis is based on the pragmatic assumption that if a change in lithology poses a change in elastic properties, it is likely to do so for electric resistivity and vice versa. In other words, the type of inversion to be selected ought to respect (but not force) a structural similarity.

With regard to the imaging of subsurface structures, reflection seismics is probably the most established of the geophysical methods. ERT, on the other hand, tends to image structures at a comparably low resolution. Thus, a structure-based inversion which starts with the seismic image gives an interesting opportunity for a sequential inversion. Hence, it seems to be suitable to arrange both methods in a sequential workflow in which reflection seismics constitutes a priori structural information that is subsequently used to constrain the ERT inversion (Figure 1.3).

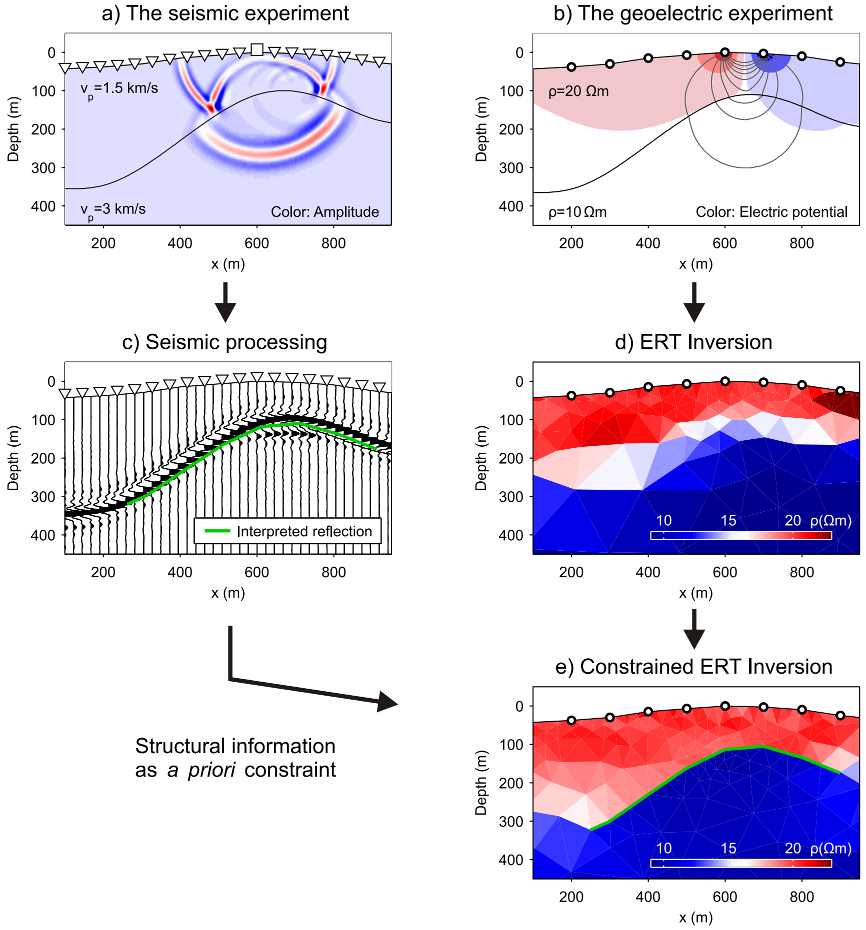

Figure 1.3: Synthetic anticline model illustrating the combination of seismic reflection and geoelectrics by means of a constrained inversion approach.

1.6 Basic concept of constrained inversion

Geophysical inverse problems are most generally ill-posed, because the models often have to be deduced from sparse and noisy observations (Ellis and Oldenburg, 1994; Jackson, 1972). In many cases this causes unstable, unrealistic models. Some guideline for overcoming this deficit is provided by the regularization technique (Zhdanov, 2002), which introduces additional conditions into the inversion. Most commonly, it is used as a control on the roughness of the inverted model. In this way, the ill-posedness is implicitly reduced by narrowing the space of possible models to those models that do not exceed a certain degree of inherent roughness. As regularization will be discussed in more detail in the next chapter, only the basic concept will be introduced in the following paragraphs.

In the practical application, inversions with strong regularization produce over-smoothed models with poor data fits (Figure 1.4). Inversions with weaker regularizations produce rougher models with better data fits and finally artificial structures for regularizations that are too weak. In the

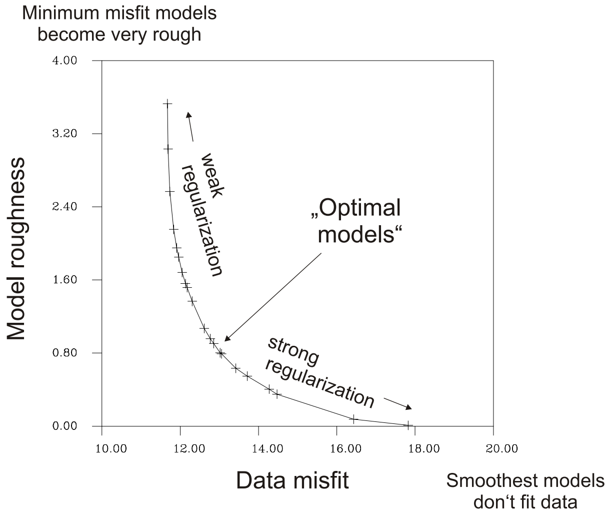

Figure 1.4: The generic form of the L-curve representing the tradeoff associated with geophysical inverse problems. Data misfit and model roughness are plotted as a curve parametrized by the regularization strength. The range of models denoted as "optimal" is indicated to be a compromise of data misfit and model roughness. Figure adapted after Vasco (1998).

latter case, the data were over-fitted with regard to their sparseness and noise content. For the selection of a regularization in a specific problem, one typically carries out a number of inversions for variable regularization. The resulting models are then arranged into L-curves, such as the one given in the example of Figure 1.4. Based on these L-curves, a specific regularization can be opted from geometrical criteria, such as those given by Hansen and O'Leary (1993) (point of maximum curvature) or Aster et al. (2005) (minimum distance to origin). Consequently, the regularization parametrizes the model space but also connects to a tradeoff between over-smoothed models and over-fitted data.

The real subsurface comprises structures of various scale and petrophysical relevance. A regularization can be optimal for some parts of the model, whereas masking important information in others. Thus, a global regularization is usually not optimal, in particular if we consider that tomographic models typically comprise well-resolved and poorly-resolved regions.

In recent years numerous studies have addressed the incorporation of prior knowledge into the inversion of geophysical data. Methodic research in this field dates back several decades and is still a present issue (e.g. Pedersen, 1979; Pous et al., 1987; Backus, 1988; Portniaguine and Zhdanov, 1999; Gholami and Siahkoohi, 2009). From a historical perspective of geophysical interpretation, this progress seems to be connected to a shift away from idealized geometrical representations towards more realistic three-dimensional bodies. This change in geophysical interpretation is founded not only on the development of sophisticated inversion approaches but also on more efficient and flexible forward algorithms. Nowadays, the term 'constrained inversion' is widely established, although no concise definition seems available. The present study has the following understanding regarding this term: a constrained inversion is a type of inversion, which integrates prior knowledge and preserves it throughout the inverse procedure.

If we have prior knowledge about a prominent geological structure in our model, we might be interested to take that into consideration already in the inverse procedure. This is the case where a local adjustment of the regularization is appropriate. For instance, inverted parameters may be allowed to behave more discontinuous across the structure, retaining the global regularization in otherwise homogeneous parts. The combination of this concept with a flexible forward operator, e.g. finite-elements, would allow then the parameterization to closely follow those geologic structures. Once the structural model of a site is established, it can be jointly owned by inversion-based methods. Geological structures can therefore be a key element for integrated geophysical assessment.

In conclusion, this thesis is committing itself to the objective of a structure-based workflow for the Ketzin data. Therefore, seismics and geoelectrics are going to be arranged in a sequential procedure. With regard to the classification given in section 1.4, the approach chosen for this thesis is a sequential inversion of unconnected (but structurally-related) parameters. Since this combination mainly relies on structure, we actually deal with a structurally constrained inversion.

In fact, using the term constrained inversion poses an interesting contradiction. A regular inversion is a subject to a global regularization, which can be considered as a control on the model roughness. Thus, the regularization is actually establishing a smoothness constraint. The intended structurally constrained inversion aims for a local weakening or complete rejection of the regularization across priorily known structures, i.e. a local de-regularization. Therefore, a less (smoothness) constrained inversion is carried out. However, for consistence with its historical use, I will keep the term constrained inversion to differentiate from regular inversion.

1.7 Research objectives and structure of the thesis

This PhD project sets the following main objectives: (1) the methodical combination of reflection seismics with ERT and (2) the application and evaluation of this combination for the time-lapse investigations carried out at the Ketzin site. These objectives divide into the following subtasks:

- Selection of an inversion approach
- Testing on synthetic data
- Application on real data
- Interpretation and discussion of the results

In order to document the investigations carried out within this PhD project, the thesis is structured as follows:

Chapter 2 gives an overview of the relevant seismic and geoelectric principles. In its last part, a description of the constrained resistivity inversion approach is given. Chapter 3 presents synthetic studies which were performed in the preparatory phase of the Ketzin project. Chapter 4 and 5 are devoted to the monitoring at the Ketzin site by presenting independently performed seismic and geoelectric experiments. The combination of both methods by means of the constrained inversion is subsequently presented in chapter 6. Finally, the findings of this thesis are summarized and perspectives are discussed.

2

Theory and method

This chapter assembles the theoretical aspects which are of relevance to this thesis. Starting with an overview on the seismic reflection, an outline on the ERT method and inversion is given. Based on the latter, a description of the constrained ERT inversion and practical aspects of the workflow proposed in Figure 1.3 follows.

Contents

2.1 The Reflection seismic method

2.1.1 Background on seismic reflection

The basis of the reflection seismic method is the controlled activation and acquisition of elastic wavefields. Waves which are reflected back to the surface convey information about geologic structures, since the reflection is caused by discontinuities in elastic parameters. Wavefield properties that are valuable in this context are travel time, amplitude, frequency content, and phase. In the

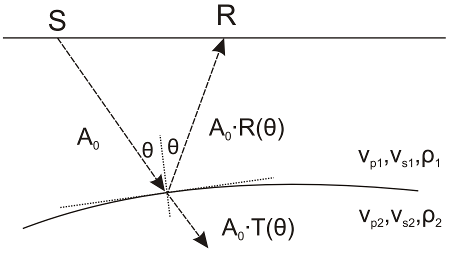

Figure 2.1: Schematic illustration of a wave ray propagating from a source location S to a receiver location R after being reflected at an interface. A_0 denotes the amplitude of the wave impinging the interface. $R(\theta)$ and $T(\theta)$ denote the proportions of A_0 that are reflected and transmitted, respectively.

following, I will focus on the amplitude, because it is the most important property for the subsequent studies. Assuming a compressional wave (p-wave) which hits a layer boundary perpendicularly (normal incidence), the amplitude coefficients for reflection and transmission are given by (e.g. Kearey et al., 2002)

$$R = \frac{v_2 \cdot \rho_2 - v_1 \cdot \rho_1}{v_2 \cdot \rho_2 + v_1 \cdot \rho_1} \quad \text{and} \quad T = -\frac{2v_1 \cdot \rho_1}{v_2 \cdot \rho_2 + v_1 \cdot \rho_1} \ . \tag{2.1}$$

Here, v_1, v_2 and ρ_1, ρ_2 denote the p-wave velocities and densities in the first and second layer, respectively. In this nomenclature, the wave is propagating from within the first layer towards the second layer. As a further assumption, a source and a receiver may be located upon the surface of the first layer at identical position (zero-offset). The receiver will then measure the reflected wave at the zero-offset two-way-traveltime (TWT), which corresponds to the wave travelling forward and backward on the same ray path. Typically, seismic acquisition is performed at finite offset, which gives rise to two implications: First, forward and backward propagation of a reflected wave will happen on different ray paths. Consequently, the traveltime likely will differ from that of a zero-offset ray. Assuming an isotropic medium with horizontal (or moderately dipping) layers, the onset time of the reflection is increasing with increasing source-receiver offset. The offset-traveltime relation can then be approximated by hyperbolic functions which define the normal moveout (NMO) of the reflection onsets (Yilmaz, 2001).

Secondly, acquisition at finite offsets leads to non-normal reflection, which makes it necessary to consider R for an arbitrary angle of incidence θ. Most often, such a case leads to conversion of p-waves to (vertically polarized) shear waves (s-waves), which implies an equation system that accounts for the p-wave velocities in the first and second layer v_{p1}, v_{p2} and the respective s-wave velocities v_{s1}, v_{s2}. Angles of reflected and transmitted waves can be assessed by Snell's law. Respective amplitudes are specified by the Zoeppritz equations (Zöppritz, 1919), which derive from the continuity of displacement and stress at the reflecting interface. Nowadays, it has become a widely adapted practice to analyse the so-called amplitude-versus-offset (AVO), or amplitude-versus-angle (AVA), response to quantitatively assess elastic properties (Castagna, 1993). Due to the inherent complexity of the Zoeppritz equations, a number of approximations have been introduced to allow for more convenient assessments (e.g. Bortfeld, 1961; Aki and Richards, 1980; Shuey, 1985; Wang, 1999). Aki and Richards (1980) presented the following 3-term approximation for boundaries with small contrasts in elastic properties (see Mavko et al., 2003):

$$R_{pp}(\theta) \approx A + B \cdot sin^2(\theta) + C \cdot tan^2(\theta) \cdot sin^2(\theta) \; . \tag{2.2}$$

In the following, only p-wave reflection from an incident p-wave is discussed, which is indicated by the notation R_{pp}. The angular reflection coefficients A, B and C read (Mavko et al., 2003)

$$A = \frac{1}{2}\left(\frac{\triangle v_p}{\langle v_p \rangle} + \frac{\triangle \rho}{\langle \rho \rangle}\right) \tag{2.3a}$$

$$B = \frac{1}{2}\frac{\triangle v_p}{\langle v_p \rangle} - 2\left(\frac{v_s}{v_p}\right)^2 \left(\frac{\triangle \rho}{\langle \rho \rangle} + 2\frac{\triangle v_s}{\langle v_s \rangle}\right) \tag{2.3b}$$

$$C = \frac{1}{2}\frac{\triangle v_p}{\langle v_p \rangle} \tag{2.3c}$$

with the following contrasts and averages across the interface

$$\triangle v_p = v_{p2} - v_{p1} \qquad \langle v_p \rangle = \frac{v_{p1} + v_{p2}}{2} \tag{2.4a}$$

$$\triangle v_s = v_{s2} - v_{s1} \qquad \langle v_s \rangle = \frac{v_{s1} + v_{s2}}{2} \tag{2.4b}$$

$$\triangle \rho = \rho_2 - \rho_1 \qquad \langle \rho \rangle = \frac{\rho_1 + \rho_2}{2} \; . \tag{2.4c}$$

A, B and C can be interpreted in terms of different angle ranges (Castagna, 1993). The term A dominates at small angles (near-offsets) and approximates, again assuming small contrasts, the normal-incidence reflection coefficient (Mavko et al., 2003)

$$A = \frac{1}{2}\left(\frac{\triangle v_p}{\langle v_p \rangle} + \frac{\triangle \rho}{\langle \rho \rangle}\right) \approx \frac{v_2 \cdot \rho_2 - v_1 \cdot \rho_1}{v_2 \cdot \rho_2 + v_1 \cdot \rho_1} = R \; . \tag{2.5}$$

The terms B and C dominate at intermediate and large angles (near the critical angle), respectively. In practice, C is often neglected, since common acquisition geometries provide reflection data mostly at small and intermediate angles. This leads to a linearized form of equation 2.2, in which A is the so-called AVO intercept and B the AVO gradient.

Practical AVO analysis is most commonly carried out by crossplots of A and B, which are used to analyse background trends and search for deviations from them (Ross, 2000). For example, the reservoir sandstone of the CO_2 storage Ketzin shows lower wave velocities and density than the caprock mudstones (Norden et al., 2010), a fact that leads to a negative AVO gradient and AVO intercept. This is also illustrated by the single interface reflection coefficients in Figure 2.2. However, it is important to recognize that the Ketzin reservoir is of sub-wavelength thickness, which generally poses additional implications on the normal incidence amplitude (e.g. Meissner and Meixner, 1969; Widess, 1973; Gochioco, 1991) and the AVO response (e.g. Juhlin and Young, 1993; Bakke and Ursin, 1998; Liu and Schmitt, 2003). For instance, if the contrasts in elastic properties of reservoir

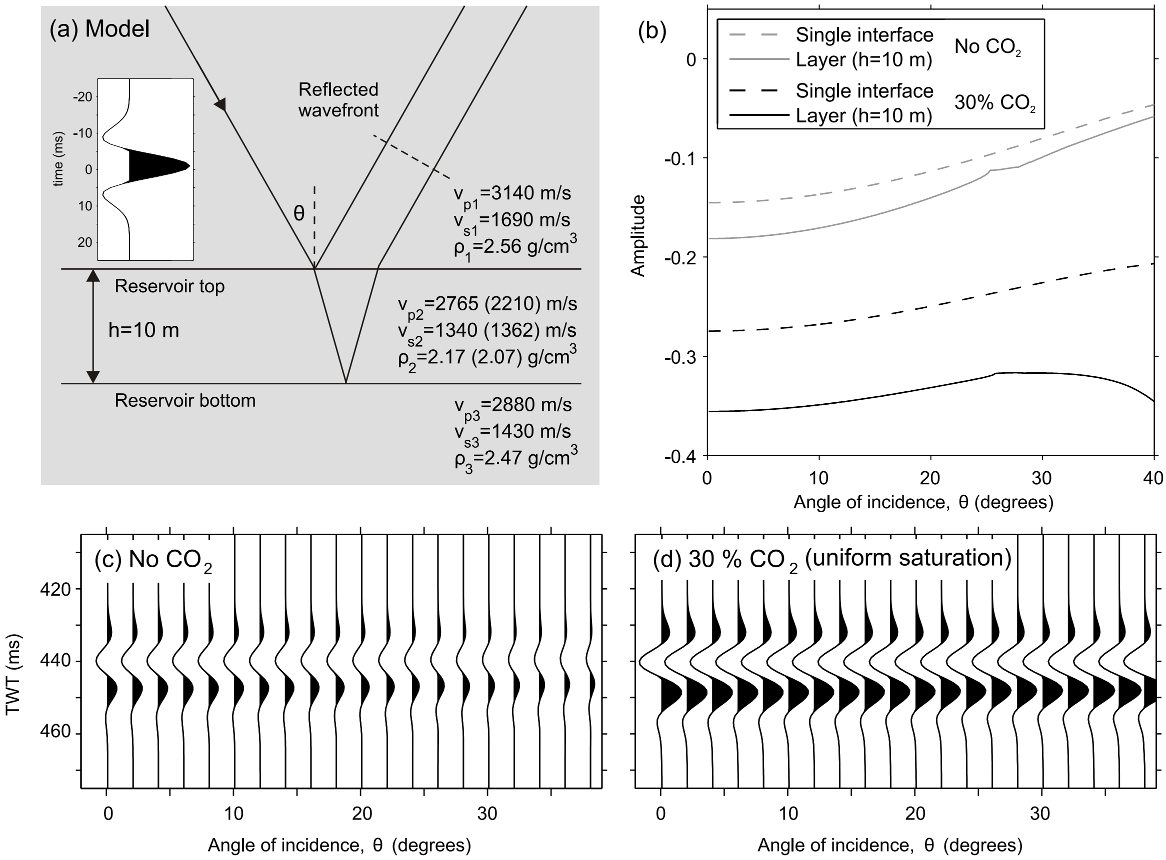

Figure 2.2: Modelled AVA reflectivity of a thin layer with Ketzin reservoir parameters after Kazemeini et al. (2010a) as input model. (a) The input model comprises a single layer representing the reservoir. Modellings have been carried out with the input model before CO_2 injection (values without brackets) and after CO_2 injection (bracketed values). (b) AVA response of the reservoir top as single interface and as a layer of 10 m thickness. Thin layer amplitudes were computed with the method of Juhlin and Young (1993) for the 50 Hz Ricker wavelet shown in subfigure (a). Computations include first-order multiples and conversions, and use the Aki-Richards approximation after Guy et al. (2003). (c-d) Modelled AVA response of the 10 m layer for the 50 Hz Ricker wavelet. Note that the traces in subfigures (a,c-d) are drawn to the same amplitude scale.

and surrounding rocks increase, not only the main assumption of equation 2.2 becomes increasingly invalid. Moreover, the AVO response cannot adequately be approximated by the superposition of the reflections off the top of the layer and off the bottom of the layer only. In such a case interbed multiples and conversions also have to be taken into account (Meissner and Meixner, 1969). Based on the Ketzin reservoir model of Kazemeini et al. (2010a), Figure 2.2 illustrates the difference in AVA response for the reservoir represented by a single boundary and a sub-wavelength layer.

2.1.2 Seismic velocities for brine/CO$_2$ substitution

The change in seismic reflection response caused by CO$_2$ replacing brine within a porous rock is conditioned by the changes in the rock's elastic parameters. The elastic parameters of interest here are the bulk modulus K and shear modulus G. The bulk modulus is defined by the relative volume change caused by an omni-directonal confinement pressure. The shear modulus is defined by the relative shear displacement, when a shear force is applied (e.g. Lay and Wallace, 1995). As there is no reset force for liquids and gases, their shear modulus is zero. The elastodynamic wave equation connects both modules for homogeneous media (Lay and Wallace, 1995)

$$\rho \frac{\partial^2 \overrightarrow{u}}{\partial t^2} = G \nabla^2 \overrightarrow{u} + \left(K + \frac{1}{3} G \right) \nabla \nabla \cdot \overrightarrow{u} \; . \tag{2.6}$$

$\overrightarrow{u}$ denotes the displacement which occurs during wave propagation. It follows from this equation that the propagation velocities of p-waves and s-waves read

$$v_p = \sqrt{\frac{K + \frac{4}{3} G}{\rho}} \qquad \text{and} \qquad v_s = \sqrt{\frac{G}{\rho}} \; . \tag{2.7}$$

From the equation for v_s we can assess that there is no s-wave propagation in fluids (due to $G = 0$), and further that v_s is always lower than v_p. For a description of fluid substitution in such materials, respective models need to consider that the pores are saturated with mixtures of the involved fluids. Two types of saturation are distinguished for such systems:

Uniform saturation

The bulk modulus of the saturated rock K_{sat} depends on the rock's porosity ϕ, the bulk modules of the dry frame K_{dry}, the matrix minerals K_0, and the pore fluid K_{fl}. A relation between them is constituted by the Gassmann model (Gassmann, 1951), which is given here after Bachrach et al. (1998)

$$\frac{K_{sat}}{K_0 - K_{sat}} = \frac{K_{dry}}{K_0 - K_{dry}} + \frac{K_{fl}}{\phi (K_0 - K_{fl})} \; . \tag{2.8}$$

We consider the pore fluid to be initially a liquid (brine) which is successively replaced by a gas (CO$_2$). The bulk modulus of the two-phase pore fluid K_{fl} is assumed to be an average of the brine and gas bulk modules (K_{brine} and K_{CO2}) which are weighted over the CO$_2$ saturation S_{CO2}

$$\frac{1}{K_{fl}} = \frac{S_{CO2}}{K_{CO2}} + \frac{1 - S_{CO2}}{K_{brine}} \; . \tag{2.9}$$

At partial saturation, the rock's density is a result of the matrix mineral density ρ_0, CO$_2$ density ρ_{CO2}, and brine ρ_{brine}

$$\rho = \phi \left[S_{CO2} \cdot \rho_{CO2} + (1 - S_{CO2}) \rho_{brine} \right] + (1 - \phi) \rho_0 \; . \tag{2.10}$$

Figure 2.3 illustrates the typical Gassmann-type behavior of the seismic wave velocities as function of CO$_2$ saturation for a model of the Ketzin reservoir sandstone. One can find a noteworthy feature in the rapid decrease of v_p for CO$_2$ saturations of approximately up to 5%. This explains by the

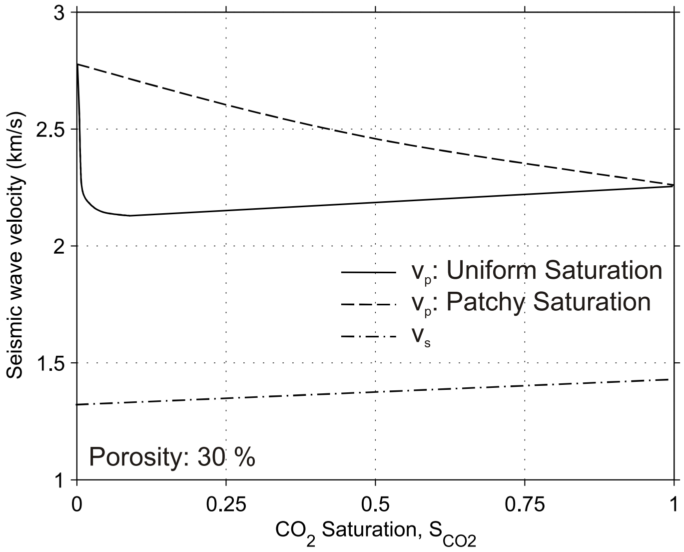

Figure 2.3: P-wave and s-wave velocities as functions of CO_2 saturation for uniform and patchy saturation for the Ketzin reservoir model (after Kazemeini et al., 2010a).

bulk modulus of the CO_2, which is low compared to that of brine ($K_{CO2} = 0.00832$ GPa, $K_{brine} = 3.68$ GPa for Ketzin reservoir conditions). Consequently, even relatively small fractions of gaseous CO_2 cause a significant drop in the effective compressional modulus (see equation 2.9), which is a feature that is also responsible for an increasing absorption of seismic waves. For larger CO_2 saturations, we can observe a gradual increase in p-wave velocity, which is due to the decrease in density (see equation 2.10 and 2.7).

It is important to note that the Gassmann model is based on the following assumptions (Mavko et al., 2003):

- The rock is homogeneous and isotropic, and the rock pores are well connected.
- The rock matrix is composed of a single mineral or different minerals of identical bulk and shear modules.
- Pore-fluid mixtures can be approximated by homogeneous fluid analogues (equation 2.9).
- Frequencies are sufficiently low, so that pore-pressures equilibrate during a seismic wave period, and a relative movement of rock and fluid (squirt flow) is prevented.
- Absence of chemical processess (e.g. dissolution, cementation).

Patchy Saturation

On a fine scale, the Gassmann model assumes homogeneous mixing of both phases. However, if mixing is heterogeneous on a coarse scale, a passing wave causes local pore-pressure differences. Assuming that the mixing can be described by geometric patches, which themselves are homogeneously saturated, there will be pressure exchange between nearby patches (Mavko et al., 2003).

On a larger scale, wave-induced pore-pressure differences should average to an equilibrated value. At a seismic wave frequency f, these pore pressure heterogeneities will equilibrate for scales smaller than the critical diffusion length L_c (Mavko et al., 2003):

$$L_c \approx \sqrt{\frac{kK_{fl}}{f\eta}} \tag{2.11}$$

with k denoting the rock permeability and η the fluid viscosity. If the patches are sufficiently small ($< L_c$), the pore-fluid mixture can be represented by a single effective fluid, which is then called to be in the condition of the previously discussed uniform saturation. If the patches are larger than L_c spatial fluctuations will tend to persist during seismic wave passage, which is called non-uniform or patchy saturation (Mavko and Mukerji, 1998). Patchy saturation can for example be caused by "fingering" of pore-fluids, which might result from spatial variations in wettability, permeability or shaliness (Asveth, 2009). Yet, it is possible to describe the individual patches by separate Gassmann models. For an ensemble of n patches of uniform shear modulus G, the effective modulus K_{patchy} can be obtained from Hill's equation (Hill, 1963; Berryman and Milton, 1991)

$$K_{patchy} = \left(\sum_{i=1}^{n} \frac{x_i}{K_i + \frac{4}{3}G} \right)^{-1} + \frac{4}{3}G \, . \tag{2.12}$$

It is an important property of the Hill's equation that it yields an analytically exact solution for K_{patchy}, which is independent of the geometrical arrangement of the patches within the ensemble. Required input parameters are the volume fractions x_i of the patch mixtures and the individual bulk modules K_i at full fluid saturation only, both of which may be assessed from an experimental or statistical basis.

Figure 2.3 also illustrates the v_p function of the Ketzin model for patchy saturation. In comparison to the uniform saturation it interestingly shows an almost linear velocity-saturation relation. This holds serious implication for seismic monitoring of CO_2: On the one hand, reservoirs which are characterized by patchy saturation offer sensitivity for v_p over the entire range of saturations. On the other hand, reservoirs which are characterized by homogeneous saturation build favourable conditions for the application of seismic methods for CO_2 detection, since the change in v_p is most drastic for the first few percent of CO_2 saturation. The application of seismic methods in such reservoirs for CO_2 quantification, however, might be difficult since the change in v_p at higher CO_2 saturations is less significant.

In reality, both models constitute upper and lower velocity bounds with the p-wave velocities for patchy saturation being higher than those for uniform saturation (Mavko and Mukerji, 1998).

2.1.3 Time-lapse seismics

The description of time-lapse seismics will be introduced with a very brief outline of reflection seismic processing, since it is also the basis of time-lapse seismic processing. Typical processing procedures comprise three main steps: (1) data preprocessing, (2) stacking, and (3) seismic migration (e.g. Yilmaz, 2001). (1) The preprocessing aims to extract the relevant reflections out of the acquired seismograms. Common preprocessing steps are the muting and suppression (filtering) of undesired signals, deconvolution, and amplitude restoration. A further important step is the application of static corrections, which will be explained in more detail below. (2) Seismic stacking comprises resorting of traces into gathers and summation along time-offset trajectories which are defined by velocity model estimations. Most commonly, the traces are resorted into common-midpoint (CMP) gathers. Then, NMO corrections are applied on the basis of velocities that are extracted from velocity analyses in the CMP domain. These velocity analyses are typically carried out in alternation with residual static corrections until the velocity models sufficiently remove the NMO (Yilmaz, 2001). Stacking is then completed with the summing of the NMO-corrected traces that belong to the same CMP gathers (Mayne, 1962). The number of traces within a CMP gather is called fold, which is an indicator for the signal-to-noise improvement that can be obtained in the stacking procedure. Aside from the CMP stack there are also alternative stacking procedures, such as the methodically related common-reflection-element (CRE) stack (Gelchinsky, 1988), multifocusing stack (Gelchinsky et al., 1999), or common-reflection-surface (CRS) stack (Jäger et al., 2001). (3) Seismic processing is typically finalized by migration which intends to relocate reflected energy to its true (temporal or spatial) origin of reflection. Seismic migration generally aims to overcome mispositioning (e.g. image angle of dipping reflectors) and can be applied in the pre-stack or post-stack domain (see, e.g. Yilmaz, 2001; Biondi, 2006). In the latter case, migration is typically carried out in conjunction with dip-moveout (DMO) corrections before stacking, which then resembles a pre-stack migration scheme (Deregowski, 1986).

The general objective of seismic processing is to modify acquired data into images that can be used for interpretation of subsurface structures. On this basis, time-lapse seismic aims for the detection of changes in the subsurface's seismic response by means of repeated data acquisitions and processings. There are several metrics which are used for the quantification of repeatability, with the normalized-root-mean-square amplitude difference $nrms$ of Kragh and Christie (2002) being the most commonly used. The $nrms$ of two traces a and b is given by

$$nrms = 100\% \cdot \frac{rms\,(a-b)}{\frac{1}{2}\left[rms\,(a) + rms\,(b)\right]} \,. \tag{2.13}$$

The $nrms$ measure ranges from 0% for identical traces to 141% for randomly uncorrelated traces, and up to 200% for 180° out of phase traces (amplitude reversal). It is very sensitive to small changes between the two input traces, whether it is in the amplitude or phase (Domes, 2010).

Beyond the impact of noise, there are a number of practical challenges to time-lapse seismic. In case of onshore surveying, unforeseen acquisition obstacles usually occur. Although the fold reduction caused by these obstacles can be compensated by relocating source and receiver locations (e.g. acquisition of the same CMP at different offset), a reduced experimental reproduction inevitably remains. Furthermore, wavelet reproducibility may be limited, because it is not only a matter of source technology but also of source-ground coupling and near-surface velocities, which needs to be approached by cross-equalization of the frequency and phase characteristics (wavelet matching) Although not considered in the petrophysical descriptions previously given, the seismic response also senses pressure changes (Todd and Simmons, 1972; Eberhart-Phillips et al., 1989). It is obvious that a time-lapse seismic interpretation for monitoring of CO_2 injection must take this into consideration. In this context, Landrø 2001 introduced a method for discriminating the fluid and pressure response in time-lapse seismic data by exploiting the AVO response. Furthermore, the practical experience gained during the work for this thesis has shown that uncorrected changes in near-surface velocities

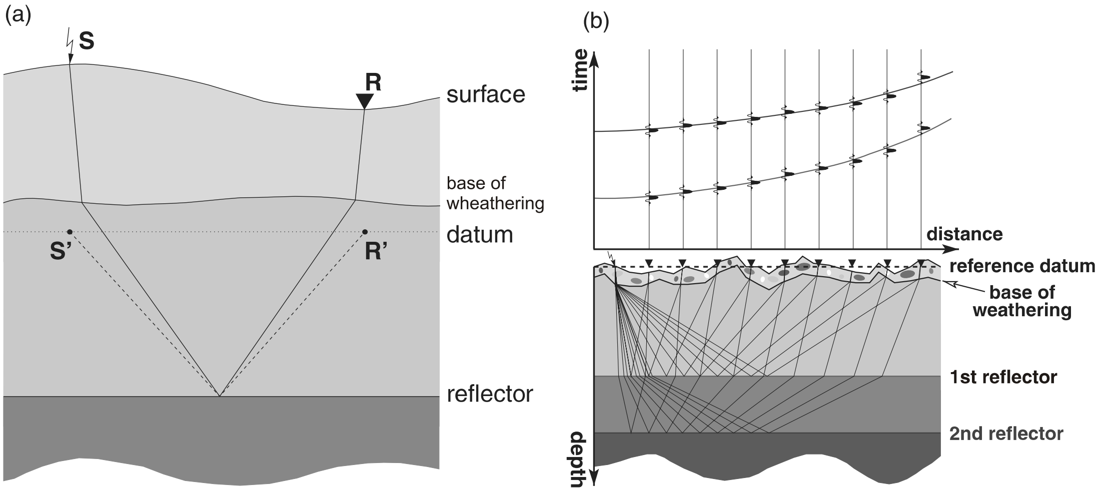

Figure 2.4: (a) Raypath through a low-velocity layer. Redatuming achieved by field static correction substitutes the actual surface by a reference datum plane beneath the low-velocity layer, i.e. source S and receiver R are moved to S' and R' on the reference datum plane, respectively. (b) Illustration of the possible influence of the weathering layer on the traces (after Koglin et al., 2006).

can also deteriorate the quality of the time-lapse image, which gives cause for the following section.

2.1.4 Time-lapse static corrections

Previous considerations made no particular assumptions about the near-surface conditions, neither in the steady state nor in the time-lapse data acquisitions. In reality, however, the surface often shows topography with near-surface layers comprising complicated velocity characteristics due to weathering effects and heterogeneous geology. Moreover, the near-surface velocities may change during acquisition periods of time-lapse surveys. Such changes can be caused by fluctuations in soil moisture (e.g. Kashubin et al., 2011) and groundwater table or man-made earthworks.

In a ray-theoretical approach, irregularities in near-surface velocities can be assessed as traveltime shifts on the reflected seismic waves, so-called static shifts (e.g. Cox, 1999). Corrections of these static shifts aim to modify the reflection arrival times as if all measurements were made upon a flat surface plane with no weathering present (e.g. Sheriff, 2002). Static corrections can be divided into the removal of topography (elevation static correction, redatuming) and the removal of near-surface velocity effects (weathering correction) (Figure 2.4). Application of weathering corrections requires near-surface velocity models, which are typically estimated from analysis of refracted waves (refraction static correction).

Thickness and velocity distribution in the weathered layer can, however, not be determined to arbitrary precision. Residual statics inevitably remain, a fact that can significantly diminish the stack quality (Cox, 1999). Consequently, residual static corrections aim to reduce relative traveltime differences of reflected phases in the NMO corrected CMP gathers. This procedure makes use of the following surface-consistent model (see, e.g. Yilmaz, 2001): Each trace receives a delay contribution from its source i and its receiver j. In other words, the delay M_{ij} of a trace is the sum of the source location delay s_i and receiver location delay r_j:

$$M_{ij} = s_i + r_j \; . \tag{2.14}$$

The residual static correction procedure projects the individual traveltime differences back onto the individual source and receiver locations. As a direct result, a set of $\mathbf{s}$ and $\mathbf{r}$ which sufficiently explains $\mathbf{M}$ can, in turn, be used to correct the trace data (Ronen and Claerbout, 1985; Cox, 1999). Motivated by the difficulties observed during the processing of the Ketzin data, I take this strategy one step further to the processing of time-lapse data sets. Difficulties encountered on the Ketzin data were to some extent attributed to changes in near-surface velocities, which could only imperfectly be resolved by refraction static corrections. For the 3D data, these difficulties even triggered a reprocessing of the baseline static corrections (Lüth et al., 2011). Testing of the time-lapse static correction approach began on the 2D seismic data, in which the same difficulties were encountered. Technical details of this approach and real application will be presented in chapter 4. Its principle idea will therefore only briefly be illustrated in the following (Figure 2.5).

Consider a baseline survey which is conducted at homogeneous near-surface condition. Subsequently, a repeat survey is conducted which differs from the baseline by a local decrease in the near-surface velocities (Figure 2.5a). Any repeat trace which is affected by this velocity decrease will show a timing delay to its corresponding baseline trace. A delay matrix $\mathbf{M}$ is gathered by measuring the relative time shifts between baseline and repeat traces from trace-wise cross-correlations (Figure 2.5b). If the delays are related to surface locations, the relative time shifts will align along rows and columns of $\mathbf{M}$. If they are related to CMP locations, the relative time shifts will align along the diagonals which cross $\mathbf{M}$ from the lower left to the upper right. In the next step, $\mathbf{M}$ is decomposed into $\mathbf{s}$ and $\mathbf{r}$, which directly should reflect the surface-related changes (Figure 2.5c). This solution can then be used to tie the repeat traces to the baseline traces on a surface-consistent basis. It is interesting to note that the search for $\mathbf{s}$ and $\mathbf{r}$ can be considered as an inverse problem for which an outline will be given in the following description of the geoelectric method.

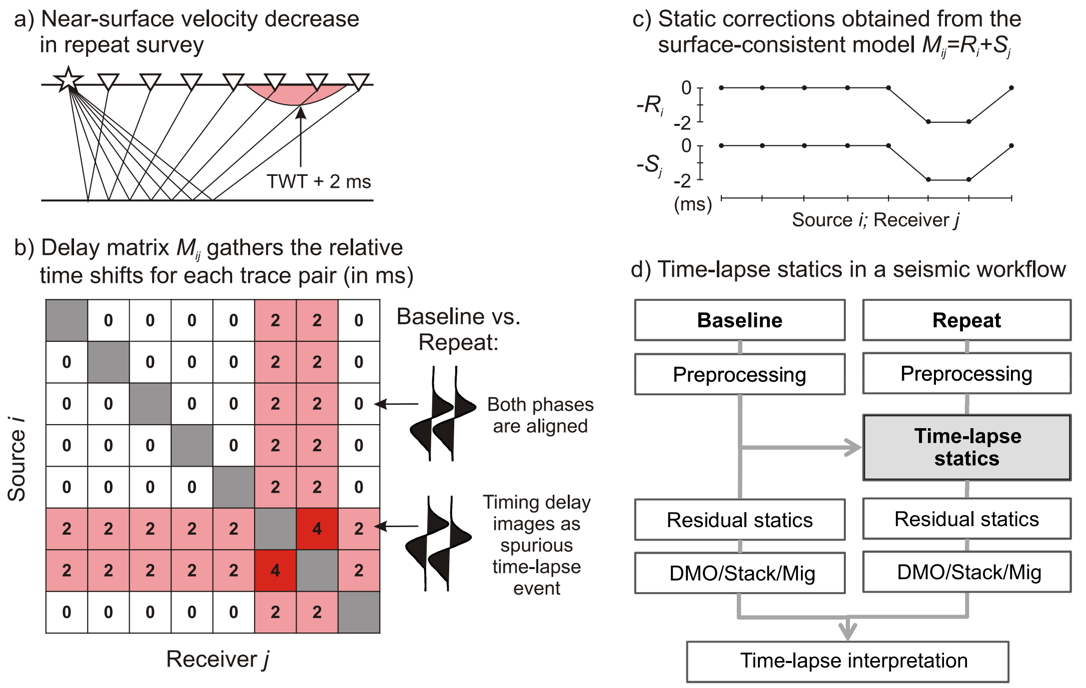

Figure 2.5: Schematic concept of the time-lapse static corrections to correct for temporal variations in near-surface velocity. a) Time-lapse seismic survey with a local decrease in near-surface velocity (pink patch) which delays passing rays by 2 ms. b) Delay matrix M_{ij} gathering the relative time shifts of baseline and repeat traces. Shot and receiver locations affected by the velocity decrease are given in pink. c) Decomposition of M_{ij} into source and receiver components yields static corrections. d) Integration of the time-lapse static corrections in a reflection seismic workflow.

2.2 Electrical resistivity tomography (ERT)

2.2.1 Background on ERT

The ERT method, here also referred to as geoelectric method, uses artificial electrical currents to investigate the distribution of electric resistivity within the subsurface. It comprises the second methodological emphasis of this thesis, and its application to CO_2 storage monitoring is motivated by the expected change in rock resistivity, when electrically well conductive brine is substituted by insulating CO_2 (Christensen et al., 2006; Nakatsuka et al., 2010). In section 1.5 the fundamental differences between reflection seismic and geoelectric imaging have been discussed. A main feature of ERT, which is also one of the main reason for the discussed differences, is the utilization of diffusive electric fields, as expressed in the governing Poisson's equation (e.g. Telford et al., 1990)

$$\nabla \cdot \left(\frac{1}{\rho} \nabla \varphi \right) = -I \, \delta(\vec{r} - \vec{r}_s) \; . \tag{2.15}$$

It entails that electric current flow is determined by the spatial arrangement of electrical sources (and sinks) as well as the distribution in electric resistivity ρ. Both factors specify the electric

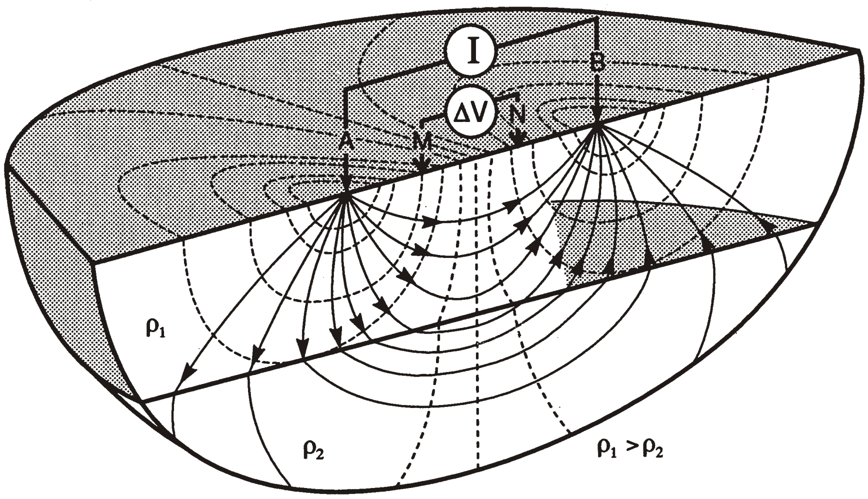

Figure 2.6: Schematic illustration of a four-point electrode arrangement after Lange (1997). Current flow lines (solid) and equipotential lines (dashed) are given for a two-layer case with higher resistivity in the first layer.

potential φ, to which gradient the current flow aligns. The right hand side of equation 2.15 places an infinitesimal source (represented by Dirac's delta) at $\vec{r}_s$, releasing an electric current I. If this source would be located on a perfectly uniform half-space with a resistivity of ρ_0, the potential could be given by

$$\varphi(\vec{r}) = \frac{I\rho_0}{2\pi|\vec{r} - \vec{r}_s|} \; . \tag{2.16}$$

A combination of current sources can be given by the superposition of their individual potential distributions. Due to the conservation of electric charge, the practical field experiment is typically carried out by a current circuit, which is realized through a pair of current electrodes (A and B). A further pair of potential electrodes (M and N) is used to measure spatial differences in φ, i.e. the electric voltage U. This so-called four-point layout is schematically illustrated in Figure 2.6.

Geoelectric surveying is commonly performed by using multiple pairs of current electrodes and voltage electrodes with an aim to achieve a dense sampling of the imaging target. From the injected current I and the measured voltage U, one can calculate a resistivity R. This resistivity shows a strong dependence on the geometrical arrangement of the electrodes. Using a uniform half-space again, it is possible to compute geometrical correction factors k which convert readings of R into apparent resistivity values ρ_{app}:

$$k \cdot \frac{\varphi(\vec{r}_2) - \varphi(\vec{r}_1)}{I} = k \cdot \frac{U}{I} = k \cdot R = \rho_{app} \; . \tag{2.17}$$

The apparent resistivity represents a weighted mean on the actual resistivity distribution $\rho(\vec{r})$. For ERT, they pose the starting point for assessing the earth's true resistivity by means of inverse procedures.

If the electrodes are placed on the surface, the geometric factor k reads (e.g. Kearey et al., 2002)

$$k = \frac{2\pi}{\frac{1}{AM} - \frac{1}{AN} - \frac{1}{BM} + \frac{1}{BN}} \ . \tag{2.18}$$

For current injections below the surface, e.g. electrodes in wells, the positions of the mirrored current electrodes A' and B' also have to be taken into account

$$k = \frac{4\pi}{\frac{1}{AM} + \frac{1}{A'M} - \frac{1}{AN} - \frac{1}{A'N} - \frac{1}{BM} - \frac{1}{B'M} + \frac{1}{BN} + \frac{1}{B'N}} \ . \tag{2.19}$$

2.2.2 Electric resistivity for brine/CO$_2$ substitution

Electrolytic ion transport is the most efficient conduction mechanism in fluid-filled sedimentary materials, in particular for those which are filled with highly salinized brines. The efficiency of the ion transport is determined by the ion concentration in the fluid and the connectivity of the pores (Kirsch, 2006). In first-order, porous sediments can be viewed as a composite system comprising the mineral matrix and the pore space. Similarly to the previous discussion, the pore-space may be filled with brine or CO$_2$ or a mixture of both. Since electrical resistivity of most matrix-building minerals is high, their contribution to electric current flow is provisionally neglected. Using this assumption, the empirical Archie equation (Archie, 1942) specifies the rock resistivity ρ with regard to the CO$_2$ saturation S_{CO2} as

$$\rho = \frac{A\rho_w}{\phi^m \left(1 - S_{CO2}\right)^n} \ . \tag{2.20}$$

ϕ denotes the rock porosity and ρ_w the resistivity of the initially present brine. The porosity exponent m reflects the pore geometry, compaction and insulation effects due to possible pore-space cementation. The saturation exponent n accounts for the presence of non-conductive fluid in the pore space. The factor A reflects the current component being conducted through the matrix. Since A, m, and n are purely empirical parameters, they need to be determined on an experimental or statistical basis. In situations where such a basis is not given, estimates often have to be drawn from literature values. For instance, the saturation exponent n is reported to be in the value range 1.715 for unconsolidated sediments and 2.1661 for sandstones (Lee, 2011). The porosity exponent m is reported to vary between 1.8 and 2.1 for sediments (Waxman and Thomas, 1974).

Archie-based resistivity models make two crucial assumptions: First, the pore-space mixture of brine and CO$_2$ is substituted with a virtual equivalent fluid. Electric current flow, however, is affected by complicated geometrical considerations, such as shape and connectivity of the pores and spatial arrangement of involved fluids within them. For example, Han et al. (2009) reported for fluid saturations < 0.2, that resistivity measured on clay-free sandstone can be notably lower than that predicted by Archie's law. They attributed this observation to liquid films that cover the rock grains and maintain considerable electric current flow even for very low fluid saturations. Secondly, the Archie equation assumes that electric current flow takes place solely within the pore-space. This is a severe simplification, because most sedimentary materials are also constituted from conductive minerals, such as clay.

Impact of clay content on rock resistivity

Electric resistivity in clay-bearing geologic materials has been often studied (e.g. Poupon et al., 1954; de Witte, 1955; Waxman and Smits, 1968; Butler and Knight, 1998) and various methods have been proposed to correct for the effect of clay on the formation resistivity (for an overview in the context of shaley sands see Worthington, 1985). Frohlich and Parke (1989) extended the Archie equation to a parallel connection of the pore-space resistivity and the clay-related resistivity ρ_s

$$\frac{1}{\rho} = \frac{\Phi^m (1 - S_{CO2})^n}{A} \frac{1}{\rho_w} + \frac{1}{\rho_s} \; . \tag{2.21}$$

In fact, ρ_s is also dependent on the clay content cc for which Rhoades et al. (1989) presented an empirical calibration (that yields ρ_s in mS/m)

$$\frac{1}{\rho_s} = \sigma_s = 2.3 \cdot cc - 0.0021 \; . \tag{2.22}$$

On the basis of the Archie model (equation 2.20) as well as the Frohlich and Parke model (equation 2.21) first-order resistivity descriptions of the Ketzin reservoir can be made: Norden et al. (2010) reported an average clay content of about 20% within the reservoir units. Taking this as input, we obtain a surface resistivity of 22.8 Ωm from equation 2.22. Following Kazemeini et al. (2010a) a porosity of 30% is assumed. In order to improve the choices of the remaining parameters, we adjust them by the results of laboratory data. Based on two core samples from the Ketzin site, Kiessling et al. (2010) reported an average resistivity ρ_0 of about 0.5 Ωm at full brine saturation. Still, A and m remain unknowns, but the ratio $\Phi^m \cdot A^{-1}$, the so-called formation factor, can be considered as a single unknown. Thus, given experimental knowledge about ρ_w, ϕ and the rock's resistivity for full brine saturation ρ_0, any set of A and m can be chosen which satisfies

$$A(m) = \frac{\Phi^m}{\rho_w} \left(\frac{1}{\rho_0} - \frac{1}{\rho_s} \right)^{-1} \; . \tag{2.23}$$

Selecting the porosity exponent m equal to 2, we obtain a value of about 1.24 for A. The respective models are shown in Figure 2.7 and generally agree in a rather moderate increase in resistivity for S_{CO2} <0.7. For larger saturations we can observe a more drastic resistivity increase with the respective maxima at full CO_2 saturation. This is a generic behaviour of Archie models, which has been well discussed regarding its potential for geoelectric monitoring of CO_2 migration (e.g. Hoversten and Gasperikova, 2005).

For CO_2 saturations up to about 70%, we find a rather neglible impact of clay. This can be explained by the (highly salinized) pore fluid which strongly exceeds the clay in terms of conductivity at low and intermediate CO_2 saturations. The difference in both models is considerable for high CO_2 saturations. In such a situation, the Archie model loses its fluid-related conduction, whereas the Frohlich & Parke model can preserve some conductivity through the clay.

This renders two implications for geoelectric monitoring of CO_2 storage: First, ERT will be less sensitive at low CO_2 saturations but will gain sensitivity as the CO_2 saturation increases. This was one of the main points in the discussion of the complementary sensitivity behavior of seismic and geoelectric methods with regard to CO_2 (section 1.5). Secondly, if quantitative estimation of

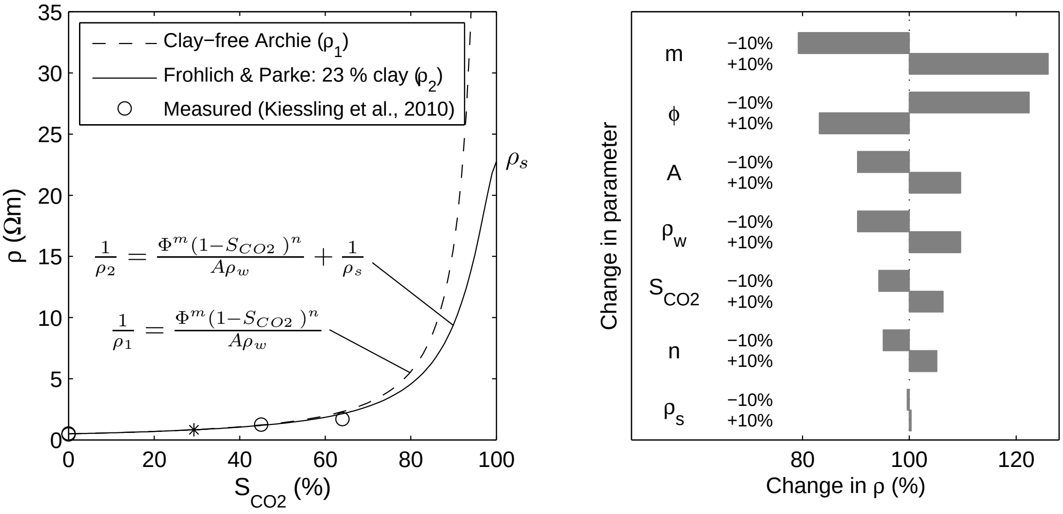

Figure 2.7: Left: Electric resistivity models as functions of the CO$_2$ saturation for the Ketzin reservoir model. A, m, and n were chosen to 1.24, 2 and 1.5, to fit experimental data reported by Kiessling et al. (2010). For further parameters of the reservoir model see text. Right: Change in model resistivity due to uncertainties in the resistivity model parameters. Analysis had been carried out for the Frohlich & Parke model with a CO$_2$ saturation of 30% (see star symbol in the left hand diagram). Estimation errors in the porosity exponent m and porosity ϕ can be seen to pose the strongest uncertainties on the resistivity predicted by the model.

CO$_2$ saturations from resistivity measurements is performed in clay-bearing materials at high CO$_2$ saturations, the utilized resistivity-saturaturation relations should be based on in-situ (laboratory) experiments or adequately calibrated clay models.
Assuming the Archie model to sufficiently describe the resistivity-saturation relation for the Ketzin reservoir to within low and intermediate CO$_2$ saturations, equation 2.20 can easily be used in reverse to estimate CO$_2$ saturations by

$$S_{CO2} = 1 - \left(\frac{A\rho_w}{\Phi^m \rho}\right)^{1/n} . \tag{2.24}$$

The use of the resistivity index RI (Guéguen and Palciauskas, 1994) allows us to substitute ρ_w with ρ_0 by

$$RI = \frac{\rho}{\rho_0} = (1 - S_{CO2})^{-n} . \tag{2.25}$$

Note that the parameters A and Φ^m become obsolete when using the ratio of two resistivities at different CO$_2$ saturations. The saturation exponent n is the only rock parameter required in equation 2.25. The rearrangment of this equation into

$$S_{CO2} = 1 - RI^{-(1/n)} = 1 - \left(\frac{\rho_0}{\rho}\right)^{1/n} \tag{2.26}$$

allows the estimation of the CO_2 saturation from a measured resistivity ρ and its baseline resistivity ρ_0. However, it is important to note that this assumes the porosity related parameters Φ^m and A to be constant throughout the fluid-substitution experiment (no dissolution or cementation).

2.2.3 ERT Inversion

Geophysical inversion generally aims to find models which sufficiently explain sets of observations, whereas 'sufficiently' indicates the restriction that such models can only be obtained within the limits given by the sparseness and noisiness of the input data. This often leads to the fact that many equivalent models can be used to explain a single set of observations. In consequence, geophysical inverse problems are notoriously ill-posed (Ellis and Oldenburg, 1994).
The geoelectric experiment yields apparent resistivities which are converted into estimates on the earth's true resistivity distributions through geophysical inversion. The inversion procedure divides into two main steps:

Forward operation

To allow for the computation of electric potentials by means of numerical methods, the investigation domain is parameterized, i.e. the continuous medium is transferred to a discretized representation. This is typically done by defining spatial elements on which computations are carried out. As far as ERT modeling is concerned, each spatial element is assigned to a resistivity ρ_i which defines the model vector $\mathbf{m}$. Likewise, the observed data are gathered in the data vector $\mathbf{d}$. Both vectors are connected through the forward operator $\mathbf{f}$ (given by equation 2.15)

$$\mathbf{d} = \mathbf{f}(\mathbf{m}) \,. \tag{2.27}$$

Various approaches have been introduced for the computation of electric potentials, covering finite-difference schemes (e.g. Scriba, 1981; Spitzer, 1995; Pidlisecky and Knight, 2008) and finite-element schemes (e.g. Pridmore et al., 1981; Wu, 2003; Rücker et al., 2006). Throughout this thesis the approach of Rücker et al. (2006) will be adopted, which operates on unstructured tetrahedral grids. This proved to be necessary, because it generally not only permits us to accurately include arbitrary electrode positions or surface topography, but also internal structure surfaces. Moreover, the use of unstructured meshs was an important pre-requisite for the inversion of the Ketzin surface-downhole ERT surveys. The survey geometry of these measurements comprises a spatial extent that is in the order of kilometres and embeds electrode spacings which are in the order of meters. In fact, parameterizations by means of regular grids would have resulted in numerically extremely demanding inversions. The use of an unstructured parameterization was found to be of great value here, since it allows for the integration of these scale differences into a single mesh (further details on the mesh construction will be given in section 2.4.1). This point will be addressed in more detail in chapter 5.

Inverse procedure

Since the sought model cannot directly be assessed from $\mathbf{f}^{-1}(\mathbf{d})$, the inverse procedure aims to search for models which minimize the discrepancy vector $\mathbf{d} - \mathbf{f}(\mathbf{m})$. This discrepancy is most often expressed in a scalar data misfit Φ_d through least-squares (ℓ_2-norm):

$$\Phi_d(\mathbf{m}) = \sum_{i=1}^{N_d} |d_i - f_i(\mathbf{m})|^2 = \|\mathbf{d} - \mathbf{f}(\mathbf{m})\|_2^2 \ . \tag{2.28}$$

In order to handle the variety of possible models which pose a minimization, Φ_d is typically amended by a model misfit Φ_m into the objective functional Φ (e.g. Ellis and Oldenburg, 1994):

$$\Phi = \Phi_d + \lambda\Phi_m = \|\mathbf{d} - \mathbf{f}(\mathbf{m})\|_2^2 + \lambda \left\|\mathbf{m} - \mathbf{m}^0\right\|_2^2 \ . \tag{2.29}$$

$\mathbf{m}^0$ is herein the reference model and λ the regularization parameter which balances the combination Φ_d and Φ_m (Zhdanov, 2002). In connection to homogeneous reference models, the regularization parameter can be used to control the smoothness of the result. Strong regularizations (large λ) yield smooth models, whereas weak regularizations (small λ) permit contrasts. The first case generally produces better data misfits than the latter case, due to resistivity contrasts that are allowed to build up in the models. However, too low regularizations accentuate spurious features in the models. This leads to Tikhonov-type trade-off decisions (Tikhonov, 1963), in which specific choices for optimal regularizations have to be made. For the selection of a regularization parameter in a specific problem, one typically carries out a number of inversions with variable regularization. Inverted models are then arranged into so-called L-curves such as that given in the example of Figure 1.4. Based on these L-curves, a regularization can be opted from geometrical criteria such as those given by Hansen and O'Leary (1993) (point of maximum curvature; see Vogel (1996) for problems on this) or Aster et al. (2005) (minimum distance to origin).

Additional regularization on the objective functional can be introduced by the weighting matrices $\mathbf{W}_d$ and $\mathbf{W}_m$:

$$\Phi(\mathbf{m}) = \|\mathbf{W}_d\left(\mathbf{d} - \mathbf{f}(\mathbf{m})\right)\|_2^2 + \lambda \left\|\mathbf{W}_m\left(\mathbf{m} - \mathbf{m}^0\right)\right\|_2^2 \ . \tag{2.30}$$

The matrix $\mathbf{W}_d = diag(1/\epsilon_i)$ contains the inverse data weights ϵ_i, for which Ellis and Oldenburg (1994) suggest the standard deviations, and Günther et al. (2006), in a more general sense, any normalized error metric which is derived from the data. Likewise, $\mathbf{W}_m$ contains weights for the individual model cells. Typically the root-mean-square value of $\mathbf{d} - \mathbf{f}(\mathbf{m})$ or $\chi^2 = \Phi_d/N$ are used to judge whether a minimization step was successful. Ellis and Oldenburg (1994) advocate the χ^2, because it takes the data errors through $\mathbf{W}_d$ into consideration. Ideal fits with respect to corresponding error models or error estimates yield χ^2 values near 1. Since the rms of the data misfit always converges towards a limiting value representing the amount of noise in the data, it does not indicate how well the data have been fitted with regard to their intrinsic error (Olayinka and Yaramanci, 2000a). Throughout this thesis the χ^2 value will therefore mainly be used in order to assess the quality of the inverted models.

The inversion is intiated from a starting model which is commonly identical to the reference model $\mathbf{m}^0$. Throughout the inversion, the model is updated by model changes. In the k^{th} iteration, when the model $\mathbf{m}^k$ is updated to model $\mathbf{m}^{k+1}$, this reads

$$\mathbf{m}^{k+1} = \mathbf{m}^k + \tau^k \triangle\mathbf{m}^k \ . \tag{2.31}$$

Here, $\triangle\mathbf{m}^k$ is the direction of model change and τ^k the step length of model change. Each iteration is confronted with a one-dimensional search for an optimum step length which minimizes Φ most efficiently (line search). Because Φ is a least-squares functional, $\Phi(\mathbf{m}^k + \tau^k\triangle\mathbf{m}^k)$ is parabolic when parameterized by τ^k. This requires the computation of $\Phi(\mathbf{m}^k + \tau^k\triangle\mathbf{m}^k)$ at only some locations. The actual line search is then carried out on the function which is interpolated from those values (inexact line search). The direction of model change can, for example, be obtained from the Gauss-Newton method to (e.g. Günther et al., 2006):

$$\triangle\mathbf{m}^k = \left(\mathbf{S}^T\mathbf{W}_d^T\mathbf{W}_d\mathbf{S} + \lambda\mathbf{W}_m^T\mathbf{W}_m\right)^{-1} \cdot \left[\mathbf{S}^T\mathbf{W}_d^T\mathbf{W}_d\left(\mathbf{d} - \mathbf{f}(\mathbf{m}^k)\right) - \lambda\mathbf{W}_m^T\mathbf{W}_m\left(\mathbf{m}^k - \mathbf{m}^0\right)\right] . \tag{2.32}$$

$\mathbf{S}$ denotes the Jacobian matrix obtained from linearization of equation 2.29 (see McGillivray and Oldenburg, 1990), given by

$$S_{ij} = \frac{\partial f_i(\mathbf{m})}{\partial m_j} . \tag{2.33}$$

Summing the sensitivities for the individual measurements yields the coverage, which can be used as a measure for the spatial illumination provided by a survey geometry. The inversion comprises the inverse procedure and the forward operation to be performed in alternation until Φ stagnates or the data are fitted within their errors ($\chi^2 \approx 1$).

For the processing of time-lapse data, the inverse procedure can be performed in sequential or simultaneous order (e.g. Hayley et al., 2011). There are also time-lapse inversion strategies that use the differences or ratios to the baseline data (e.g. LaBrecque and Yang, 2001; Hayley et al., 2011). For the Ketzin data, time-lapse inversions have been performed through the control of the starting model $\mathbf{m}^0$. The resistivity model resulting from the baseline inversion was used as input model to the subsequent timesteps.

2.3 Constrained ERT inversion

So far, intrusion into the inversion is restricted to controlling the smoothness of the inverted models by means of the regularization. However, in the beginning of an inversion one might be aware of realistic parameter ranges or have detailed knowledge about them from well logs. Where sedimentary formations are known to be strongly stratified, the resistivities can be expected to be anisotropic to some extent. Or, as a particular task of this thesis, one might know that a prominent geologic structure is present which should be considered by the inversion accordingly. In the end, any model obtained from a geophysical inversion is required to be plausible in terms of geology. Likewise, it seems sensible to integrate respective geological constraints already into the inversion.

In recent years numerous studies have addressed the incorporation of a priori information into the inversion of geophysical data (e.g. Pedersen, 1979; Pous et al., 1987; Backus, 1988; Portniaguine and Zhdanov, 1999; Yi et al., 2003; Gholami and Siahkoohi, 2009). As far as this thesis is concerned, I will adopt the ideas of Ellis and Oldenburg (1994); Günther et al. (2006); Günther and Rücker (2006) to implement structural constraints in the inversion of the Ketzin data sets.

2.3.1 Constraint formulation

In the following, three types of constraints will be highlighted: (1) Parameter bounds which enforce resistivities to be bounded within certain ranges, (2) directional weighting of the model misfit which can be used to stimulate an anisotropic appearance of the resulting models, and (3) incorporation of structural information by means of local regularization.

Parameter bounds: Prior to the inversion it might be known that the true resistivity of a cell i is in the range $a_i < m_i < b_i$. Following the approach of Kim et al. (1999), m_i can be substituted by the transformed parameter

$$m_i' = ln\left(\frac{m_i - a_i}{b_i - m_i}\right) \ . \tag{2.34}$$

This causes the values $m'(a)$ and $m'(b)$ to be scaled to negative to positive infinity. The new direction of model change is then given by

$$\triangle m_i' = \frac{b_i - a_i}{(m_i - a_i)(b_i - m_i)} \triangle m_i \ . \tag{2.35}$$

Back-substitution for use in equation 2.31 leads to

$$\triangle m_i^k = \frac{a_i\left(b_i - m_i^k\right) + b_i\left(m_i^k - a_i\right) e^{\triangle m_i'}}{b_i - m_i^k + \left(m_i^k - a_i\right) e^{\triangle m_i'}} \ . \tag{2.36}$$

Directional weighting: Following the approach of Ellis and Oldenburg (1994), $\mathbf{W}_m$ can be constructed in such a way that horizontal or vertical structures are pronounced

$$\begin{aligned}\mathbf{\Phi}_m &= \left\|\mathbf{W}_m\left(\mathbf{m} - \mathbf{m}^0\right)\right\|_2^2 \\ &= \alpha_s\left\|\mathbf{W}_s\left(\mathbf{m} - \mathbf{m}^0\right)\right\|_2^2 + \alpha_l\left\|\mathbf{W}_l\left(\mathbf{m} - \mathbf{m}^0\right)\right\|_2^2 + \alpha_z\left\|\mathbf{W}_z\left(\mathbf{m} - \mathbf{m}^0\right)\right\|_2^2 \ .\end{aligned} \tag{2.37}$$

$\mathbf{W}_s$, $\mathbf{W}_l$, $\mathbf{W}_z$ can be used to separately control the similarity to the reference model, the lateral variation of the model, and the z-variation of the model, respectively. Horizontal weighting by means of $\mathbf{W}_l$ can, for instance, be reasonable when the subsurface is dominated by subhorizontal layering.

Structural constraints: The model norm in equation (2.30) allows model cells to be individually weighted by the entries $\mathbf{W}_m$. This might for instance be useful to down-weight cells that are poorly covered by a survey geometry. Günther and Rücker (2006) suggest a generalization of $\mathbf{W}_m$ by introducing two additional matrices:

$$\left\|\mathbf{W}_m\left(\mathbf{m} - \mathbf{m}^0\right)\right\|_2^2 \rightarrow \left\|\mathbf{W}_m\mathbf{C}\mathbf{W}_c\left(\mathbf{m} - \mathbf{m}^0\right)\right\|_2^2 \ . \tag{2.38}$$

$\mathbf{C}$ denotes the roughness operator which specifies the neighbour-relations among the cells and $\mathbf{W}_c$ the according interdependency weights. A fully weighted $\mathbf{W}_c$ realizes a uniform regularization, i.e.

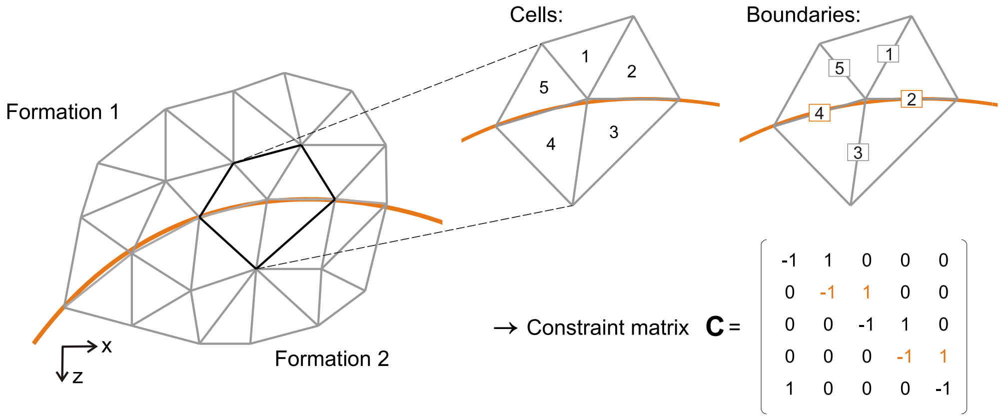

Figure 2.8: Example for the compilation of the constraint matrix $\mathbf{C}$. Tetrahedral parameterization along a structural change separating two formations (left). The example comprises a subset of the parameterization with five cells and five boundaries which define the elements of $\mathbf{C}$ (upper right). The orange line shows the position of the structural boundary, which is embedded in the parametrization. The lower right part of the figure shows in orange those matrix elements of $\mathbf{C}$ that correspond to the boundaries.

regular inversion. In the previously mentioned directional weighting, it was seen that a uniform regularization may be given up in favour of inversions which, for example, pronounce lateral structures. In addition, the individual entries of $\mathbf{W}_c$ can be used to down-weight the strength of interdependence for specified boundary segments. In fact, this suppresses the smoothing of the regularization which, in local parts, returns more freedom to the model. Consequently, modification of $\mathbf{CW}_c$ can be used to permit resistivity contrasts across structural boundaries and retain a uniform regularization in more homogeneous regions of the model.

2.3.2 Implementation of structural constraints

Figure 2.8 shows an example of how the constraint matrix $\mathbf{C}$ may be assembled for a mini-subset of an arbitrary tetrahedral mesh. Non-zero elements of $\mathbf{C}$ constitute the neighbor-relations among the cells, i.e. columns represent the model cells and rows represent the cell boundaries. For example, the first column specifies that cell 1 is linked to boundary 1 and 5. In reverse, the fifth row specifies that boundary 5 is linked to cell 1 and 5. Both cells are connected through a common face and marked with values of opposite sign.

Figure 2.9a depicts a situation which refers to the example given in Figure 1.3e. Here, a structural boundary of finite lateral extent has been placed into the model. The interdependency strengths of the model cells are indicated by blue lines joining the cell midpoints (Voronoi diagram). These interdependency strengths can be re-weighted as given in equation 2.38. Interdependence weights in the inversion example of Figure 1.3e have been set to zero across the structural boundary which enables a suppression of the regularization (indicated by missing connections in Voronoi diagram).

In the last example, the resistivity image obtained from the constrained inversion is investigated in more detail. Therefore, a simple model is investigated, which integrates the main geometrical

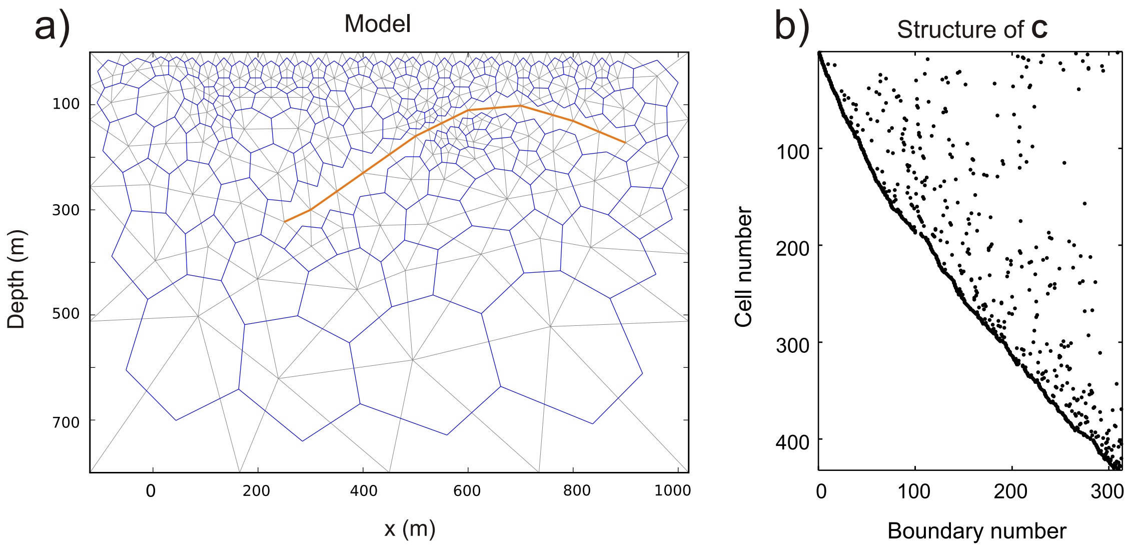

Figure 2.9: a) Geometrical representation of interdepency strengths for inversion mesh shown in Figure 1.3e. Model cells (thin gray lines) and anticlinal boundary structure (orange) are shown. Strength of interdependence for neighbouring cells (elements of $\mathbf{W}_c$) are represented by the Voronoi diagram of the cell triangularization (blue). b) Sparsity pattern of the constraint matrix $\mathbf{C}$.

features of the surface-downhole ERT at the Ketzin site. Consequently, this investigation is not only relevant for the evaluation of the constrained inversion, but also for the subsequent application to the real data. The model comprises two wells representing the situation at the Ketzin wells Ktzi200 and Ktzi201 (Figure 2.10a). Each well is equipped with 15 electrodes which are placed with a vertical spacing of 10 m. Electric current dipoles are located at the surface and voltage measurement is simulated for the surface dipoles as well as downhole dipoles. A CO_2 distribution was inserted, that is based on a fluid-flow simulation of a CO_2 migration in a homogeneous sandstone layer. Details regarding this simulations will be presented in chapter 3.

For inversion of modelled resistivities, a structural boundary was inserted along the reservoir caprock boundary, similar to that which was used in the fluid-flow simulations. Inversions were carried out with variable regularization and constraint strengths, and were then arranged into L-curves (Figure 2.10b). An overview on the inverted models is illustrated in the selective examples of Figure 2.11. In general, inverted models show that, within certain ranges of the regularization, the true model can be reconstructed to some extent.

When analyzing the rows in Figure 2.11 from top to bottom, one finds that the increasing constraint strength is aligned to a build-up in resistivity contrast across the reservoir-caprock boundary. It appears that here the constrained model is permitted to relax towards stronger contrasts, since it is only partly a subject to the smoothing of the regularization. Correspondingly, one can find from Figure 2.10b that this is connected to a shift of the L-curves towards lower data misfits.

It is observable, that the L-curves are generally similar in appearance, i.e. the shape of the L-curve for the regular inversion seems to be roughly preserved when the constrained strength is increased. In consequence, searching procedures for optimal regularizations can be transferred to the constrained

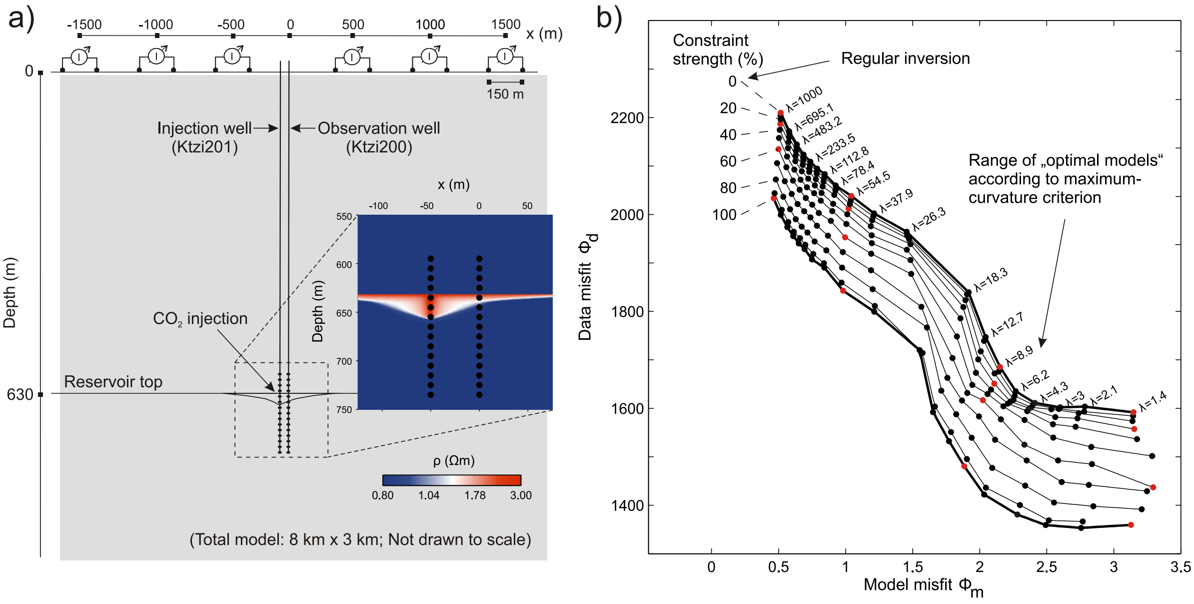

Figure 2.10: a) Synthetic forward model and b) L-curves of inverted models for variable constraint strength. For a better comparability of the results, the sensitivities have not been recalculated in the individual inversion iterations. Inverted models indicated by the red dots are shown in Figure 2.11.

models, and hints for appropriate ranges can already be deduced from the regular inversions. In summary, the models indicate that a structural constraint along the reservoir top can yield a better delineated resistivity image alongside with a decreased data misfit.

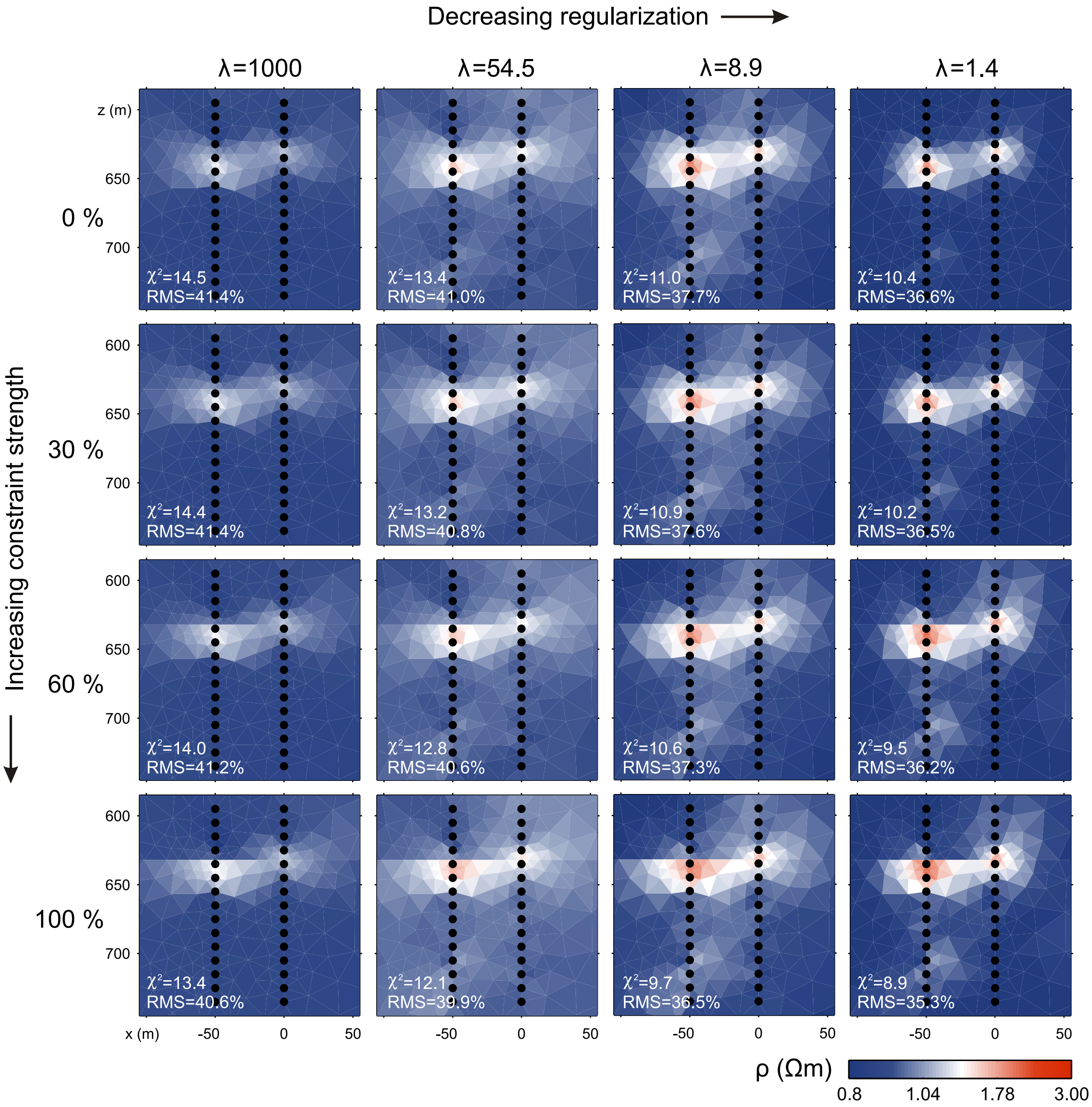

Figure 2.11: Resistivity models selectively illustrating the impact of the regularization and constraint strength on the inversion (see red dots in Figure 2.10b). The top row represents the results of a regular inversion with uniform regularization. Input data to the inversions are apparent resistivities that were computed from the synthetic model given in Figure 2.10a. These apparent resistivities have been weakly noisified which yields relatively high χ^2 errors. Note that an increase in constraint strength leads to an improved data fit.

2.4 Practical aspects

Before proceeding with how the meshes are constructed, I would like to briefly elaborate on another aspect which seems to be of crucial importance. The proposed constrained inversion workflow intends to combine reflection seismics and electric resistivity tomography. In terms of planning seismic and geoelectric acquisition geometries for a common imaging target, it could be a potential pitfall that ERT coverage and seismic fold act spatially disparate.

The coverage in geoelectric surveying is best where current density is highest, e.g. near the electrodes. This causes the ERT coverage to decrease with increasing depth when electrodes are deployed at the surface only. In contrast, the image of a surface-based seismic survey is conditioned by the arrangement of first-break coda, ground-roll, and NMO stretching within the acquired seismograms. These effects define an optimal window (Pelton, 2005) from which the seismic image is deduced and cause the fold to increase with depth. As a consequence of combined surveys, it is recommendable to consider the individual imaging characteristics of both methods priorily in a joint manner.

In the particular case of a time-lapse survey design, seismic and geoelectric survey periods are ideally aligned to each other. Practical realization, however, might be difficult due to logistic matters and coinciding access demands. In fact, this implication applies only partly proposed constrained inversion workflow, because the inserted structural constraints will be static by nature. As the workflow arranges both methods sequentially, it requires a baseline seismic processing and structural interpretation to be carried out before the constrained ERT inversion. However, it is also important to evaluate whether a structure interpreted from seismic reflection also comprises sufficient petrophysical relevance for ERT imaging. As the constrained inversion approach assumes a structural similarity, it is crucial to note that not every contrast in elastic parameters also comprises a contrast in electric resistivity. Finally, this issue is linked to the discussion about the differences in seismic and geoelectric imaging with regard to the petrophysical domain (section 1.5). For the inversion of the Ketzin data sets, this issue will be revisited in section 6.5.1 by an analysis of well logs from the Ketzin site.

2.4.1 Model parameterization

For the geoelectric part of this thesis, the open-source software code BERT (Boundless Electrical Resistivity Tomography, www.resistivity.net) was mostly used. This code combines a finite-element forward operator (Rücker et al., 2006) with a Gauss-Newton inverse procedure (Günther et al., 2006). During the practical implemention of the structural constraints it was found that the actual model parameterization plays a major role in the definition of the inverse problem, which will therefore be addressed in more detail below.

An appropriate model parameterization has to fulfill two requirements: First, it must represent the structural setting adequately, e.g. topography, internal constraint boundaries, and eventually faults. Secondly, it must allow for an accurate and efficient inversion. Generally, the ill-posedness of the inverse problem (as well as the numerical demand) depends on the number of model cells. It has been pointed out in section 2.2.3 that the scale differences inherited by Ketzin surface-downhole experiments gave preference to a tetrahedral model parameterization. This brings up a further implication which is given by the fact that the tetrahedra cannot be fully arbitrary in shape,

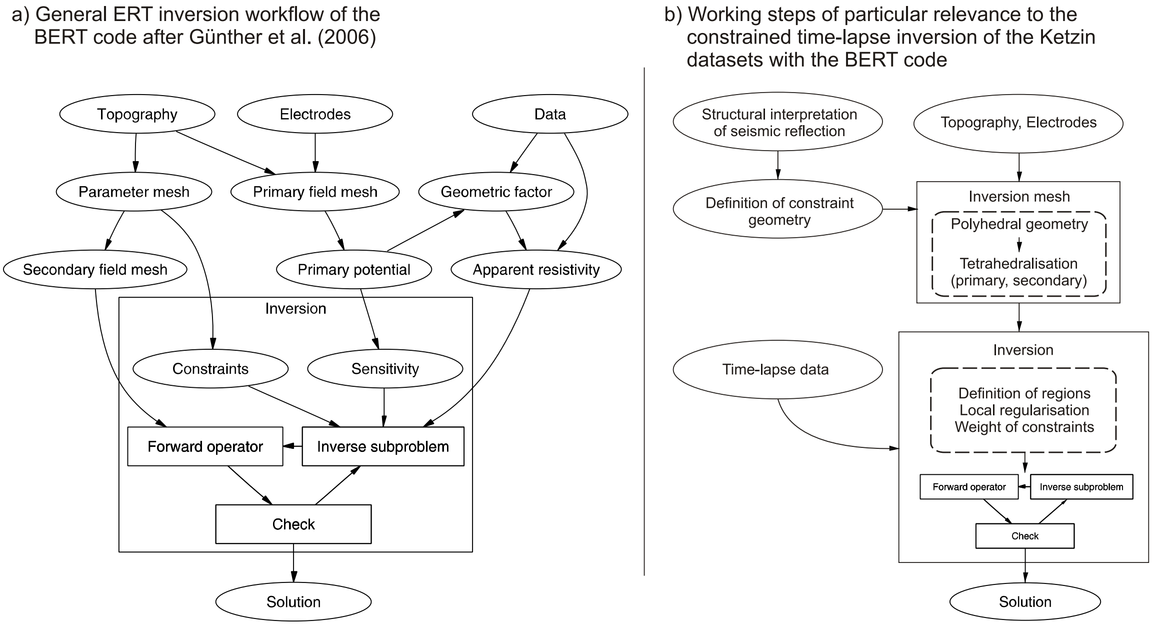

Figure 2.12: Inversion schemes of the BERT code. The frames indicate the central loop of the forward and inverse step until the stopping criterion is reached and a solution is obtained.

since very flat or distorted tetrahedra, so-called slivers, penalize the accuracy of the finite-element operation.

The basic principle of the mesh parameterization by means of triangles (2D) or tetrahedra (3D) is the Delaunay triangularization. This procedure inherently aims to maximize the minimum angle occurring in a triangularization. There are several metrics which allow assessment of the shape-related quality of the tetrahedra (for a discussion see e.g. Parthasarathy and Hathaway, 1994). A specific metric is the radius-edge ratio Q which is based on the circumsphere that is defined by the four corner points of a tetrahedron. The radius-edge ratio is given by $Q = R/L$, where R is the radius of the circumsphere and L is the length of the shortest edge. As a rule of thumb, Q is smaller than 2.5 for properly shaped tetrahedra. However, there can be specific situations where slivers show Q values below that. Regular tetrahedra, for which the six edges are in equal length, achieve the minimal Q of about 0.612. An upper bound for Q should be specified for the triangularization and visual inspection should be carried out at locations where this bound is not met.

In combination with the BERT code, the triangularization precedes the inversion and can be carried out with the mesh generation packages of Shewchuk (1995) and Si (2003, 2008). The rough framework which is filled by the triangularization is defined by piece-wise linear complexes (PLC). PLCs are polygonal descriptions which contain the overall geometrical features, such as external and internal boundaries, boundary conditions, and electrode positions. Once the PLC definition and triangularization have been performed, the mesh can be passed on to the actual BERT inversion procedure (Figure 2.12).

In order to overcome the strong gradients in electric potential near the electrodes, BERT employs a

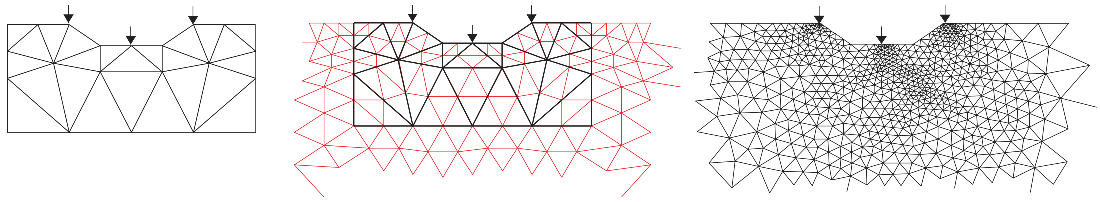

Figure 2.13: Example for the three meshes used by BERT after Günther et al. (2006): Parameter mesh (left), secondary field mesh (centre), and primary field mesh (right).

triple-grid approach (Günther et al., 2006). The strong gradients are caused by the singularities in the electrode positions (see Dirac's delta in equation 2.15) and would require the mesh to be highly refined in the vicinity of the electrodes. As a solution, Coggon (1971) suggested the potential field to be separated into a field that derives from a uniform resistivity distribution (primary field) and a field that derives from the variations in the resistivity distribution (secondary field). Rücker et al. (2006) implemented this approach by carrying out computations on three meshes (Figure 2.13):

- The **paramater mesh** defines the inversion domain.
- The **secondary field mesh** is a refined and elongated version of the paramater mesh on which electric potentials with regard to spatial variation in the current resistivity model are computed. Elongation takes place to avoid boundary effect within the inversion domain.
- The **primary field mesh** is similar to secondary field mesh but highly refined in the vicinity of electrodes positions. The primary field mesh is used once prior to the inversion in order to compute electrode potentials that include the gradients near the electrodes.

Figure 2.14 illustrates how these meshes were arranged for the inversion of the Ketzin surface-downhole ERT measurements.

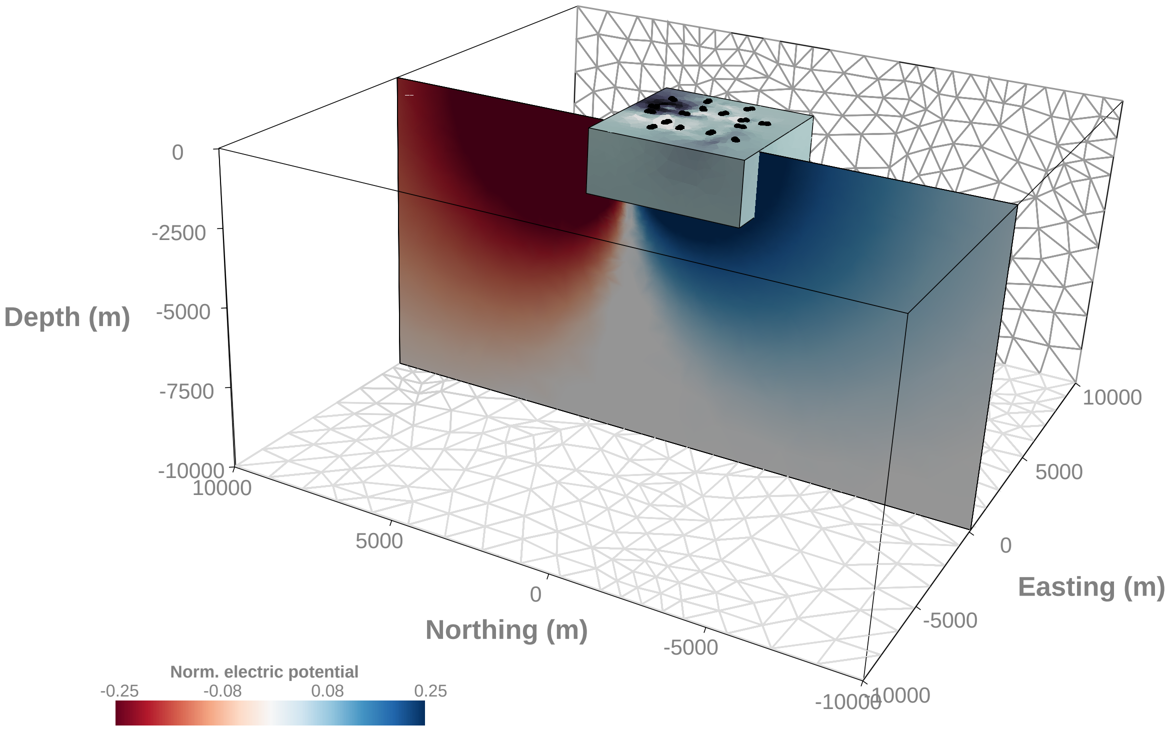

Figure 2.14: Example of the meshes used for the inversion of the Ketzin 3D surface-downhole data sets. The extent of the inversion domain is represented by the gray cube in the center. Black dots on top of the gray cube indicate positions of surface dipoles. The inversion domain is embedded into a larger cube on which potential field computations are performed. Meshs shown on the bottom and backside of this cube belong to the secondary field mesh. The colored plane represents a slice through the 3D electric potential from a forward modelling. Not shown here is the feature that the mesh refines towards the center of the inversion domain where the borehole electrodes are located.

Conclusions from this chapter

The main findings of this chapter can be summarized as follows:

- Replacement of brine by CO_2 leads to an adverse response in seismic p-wave velocity and electric resistivity (decrease in v_p, increase in ρ).
- CO_2-induced changes in v_p and ρ can take place in complementary ranges of CO_2 saturation.
- Based on a first-order Ketzin model, the replacement of brine by CO_2 can be assessed to reduce the initially negative (normal incidence) reflection coefficient of the Ketzin reservoir.
- Seismic monitoring can benefit from analyses of the time-lapse AVO response.
- ERT imaging can benefit from an incorporation of structural information that is interpreted from seismic reflection. Consequently, there is a potential to enhance geophysical monitoring of CO_2 storage by a sequential coupling of seismics and ERT by means of common structural constraints.

3

Synthetic investigations

Publication I

Modelling the geoelectric and seismic reservoir response caused by carbon dioxide injection based on multiphase flow simulation: Results from the CO_2SINK project

P. Bergmann[1], U. Lengler[1], C. Schmidt-Hattenberger[1], R. Giese[1], and B. Norden[1]

Published in Chemie der Erde - Geochemistry 70, S3, pp. 173–183, August 2010

Contents

Abstract: Results from crosshole geoelectric and surface seismic monitoring for geological storage of carbon dioxide (CO_2) were investigated by forward modelling within the framework of the CO_2SINK project. Selected geological and petrophysical parameters reflect the conditions of the CO_2SINK site. CO_2 saturation distributions were derived from multiphase flow modelling, whereas the alteration of the geophysical rock properties by CO_2 was obtained from laboratory experiments. Crosshole geoelectric modelling was performed for three electrode combinations and three time-dependent CO_2 migration scenarios with different reservoir permeabilities. The magnitude and alteration of modelled

---

[1] Helmholtz Centre Potsdam, GFZ German Research Centre for Geosciences, Centre for CO_2 Storage, Telegrafenberg, 14473 Potsdam, Germany

resistances were analyzed in the pre-inversion domain. Time-lapse alterations were observable on the synthetic data, with diverse characteristics dependent on applied electrode configuration. Analysis of the alterations showed the opportunity to differentiate the migration scenarios within the constraints of the ambient noise level.
The synthetic time-lapse seismic reflection experiment was performed for the anticline used for CO_2 storage. The geological model incorporates the structural framework, as determined from the seismic interpretation, and velocities derived from seismic processing and velocity logs. Common depth point (CDP) processing of the synthetic shot gathers of a baseline and repeat experiment provided the data for a difference stack section exhibiting a CO_2 induced time-lapse signature. Interpretation of the signature in conjunction with the underlying CO_2 distribution has shown that the lateral extent of the plume may be accurately detected. The vertical plume extent is concealed in the waveform coda and is unlikely to be retrievable from standard seismic processing.

3.1 Introduction and objectives

CO_2 capture and storage in deep geological formations is an option for reducing greenhouse gas emissions into the atmosphere (IPCC, 2005). Saline aquifers are thought to be the most promising type of geological storage for power plant-captured CO_2 in Europe, as they exceed depleted oil and gas fields in terms of ubiquity and storage capacity. The CO_2SINK project was initiated in 2004 to investigate the storage of CO_2 within an onshore saline aquifer near the town of Ketzin, Germany (Figure 3.1).
The project aims to improve the understanding of in-situ physical, chemical and biological processes, provide practical and operational experience and to assist in the development of standards and regulations for future geological storage of CO_2. A primary task involved in achieving these aims is the development and testing of efficient geophysical monitoring procedures. The CO_2SINK site is situated in the eastern part of the Roskow-Ketzin double anticline (Figure 3.1). The anticline was formed above an elongated salt pillow situated at a depth of 1500–2000 m (Förster et al., 2006). One injection well (CO2 Ktzi201) and two observation wells (CO2 Ktzi200 and CO2 Ktzi202) were drilled into the southern flank of the Ketzin anticline in 2007. The condensed lithology of CO2 Ktzi200 is depicted in Figure 3.2.
The Stuttgart Formation within the Triassic Keuper section is used as the injection reservoir. It is lithologically heterogeneous, consisting of sandy channel-(string)-facies rocks with good reservoir properties alternating with muddy floodplain facies rocks of poor reservoir quality (Förster et al., 2006; Norden et al., 2008). All wells penetrate into the Stuttgart Formation to depths of 750-810 m. From well cores, the sandy channel-(string)-facies sandstones intended to be used for injection were found to occur with varying thickness at depths of 630-650 m. Since 30th June 2008, food-grade quality CO_2 has been injected into the saline-water-bearing sandstone units via CO2 Ktzi201. The upper seal of the Stuttgart Formation is the Weser Formation, consisting mainly of clayey and sandy siltstones that alternate with carbonates and evaporites (Beutler and Nitsch, 2005). The high clay mineral content and the observed pore-space geometry make these rocks a suitable seal for the CO_2 storage reservoir (Förster et al., 2007). The Weser Formation is overlain by mud/clay-carbonates of the Arnstadt Formation (Beutler and Nitsch, 2005), which exhibits similar sealing properties. The geophysical monitoring programme at the Ketzin site is mainly based on electrical resistivity

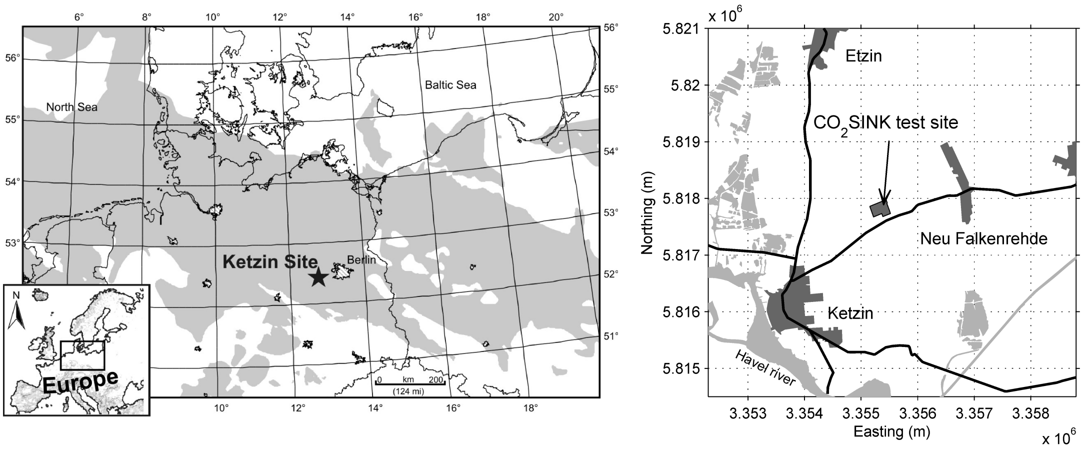

Figure 3.1: Left: Location of the Ketzin site in the mid-European Permian Basin (gray shaded). Figure taken from Förster et al. (2006). Right: Detailed view of the site location.

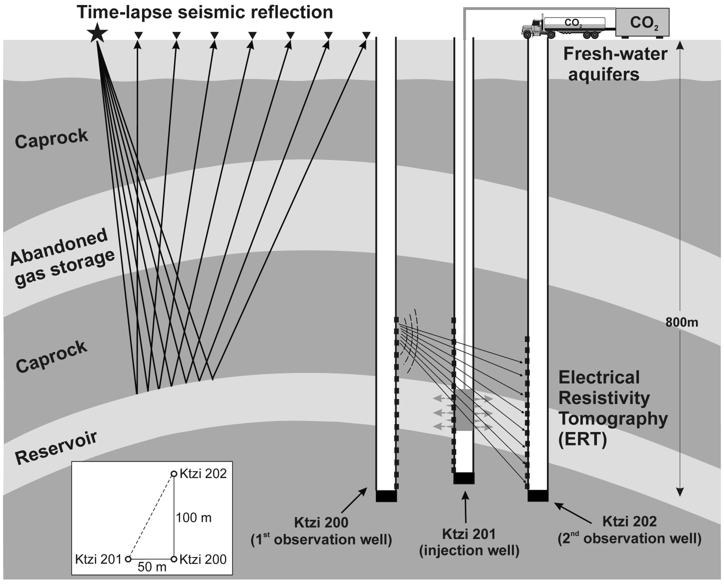

Figure 3.3: Sketch of the geophysical methods, depicting parts of the monitoring program conducted at the Ketzin site.

tomography (ERT) and seismic methods (Figure 3.3).

In this study, modelling is used to investigate the results of crosshole geoelectric and surface seismic reflection experiments. This article aims to investigate the alteration in geophysical monitoring data caused by CO_2 injection. In general, geophysical modelling can aid in the improvement of acquisition geometries and processing routines. In particular, it is required to cross-validate field results and improve the knowledge of spatiotemporal effects occurring within the reservoir. Modelling is especially important when alterations are subtle and coinciding with environmental or technical noise (e.g. injection flow). The processes involved raise questions which cannot be solved analytically, at least not in their full complexity. Therefore, numerical methods are applied for multiphase flow simulation as well as geophysical modelling. The expression multiphase flow simulation, as used in this article, refers to the two phase flow of supercritical CO_2 in the liquid brine and the expression geophysical modelling to the synthetic forward modelling of geophysical experiments.

Multiphase flow modelling yields predictions about time-dependent CO_2 distributions and migration within the reservoir. Petrophysical data are used to relate the CO_2 saturations to the relevant geophysical parameters, namely resistivity and seismic velocity. The cross-validation of modelled geophysical data and field data is likely to improve reservoir imaging, in turn enhancing the reservoir models used in multiphase flow modelling. The updated fluid flow prediction can subsequently be used to optimize a second iteration of geophysical modelling. A sequential workflow of iterations may therefore be used to attain an improved understanding of reservoir characteristics. It is the authors' opinion that such a workflow is essential for the integration of fluid flow prediction and geophysical modelling in a shared earth-like model as a contribution to CO_2 storage monitoring. This article focuses on the first step of such a workflow, i.e. the modelling of the geophysical reservoir response to the presence of CO_2. The adopted models are first-order models of the reservoir integrating the main features of the Ketzin geology. These models contain the major characteristics acquired from downhole logging, crosshole and surface data. A simplification in the reservoir models was made for two reasons. First, the reservoir is highly heterogeneous and its inherent complexity is not yet fully explored. From well logs, it is known that the spatial distribution of permeability and porosity is highly variable, at least on a decimeter scale. Additional effects such as anisotropy in seismic velocity and resistivity are also likely to play a considerable role. As the modelling of reservoir heterogeneity would involve an increased number of assumptions, it is preferable to keep the model as simple as possible. The second reason for simplification is to allow a systematic investigation of the controlling reservoir parameters.

3.2 Multiphase flow simulation

The migration of CO_2 in storage formations is strongly affected by the heterogeneity of the reservoir. A lack of knowledge of the actual geometry of the geological units and the petrophysical properties within a unit, such as the spatially variable distribution of permeability, is significant for the uncertainty of the numerical model. The impact of the least certain parameters has been tested by sensitivity analysis. It has been shown that permeability is one of the most significant parameters affecting the CO_2 distribution (Sifuentes et al., 2009).

The permeability of the numerical model can be adjusted with the transient pressure data measured at the injection well CO2 Ktzi201. There are several possibilities for adjusting the permeability of the model. One is to find an equivalent reservoir permeability which depends on the geometry, boundary conditions and on the time scale of the particular hydrodynamical problem. The upscaling of the actual heterogeneous permeability distribution into an equivalent permeability leads to a homogeneous model, which simplifies the numerical model. Another possibility for adjusting the block permeabilities of the model, which would allow for the incorporation of the formation heterogeneity, consists of stochastic permeability treatment, i.e. several equally probable possible realizations for the heterogeneous field of permeability are generated based on a probabilistic spatial model.

The numerical models were set up using the data from on-site monitoring at the CO_2SINK site. The focus was on the near field around the injection well, which can be approximated with radially symmetric fluid-flow. The results of the heterogeneous models are compared to a homogeneous model. It was shown that the homogeneous model with an equivalent permeability satisfactorily predicts the CO_2 arrival time at CO2 Ktzi200, but does not predict the distribution of the CO_2 plume within the sandstone channel. Together with the uncertainty of the actual spatial permeability distribution, the spatial distribution of the CO_2 gas saturation at Ketzin can only be determined by measurements, which in turn could verify the numerical model. However, the methods for monitoring the CO_2 gas saturations, especially at high resolutions, are currently being developed and has been tested at the Ketzin site. The electrical resistivity tomography presented in this paper is tested by forward modelling of the results of numerical simulations. The numerical models were based on simple homogeneous models, for which the complexities in geometry and heterogeneity can be increased in future studies. As a preliminary sensitivity study on the impact of permeability and CO_2 gas distribution on the electrical resistivity tomography measurements, we investigated a simplified model of Ketzin with a single porous channel-facies sandstone layer with a thickness of 15 m and radially symmetric flow. We tested the impact of three homogeneous permeabilities of 20×10^{-15}, 200×10^{-15} and 2000×10^{-15} m^2 in horizontal direction, which are equivalent to 20 mD, 200 mD and 2000 mD. All three permeabilities are in line with the petrophysical core data (Norden et al., 2008) and were chosen to obtain three different CO_2 migration scenarios, which were then used to test the impact of the CO_2 distribution on the geoelectric reservoir response.

Among other simulators, TOUGH2, a numerical simulator for nonisothermal flows of multicomponent, multiphase fluids in porous and fractured media was supplemented with the property module ECO2N to model the processes due to CO_2 storage. The simulator was tested in a code intercomparison study. The discretization was made by using the MESHMAKER option of TOUGH2 Version 2.0. In the study area, the generated mesh is regularly spaced with 0.3 m and 3.0 m steps in the vertical and horizontal directions, respectively. The model boundary is set 6 km from the injection well, to ensure that the simulated flow is not affected by the boundary conditions. The material properties and initial conditions of the modelled reservoir are listed in Table 3.1. To calculate the relative permeability (RP) and capillary pressure (CP), the van Genuchten-Mualem and van Genuchten functions were chosen, respectively, in accordance with TOUGH2 Version 2.0 (Pruess et al., 1999). To simulate the vertical injection well, the vertical permeability for the well elements was set 104 times higher than in the sandstone layer, and the injection rate was applied to only the uppermost element of the well column. This approach results in the charging of all elements of the well column. The injection rate was modelled with a constant rate of 0.4762 kg/s (1.7 t/h). As expected, the simulated migration of the CO_2 gas depends on the permeability (Figure 3.4). While for low permeabilities the front of the CO_2 gas saturation front is steeper, the distribution in highly permeable sandstones is dominated by buoyancy, creating a thin CO_2 gas plume beneath the caprock. These time-dependent CO_2 distributions are migration scenarios, ranging from low to high permeabilities and varying in the influence of buoyancy forces, used for modelling of the geoelectric reservoir response.

Table 3.1: Material properties and initial conditions.

Material property			
Porosity (-)	0.261		
Horiz. perm. (m^2)	$20 \cdot 10^{-15}$	$200 \cdot 10^{-15}$	$2000 \cdot 10^{-15}$
Vertic. perm (m^2)	$6.67 \cdot 10^{-15}$	$66.7 \cdot 10^{-15}$	$667 \cdot 10^{-15}$
Parameters for relative permeability and capillary pressure function according to TOUGH V2 (Pruess et al., 1999):			
λ	0.75		
S_{lr}(-)	0.35		
S_{gr}(-)	0.05		
S_{ls}(-)	0.999		
$1/P_0$(bar^{-1})	10^{-4}		
P_{max}(bar)	10^5		
Initial conditions:			
Pressure (MPa)	6.2		
Temperature (°C)	34 (isotherm)		
Salinity (wt% NaCl)	23.5		

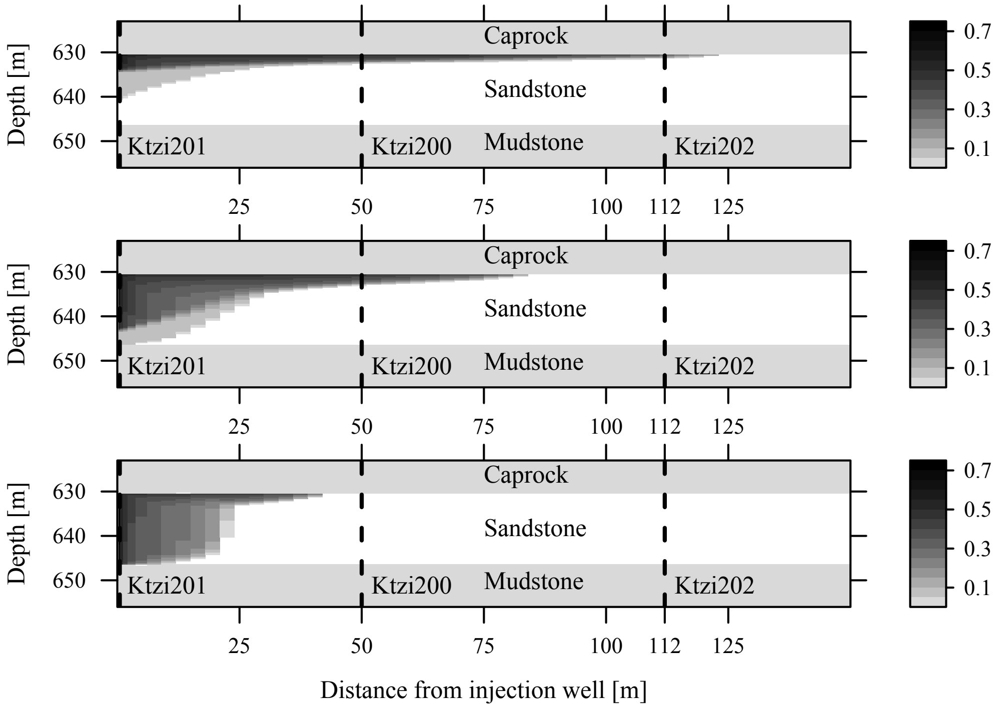

Figure 3.4: CO_2 gas saturation after 28 days for a reservoir permeability of 2000 mD (top), 200 mD (center) and 20 mD (bottom).

3.3 Geoelectrics

3.3.1 Geoelectric monitoring at Ketzin site

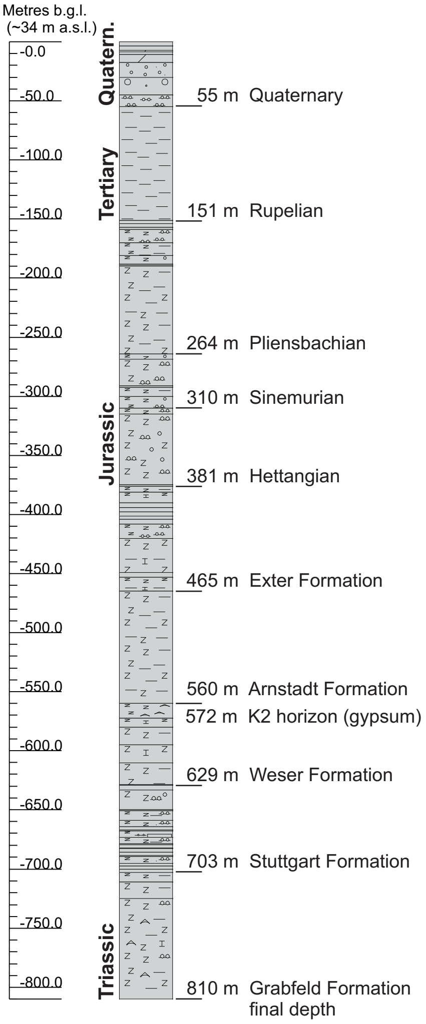

Figure 3.2: Condensed lithology of well CO2 Ktzi200. Figure from Prevedel et al. (2009).

The geoelectric measurements were designed to monitor resistivity alteration caused by the migration of the CO_2 phase (Christensen et al., 2006). For this purpose, a permanent electrode array has been installed in the three wells CO2 Ktzi200, CO2 Ktzi201 and CO2 Ktzi202. Each well was equipped with 15 ring-shaped steel electrodes with depths ranging from 590-735 m and an electrode spacing of 10 m. The electrode array provides coverage of the cap rock (Weser Formation), the Stuttgart Formation and parts of the Grabfeld Formation beneath. Each measurement of the permanent electrode array uses four electrodes. The first pair of electrodes is employed for current injection, and the second pair for voltage measurement. Four-point measurements have the advantage over two-point measurements in that they allow the acquisition of several voltage values per current injection and avoid the influence of contact resistance at the electrodes. Due to the regulations of the mining authority, the maximum injection currents are limited to 2.5 A. Voltages vary between 50 μV to 100 mV. Each measurement configuration consists of several electrode combinations. Each electrode combination consists of four electrodes yielding a single apparent resistivity value for a certain time step. Apart from several user-defined configurations, the four-point electrode configurations applied are bipole-bipole (BB), dipole-dipole (DD) and dipole-dipole cross (DDc). These configurations are subdivided into regular (Figure 3.5) and modified combinations. Regular and modified combinations are related by shifting electrodes or electrode pairs. Modified combinations were integrated into the configurations to acquire an increased measurement density in the reservoir area and additional reciprocal measurements.

The configurations were bundled in schedules which were repeatedly measured with varying repetition rates. Three phases were defined, with daily, semi-weekly and weekly repetition periods. The first phase starts with the injection and ends with the arrival of CO_2 at the CO2 Ktzi200 observation well, which is the beginning of the second phase. The arrival of CO_2 at the CO2 Ktzi202

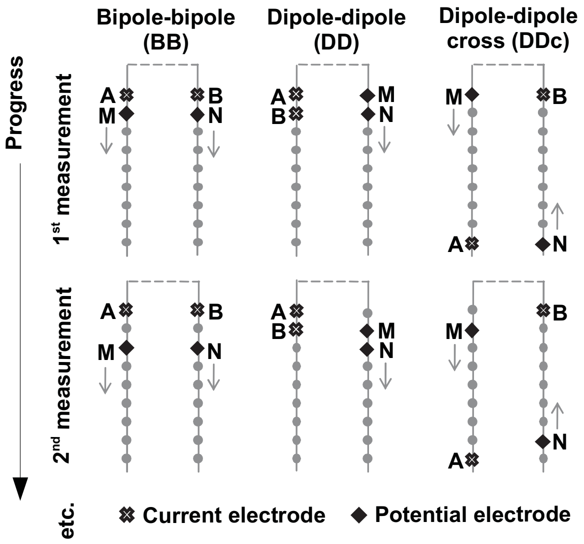

Figure 3.5: Electrode combinations within the regular electrode configurations.

observation well marks the end of the second phase and the beginning of the third phase which is currently ongoing.

3.3.2 Electrical resistivity

As a first-order approximation, porous sediments (acting as conductors) can be thought of as multiphase systems consisting of the mineral matrix and pore space that, in this study, is filled with brine or CO_2 or a mixture of the two components. Since the electrical resistivity of most matrix-building minerals is high, the main part of the electric current flows through the pore space. A major exception occurs, when the matrix contains highly conductive minerals such as clay. For clay-free sandstones, Archie's law (Archie, 1942) gives the dependence of the resistivity, ρ, on porosity, Φ, and CO_2 saturation, S_{CO_2}:

$$\rho(S_{CO_2}) = \frac{A\rho_w}{\Phi^m\left(1 - S_{CO_2}\right)^n}\ , \tag{3.1}$$

where ρ_w is the brine resistivity, equal to 0.037 Ωm for the Ketzin brine. The factor A reflects the current component being conducted through the matrix and is in the range of 1 for most sandstones. The porosity exponent m is influenced by pore geometry, compaction and the insulating properties of the cementation. The saturation exponent n accounts for the presence of non-conductive fluid in the pore space. The porosity and saturation exponent are in the range of 2 for most sandstones. Resistivities of core samples measured during autoclave flow-through experiments indicate a CO_2-induced resistivity increase of a factor 2-3 (Table 3.2). The increase was measured after the fluid was switched from a synthetic brine to pure CO_2. The experiments were conducted under Ketzin reservoir temperature and pressure conditions (T=40 °C, p_{pore}=7.5 MPa, p_{conf}=15 MPa). Due to the instability of the samples, the residual brine content was roughly determined as approx. 60-70%. A new set of laboratory experiments with suited residual brine saturation determination is currently in the planning phase (Kummerow and Spangenberg, 2009, pers. comm.).

Table 3.2: Resistivities from laboratory flow-through experiments (Kummerow and Spangenberg, 2009, pers. comm.).

Sample of CO2 Ktzi200	Full brine ρ (Ωm)	Brine+CO$_2$ ρ (Ωm)	Alteration (%)
B2-3b	0.53	1.71	+223
B3-1b	0.46	1.26	+147

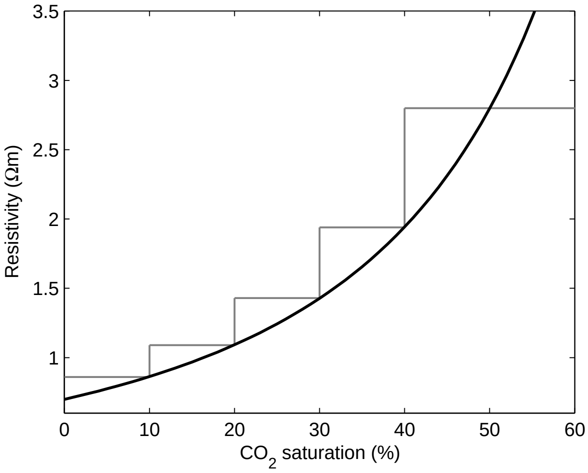

Figure 3.6: Resistivity saturation relation derived from Archie's equation (black line) for brine resistivity ρ_w=0.037 Ωm, A=1, m=n=2 and porosity Φ=23%. The grey line depicts the discretized resistivity saturation relation utilized in forward modelling.

Based on the laboratory results and resistivity logs, Kiessling et al. (2010) derived a first-order reservoir model consisting of three formations (overburden, injection formation and formation beneath) of which the injection formation can be either in the fully brine-saturated or partially saturated state. A comparison between the Archie model of equation 3.1 and the first order reservoir model of is given in Figure 3.6. Transformation of the modelled CO$_2$ saturations to resistivities has been done with a stepwise discretisation of this relation (Figure 3.6, grey line).

3.3.3 Geoelectric modelling

The time-dependend CO$_2$ distributions obtained from multiphase flow simulation were used for forward modelling of electrical resistivity experiments. The time of modelling spans the first thirty days of injection, being approximately twice the time need for the CO$_2$ to migrate to the first observation well (CO2 Ktzi200). In two-day intervals, the three CO$_2$ distributions, as defined by the reservoir permeability (20 mD, 200 mD and 2000 mD), were transferred to resistivities and modelled for the BB, DD and DDc configurations (Figure 3.5). To keep the amount of data analysable the investigation is constrained to 2D measurements between the CO2 Ktzi200 and CO2 Ktzi201 wells. Representative subsets of BB, DD and DDc were selected containing regular and modified electrode combinations. Forward modelling was performed on an unstructured finite element grid utilizing the resistivity modelling and inversion software BERT (Rücker et al., 2006; Günther et al., 2006).

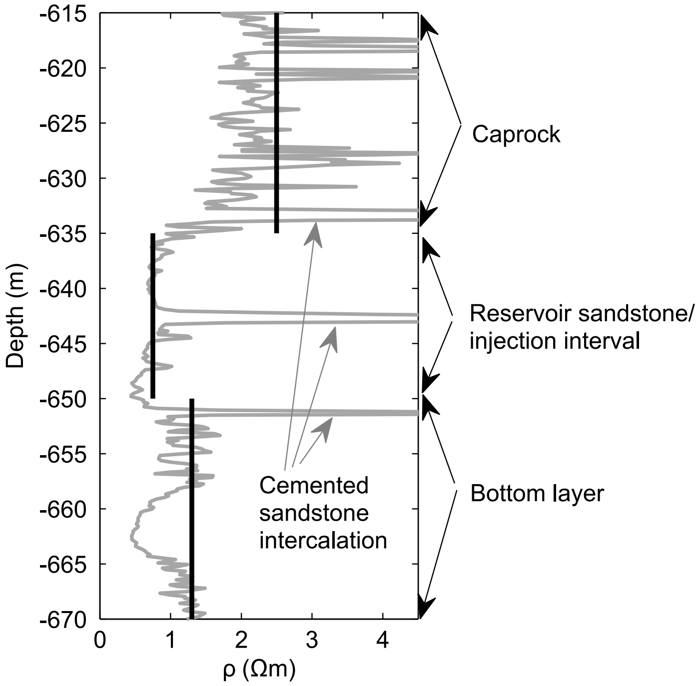

Figure 3.7: Resistivity log of CO2 Ktzi201 (grey line) and averaged resistivities for synthetic reservoir model building (black lines).

The choice of suitable boundary conditions as well as the extrapolation of the model to a width of 6 km and a depth of 4 km were conducted to avoid boundary artefacts. The baseline reservoir model consists of a three layers (overburden, reservoir and the formation beneath), after the model of Kiessling et al. (2010). The resistivities of the layers are the formationwide averages of the resistivity logs (Figure 3.7).

The result of the geoelectric modelling is the resistance, R, for each electrode combination ,which is dependent on the duration of injection and the three choices of reservoir permeability. In the course of this study we we have used R instead of the apparent resistivity, ρ_{app}. These parameters can be converted from one to the other through application of a geometrical factor that takes the distances between the electrodes into account. In practice observation of ρ_{app} is useful because it allows for easy comparison of nearby measurements. R was chosen because it reflects the magnitude of the values to be measured. Therefore, it allows the identification of electrode combinations that are problematic in terms of field application, in cases where the small size of R may be disguised by the ambient noise level. The temporal development of R has been found to be very heterogeneous with regard to the electrode combination and the reservoir permeability (Figure 3.8).

Even decreased R can be observed, although the spatial average of the reservoir resistivity is increasing has increased with progressing injection. This behaviour gives evidence about the presence of areas of negative sensitivity. A local resistivity increase within this area caused a decrease in the R. The shape and extent of this area is highly dependent on the geometry of the particular electrode combination and the resistivity distribution in the proximity (e.g. Spitzer, 1998). Resistance alterations were mainly sensitive to fluctuations in the near-wellbore saturation. In general,

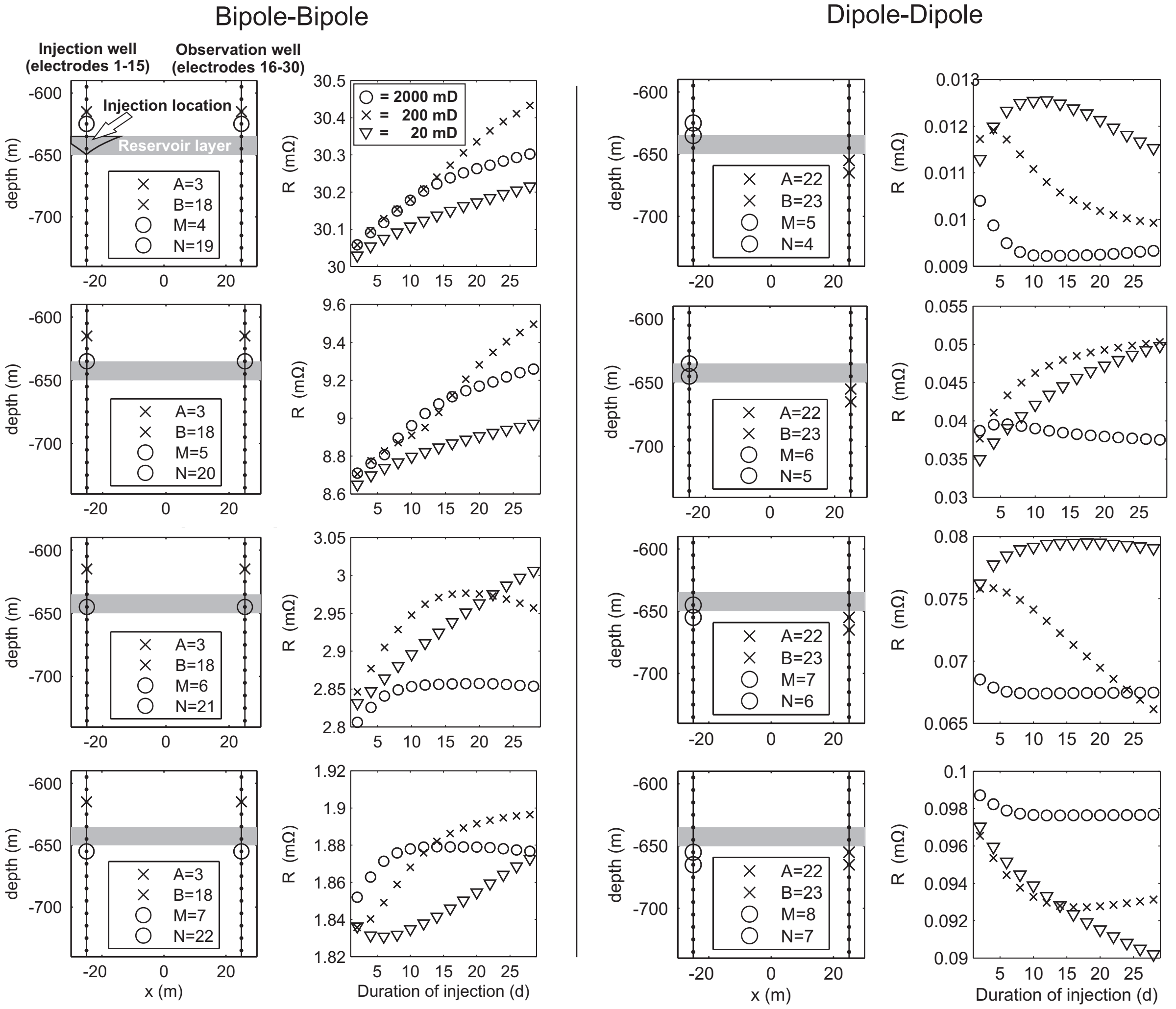

Figure 3.8: Examples of electrode combinations from the BB and DD configuration (first and third column) and the respective temporal development of the resistance R (second and fourth column) for three different cases of reservoir permeability (20, 200 and 2000 mD). Square legends indicate the position of the current electrodes (A, B) and potential electrodes (M, N) in the injection well (electrode positions 1–15, from top to bottom) and the obervation well (electrode positions 16–30, from top to bottom).

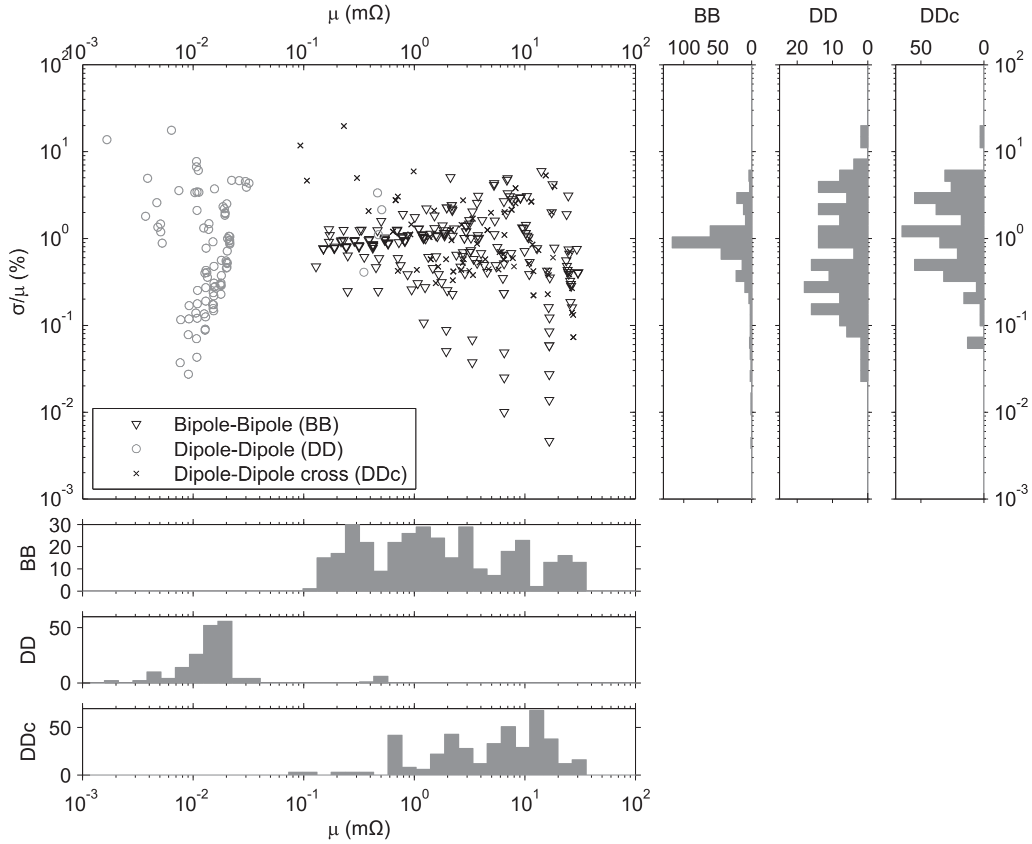

Figure 3.9: Histograms of the mean, μ, and standard deviation, σ, of the temporal developments of the resistance for the electrode combinations, as partially drawn in Figure 3.8.

sensitivity decreases with increasing distance to the wells (al Hagrey, 2009).

Thus, the limit for the lowest amount of CO_2 detectable decreases away from the wells. This finding has serious implications which have to be considered in the ERT monitoring system design and the interpretation of inversion results. For the case of high reservoir permeability (2000 mD), fluid flow simulation indicates that the CO_2 migration at some distance to the well is conducted through a thin layer beneath the caprock. This implies that this migration scenario is difficult to detect with ERT measurements. To determine the usefulness of the single electrode configurations, the mean R over time, μ, and the ratio of the standard deviation, σ, to μ were investigated (Figure 3.9).

For the BB and DDc measurements, the majority of the averaged resistances were between 0.1-10 mΩ. The majority of the DD measurements were between 0.001-0.1 mΩ (Figure 3.9, lower histograms). For all configurations, it generally holds that R decreases with increasing offset between the electrode pairs. For practical operations, the usefulness of electrode combinations that provide small R must be evaluated, particularly in the presence of noise. For Ketzin, the evaluation is being conducted by way of observation of the time domain current and voltage signals as well as the verification of reciprocal measurements. At this time it can be stated that especially DD combinations providing a mean R of less than 0.01 mΩ are incapable of inversion. Further work is intended to find criteria for refusal of insufficient measurement values, taking into account the time domain signals from which R is derived, the time-dependent scattering of R and the degradation

Table 3.3: Characteristics of the resistances for the CO_2 migration scenarios (left column) and electrode configurations (top row)

Reservoir perm.		Bipole-bipole (BB)	Dipole dipole (DD)	Dipole-dipole cross (DDc)
k=20 (mD)	$\langle\|\mu\|\rangle(\Omega m)$	5.00	0.02	5.10
	$\langle\frac{\|\sigma\|}{\|\mu\|}\rangle(\%)$	0.95	2.04	4.66
k=200 (mD)	$\langle\|\mu\|\rangle(\Omega m)$	5.04	0.02	5.15
	$\langle\frac{\|\sigma\|}{\|\mu\|}\rangle(\%)$	1.08	1.95	2.85
k=2000 (mD)	$\langle\|\mu\|\rangle(\Omega m)$	4.99	0.02	5.01
	$\langle\frac{\|\sigma\|}{\|\mu\|}\rangle(\%)$	0.44	1.06	0.74

of the subsurface installation.
The ratio of standard deviation to the mean, σ/μ reflects the temporal alteration of R. Large ratios created by large standard deviations are desired to provide high sensitivities with respect to model alterations. It is possible to cover the same range of ratios for all three configurations, with BB measurements showing a unique σ/μ peak near 1% (Figure 3.9, side histograms). These result indicates that μ is the most significant value for assessing the electrode configurations, with preference to BB and DDc measurements. Table 3.3 gives an overview of the characteristics of the observed migration scenarios. It demonstrates that the difference in mean R between BB or DDc or DD is observable for all migration scenarios. The DDc measurements tend to show decreasing σ/μ with increasing reservoir permeability. Therefore, interpreting σ/μ as time-dependent alteration, DDc measurements would be preferred for low-permeability reservoirs. In general, a time-lapse signature in the modelled data is observable. Due to the variations in the time-dependent response of the electrode configurations (Figure 3.8), there is a hypothetical opportunity to distinguish the different migration scenarios caused by the different reservoir permeabilities.

3.4 Seismics

3.4.1 Seismic monitoring at the Ketzin site

The seismic monitoring program comprises surface seismic, downhole seismic as well as crosshole seismic measurements. Seismic measurements at Ketzin started with a 2D pilot study in 2004 followed by a 3D baseline survey in autumn 2005 (Juhlin et al., 2007). Additional 2D surveys (surface to surface), 2D vertical seismic profiling (surface to borehole, borehole receiver moving), 2D moving-source profilings (surface to borehole, surface source moving) and crosshole seismic measurements between the observation wells were performed. The 2D repeat surface seismic campaign was completed in autumn 2009. Apart from the pilot study, which was designed to test available source types, acquisition of the 2D seismic datasets was performed along seven lines (Figure 3.10).

These lines were placed in a star-shaped pattern, with the ends pointing towards the well locations. The minimum source-well offset was limited due to incomplete acquisition permission at the injection site. During the 2D surveys, the complete seven lines were used as an active spread to allow acquisition in a classical 2D line mode as well as in a pseudo-3D manner with sparse cover-

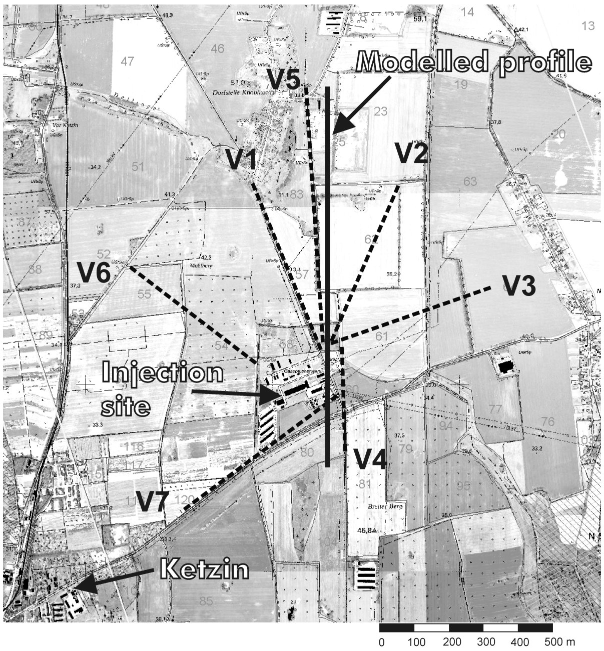

Figure 3.10: Location of the 2D seismic lines (dashed lines) used for surface seismics, VSP and MSP measurements. The solid line represents the profile used in forward modelling.

age between the lines. The surface seismic measurements were designed to verify earlier geologic interpretations of structure (based on vintage 2D seismic and borehole data) as well as to evaluate the contribution of each measurement type to the monitoring.

The interval velocity model used in forward modelling uses surface seismic and sonic log data as well as the structural geologic interpretation. Velocity analysis of CDP supergathers of the 3D seismic data were used to create vertical stacking velocity profiles (Figure 3.11a). The stacking velocities were converted to interval velocities (Figure 3.11b) at depth using Dix's equation (Sheriff and Geldart, 1995). Sampling points in depth of the interval velocities are adjusted to the horizons of the structural interpretation (Figure 3.11c). A laterally-varying and vertically-constant interval velocity distribution was obtained for each formation. The accuracy of the determination of interval velocities from stacking velocities decreases with depth, since the velocity errors of the overburden formation are cumulative and the normal moveout of reflection events becomes small. To deal with this inaccuracy, velocities for the Weser, Stuttgart and Grabfeld Formation were adjusted to the sonic log velocities at the CO2 Ktzi200 well location (Figure 3.12), laterally extrapolated and superimposed with the long-wavelength undulation of the interval velocities determined from NMO analysis (Figure 3.11d).

3.4.2 Seismic velocity and forward modelling

In laboratory experiments conducted on outcrop samples from the Stuttgart Formation, Schütt et al. (2005) determined that the decrease in compressional wave velocity due to CO_2 saturaton is 5-10%. Kummerow and Spangenberg (2009, pers. comm.) measured a velocity drop from 3219 m/s to 2800 m/s in flow-through experiments on core samples from well CO2 Ktzi200. The heterogeneity of the

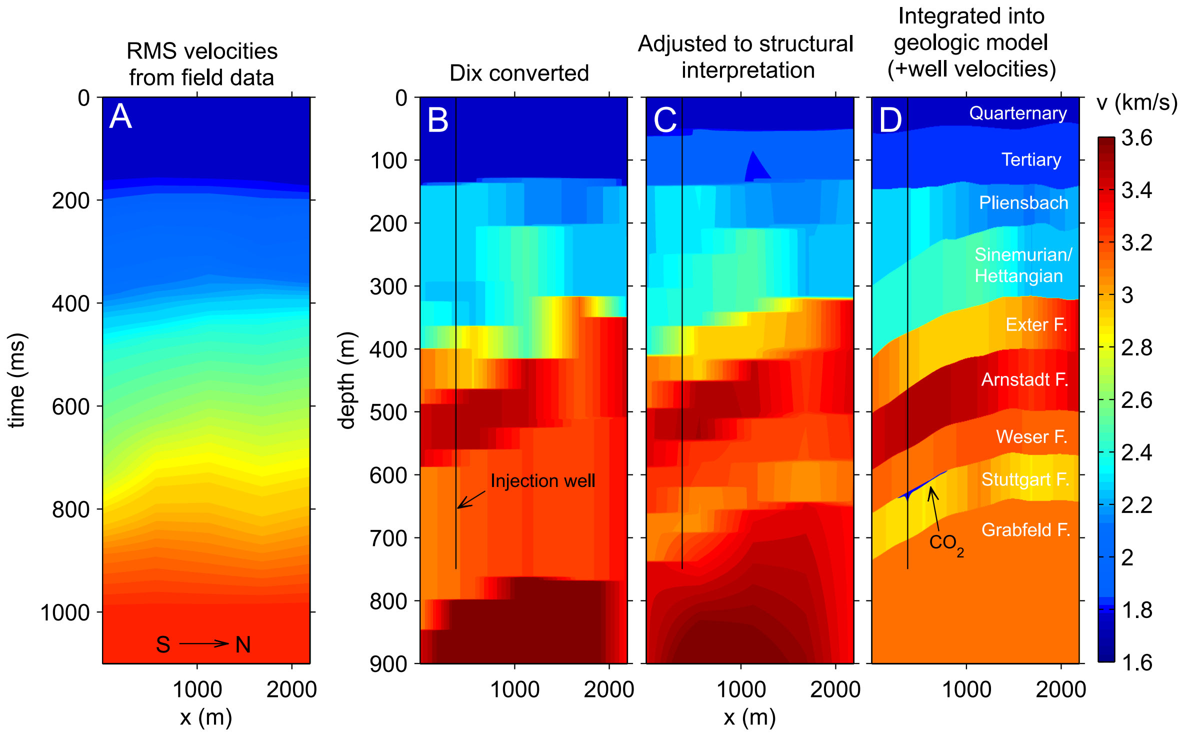

Figure 3.11: Steps of the velocity model building workflow. The location of the profile is depicted in Figure 3.10 (solid line). RMS velocities taken from 3D baseline seismic processing (Juhlin et al., 2007).

reservoir velocities can be observed in the sonic velocities (Figure 3.12) logged in well CO2 Ktzi200. The velocities vary between 2500-3500 m/s, occasionally exceeding 4500 m/s. The average of 2890 m/s was used as the compressional wave velocity for the brine saturated reservoir formation. With approximately 3100 m/s as averaged velocities for the Weser and Grabfeld formation, the Stuttgart Formation forms a low-velocity layer. The average wave velocity of the Stuttgart formation is scaled by the percentage drop measured in the laboratory experiments (Table 3.4). As described in the geoelectric section above, complications in the determination of the residual water saturation arose during the laboratory measurements. A new set of measurements is planned to investigate the velocity changes with varying CO_2 content and to build a Biot-Gassman like model.

Forward modelling was performed by a finite difference approximation of the wave equation in the 2D domain (Kelly et al., 1976). For this study, a simplified version of the elastic wave equation has been adapted, which requires the compressional wave velocity and density distribution. Also input were the source and receiver geometry as well as the source wavelet, which was represented as a minimum-phase Ricker wavelet. The mean wavelet frequency was chosen to be 50 Hz, which is the upper frequency limit of the vintage data and approximately equal to the mean frequency selected in the 3D baseline processing at the target depth (Juhlin et al., 2007). The synthetic shot gathers were noisified with random signal and synthetic groundroll. The data then underwent a conventional CDP processing scheme which comprised sorting into CDP gathers, NMO correction and stacking. Kirchhoff poststack time migration and time-depth conversion was conducted with the interval

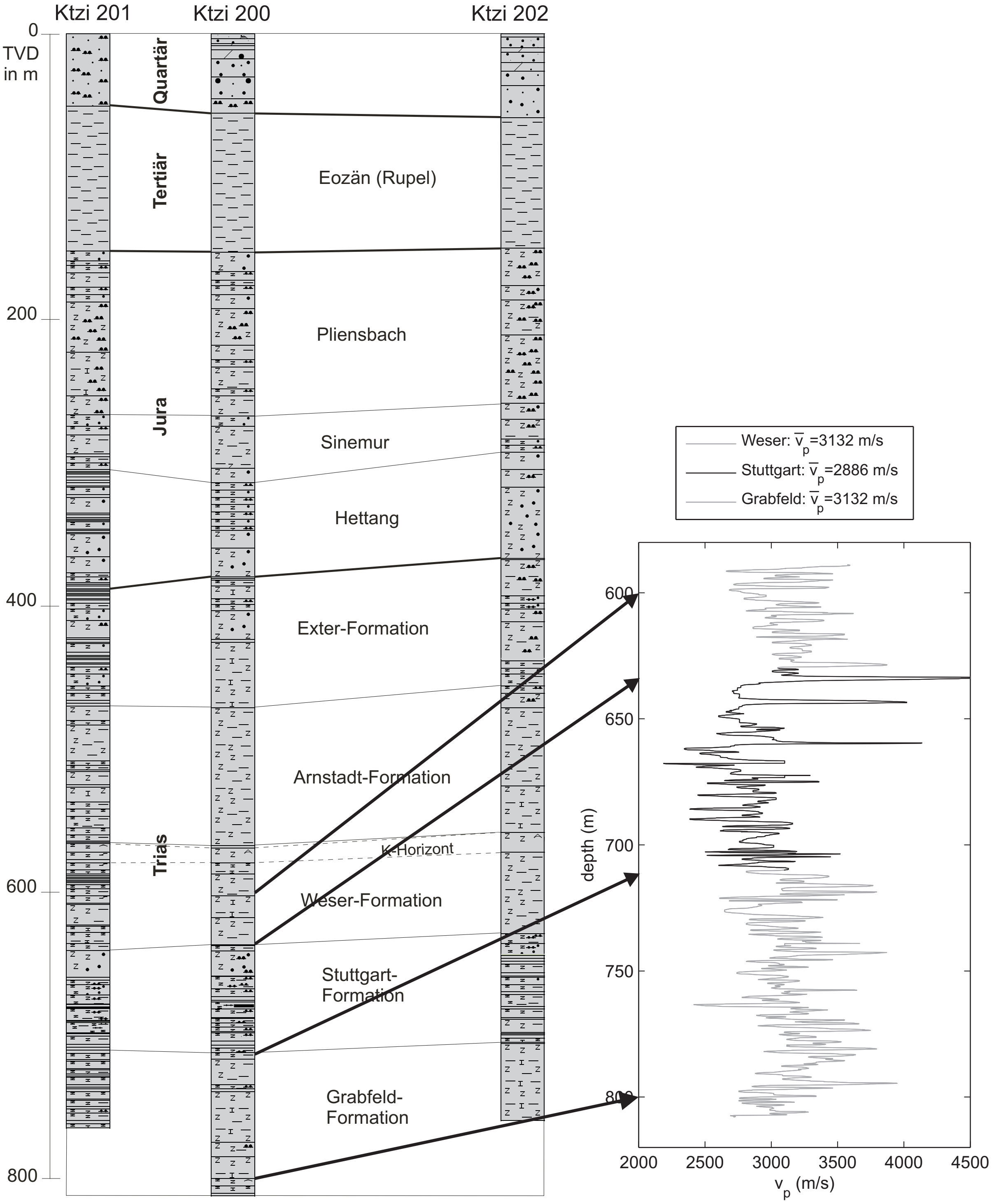

Figure 3.12: Lithology of the three wells and sonic log velocities of CO2 Ktzi200. Lithology taken from Engelmann et al. (2008).

Table 3.4: Geometry and reservoir rock model parameters for seismic modelling.

	Baseline survey	Model
No. of source points	Line 4: 33 Line 5: 126	182
Source point spacing (m)	12	12
No. of receiver points	Line 4: 22 Line 5: 62	91
Receiver point spacing (m)	24	24

Rock model:	100% brine	50% CO_2, 50% brine
v_p (m/s)	2890	2514
ρ (g/cm^3)	2.202	2.09

velocities as they were used for the forward modelling. The entire sequence was performed for a baseline model and a repeat model with a certain amount of cells affected by the replacement of brine by CO_2. The modelling and processing has been performed with the seismic processing software ProMAX (Landmark, version 2003.12.1). Equal processing of baseline and repeat datasets and subtraction of the resulting stacks is the simplest form of time-lapse seismic processing. Additional processes such as surface-consistent amplitude scaling, frequency or wavelet shaping and additional static corrections are likely to become crucial in the processing of real data. Such additional processes might be added to account for variations induced by acquisition, such as differences in source and receiver coupling, changes in near-surface velocities and acquisition geometry. Due to the good control and therefore repeatability of the synthetic modelling, the processing was kept simple to avoid introducing artefacts.

The CO_2 distribution used in the seismic forward modelling of the repeat model was derived from a simplified migration scenario for 25,000 t of injected CO_2, which is approximately equal to the amount of CO_2 injected until the repeat campaign in autumn 2009. The migration scenario assumes a flat and perfectly homogeneous reservoir model. The only parameter inserted was the permeability anisotropy, which forced the CO_2 to spread in an ellipsoid shape. Assuming a porosity of 22%, an average CO_2 saturation of 50% and 20% dissolved CO_2, an average height of 2.2 m was estimated for the CO_2 spreading layer (Köhler and Zemke, 2009, pers. comm.). The depth-converted difference stack section is given in Figure 3.13. A time-lapse signature is observable in the reservoir formation. The lateral extent of the signature corresponds well with the width of the causative CO_2 distribution. The wavelength of the signature exceeds the thickness of the CO_2 layer by several times. MSP and VSP measurements are likely to exploit higher frequencies resulting in a sharper wavelet. An alteration of the waveform coda indicates the injection location which is characterized by a larger plume thickness. The amplitude deflection relative to the CO_2-free background is likely to be quite optimistic, for several reasons. First, the added noise is of regular type which is most effectively eliminated by CDP-stacking and poststack migration. The amplitude decay in 2D modelling is smaller than for real 3D wave propagation, which is not only affected by spherical divergence but also by inelastic attenuation. Processing routines have to be adjusted to overcome these effects. Incorporation of these effects into the model is of eminent importance to allow systematic comparability with field data. Nevertheless, a signature can be observed, indicating that the lateral

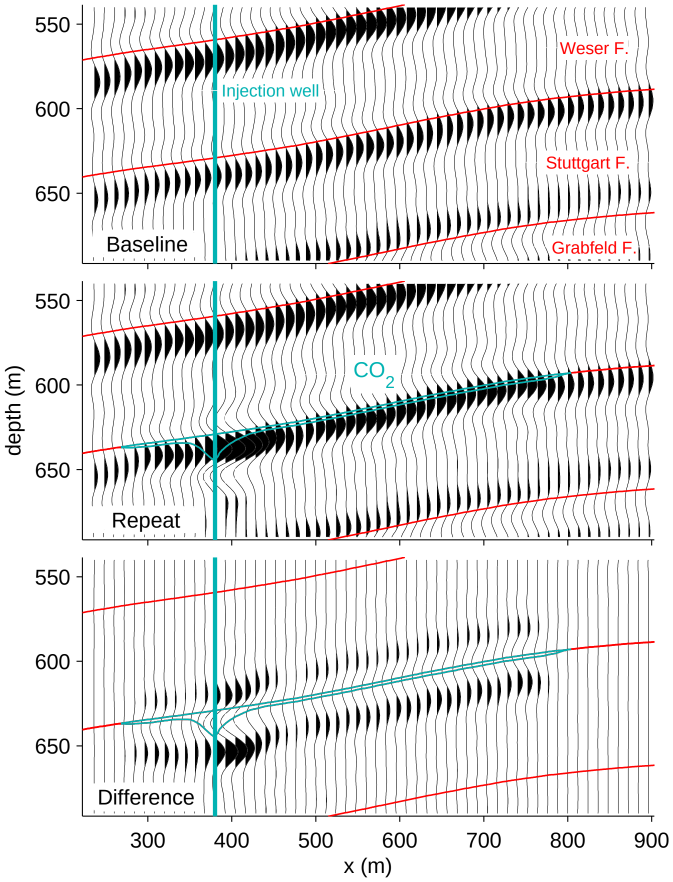

Figure 3.13: Detailed view of stack sections from noisified synthetic data for the baseline model (upper display) and repeat model (center display). The geologic formation boundaries are marked in red. The injection well and the CO_2 distribution of the repeat model are marked in turquoise. The poststack difference of the baseline and repeat stack is given in the lower display. All traces are displayed with equal gain.

extent of thin-layered CO_2 migration is potentially detectable. On the other hand, the thickness of the plume is expressed by the waveform coda. Future work is planned to determine, whether the thickness and saturation may be retrieved from the waveform. If so, advanced processing methods such as waveform inversion are likely to be required.

3.5 Conclusions

In this study, forward modelling of synthetic geophysical experiments was conducted in the framework of the carbon dioxide storage project CO_2SINK (Ketzin, Germany). Modelling was performed for a crosshole ERT setup and a surface seismic experiment. The investigated scales range from meters, in the crosshole case, to several hundreds of meters, in the surface seismic measurements. Treatment of geophysical field data of different methods and scales dealing with time-lapse effects is a difficult task and modelling is intended for guidance. Results of the forward modelling provide implications for survey design as well as practical advice for the processing and interpretation of real data. Reservoir models have been compiled from the available data, such as well logs and structural interpretation. Within these models CO_2 distributions were integrated as they are available from multiphase flow simulation. In the case of ERT, a sequence of synthetic datasets has been created, covering the initial injection time. A time-lapse signature in the modelled data is observable, showing a clear dependence on the different migration scenarios caused by varying reservoir permeabilities. It is to validate with real field data, whether these signatures might easily be disguised by the ambient noise level.

Baseline and repeat models have been constructed to perform a synthetic time-lapse seismic reflection experiment. The time-lapse signature observed in the difference stack section indicates that the lateral extent of the CO_2 plume is detectable. On the other hand, the thickness of the plume is expressed by the waveform coda, presumably requiring advanced processing methods for interpretation. The forward modelled datasets indicate that CO_2 migration is observable within the specific limitations of the method in application and the spatial scale of investigation (e.g. thin layer detection with ERT). Further modelling and refinement of the reservoir models is thought to be a promising direction for future work. Potential improvement may include the joint use of both methods, in terms of both modelling and the processing of field data.

Acknowledgements

This work was performed in the framework of the joint Project GeoEn (Grant 03G0671A/B/C), a national scientific initiative in the field of energy research. We would like to thank all partners of the CO_2SINK project for their continued support and contributions. The CO_2SINK project receives its funding from the European Commission (Sixth Framework Program, FP6) and two German ministries, the Federal Ministry of Economics and Technology (CO_2-Reduction Technologies for fossil fuelled power plants, COORETEC Program), and the Federal Ministry of Education and Research (GEOTECHNOLOGIEN Program). Kirsten Rempel, Andrea Förster and two anonymous reviewers are acknowledged for helpful comments on the manuscript.

4

Seismic investigations

Publication II

Time-lapse processing of 2D seismic profiles with testing of static correction methods at the CO_2 injection site Ketzin (Germany)

P. Bergmann[1], C. Yang[2], S. Lüth[1], C. Juhlin[2], and C. Cosma[3]

Published in Journal of Applied Geophysics 75, 1, p. 124-139, September 2011

Contents

Abstract: The Ketzin project provides an experimental pilot test site for the geological storage of CO_2. Seismic monitoring of the Ketzin site comprises 2D and 3D time-lapse experiments with baseline experiments in 2005. The first repeat 2D survey was acquired in 2009 after 22 kilotons of CO_2 had been injected into the Stuttgart Formation at approximately 630 m depth. Main objectives

---

[1] Helmholtz Centre Potsdam, GFZ German Research Centre for Geosciences, Centre for CO_2 Storage, Telegrafenberg, 14473 Potsdam, Germany

[2] Uppsala University, Department of Earth Sciences, Villavägen 16, 75236, Uppsala, Sweden

[3] Vibrometric Oy, Vantaa, Finland

of the 2D seismic surveys were the imaging of geological structures, detection of injected CO_2, and comparison with the 3D surveys. Time-lapse processing highlighted the importance of detailed static corrections to account for travel time delays, which are attributed to different near-surface velocities during the survey periods. Compensation for these delays has been performed using both pre-stack static corrections and post-stack static corrections. The pre-stack method decomposes the travel time delays of baseline and repeat datasets in a surface consistent manner, while the latter cross-aligns baseline and repeat stacked sections along a reference horizon. Application of the static corrections improves the S/N ratio of the time-lapse sections significantly. Based on our results, it is recommended to apply a combination of both corrections when time-lapse processing faces considerable near-surface velocity changes. Processing of the datasets demonstrates that the decomposed solution of the pre-stack static corrections can be used for interpretation of changes in near-surface velocities. In particular, the long-wavelength part of the solution indicates an increase in soil moisture or a shallower groundwater table in the repeat survey. Comparison with the processing results of 2D and 3D surveys shows that both image the subsurface, but with local variations which are mainly associated to differences in the acquisition geometry and source types used. Interpretation of baseline and repeat stacks shows that no CO_2 related time-lapse signature is observable where the 2D lines allow monitoring of the reservoir. This finding is consistent with the time-lapse results of the 3D surveys, which show an increase in reflection amplitude centered around the injection well. To further investigate any potential CO_2 signature, an amplitude versus offset (AVO) analysis was performed. The time-lapse analysis of the AVO does not indicate the presence of CO_2, as expected, but shows signs of a pressure response in the repeat data.

4.1 Introduction

Geological storage of carbon dioxide in a saline aquifer is being investigated at a pilot test site near the town of Ketzin, Germany (Figure 4.1, left). Investigations started in 2004 with the initiation of the EU funded CO_2SINK project (CO_2 storage by injection into a natural saline aquifer at Ketzin). The research at the Ketzin pilot site seeks to improve the understanding of the in-situ physical, chemical, biological and engineering processes associated with CO_2 storage, construction and operations (Giese et al., 2009). The operation site, referred to as the Ketzin site, is situated on the southern flank of an anticlinal structure. The anticline formed by the movement of an elongated pillow structure of Zechstein salt situated at a depth of 1500–2000 m (Förster et al., 2006). Drilling operations started in 2007 with the sinking of the injection well CO2 Ktzi201 and two additional observation wells (CO2 Ktzi200 and CO2 Ktzi202), each to a depth of approximately 800 m. Storage operations started in June 2008 by injection of CO_2 into the Stuttgart formation at a depth of 630–650 m. The Stuttgart formation is Middle Keuper (Upper Triassic) in age and is fluviatile in origin with sand channels incising muddy flood-plain rocks. Sandstone intervals within the Stuttgart formation may attain thicknesses of several meters and show significant heterogeneity, with porosity and brine permeability varying from 5% to >35% and from 0.02 mD to >5000 mD, respectively (Norden et al., 2010). The Stuttgart formation slopes upwards to depths of about 500 m within the anticline crest, which is located approximately 1.5 km north of the injection site. The simplified geology of the Ketzin site is shown in Figure 4.1, right.

The Weser formation is the first caprock barrier, approximately 80 m thick, and is composed mainly

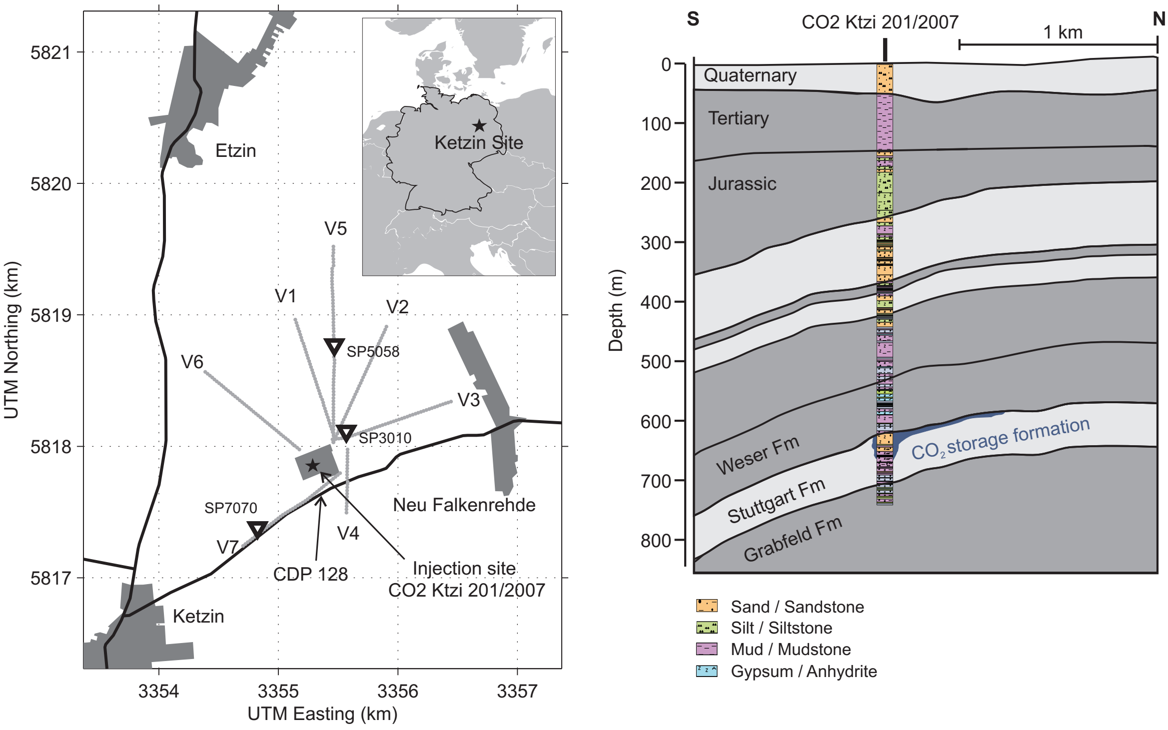

Figure 4.1: Left: Location of the Ketzin site in Germany (upper right) and 2D seismic lines (V1–V7) shown in gray. Triangles show source locations of data examples given in Figure 4.2 and Figure 4.4. Right: Simplified geology of the Ketzin anticline with lithology of the injection well CO2 Ktzi 201/2007. Aquifer units are depicted in light gray, aquitard units in dark gray. Figure modified after Förster et al. (2006).

of clayey and sandy siltstones with carbonitic and evaporitic interlayering (Beutler and Nitsch, 2005). The top of the Weser formation contains a 10–20 m thick anhydrite layer, known as the Heldburg-Gips or K2 (Keuper) reflector. The Weser formation is overlain by the Arnstadt formation of mud/clay-carbonate content (Beutler and Nitsch, 2005) and has similar sealing properties as the Weser formation. The shallower sandstones of the Sinemurian formation were used for industrial storage of natural gas at depths of 250–400 m. Storage operations were abandoned in 2000 due to economic reasons. The sealing caprock to the former gas storage is the Pliensbach formation, providing a second barrier to the deeper CO_2 storage. The shallowest layers are composed of Quaternary sands, exhibiting a relatively flat surface topography with some isolated highs.

4.1.1 Time-lapse seismic methods at Ketzin

The Ketzin project was designed to investigate the technologies necessary for geological storage of CO_2, with a particular focus on geophysical monitoring. In recent years, several authors have reported that time-lapse seismics are a practical tool for geological CO_2 storage monitoring (e.g. Arts et al., 2004; White, 2009). Nevertheless, the feasibility of time-lapse seismic surveys has to be evaluated for every site individually, since the geological properties of storage sites are variable and monitoring expenses will always be limited.

Several feasibility investigations and analyses of the time-lapse seismic signature at the Ketzin site have been conducted. These include: (1) changes in the petrophysical properties of the sandstone of the Stuttgart formation due to the replacement of brine by CO_2, (2) seismic modeling studies based on the Ketzin geology (Bergmann et al., 2010b; Kazemeini et al., 2010a; Verdon and Campman, 2010), (3) amplitude mapping of the CO_2 signature in the vicinity of the injection well in the 3D time-lapse data (Ivanova et al., submitted), and (4) modeling and field data processing of moving source-profile (MSP) measurements (Yang et al., 2010).

Practical seismic monitoring comprises surface-to-surface 2D/3D seismic reflection surveys, 2D/3D moving source profiling (MSP), vertical seismic profiling (VSP) and crosswell surveys (Lüth et al., 2011) and started with a pilot study in 2004 (Yordkayhun et al., 2009a), which aimed at evaluating several sources. The pilot study was performed along two perpendicular profiles, located about 2 km northeast of the injection site, for which Yordkayhun et al. (2007) deduced velocity models using first break inversion. A comprehensive 3D baseline survey was carried out in autumn 2005 that imaged the southern flank and crestal part of the Ketzin anticline (Juhlin et al., 2007). This 3D survey allowed the derivation of a structural model which provided information about the strongly faulted crestal part of the anticline. Furthermore, it allowed the detection of natural gas remaining from the abandoned gas storage operation (Kazemeini et al., 2009). In autumn 2009 the first 3D repeat survey was conducted over a subset of the baseline survey around the injection location. Preliminary time-lapse processing results of the baseline and repeat 3D datasets imaged a CO_2 induced change of reflection amplitude centered at the injection well (Bergmann et al., 2010a). Reprocessing and refinement of the static corrections allowed a preliminary quantification of the imaged CO_2 (Ivanova et al., submitted).

2D seismic data were acquired in a baseline survey in 2005 and a repeat survey in 2009. Both surveys were carried out in close temporal succession to the respective 3D survey. This article describes first the acquisition and processing of the 2D seismic data of both surveys. We focus in particular on the role of static corrections in the processing. We find that the size of the static correction that needs to be applied depends highly on the near-surface conditions at the time of the survey. Our results are important for processing of the 2D lines described here, but also for the processing and interpretation of the other surveys carried out at the site.

4.2 Data acquisition

Based on the 2004 pilot study (Yordkayhun et al., 2009a) test, a VIBSIST source was chosen for the acquisition of the 2D lines. VIBSIST is a swept impact seismic source (Park et al., 1996) which combines the Vibroseis sweep-frequency and the Mini-Sosie (Barbier et al., 1976) multi-impact techniques. Impulsive impacts are generated in a sequence with increasing impact frequency. For the surveys, a linearly increasing impact rate was used with up to 680 impacts per minute. The impact sequence is recorded on a pilot trace by a geophone mounted on the base plate. Generation of a single impact seismogram is performed by the "shift-and-stack" method (Cosma and Enescu, 2001; Park et al., 1996).

The baseline 2D survey started on 22 November 2005 and was completed within six working days. Measurements started with surveying and cable layout of the source and receiver locations for seven lines (V1–V7, Figure 4.1). The lines were chosen to be directed towards the approximate location

Table 4.1: Acquisition parameters of the 2D seismic surveys. Numbers of sources and receivers are given with regard to the 2005 baseline survey.

Parameter	Value
Source point spacing	12 m
Receiver point spacing	24 m
Spread type	Fixed (all lines)
CDP Bin size	6 m
Geophones	28 Hz single
Sampling rate	1 ms
Record length	2005: 3000 ms 2009: 1500 ms
Source	VIBSIST-1000 Impact energy: 2500 J Impact frequency: 340–680 blows/min Operating weight: 2200 kg
Recording instrument	SERCEL 408UL

Line	Nb. of source stations	Nb. of receiver stations
V1	84	42
V2	84	42
V3	84	44
V4	32	21
V5	126	63
V6	84	42
V7	84	42

of the injection well, and thus a star-like distribution was realized. The location of the lines was partly governed by logistics, but was also controlled by the aim of improved sub-surface coverage towards the top of the anticline, to which CO_2 was most likely expected to migrate. Access to the injection site was not given due to construction works. Acquisition was conducted with a fixed spread, and all seven lines were simultaneously active. Two additional receiver lines were added to the spread (Lines 19 and 20) belonging to the acquisition geometry of the 3D surveys. The acquisition geometry was such that two source locations per receiver were activated. Sources were placed 6 m before and 6 m behind the respective receivers, with a receiver spacing of 24 m. Data recording was conducted with 28 Hz single geophones, planted in 0.2 m deep holes, and a Sercel 408UL acquisition unit. In-field quality control was comprised of visual inspection of the data and geometry, as well as documentation of external circumstances, e.g. weather conditions and technical breakdown times. Weather conditions during the baseline survey were calm and partly snowy.

The first 2D repeat survey was carried out between the 17th and 21st of September 2009, preceding the first 3D repeat survey. Roughly 22 kt of CO_2 had been injected at the time of the repeat survey. Station locations of the 2005 measurements were resurveyed with a DGPS accuracy of 0.2 m. Some modifications occurred on line V4, where it was not possible to re-occupy several stations due to problems with cable logistics. The technical setup, comprising the acquisition system, geophones and sources, was chosen to match the setup of the baseline survey. The VIBSIST source was

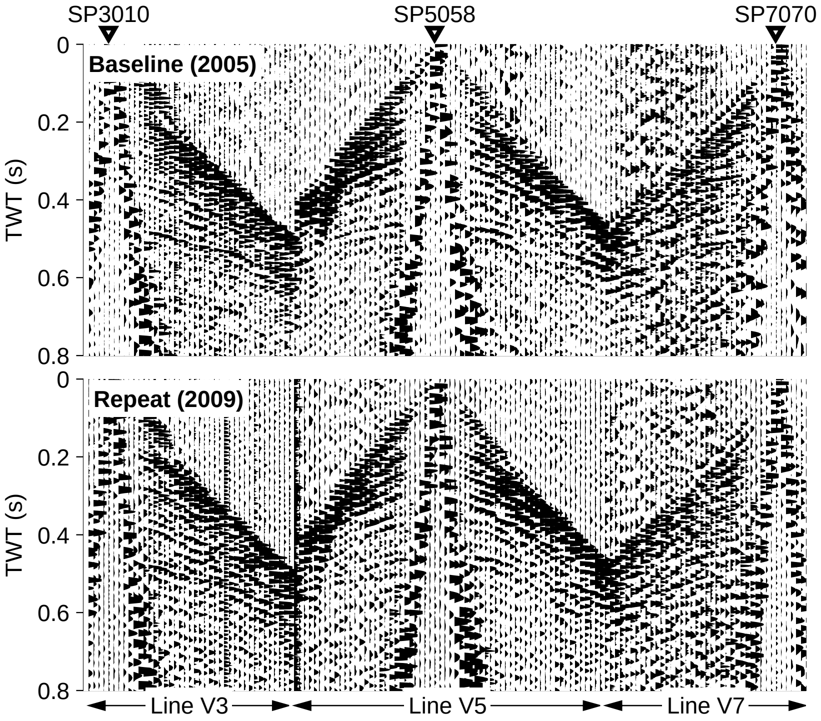

Figure 4.2: Example of three raw source gathers of the baseline survey (top) and repeat survey (bottom). Source locations are shown in Figure 4.1. Lower S/N ratio at line V7 is caused by road traffic.

modified by mounting it on a construction vehicle, which allowed better mobility and a higher production rate with less ground damage. Table 4.1 gives the acquisition parameters of the 2D surveys.

The fixed spread acquisition results in an irregular midpoint distribution, with high-fold 2D along the lines and patchy-fold in between the lines allowing pseudo-3D processing (Yang et al., 2010). Nominal fold along the 2D lines peaks at the line centers, with a maximum value of 50 on line V5, and decreases to zero at the line beginnings and ends. A data example is given in Figure 4.2. Visual inspection of the complete datasets shows that these are in general of good quality with easily identifiable reflections observed at 100– 550 ms. The top of the Weser formation (K2) is the most significant reflection event with an approximate zero-offset time of about 430 ms. The lowest S/N ratios are due to traffic noise, appearing to be most significant on line V7 which is located along the main road to Ketzin.

It has been shown that consideration to near surface conditions must be made for land seismic time-lapse surveys (e.g. Pevzner et al., 2011). To increase reproducibility, both surveys at the Ketzin site were performed in the same season, e.g. shortly after the harvesting season in early-late Autumn. However, this practice does not guarantee identical weather and ground conditions. A comparison of the 3D seismic baseline and the repeat data showed considerable near-surface velocity variations most likely caused by different weather conditions, which necessitated a new re-calculation of static corrections for the repeat data (Lüth et al., 2011; Ivanova et al., submitted).

Similar observations were noted for the 2D data, leading to the testing of advanced static correction methods described here, circumventing the need for reprocessing of the baseline data. Furthermore, the 2D seismic surveys at Ketzin were conceived to combine surface-to-surface measurements and MSP. Simultaneously acquired surface-to-surface datasets and MSP datasets contain the same source related statics. Therefore, the static corrections from the 2D datasets are important for the processing of the MSP and pseudo-3D datasets.

4.3 Processing

The processing workflow was selected in an iterative manner, relying on the raw structure of the 3D processing workflow given by Juhlin et al. (2007). The workflow is a conventional CMP stacking routine with subsequent post-stack time migration, which is kept simple and avoids extensive usage of wavelet processing to reduce the risk of introducing artifacts. Parameters of each processing step were tested until a satisfying parameter combination was found. Afterwards this parameter choice was appended to the existing sequence. Processing was carried out with Promax (Landmark) except for first break picking and calculation of refraction statics, which were performed with Claritas (GNS Science). An overview of the processing steps is given in Table 4.2.

After shift and stack of the raw SEGD field data the processing started with importing of the decoded SEGY data and geometry. Bin grid definition was performed in a straight-line manner with creation of a rectangular bin layout with 6 m inline spacing, aiming to achieve binning of baseline datasets and repeat datasets with the same grids. Subsequently, a comparison of baseline and repeat data was done for every line. Traces which were not present in both the baseline and repeat dataset were excluded from further processing, yielding baseline and repeat datasets with identical trace content. Trace edits and polarity reversals were picked on the complete datasets comprising the traces activated and acquired on different lines. Trace editing was conducted in a two step process. The first step consisted of the manual picking of traces with low S/N ratio within common source gathers, with an offset amplitude balancing gain applied, and focused on identification of noisy wave coda. The second step consisted of manual picking within offset bin gathers and focused on traces which showed significant amplitude deviations compared to traces of similar source–receiver offset. An example for the processed pre-stack data is given in Figure 4.3.

Refraction static corrections were carried out for baseline and repeat datasets separately and started with manual picking of first breaks. Insufficient S/N ratio prohibited reliable determination of first breaks at several locations, with most significant losses on line V7. Where first breaks could not be picked, better pronounced secondary phases were used and corrected to the primary onset times. The source–receiver offset range was constrained to offsets larger than 20 m. Inversion of the pick times started from a two layer model, with initial velocities determined from the apparent velocities found in the data (1st layer: 600 m/s, 2nd layer: 2300 m/s). Final inversion velocities were constrained to 300–1200 m/s for the first layer and 1500–3000 m/s for the second layer. At locations where inverted velocities exceeded these velocity intervals, constraints were iteratively relaxed. The inversion yields two types of refraction statics. (A) Model refraction statics, which are calculated from the inverted velocity model. (B) Residual refraction statics, which are calculated from the decomposition of the difference between the picked arrival times and the arrival times deduced from the inverted velocity model. Model refraction static corrections were calculated for

Table 4.2: Processing sequence applied to the 2D datasets.

Preprocessing	• SEGY data
	• Apply geometry & binning
	• Amplitude balance precompute
	• Retrieve intersection of baseline and repeat dataset
	• Bulk source statics: -25 ms
	• Trace edits and polarity reversals
	• Brute velocity analysis with preliminary AGC (every 60th CDP)
	• Elevation statics: processing datum = final datum (30 m a.s.l.) 1800 m/s replacement velocity
	• Refraction statics: Derived from first breaks with offsets > 20 m Refraction residual statics partly applied
	• Mute: top and bottom
	• Amplitude recovery: $1/(v^2t)$ with brute velocities max time of application 700 ms
	• Amplitude Balance: Surface consistent amplitude decomposition into source, receiver and offset domain (5 iterations, 20% alpha-trimmed mean). Derived on complete dataset Application after manual editing of near-offsets within offset decomposition.
	• Bandpass filtering: time dependent
	• Deconvolution: minimum-phase predictive, 40 ms operator length, 16 ms prediction distance, 0.1% white noise level
Residual statics	• 1st pass residual statics: 3 iterations, ±12 ms max allowed statics
	• Velocity analysis (every 30th CDP)
	• 2nd pass residual statics: 3 iterations, ±12 ms max allowed statics
	• Velocity analysis (every 10th CDP)
DMO/PostSTM	• DMO correction: Source ensemble DMO in T-X domain
	• Velocity analysis (every 10th CDP)
	• NMO correction: 50% stretch mute
	• Stack
	• Migration: 2D Kirchhoff in poststack time domain using smoothed stacking velocities

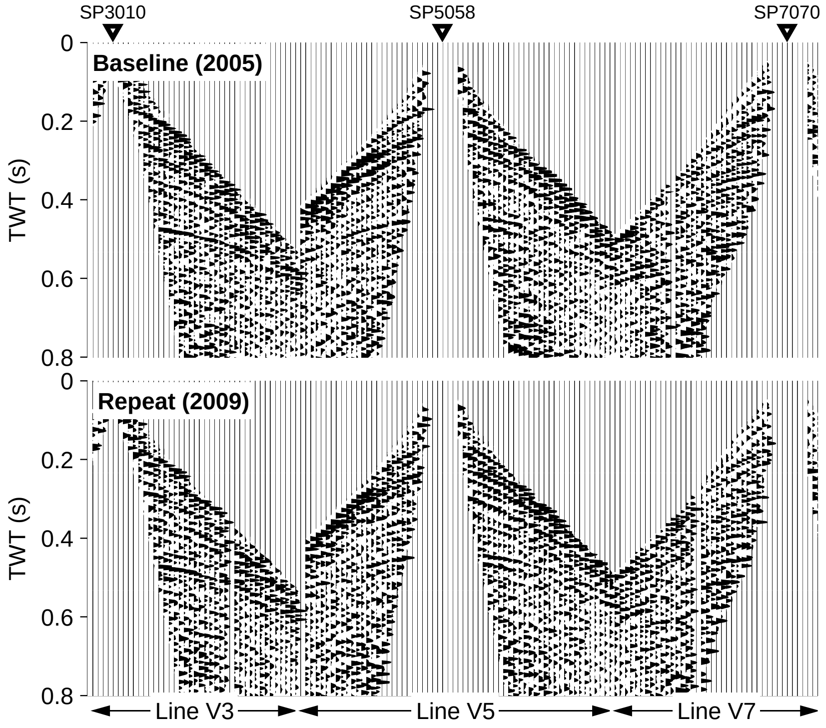

Figure 4.3: Source gather examples of Figure 4.2. after preprocessing. Source point locations are shown in Figure 4.1.

the first layer and showed values of up to 8 ms on line V3. Calculated residual refraction statics were found with values of up to 20 ms, but were constrained to the respective maximum of the model refraction statics. Application of model refraction statics and constrained residual refraction statics generally improved stack coherence.

Stacking velocities were determined by manual picks on semblance spectra on CDP super-gathers. Velocity analyses were performed in four passes during the processing. The first pass started with an average velocity function which had been determined on selected CDPs of the baseline survey. The second pass was performed after the preprocessing and first iteration of residual statics. The third pass after performance of the second residual statics iteration. The fourth pass after performance of DMO corrections. CDP spacing for the velocity analyses was chosen to be 60 for the first pass, refined to 30 in the second pass and to 10 in the two latest passes, respectively.

The K2 and Base Tertiary reflections could be clearly followed throughout the complete analyses. The Base Tertiary reflection was picked with an average RMS velocity of about 2200 m/s in the two-way-time range 150–170 ms. RMS velocities along the deeper Top Triassic reflection were determined to be about 2500 m/s and to the K2 reflection about 2850 m/s, respectively. Velocity determination for lower amplitude reflections was conducted by means of picking along interpreted horizons.

In a first approach, processing of the baseline and repeat datasets was tested with identical processing parameters, except for stacking velocities that were determined independently to produce maximum individual stack power. Comparison of such processed stacks revealed that even relatively small stacking velocity variations (<5%) produced significant differences, and are thus a likely source for generating artifacts in the time-lapse signatures. Therefore, it was decided to derive a single velocity model for each line from the baseline data, which was then used for processing the respective repeat line.

4.4 Testing of static correction methods

Time-lapse seismic methods have undergone considerable development in the past decades. Several case studies have demonstrated that 4D seismic surveying can play an important role in hydrocarbon reservoir characterization and monitoring (e.g. Landrø et al., 1999; Lumley, 2001). Most reported surveys were conducted for production monitoring of offshore reservoirs. Only a minority of the publications deal with onshore surveys. Although methodically similar, onshore time-lapse surveying is, compared to offshore surveying, faced with somewhat different issues affecting the repeatability. Based on available publications and our experience gained on the Ketzin datasets, changes of near-surface velocities and source wavelet reproducibility appear to be the most important issues.

While wavelet reproducibility can be improved by automatic wavelet matching procedures, the correction of near-surface velocities can be addressed by two approaches: Ray-based refraction static corrections and wave-equation-based datuming. Refraction static corrections require the determination of first breaks from which travel time corrections are derived (Lawton, 1989). First break pick accuracy depends on the available frequencies and S/N ratio of the data, as well as to some extent on the subjectivity and experience of the processor. Besides for methodical reasons (e.g. Palmer, 2010), refraction statics can, therefore, never yield arbitrarily accurate solutions. The issue becomes more serious when refraction static corrections of repeated surveys are performed by different processors. Zhang and Schmitt (2004) report that minimal time shifts introduced in the refraction static corrections can generate a time-lapse false signal, and that these shifts may even be of subsample order. Such time shifts can easily be caused by fluctuations in the groundwater table, moisture changes in the vadose zone or man-made earthworks, which prohibits the application of the baseline statics to the repeat surveys. In some cases, static corrections can be improved by low-velocity measurements, which provide short spreads and geophone spacings at selected locations of the survey area. Nevertheless, the observation that refraction static corrections often do not deliver satisfying solutions is supported by the need for subsequent residual static corrections.

A comparison of baseline and repeat traces of the Ketzin datasets showed that relative static shifts are present, which were imaged as noise on the difference sections. Changes in the near-surface velocities were identified as the most likely source for these shifts. Refraction statics, independently performed for the baseline and repeat datasets, resulted in just a limited reduction of these static shifts. Therefore, the following static correction methods were added to the processing sequence given in Table 2, which is termed as workflow A (Figure 4.4).

- Pre-stack static corrections derived in a surface-consistent manner, decomposing static shifts into the source and receiver domains (workflow B).
- Post-stack static corrections derived along a reference horizon used for alignment of the repeat stack section to the baseline stack section (workflow C).
- Combination of pre-stack and post-stack static corrections (workflows B+C).

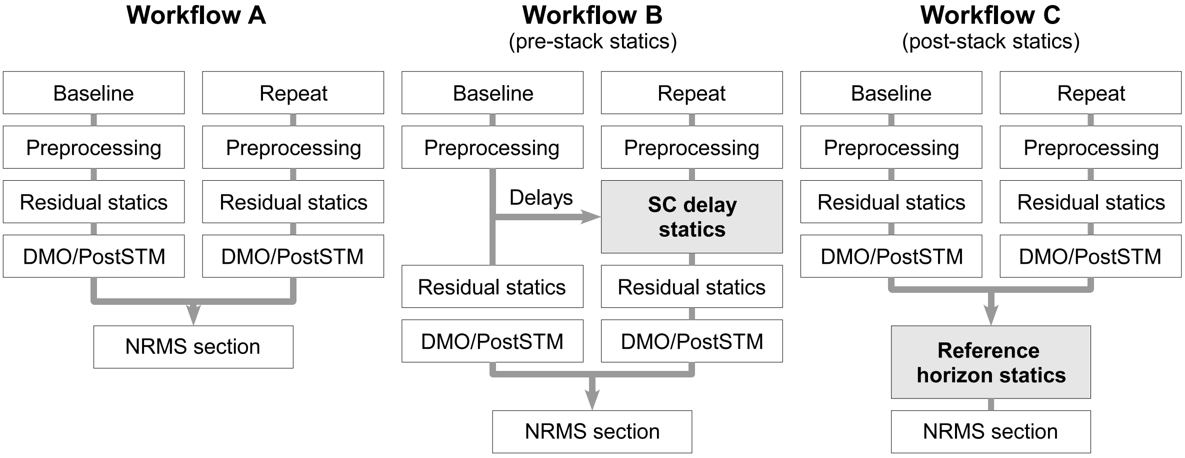

Figure 4.4: Static correction methods evaluated as follows. Workflow A corresponds to the processing sequence given in Table 2. Workflow B is an extended version of workflow A, including surface-consistent (SC) static corrections applied in the pre-stack domain. Workflow C is an extended version of workflow A, including reference horizon static corrections applied in the post-stack domain. Additionally, a combination of workflows B and C is investigated. Processing of repeat data was done with the stacking velocities derived from the respective baseline data.

4.4.1 Pre-stack statics

Near-surface related travel time delays, arising from the baseline and repeat surveys being acquired at different times, can produce noise or even artificial events in the time-lapse section. Therefore, a static correction approach is suggested to compensate for spatiotemporal velocity changes in the near-surface. This approach seeks to decompose the static delays, found by comparison of the baseline and repeat traces, into the source and receiver domains in a surface-consistent manner. Static corrections derived from the decomposition are applied to the repeat dataset to improve alignment with the baseline dataset. It is designed to be a fully data-driven approach, which ties repeat surveys to previous surveys, circumventing the necessity of reprocessing baseline static corrections. The conceptual workflow of the pre-stack static corrections is shown in Figure 4.5.

Timing delays of baseline traces and their repeat equivalents are determined by trace-wise cross-correlation and are then assembled in the delay matrix D. The element D_{ij} equals the timing delay found for a trace pair belonging to the source station index i and receiver station index j. Delays are assumed to be caused by near-surface delays M and delays δ, which are caused by other than near-surface effects (Figure 4.5a). Those effects can be spuriously generated delays, which, for instance, might be caused by inaccuracies in the source wavelet reproduction or ambient noise. The near-surface delay M_{ij} is assumed to be composed of a source station delay S_i and a receiver station delay R_j. I_i denotes a vector with unity elements and a length equal to the number of receivers. I_j respectively, but with a length equal to the number of sources. Transposed multiplication of these vectors with S and R yield matrices of the same size as D, but with S_i arranged in columns and R_i arranged in rows, respectively.

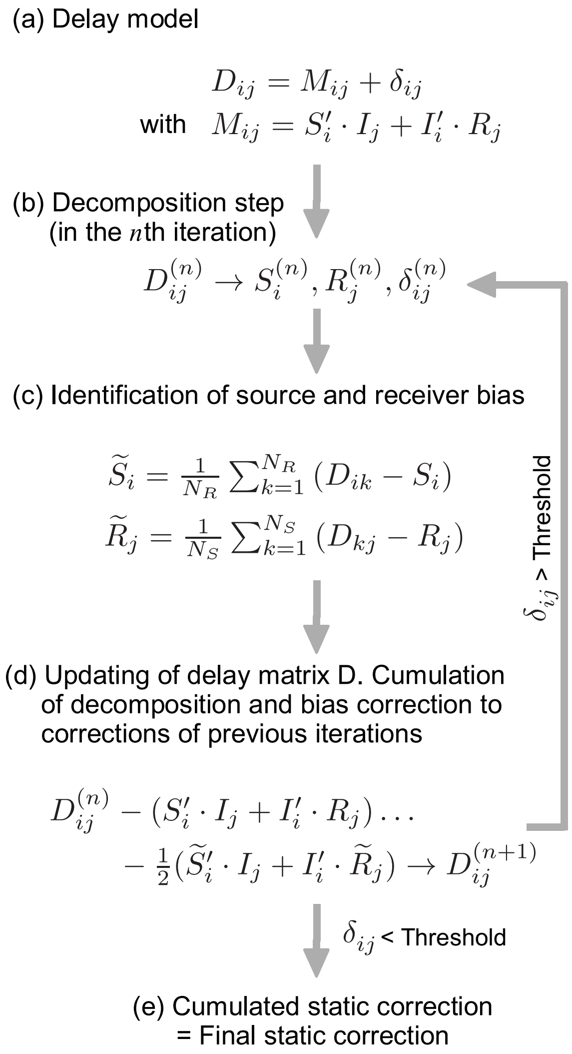

Figure 4.5: Conceptual chart of the iterative determination of pre-stack static corrections aimed to correct surface-related misalignment of baseline and repeat traces (Workflow B).

Since δ remains when the near-surface delays M are subtracted from the measured delays D, it is termed the residual delay matrix. The iterative loop starts with the decomposition of D into the source and receiver domains (Figure 4.5b), which is performed by a modification of the residual static correction method of Ronen and Claerbout (1985). The significant difference is that the decomposition is not applied to reduce relative delays in CDP gathers of a single dataset, but to reduce delays deduced from time-lapse datasets. The approach of Ronen and Claerbout maximizes stack power by aligning phases at CDP specific times. These times, which are related to the mean of the phase arrival times in the respective CDP, are considered as bias. Bias corrections are deduced for sources $\tilde{S}$ and receivers $\tilde{R}$ for subsequent removal (Figure 4.5c). $\tilde{S}$ equals the mean difference of measured delays, from a common source gather, and the respective source delay S. $\tilde{R}$ is determined vice versa. N_S and N_R denote the number of sources and receivers, respectively. The bias correction applied within the iteration is the mean of source bias and receiver bias (Figure 4.5d).

Table 4.3: Mean and standard deviation (both given in ms) of the delay distributions before and after application of pre-stack static corrections. Application of pre-stack static corrections results in decreased delay means and standard deviations. Detailed distributions for lines V3 and V5 are given in Figure 4.6.

Line	Mean delay without pre-stack static correction	Mean delay with pre-stack static correction
V1	-0.58 ± 1.61	-0.21 ± 1.20
V2	-0.29 ± 1.60	-0.17 ± 1.10
V3	-0.83 ± 1.58	-0.26 ± 0.97
V5	-0.92 ± 1.63	-0.30 ± 1.22
V6	-1.25 ± 1.53	-0.40 ± 1.41
V7	-0.76 ± 1.37	-0.42 ± 1.11

The iterative loop is continued by updating the delay matrix D with the current source and receiver static corrections and bias corrections. Corrections are accumulated for later application as final static corrections (Figure 4.5e). Figure 4.6 shows the delays, static corrections and residual delays for lines V3 and V5.

Cross-correlation delays were constrained not to exceed a half signal period (about 10 ms), which is presumed to be a reasonable range for correcting near-surface variations and avoiding cycle skips. Correlations were conducted on the preprocessed data in time gates centered at the imaging target time. The Top Stuttgart is defined by a weak reflection which splits the time gates in two parts. The lower part contains no significant reflections, unlike the upper part which contains the strong K2 reflection. Therefore, the correlation is dominated by the reflectivity in upper part of the time gate. Thus, we estimate the consequence on the pull-down reflections beneath the reservoir to be minor.

If time gates would cover the overburden only, most of the far-offset traces (which have smaller time differences between first-break and the Top Stuttgart than short-offset traces) would have been omitted, due to too short gate lengths. Thus, we decided to center the time gate on the imaging target time to compromise between reflectivity contributions from the overburden and from the far-offsets. Trace pairs containing less than 120 ms worth of live samples within these time gates were excluded and are shown as gray elements (Figure 4.6). Despite the large number of gray elements for line V5, the determination of near-surface delays is possible, although the system is not as over-determined as for line V3. Delay histograms before application of the pre-stack statics show peaks, which are centered at negative delay means. Table 4.3 shows that the application of the pre-stack static corrections results in decreased delay means (centered almost at zero) with decreased standard deviations (narrower delay distributions).

Decomposed source and receiver static corrections are given in Figure 4.7, showing stronger scattering for the sources than the receivers. This behavior might be an indication for trigger scattering or non-uniform soil consolidation during the impact sweep sequence. Horizontally aligned patterns observed in the static correction plots of Figure 4.6 are attributed to the dominance of stronger scattering of the sources. An indication of these patterns can also be observed in the measured delays (Figure 4.6), yielding two conclusions. First, source delays contribute more to measured delays than receivers. Second, in the decomposed solutions the dominant source contribution and

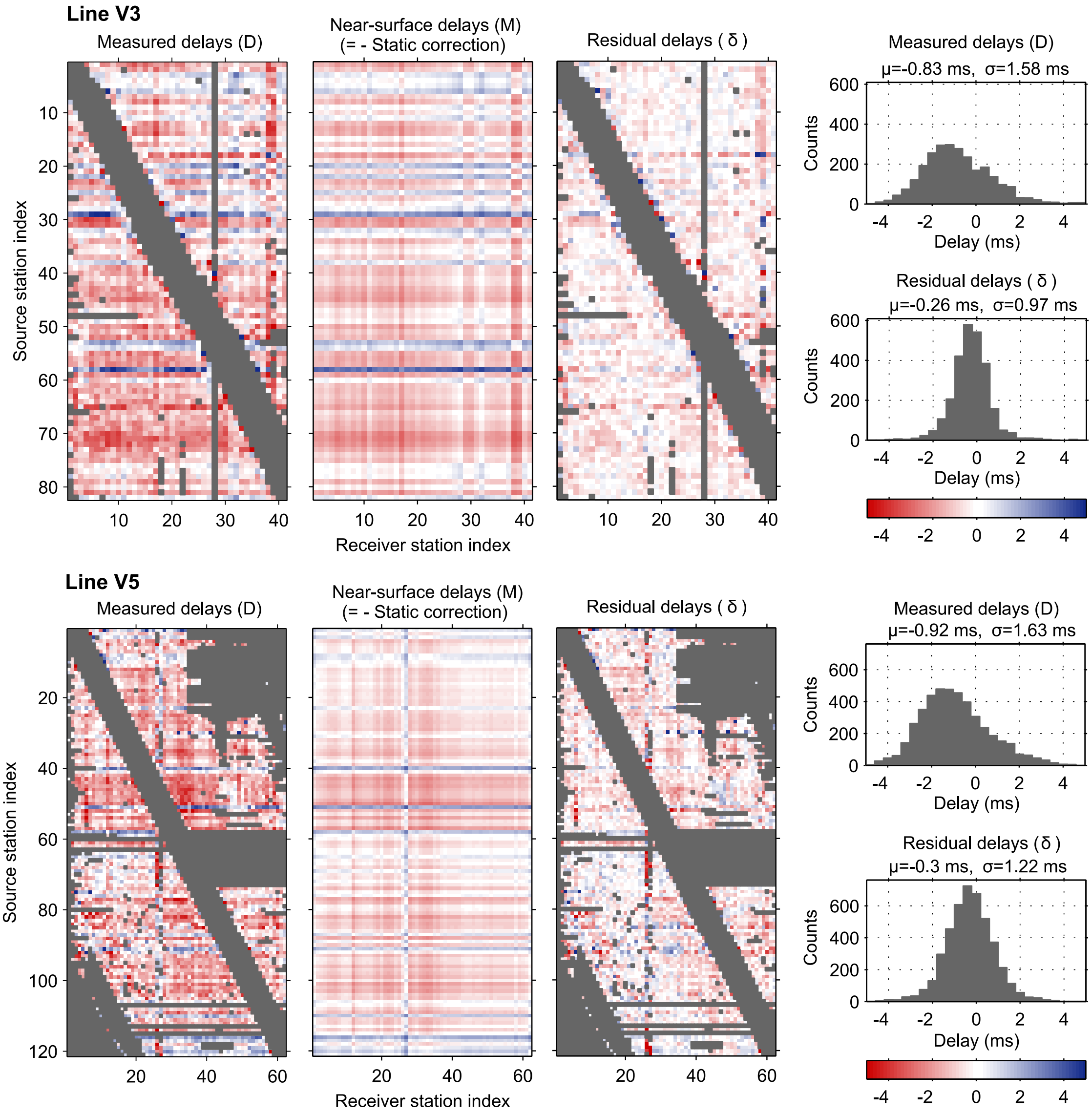

Figure 4.6: Measured delays, near-surface delays and residual delays for line V3 (top panel) and line V5 (bottom panel). Left matrix plots depict the measured timing delays of baseline and repeat data deduced from correlation analysis. Center matrix plots depict the static corrections obtained from surface-consistent decomposition of the measured delays. Right matrix plots depict the residual delays remaining after application of the static corrections to the measured delays. Gray elements near the main diagonals represent traces excluded, because of being affected by ground-roll. Other gray elements depict traces excluded due to too low SN ratio. Right histograms show delay distributions before and after application of the static corrections with mean μ and standard deviation σ. For both lines the application leads to a centring at the origin with narrowed delay distributions. Values for the other lines are given in Table 3.

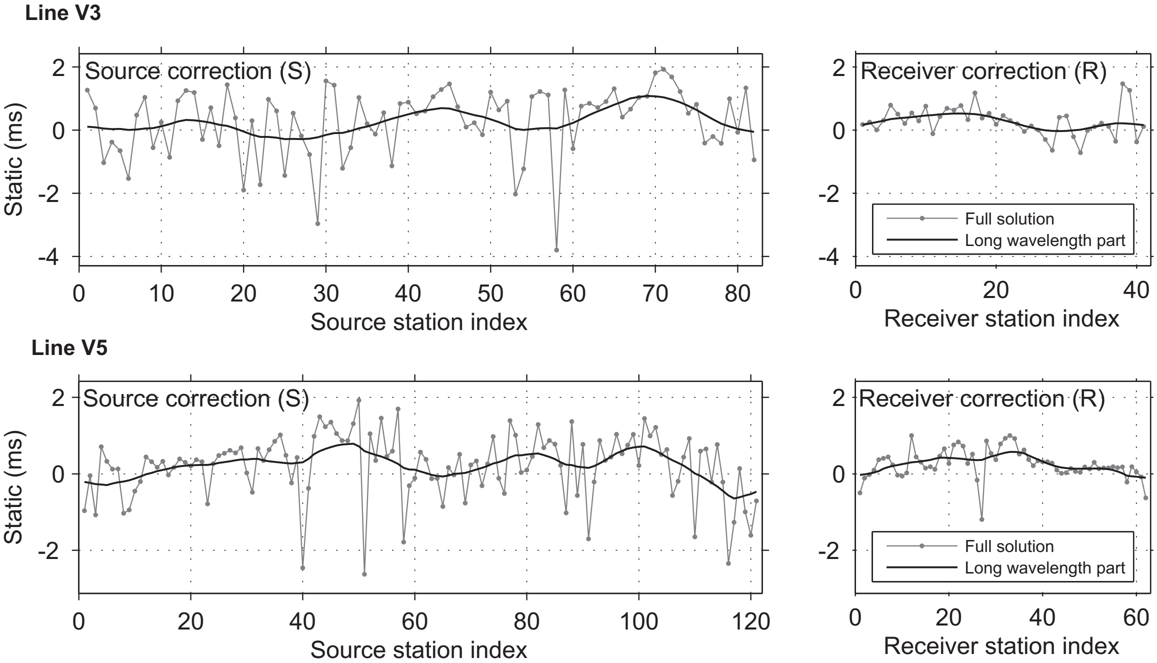

Figure 4.7: Full solution and long-wavelength part of the decomposed static corrections for sources (left column) and receivers (right column) of line V3 (top row) and V5 (bottom row). The solutions produce the static correction M shown in Figure 4.6. Long-wavelength parts are deduced from moving-average filtering. Maps with the spatial distribution of long wavelength-parts are shown in Figure 4.8. The stronger scattering of the sources is observed along the whole of all the lines.

the pre-stack static correction balance both contributions.

Figure 4.8 shows maps of the long-wavelength part of the decomposed solutions. Sources and receivers show limited correlation, but indicate a significant change in the northern part of line V5, where the line reaches the faulted zone at the anticlinal crest. The smallest static correction values are found on line V7, which indicates minor changes in the near-surface velocities. Alternatively, since the line is located near the main road to Ketzin, high noise levels might be the reason for the anomalously small correction values.

Near-surface delays and static corrections are equal, but of opposite algebraic sign. A travel time delay is defined as subtraction of the travel times in a repeat trace from the travel times in a baseline trace (delay=$t_{baseline}-t_{repeat}$). Thus, the static corrections hold to the convention that a positive correction corresponds to the downward shift of a trace. Pre-stack static corrections given in Figure 4.8 are mainly positive, which means that repeat traces on average are shifted downwards to be aligned with baseline traces, i.e. repeat phases arrived earlier than the corresponding baseline phases. Since the pre-stack static corrections reflect near-surface variations, this is interpreted as increased near-surface velocities being present during the repeat survey. A near-surface velocity increase is thought to be caused by a rise of the ground water level. This explanation is supported by the observation that several stations had to be skipped in the succeeding 3D repeat survey due to inundation by water.

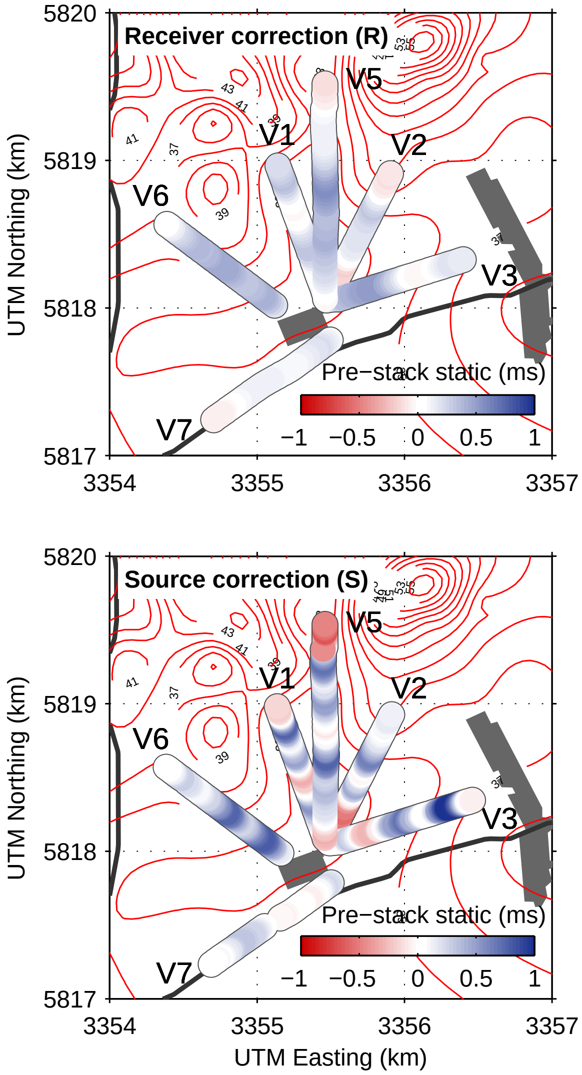

Figure 4.8: Long-wavelength part of the pre-stack statics solutions for sources and receivers (detailed values for lines V3 and V5 given in Figure 4.7). Red contours show the elevation of the ground surface.

4.4.2 Post-stack statics

In a second step, static corrections of the post-stack sections are tested. These corrections are derived from timing delays of cross-correlated baseline and repeat CDPs. Correlation is conducted in a time window centered on a reference horizon reflection, which is taken to represent a boundary that has not changed between the baseline survey and the repeat survey. Static corrections are applied to the repeat stack section, aiming to improve alignment with the baseline stack section. This method provides an approach to determine velocity push-down effects and perform reservoir storage quantification by time-lapse seismic surveying (e.g. Chadwick et al., 2005). As with pre-stack static corrections, the post-stack static correction aims to allow processing of repeat surveys without reprocessing static corrections of previous surveys. The Top Weser formation (K2) was chosen to be

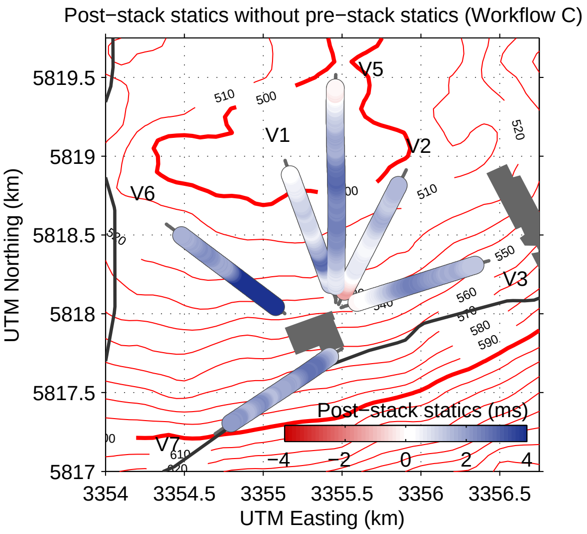

Figure 4.9: Display of the post-stack statics derived from reference horizon alignment along the Top Weser Formation (K2). Red contours image the depth of K2. Gray lines at the starts and ends of profiles show segments which were excluded from post-stack statics, due to low fold imaging of K2.

the reference reflection for the 2D data for two reasons. First, K2 is the most significant reflection observed in the stacked sections, showing continuous polarity and well preserved waveform coda for the entire area. A similar character was observed on the baseline 3D survey (Juhlin et al., 2007). Secondly, the Top Weser formation belongs to the overburden of the injection formation. Assuming that the injected CO_2 causes a pull down effect, a reference horizon located below would cause a spurious time-lapse signature, ranging from the reference horizon to the shallow reflections. CO_2 migrating upward through the Weser Formation and K2, would need to be detected by reflection amplitude changes. This case would demand detailed investigation, in order to check whether assumptions for the reference horizon choice are satisfied, eventually necessitating the selection of a new reference horizon in the overburden.

Post-stack static corrections of the 2D lines (Figure 4.9) show mainly positive values, indicating a velocity increase for the repeat survey. This observation is consistent with the interpretation of the pre-stack static corrections. However, in contrast to the pre-stack static corrections, the post-stack static corrections just give a limited indication at which depth such a velocity increase could be located, since they are derived from travel times integrated from the surface to the reference horizon and back. Comparison of the post-stack static corrections (Figure 4.9) and the long-wavelength solutions of the pre-stack static corrections (Figure 4.8) shows a correlation for line V6, the northern part of line V5 and the southern part of line V2. Since post-stack static corrections reflect at least partly near-surface delays, travel time delays at these locations might be dominated by the near-surface conditions.

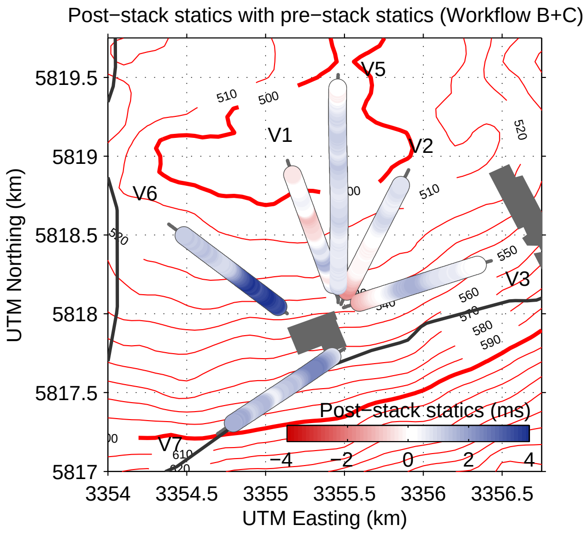

Figure 4.10: Display of the post-stack statics derived from reference horizon alignment of K2 after application of pre-stack statics. Red contours show the depth of K2.

Table 4.4: Mean and standard deviation (both given in ms) of the post-stack static corrections with and without application of pre-stack statics. Maps of the detailed values are given in Figures 4.9 and 4.10.

Line	Workflow C (without pre-stack static correction)	Workflow B+C (with pre-stack static correction)
V1	1.26 ±0.67	0.25 ±0.67
V2	0.75 ±0.83	0.12 ±0.74
V3	1.56 ±0.80	0.63 ±0.78
V5	1.83 ±0.85	0.84 ±0.28
V6	3.38 ±1.39	2.37 ±1.19
V7	2.10 ±0.44	1.59 ±0.53

4.4.3 Pre-stack and post-stack statics

In a third step, a combination of pre-stack static corrections and post-stack static corrections was tested. Since incorporation of pre-stack static correction leads to changed residual statics, the post-stack static correction was incorporated as an extension to workflow B. If a set of pre-stack static corrections shows at least a long-wavelength trend, it should have an impact on the resulting stack. As pre-stack static corrections are meant to align repeat traces to baseline traces, its application should lead to a reduction of the post-stack statics, which are necessary to tie a repeat stack to its respective baseline stack. A map showing post-stack static corrections after application of pre-stack static corrections is given in Figure 4.10. Comparison with the post-stack static corrections of workflow C (Figure 4.9) shows that the application of pre-stack statics yields a reduction of the post-stack static corrections. Mean values and standard deviations for post-stack static corrections only (workflow C) and combined static corrections (workflow B+C) are given in Table 4.4.

It shows that the application of pre-stack static corrections causes mainly a reduction of the mean values. Comparison of Figures 4.9 and 4.10 indicates that the application of pre-stack static corrections equals a trend removal for the post-stack static corrections of up to 1 ms. It should be mentioned that the static corrections of workflow C and workflow B+C can be directly compared since both static correction approaches are fully data-driven and the processing used the fixed baseline velocities.

4.5 Discussion

Here, we use the normalized root mean square (NRMS) amplitude ratio displays after Kragh and Christie (2002) to perform post-stack analysis of the time-lapse sections. For a baseline CDP trace a and its repeat equivalent b, the NRMS ratio is defined as

$$NRMS(a,b) = \frac{2 \cdot RMS(a-b)}{RMS(a) - RMS(b)} \tag{4.1}$$

Assuming two wavelets of similar form and polarity, the NRMS equals zero. Switching the polarity of one of the wavelets corresponds to a NRMS of 200%. Therefore, 0% and 200% span the value range for NRMS ratios. NRMS amplitude ratios were calculated in 40 ms sliding time windows. Wavelet matching of baseline and repeat stacks was not conducted at this stage and is shifted to the subsequent time-lapse interpretation, since the focus here is on testing of static corrections. Figure 4.11 shows NRMS sections of line V3 for the different workflows (Figure 4.4).
The following observations can be made from Figure 4.11.

- Workflow A (no additional statics) shows significant NRMS ratios at about 200 ms and about 500–600 ms. NRMS ratios (b100%) are smeared over the entire NRMS section.
- Workflow B (pre-stack statics) leads to an overall reduction of the NRMS level. Segments with significant NRMS ratios remain (e.g. at 200 ms), but appear focused.
- Workflow C (post-stack statics) leads to a further decrease of the overall NRMS level. Local segments of significant NRMS remain, but appear further focused. Since K2 (Top Weser formation) was used as the reference horizon for post-stack static corrections, nearby NRMS ratios are close to zero. NRMS ratios between about 250– 450 ms (Top Sinemurian to K2) are subdued and would, in contrast to workflow A, suggest no time-lapse signature.
- Workflow B+C shows similar results to workflow C. The combination of pre-stack and post-stack statics does not result in a further reduction of the NRMS level.

The trend of decreased NRMS level by application of workflow B and workflow C is confirmed for the other lines (Table 5). The combined workflow B+C does not improve the average NRMS ratio significantly, but decreases the average level of post-stack statics. The significant improvement of the average NRMS ratio is attributed to the pronounced amplitude and spatial continuity of K2. Therefore, if post-stack static corrections are based on a suitable reference horizon, pre-stack static corrections can be considered to be of minor importance. Nevertheless, pre-stack static corrections are useful since they allow for removal of near-surface statics by construction of a source/receiver delay model. Furthermore, pre-stack static corrections could support pre-stack analysis of datasets,

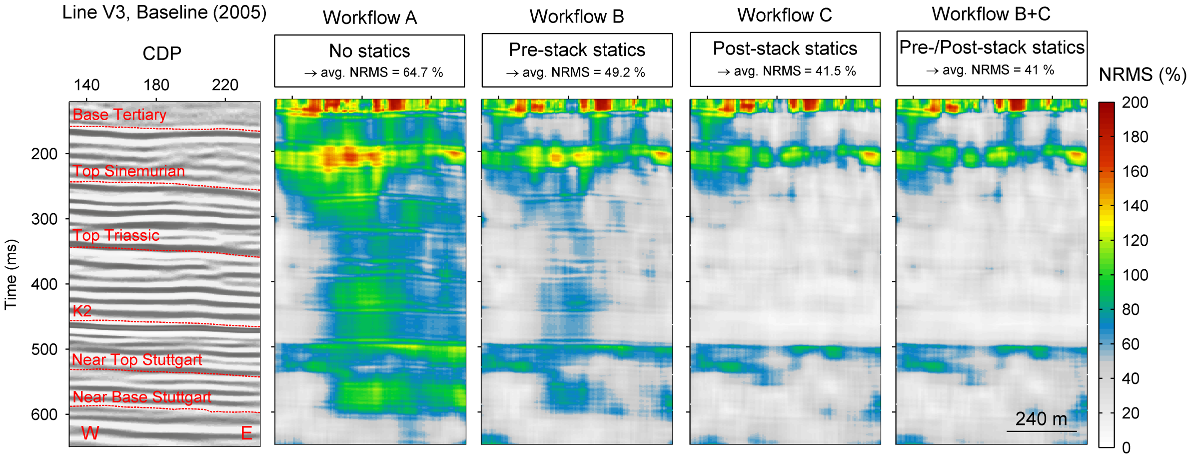

Figure 4.11: NRMS sections of line V3 processed with the static correction methods given in Figure 4.4. Workflow A depicts the NRMS section of the data without any additional time-lapse static correction applied. Workflow B depicts the section with pre-stack static corrections applied, which leads to a reduction of the averaged NRMS level while preserving the most significant time-lapse signatures observed for workflow A. Workflow C depicts the NRMS section after application of post-stack statics, which reduces the NRMS level compared to workflow A. The combination of workflow B and C (right display) leads to an averaged NRMS level, which is about the averaged NRMS level of workflow C. Horizontal patterns in the NRMS sections are observable where strong reflection events are present in the stacked section (left). Strong NRMS amplitudes are present in the time range below K2 and above Top Stuttgart at about 500 ms. These NRMS amplitudes are caused by differences in the baseline and repeat wavelets. Since wavelet matching is performed in the post-stack domain, we use the unmatched sections to allow for comparison with the pre-stack static corrections.

e.g. time-lapse AVO. If, in a general case, post-stack static corrections need to be deduced along a reference horizon of poor suitability (e.g. low reflectivity or low S/N ratio), the combination of pre-stack and post-stack static corrections might be useful, allowing for identification of near-surface velocity changes.

4.6 Comparison with 3D data

Since the 3D surveys form a comprehensive basis for the seismic monitoring at the Ketzin site, a comparison of the 2D and 3D processing results was made. The baseline 3D survey was acquired in 2005, and the repeat survey in autumn 2009. The geophones and acquisition unit used in the 3D surveys were the same as those used in the 2D surveys. However, instead of the swept-impact VIBSIST, an EWGIII weight drop source was used for the 3D surveys. Processing workflows of the 2D and 3D datasets consist of a CDP stacking, post-stack time migration and a scheme with static corrections performed in a comparable manner. For details of the 3D baseline acquisition and processing the reader is referred to Juhlin et al. (2007). Differences in the 2D and 3D processing are the application of a DMO correction and exclusion of post-stack FX-deconvolution and zero-phase

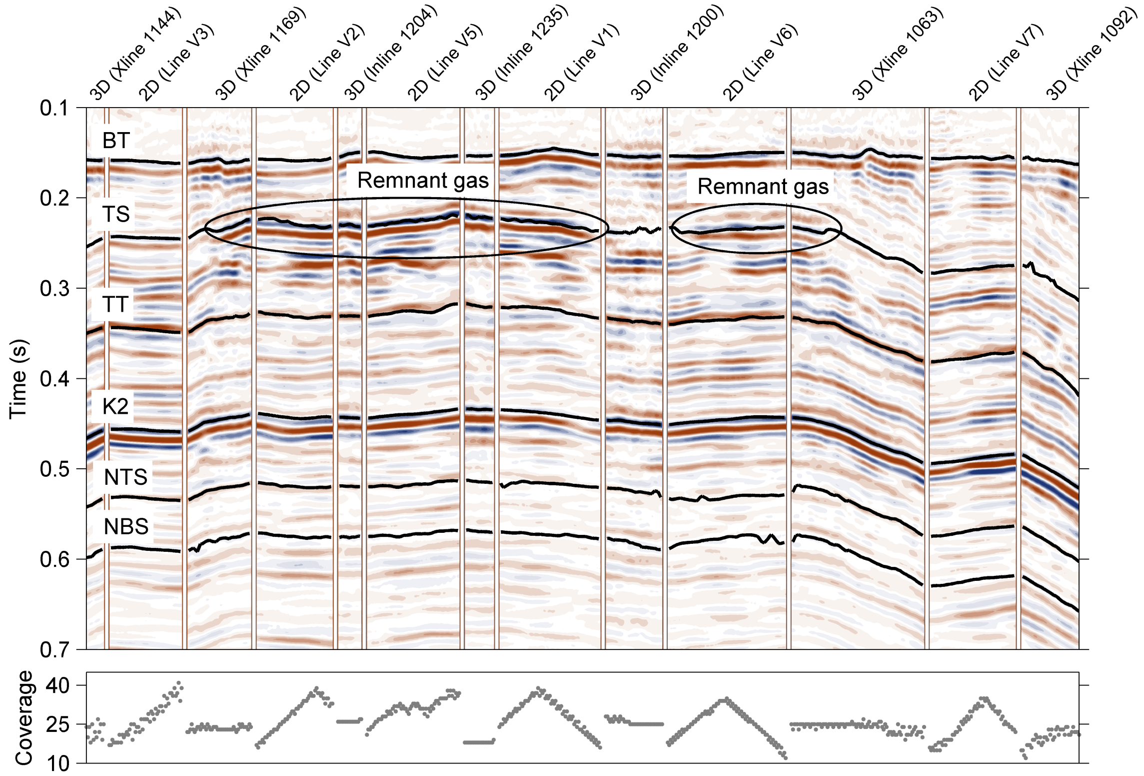

Figure 4.12: Comparison of the 2D lines (baseline, 2005) and 3D stack (baseline, 2005) along the line-tie-track shown in Figure 4.13, left. Annotations indicate Base Tertiary (BT), Top Sinemurian (TS), Top Triassic (TT), Top Weser Formation (K2), Near Top Stuttgart (NTS) and Near Base Stuttgart (NBS). Note that the bin distance of the 3D data is twice that of the 2D data, but traces are displayed with equal spacing.

conversion for the 2D data. A line-tie comparison of the 2D baseline stacks and the 3D baseline stack is given in Figure 4.12.

The Base Tertiary and Top Weser formation (K2) constitute the main reflections, showing good correspondence in the 2D and 3D stacks. Both are imaged as double reflections (peak–trough–peak) of pronounced continuity. Due to the faults in the anticline crest, the Base Tertiary is imaged poorly at the northern end of line V5. The fault system was found by the 3D baseline survey as trending in an east– west direction across the central part of the Ketzin anticline (Juhlin et al., 2007), striking approximately perpendicular to line V5. Reflections between the Base Tertiary and K2 show less continuity and lower reflection strength. Amplitude brightening, reflecting the presence of remnant gas, is observable on lines V1, V5 and V2 (Figure 4.12), being consistent with the 3D stack. Weaker amplitude brightening is observed on line V6, also being consistent with cross-line 1063 of the 3D stack. The remnant gas distribution as given in Figure 4.13 is based on a report by 'UGS Untergrundspeicher- und Geotechnologie-Systeme GmbH' (Kazemeini et al., 2009), which operated the former natural gas storage at Ketzin. The waveforms of most reflections in the 2D and 3D datasets match each other, with differences mainly found for the deeper reflections (>800

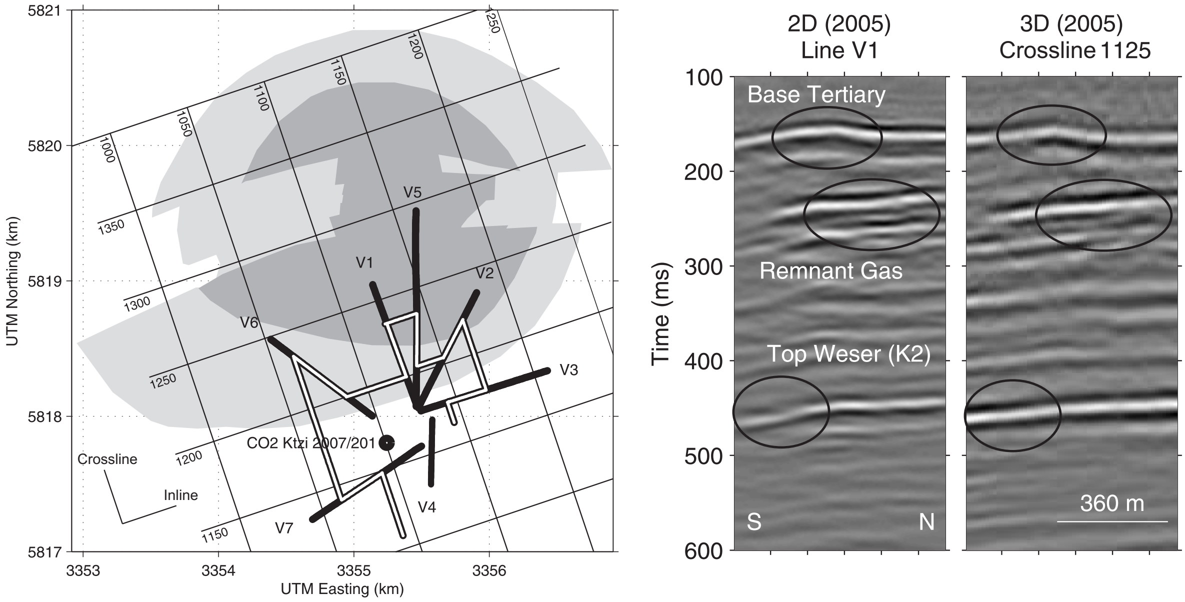

Figure 4.13: Left: 3D seismic survey area with the system of inlines and crosslines and the location of the 2D seismic lines (black lines) and the line-tie-track used in Figure 4.12 (white line). Medium gas distribution (light gray) and maximum gas distribution (dark gray) for the area in 2004 based on the UGS report is shown near the top of the anticline. Right: Direct comparison of line V1 and the corresponding section of the 3D stack. The 2D stacked section shows better imaging of the shallow Base Tertiary reflection. The 3D stack section shows better imaging of the deeper Top Weser reflection. The depth-dependent difference in imaging is assumed to be caused partly by the different acquisition characteristics, e.g. the 2D surveys used a denser station sampling, but acquired less traces with large source–receiver offsets than the 3D surveys.

ms). At some locations below the amplitude brightening, the 3D stack tends to image the reflection at 850–950 ms with more wave cycles than the 2D stacks. A direct comparison of the 2D stack section of line V1 and the 3D stack shows the different imaging characteristics (Figure 4.13, right). The Base Tertiary is imaged with similar waveforms in both stacks, but shows better resolution in the 2D stack. In contrast, K2 is imaged with stronger reflection amplitude in the 3D stack. In particular, a decrease in the reflection strength of K2 in the southern part of line V1 is indicated, which is not observed by the corresponding section of the 3D stack (Figure 4.13). The remnant gas is imaged in a similar manner as a trough-peak reflection, with the 2D stack showing more details directly below the main gas reflection. Since the line-tie comparison of the 2D and 3D data shows a good correspondence, the geologic interpretation of the 3D data (Juhlin et al., 2007) has been extended to the 2D data.

4.7 Time-lapse interpretation and AVO analysis

Comparison of the baseline and repeat 3D surface seismic data shows an amplitude anomaly at the reservoir level (Figure 4.14) that is approximately centered on the injection well (Ivanova et al.,

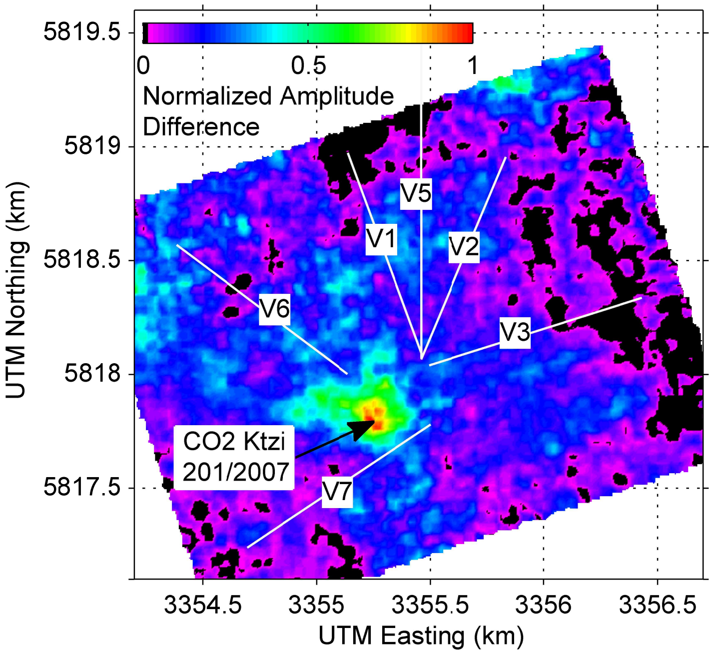

Figure 4.14: Normalized amplitude difference map derived from time-lapse processing of the 3D seismic data (Ivanova et al., submitted) and location of the 2D lines. Main amplitude differences centered at the injection well CO2 Ktzi 201/2007 are caused by the injected CO_2.

submitted). The surface traces of the 2D lines (red lines) examined in this study are located outside of the amplitude anomaly area. Therefore, we do not expect to see any significant differences between the baseline and repeat 2D surveys. To test if this is the case we processed the 2D baseline and repeat lines for time-lapse differences and have also investigated if there are changes in the AVO response of the two data sets. We used the data that have undergone the combined pre-stack and post-stack static correction procedure (workflow B+C).

The time-lapse interpretation procedure consists of: phase and time shift, shaping filter, cross-correlation shallow statics (used to interpret time differences) and time-variant shifts (used to interpret amplitude differences). The general procedures of these steps are based on the processing manual of Pro4D, the employed time-lapse processing software from CCG Veritas. Here the detailed parameters will be discussed for line V7, which is the line with the shortest distance to the injection borehole. In the first step, phase and time shift matching, the design window was chosen to range from 100 to 650 ms, which includes the K2 anhydrite layer. After testing, the trace-by-trace processing mode was applied on the entire calibration procedure. Wavelet matching is used to match a static time shift, phase, amplitude, and frequency content between the two surveys by calculating a convolutional shaping filter. This procedure was conducted in the chosen design window using the Wiener-Levinson filtering algorithm (Rickett and Lumley, 2001). Subtracting the cross-correlation lags of the Baseline data with the autocorrelation of the repeat data into the matrix equations, the Wiener shaping filter coefficients can be derived. Then, the coefficients were convolved with the repeat data. Again, a design window from 100 to 650 ms was used. The cross-correlation shallow statics step applies a time shift that is derived from cross correlation analysis. This procedure has also been referred to as applying a "wrap" and is used to align mispositioned events (Rickett and Lumley, 2001). The last calibration step is to apply time variant shifts (Figure 4.15b), which is similar to the post-stack static correction in the previous step except that more design windows are chosen so that the data is matched above, within, and below the reservoir. Since time discrepancies are minimized, subtraction of the two data sets from one another results in a section where the amplitude differences are enhanced (Figure 4.16). The NRMS value for the reservoir layer is very small, implying that there is essentially no difference between the baseline and the repeat survey in this interval.

As a confirmation that the difference in the two surveys is minimal, we continued with an AVO analysis of both data sets. First, AVO modeling was done to determine whether an AVO anomaly is to be expected and, if so, which type. The input model for the baseline survey was based mainly on well logging data and lithological information (Kazemeini et al., 2010a), and the thickness of reservoir was assumed to be 20 m. Results showed that the top of the Stuttgart sand has a negative normal incidence reflection coefficient and it increases in absolute amplitude value with increasing offset; therefore, it belongs to a Class III AVO type (Ross and Kinman, 1995). The modeling study by Verdon and Campman (2010) indicates, that if the thickness of the reservoir is less than 10 m, the AVO anomaly is not clear. However, from the time-lapse 3D surface seismic data, the AVO anomaly near injection area is obvious (Yang et al., 2011), and it can be matched with modeling results. In the following we test AVO analysis on line V7 to check if similar injection effects are visible for the 2D data. For the real baseline and repeat data of line V7, super-gathers were generated by averaging over 3 CDPs to improve the S/N ratio. Even though the CDP super-gathers look clearer than the original CDP gathers, no significant time-lapse AVO differences are observed.

AVO attribute inversion was performed on both the baseline and repeat super-gathers of line V7. The AVO attribute product: scaled Poisson's ratio change (Figure 4.17), shows no anomaly around CDP 128, the nearest point to injection borehole. All differences between the two sections appear to be due to noise, with no meaningful AVO anomalies observed from CO_2 migration.

Cross plots of the zero-offset intercept (P) and the AVO gradient (G) are useful for detecting changes in the physical conditions of the reservoir (Figure 4.18). If brine in the reservoir is replaced by a relatively compressible pore fluid such as gas or light oil, v_p would decrease and v_s would increase slightly because of the lower density. Thus, the magnitude of the displacement from the fluid line (red dotted line in Figure 4.18) increases as porefluid compressibility increases, with the total amount of displacement depending on the v_p/v_s contrast (Foster et al., 2010). If the CO_2 had migrated into the area where line V7 allows imaging, the data points in the repeat cross plot would deviate from the fluid line, as is schematically indicated in Figure 4.18.

The baseline and repeat cross plots do not show any systematic deviation from the fluid line which would indicate a Class III AVO anomaly. The only potential significant difference in the cross plots is some anomalous data points located in the lower right corner of the repeat cross plot (Figure 4.18, orange ellipse). When traced back to the seismic profile, we found these points to be associated to the CDPs near CDP 128, those having the shortest distance to the injection site (Figure 4.1). The CO_2 injection causes the brine to move and also increases the pore pressure in the reservoir. When the pore pressure increases with the overburden pressure remaining constant, the effective

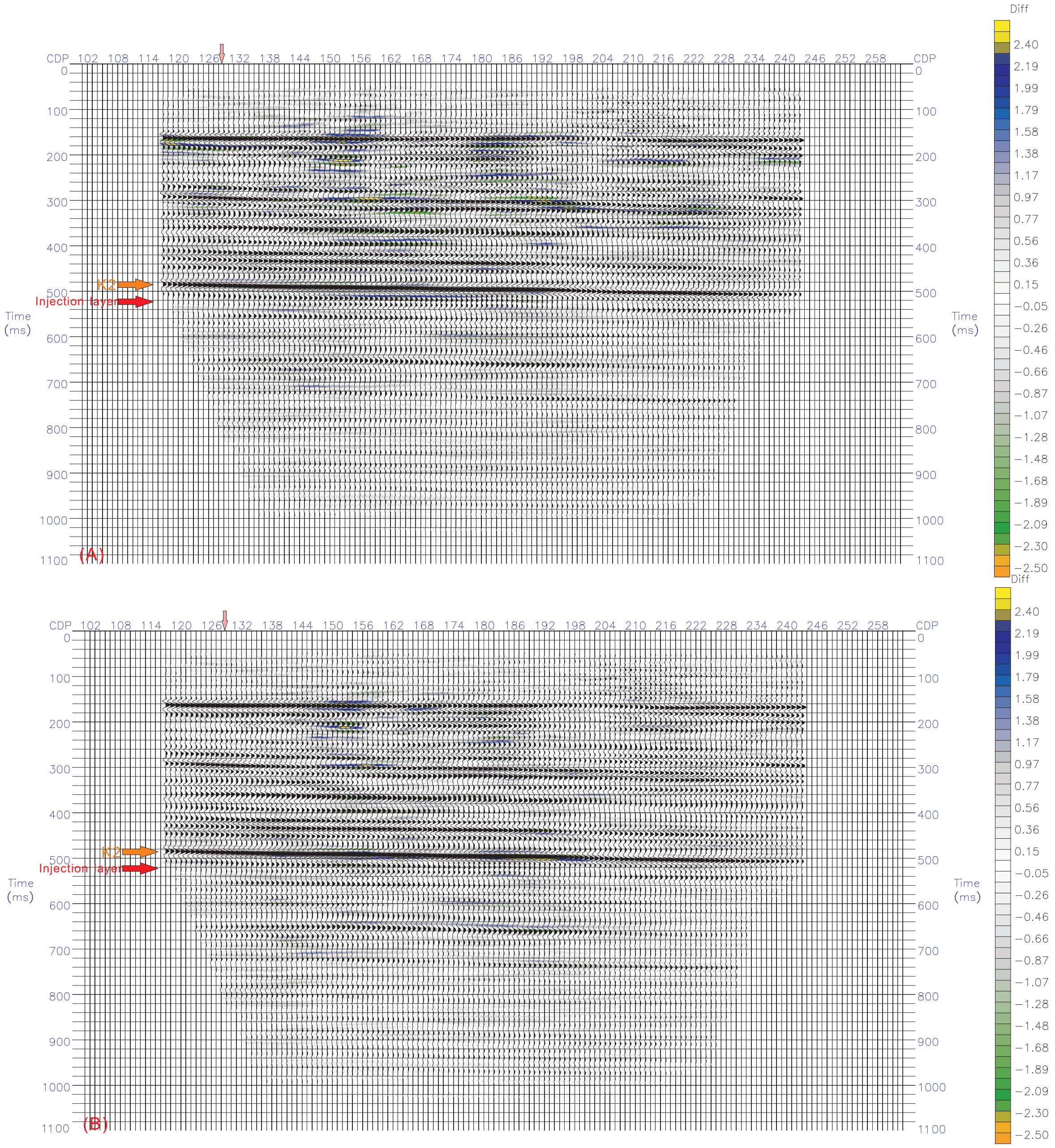

Figure 4.15: a. Original amplitude difference of line V7 between baseline and repeat survey. b. After time-lapse processing, amplitude difference. The color bar shows the difference and the seismic traces are baseline data. The K2 reflection and reservoir are indicated, and the pink arrow on the top shows the CDP point (around CDP 128) nearest to the injection area.

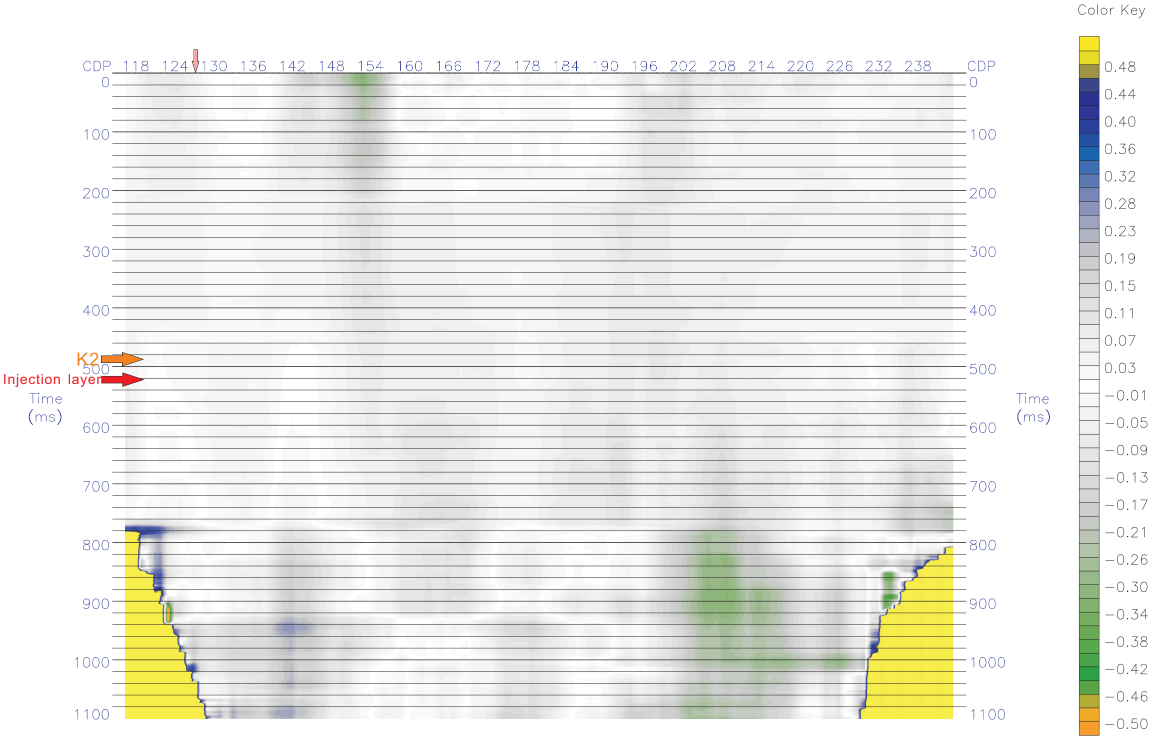

Figure 4.16: The NRMS difference between the two data sets after time-lapse processing for line V7. Color bar shows the signed amplitude of the difference. Yellow areas at the bottom left and right are due to no data being input in these regions. NRMS computation was performed with the equation used by Pro4D: NRMS =2*[RMS(a)-RMS(b)]/[RMS(a) + RMS(b)].

pressure in the reservoir will decrease. Therefore, the p-wave velocity will decrease and the normal incidence reflection coefficient (P) increase. In our case, the impedance in the reservoir is lower than in overburden rocks and decreased effective pressure could be an explanation for the data points moving towards higher AVO intercepts. However, higher CO_2 brine saturation will increase v_p. Therefore, brine saturation and effective pressure compete with each other in our case, at least partially (Wang, 2001), and it can be difficult to separate one from the other using solely AVO analysis. Regardless, from the data point distribution in the repeat cross plot (Figure 4.18) we conclude that the only potential significant changes for line V7 are at around CDP 128. These changes, if significant, are most likely due to an increase in effective pressure. Based on the time-lapse observations discussed earlier and this AVO analysis we conclude, that, at the time of the 2009 repeat survey, the CO_2 had not reached the area traced by the 2D seismic lines. This conclusion is supported by the amplitude anomaly mapped in the 3D time-lapse data (Figure 4.14). Further AVO analysis of the 3D data may allow the pressure front to be mapped and confirmation of the interpretation presented here.

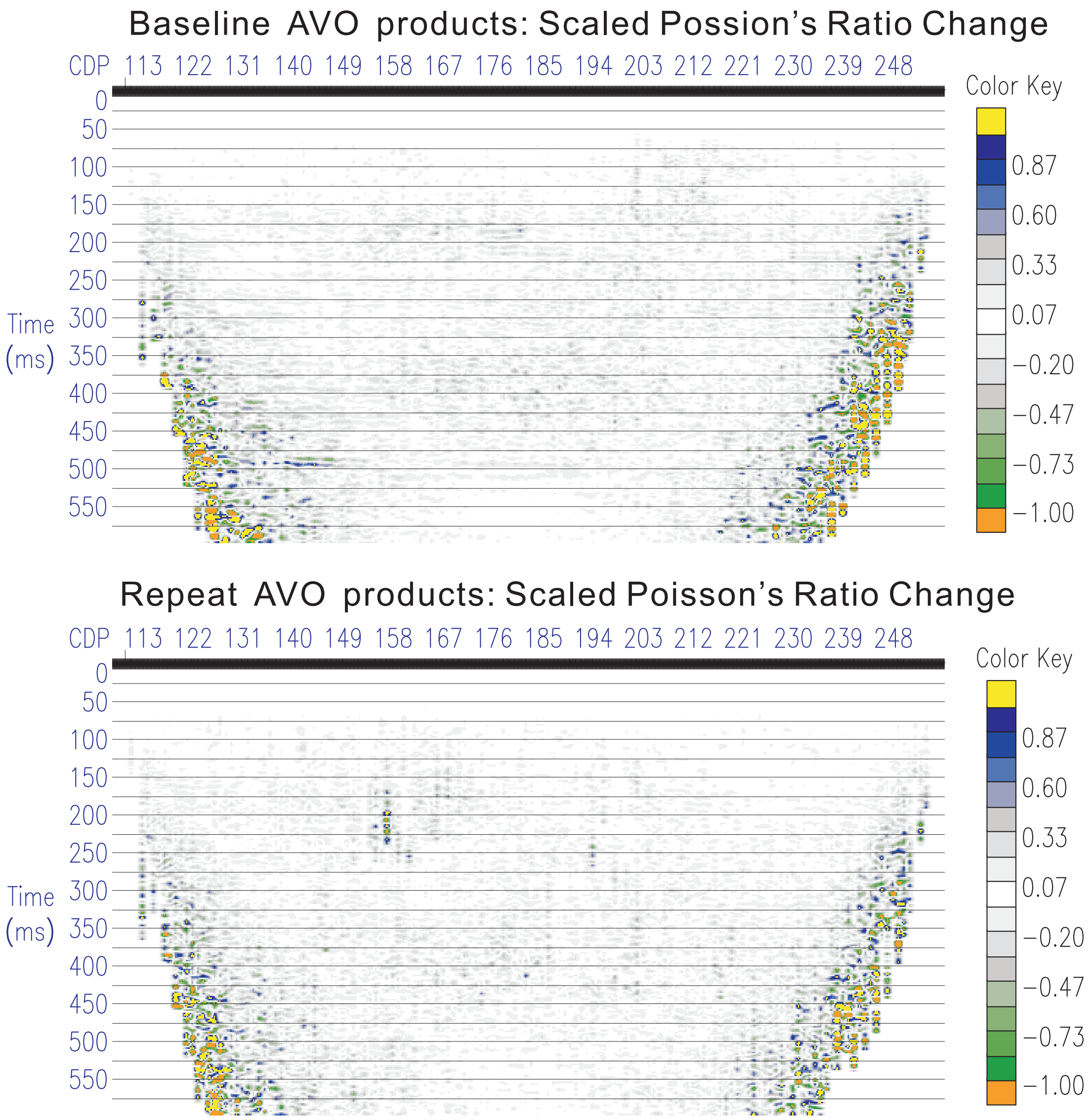
Baseline AVO products: Scaled Possion’s Ratio Change

Repeat AVO products: Scaled Poisson’s Ratio Change

Figure 4.17: AVO attribute product for line V7: Scaled Poisson’s Ratio Change: (Intercept +Gradient)/2. Most of the difference in the two figures is due to noise and no clear AVO anomaly can be seen on the repeat data set.

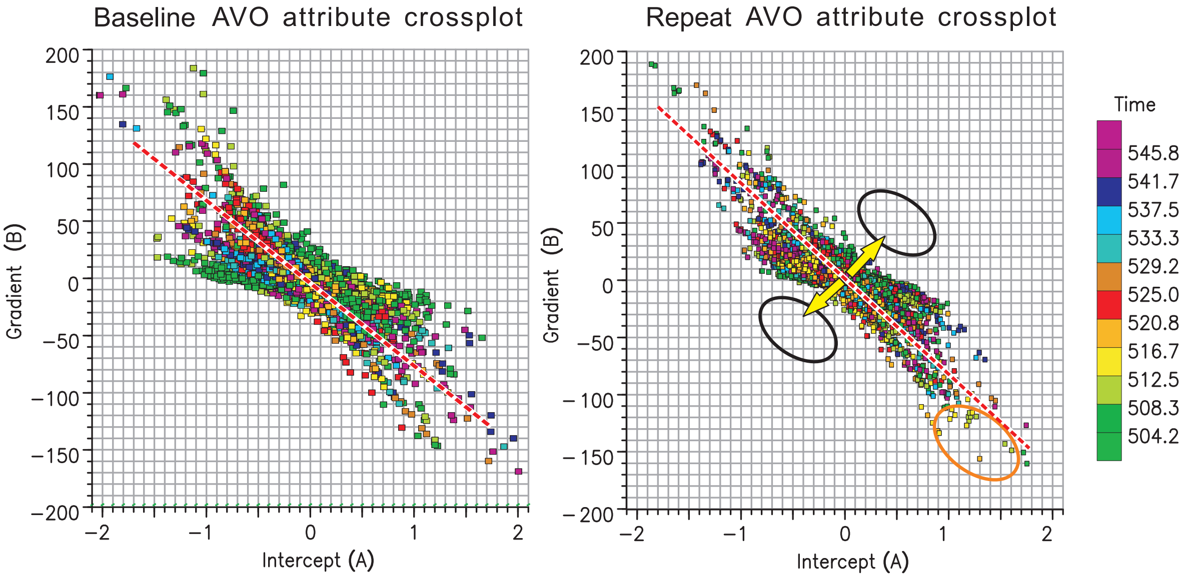

Figure 4.18: Intercept vs. Gradient cross plot for baseline and repeat data of line V7. No significant difference between two data sets is observed. Minor differences in the upper left and lower right corners can be effects from noise or water saturation in the reservoir. The two yellow arrows in the repeat cross plot indicate the expected movement of data points from the fluid line (red dashed) when gas replaces the reservoir brine. The data points in the orange ellipse (located at around CDP 128) at the lower right corner show possible pressure and/or water saturation effects after injection.

4.8 Conclusions

Two 2D seismic surveys have been acquired to date in the framework of the Ketzin CO_2 storage monitoring. The first survey was performed in 2005 before the start of the CO_2 injection. The second survey was performed in 2009, after roughly 22 kt of CO_2 had been injected, showed a good repeatibility. This repeat survey aimed to image the injected CO_2 and to allow for comparison with other monitoring methods, in particular with the 3D seismic surveys acquired. Time-lapse processing of the datasets showed that statics, caused by changes in the near-surface velocities, can produce spurious artifacts in the difference section. Refraction static corrections aim to correct for near-surface velocities in single-state datasets, but do not necessarily yield the required cross-alignment of time-lapse datasets. Therefore, two additional approaches of static corrections were tested: (A) Pre-stack static corrections, which decompose the timing delays of baseline and repeat traces for sources and receivers in a surface-consistent manner. (B) Post-stack static corrections, which cross-align baseline and repeat stacked sections along a reference horizon. Both approaches reduced the noise in the time-lapse sections of the datasets considerably. Post-stack static corrections caused a similar reduction compared to the combination of pre-stack and post-stack static corrections.

When processing of time-lapse onshore seismic data is faced with challenging statics, we recommend refraction static corrections followed by a combination of pre-stack and post-stack static corrections. In particular, in areas where the assumptions for post-stack reference horizons (location above monitoring target, strong reflectivity and good continuity) are only met partly.

Furthermore, processing of the Ketzin datasets demonstrated that the source and receiver solutions of the pre-stack static corrections can allow for interpretation of changes in the near-surface velocities. The long wavelength component of the pre-stack static corrections indicated, that near-surface velocities at the 2009 survey were larger than for the 2005 baseline survey, which is consistent with water level observations at the surface.

Comparison with the processing results of the 2D and 3D surveys showed that both image the subsurface, but with local differences due to the different acquisition geometries and source type used. Time-lapse interpretation showed that in 2009 no CO_2 related time-lapse signature is observable where the 2D lines allow monitoring of the reservoir. This finding agrees with the time-lapse results of the 3D surveys, which image a reflectivity increase that is centered at the injection well, but does not reach the area monitored by the 2D lines. For further investigation, an AVO analysis was conducted, which (i) confirmed that the CO_2 had not migrated as far as the 2D lines and (ii) gives an indication for an injection induced pressure change in the reservoir.

Acknowledgements

We thank several people for being involved in the field operations. In particular, Rüdiger Giese for operational support during the surveys and Hans Palm and Sverker Olson for operating the cable crew and field equipment. The Geophysik-GGD (Leipzig) survey crew and the Vibrometric Oy source crew are acknowledged for good cooperation. James Mechie is thanked for helpful comments on the manuscript. We thank the two anonymous reviewers for their constructive comments.

The first author would like to acknowledge the GeoEn project (Grant 03G0671A/B/C), a national scientific initiative in the field of energy research. The European Commission is gratefully acknowledged for funding CO_2 Storage by Injection into a Natural Storage site at Ketzin (CO_2SINK), project no. 502599.

5

Geoelectric investigations

Publication III

Surface-downhole electrical resistivity tomography applied to monitoring of CO_2 storage at Ketzin, Germany

P. Bergmann[1], C. Schmidt-Hattenberger[1], D. Kiessling[2], C. Rücker[3], T. Labitzke[1], J. Henninges[4], G. Baumann[4], and H. Schütt[5]

Published in Geophysics, Vol. 77, No. 6, B253-B267, November 2012

Contents

---

[1] Helmholtz Centre Potsdam, GFZ German Research Centre for Geosciences, Centre for CO_2 Storage, Telegrafenberg, 14473 Potsdam, Germany

[2] University of Leipzig, Institute of Geophysics and Geology, Talstraße 35, 04103 Leipzig, Germany

[3] Technical University Berlin, Department of Applied Geophysics, Ernst-Reuter-Platz 1, 10587 Berlin, Germany

[4] Helmholtz Centre Potsdam, GFZ German Research Centre for Geosciences, Reservoir Technologies, Telegrafenberg, 14473 Potsdam, Germany

[5] Statoil ASA, Grenseveien 21, 4035 Stavanger

Abstract: Surface-downhole electrical resistivity tomography (SD-ERT) surveys were repeatedly carried out to image CO_2 injected at the pilot storage Ketzin, Germany. The experimental setup combines surface with downhole measurements by using a permanent electrode array that has been deployed in three wells. Two baseline experiments were performed during the site startup and three repeat experiments were performed during the first year of CO_2 injection. By the time of the third repeat, approximately 13,500 tons of CO_2 had been injected into the reservoir sandstones at about 650 m depth. Field data and inverted resistivity models showed a resistivity increase over time at the CO_2 injector. The lateral extent of the related resistivity signature indicated a preferential CO_2 migration toward the northwest.

Using an experimental resistivity-saturation relationship, we mapped CO_2 saturations by means of the resistivity index method. For the latest repeat, CO_2 saturations show values of up to 70% near the injection well, which matches well with CO_2 saturations determined from pulsed neutron-gamma logging. The presence of environmental noise, reservoir heterogeneities, and irregularities in the well completions are the main sources of uncertainty for the interpretations. The degradation of the permanently installed downhole components is monitored by means of frequently performed resistance checks. In consistency with the SD-ERT data, these resistance checks indicate a long-term resistivity increase near the CO_2 injector. In conclusion, the investigations demonstrate the capability of surface-downhole electrical resistivity tomography to image geologically stored CO_2 at the Ketzin site.

5.1 Introduction

The capture and storage of CO_2 in deep geologic formations is an option for reducing greenhouse gas emissions into the atmosphere (IPCC, 2005). Reliable long-term storage requires monitoring of CO_2 migration and related processes, e.g., brine displacement. In general, geophysical methods provide the images of physical parameters in regions of the subsurface that are other-wise inaccessible for direct observations. Time-lapse measurements allow for imaging of changes of these physical parameters over time, thus, offering an opportunity for long-term monitoring of CO_2 storage. Electrical resistivity tomography (ERT) is suitable in this context because the electric resistivity of porous sediments significantly increases when electrically conductive brine is displaced by CO_2. Depending on the phase of the CO_2, dissolution in brine and uptake of dissolved solids can adversely decrease the resistivity. As an example for the reservoir conditions at the Ketzin site, laboratory data published by Fleury and Deschamps (2008) show that the effect of CO_2 dissolution on electrical brine conductivity — and therefore, bulk reservoir resistivity — is negligible. However, only short-term data are reported and, thus, additional physico-chemical fluid-solid interactions may affect the resistivity in the long-term.

Considering the rapid development of geoelectric instruments and inversion tools over the last few decades (e.g. Daily et al., 2004), ERT becomes an attractive monitoring option. The usefulness of time-lapse ERT is well documented, e.g., for steam injection (Ramirez et al., 1993), leak detection (Ramirez et al., 1996), salt tracer tracking (e.g. Slater et al., 2000; Kemna et al., 2002; Cassiani et al., 2006), and other processes related to subsurface fluid flow (LaBrecque and Yang, 2001; Nimmer et al., 2007; Clément et al., 2010). These applications are of high relevance for CO_2 storage monitoring because the methodical aspects and many practical problems are similar. Of special interest, however, are studies focused on the ERT imaging of subsurface CO_2 migration. Several modeling studies pointed out the potential for CO_2 storage monitoring by means of ERT (Ramirez et al., 2003; Christensen et al., 2006; al Hagrey, 2011a). Practical application is being performed at the Nagaoka site in Japan (Xue et al., 2009; Nakatsuka et al., 2010), the SECARB Cranfield site in the USA (Carrigan et al., 2009), and the Ketzin site in Germany (Kiessling et al., 2010).

It is remarkable that most of these theoretical and practical studies deal with crosswell setups. This is because crosswell setups can be realized by permanent electrodes, which offer cost-competitive and environmentally sound long-term monitoring. In this article, we present the ERT surveys at the Ketzin site, which include a combination of well-based and surface-based data acquisition. Successful application of surface-based ERT for large- and mid-scale resistivity imaging are reported by Brunner et al. (1999), Storz et al. (2000), and Schütze and Flechsig (2002). At the Ketzin site, large-scale geoelectrical measurements are adapted to the demand of high-resolution monitoring of the Ketzin storage reservoir by joint operation with a permanent borehole electrode array (Schmidt-Hattenberger et al., 2011, 2012), which allows for additional surface-downhole ERT (SD-ERT) data acquisition.

In this paper, we report the results of the SD-ERT surveys covering the startup of the Ketzin site and the first year of CO_2 injection by two baseline and three repeat surveys. The article is structured as followed: first, we give an overview on the Ketzin project and continue with the description of the SD-ERT surveys. We then describe the preprocessing and inversion of the field data. Subsequently, we estimate CO_2 saturations and compare them with results of pulsed-neutron-gamma logs. Finally, we discuss the value, implications, and limitations of SD-ERT for CO_2 plume tracking.

5.2 Field surveys at the Ketzin site

5.2.1 Site description

The Ketzin project provides an experimental test site for the geologic storage of CO_2 in an onshore saline aquifer near Berlin (Schilling et al., 2009; Würdemann et al., 2010; Martens et al., 2011). Supercritical CO_2 is injected into Triassic sandstones of the Stuttgart Formation at approximately 650 m depth. Site operations were initiated by the CO_2SINK project in 2007, which was succeeded by the CO_2MAN project in 2010, both of which are here referred to as the Ketzin project. The objective of the Ketzin project is the improved understanding of in situ processes and the provision of practical experience for future geological storage of CO_2 (Giese et al., 2009). A primary task is the development and testing of geophysical monitoring procedures. Therefore, a wide range of activities is performed, such as active seismic experiments (e.g. Juhlin et al., 2007; Ivanova et al., 2012), combined active and passive seismic experiments (Arts et al., 2011), geoelectric experiments (Kiessling et al., 2010; Schmidt-Hattenberger et al., 2011), and electromagnetic experiments (Girard et al., 2011; Streich et al., 2011).

The Ketzin site is situated in the eastern part of the Roskow-Ketzin double anticline, which formed above a salt pillow situated at a depth of 1500-2000 m (Förster et al., 2006). One injection well (Ktzi201) and two observation wells (Ktzi200 and Ktzi202) have been drilled each to a depth of about 800 m. The wells are arranged in a rectangular triangle geometry (Figure 5.1a). All wells were

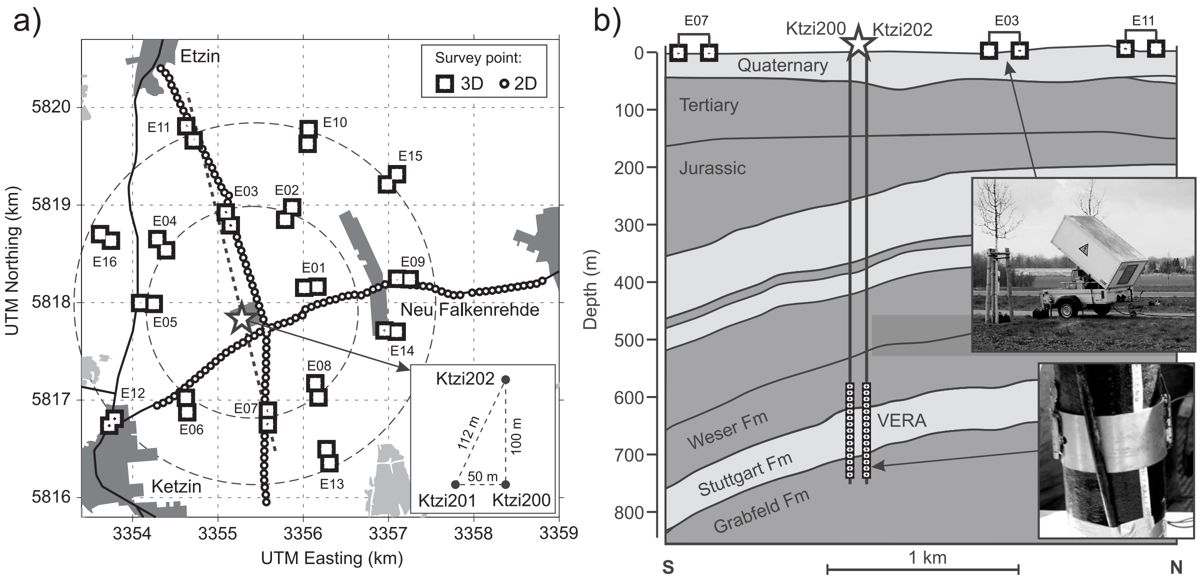

Figure 5.1: (a) Acquisition geometry for the SD-ERT. Surface dipoles E01-E08 are deployed on a circle with a radius of 800 m and surface dipoles E09-E16 are deployed on circle with a radius of 1500 m. Location of the injection site is shown by a star. (b) Schematic cross section through the Ketzin anticline and setup of the combined surface-downhole ERT experiments. Aquifer units are depicted in light gray, aquitard units in dark gray. The approximate position of the cross section is illustrated by a dotted line in the subfigure in (a). Upper inlay in (b) shows the TSQ-4 power source (property of Leipzig University). Lower inlay shows a VERA electrode mounted on the electrically insulated well pipe.

drilled through the Stuttgart Formation, which is located in the depth range of about 630-700 m for the well Ktzi201. The Stuttgart Formation consists of sandstone channel-facies rocks with good reservoir properties alternating with muddy floodplain-facies rocks of poor reservoir quality (Förster et al., 2006; Norden et al., 2008). CO_2 has been injected into the saline-water-bearing sandstone units since 30 June 2008 via Ktzi201. The caprock overlying the Stuttgart Formation is the Weser Formation, which mainly consists of clayey and sandy siltstones alternating with carbonates and evaporites (Beutler and Nitsch, 2005). A high clay mineral content and the observed pore-space geometry make these rocks a suitable seal for the CO_2 storage reservoir (Förster et al., 2006). A 10-20 m thick anhydrite layer, known as K2 (Keuper), outlines the top of the Weser Formation. The Weser Formation is overlain by mud/clay-carbonates of the Arnstadt Formation, which exhibits similar sealing properties. Until the year 2000, the shallower Hettangium formation (300-400 m) was used for industrial storage of natural gas (for further details see Juhlin et al., 2007; Kazemeini et al., 2009).

Drilling operations started in summer 2007 with the sinking of the well Ktzi200. Well completion was performed with steel casings and preperforated screens in the reservoir zone (Prevedel et al., 2009). A vertical electrical resistivity array (VERA) has been deployed in the three wells to allow for reservoir monitoring by means of geoelectric crosshole measurements. Each well hosts 15 electrodes, which are installed in the depth range 590 to 740 m with a vertical spacing of 10 m (Figure 5.2).

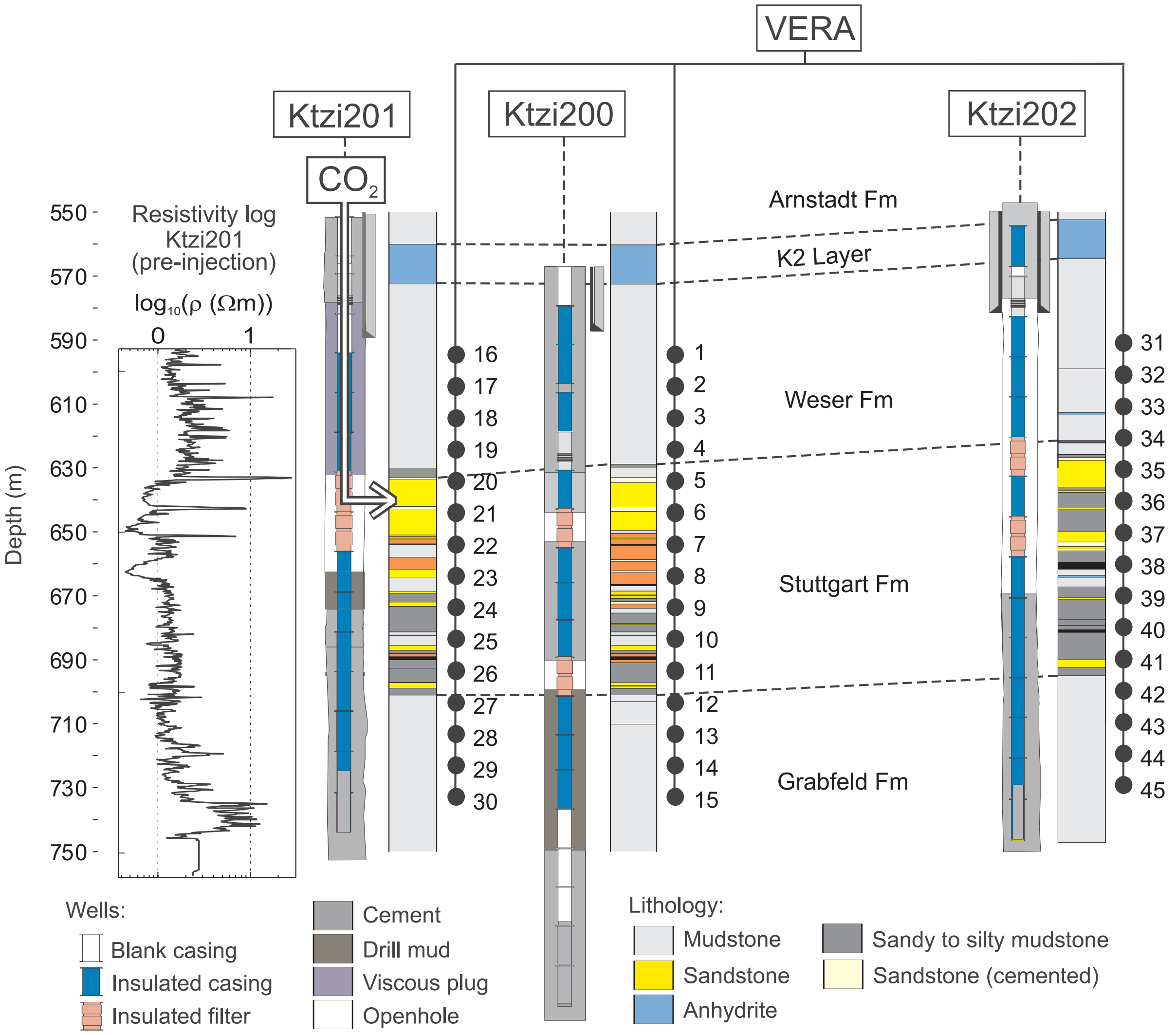

Figure 5.2: Well completion, lithology (after Förster et al., 2006) and electrode positions of the vertical electrical resistivity array (VERA) system (black dots) for the three wells at the Ketzin site. Ktzi201 is the injection well, Ktzi200 and Ktzi202 are observation wells. The left hand plot gives the logged resistivity for Ktzi201 acquired in the baseline period (after Norden et al., 2010).

These electrodes consist of stainless steel rings that were mounted on the 5.5 inch casing strings. In the depth range of the electrodes, the casings were electrically insulated by an external coating that combines an epoxy matrix and a polyphenylene sulfide membrane (Kiessling et al., 2010). For connection of the electrodes to the surface, one multiconductor cable was used per well. To connect the individual electrodes to the cable, watertight cable outlets with watertight connectors have been realized (Schmidt-Hattenberger et al., 2011). Customized centralizers were deployed to center the strings inside the boreholes and protect the cables from mechanical damage. Mounting the electrodes and feeding the cables through the well head was performed during the well-completion operations and took about 24 hours per well (Prevedel et al., 2009). To prevent damage on the multiconductor cables the electric current passed through any two electrodes of the VERA is limited

to 3 A (Kiessling et al., 2010).
A swellable packer was used for a staged cementation allowing the filter intervals to be excluded from the cementation. Thus, perforation of the steel casings was avoided that otherwise would have caused unmanageable risks of damaging the multiconductor cables (Prevedel et al., 2009). To eliminate the risk of clogging the pre-perforated filter screen, no such staged cementation was performed in Ktzi202 for the interval above the filters.
Injection of CO_2 started on 30 June 2008 with an average injection rate of about 3 tons/h for the first year. During this year, a total amount of about 17,900 metric tons of food-grade CO_2 has been injected through Ktzi201. Gas-chemical monitoring detected the arrival of CO_2 at the first observation well Ktzi200 (50 m away from Ktzi201) after about 530 tons of injected CO_2 on July 15th, 2008. Arrival at the second observation well Ktzi202 (112 m away from Ktzi201) was detected on 21 March 2009 after about 11,000 tons of CO_2 had been injected (Zimmer et al., 2011; Martens et al., 2011). The notable delay in the arrival at Ktzi202 is an indicator of the reservoir heterogeneity for which its channel-structure is likely to play a major role.

5.2.2 SD-ERT data collection

Geoelectric methods, alongside seismic methods and well logging, play an important role in the geophysical monitoring concept of the Ketzin site. Comprehensive CO_2 storage monitoring requires coverage at various temporal and spatial scales. All geophysical methods have their specific resolution, investigation depth, and sensitivity to reservoir properties. Therefore, geoelectric monitoring at Ketzin comprises the following three survey types to complement each other (Figure 5.1):

- 3D SD-ERT: Current injection and voltage acquisition are performed at the surface using a sparse circular dipole geometry (surface-to-surface). Additional voltage acquisition is conducted in the three wells (surface-downhole) using the VERA system.
- 2D SD-ERT: Current injection and voltage acquisition are performed by dipoles along two separate profiles that intersect near the injection location (surface-to-surface). Additional voltage acquisition is conducted in the well Ktzi201 (surface-downhole) using the VERA system. Two-dimensional SD-ERT surveys have been carried out exclusively in the CO_2 injection phase.
- Crosshole ERT: Current injection and voltage acquisition are performed by the VERA system.

In the following section, we will concentrate on the 3D SD-ERT, which consists of 16 surface dipoles deployed on two concentric circles approximately centered on the injection location 5.1. The surface dipoles have a length of 150 m, are oriented toward the injection site, and are used for current injection and for voltage acquisition. Current injection was performed by a TSQ-4 (Scintrex Limited, Canada) power source with a maximum power of 10 kW. Electrical currents of up to 11 A at a voltage of up to 3.3 kV were used. Injection was performed by a pulsed square-wave direct current (DC) with changing polarity (4s on $+$, 4s off, 4s on $-$, 4s off), with a signal period of 16 s. At each location, currents were injected for a period of approximately 45-60 minutes. These periods were divided into three intervals that were used for sequential voltage acquisition in the

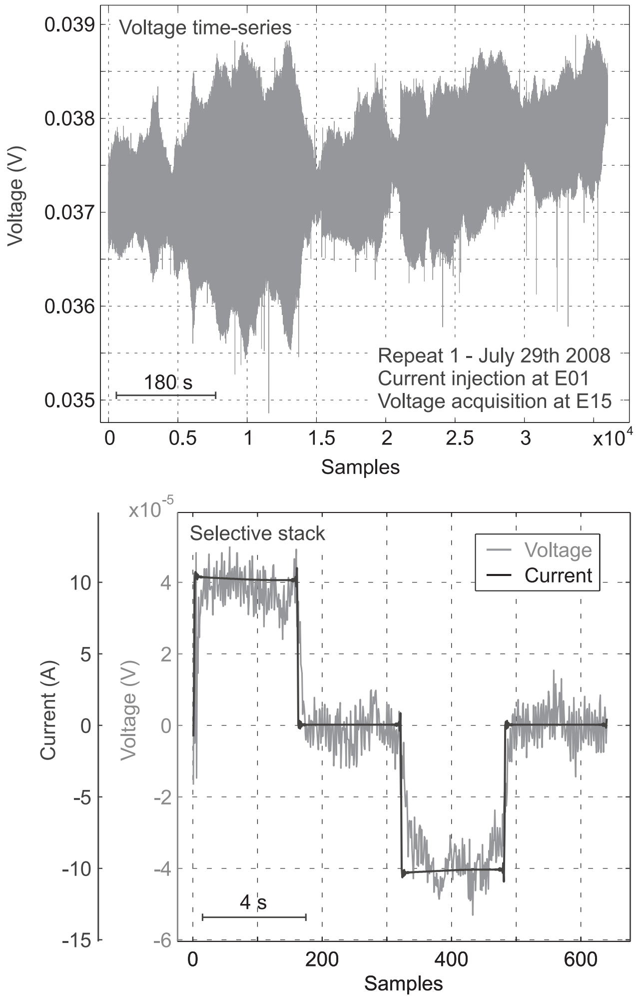

Figure 5.3: Example of a SD-ERT voltage time-series (top) and corresponding result after selective stacking (bottom).

three wells. Voltage registration was realized by Texan-125 recorders (Refraction Technology Inc., USA). Survey crews typically consisted of five people and the surveys were usually completed within five working days.

The SD-ERT surveys were performed on a periodic basis and aligned to the arrival times of the CO_2 at the observation wells and operational circumstances (e.g., harvesting periods). The first baseline survey was performed in October 2007 and aimed to provide a noise test with full data acquisition. It showed a strong presence of environmental noise, with a particular source identified as pulsed electrical anticorrosion currents of a nearby gas pipeline. As an outcome of the noise analysis, the following surveys were performed within break periods that were arranged with the pipeline operator. A second baseline survey was carried out in April 2008 and showed an improved signal-to-noise ratio (S/N), which we will use as reference baseline. The first repeat survey was carried out in July 2008 after the detection of CO_2 at the first observation well Ktzi200. A second repeat survey was performed in November 2008 and a third repeat survey in April 2009 after CO_2 had been detected at the second observation well Ktzi202.

5.3 ERT data processing

5.3.1 Pre-inversion processing

There are a number of infrastructural facilities near the Ketzin site that lead to a moderate S/N for the acquired voltage time series. Decentralized surface dipoles allowed to avoid long cable layouts that consequently reduced the risk of antenna effects and cable faults. However, significant noise remained and was addressed by a selective stacking approach after Storz et al. (2000). The approach aims to stack the acquired voltage time-series into single cycles and was implemented in the following steps:

1. Noise removal (Drift correction, Despiking)
2. Notch filtering (2.8 Hz, 8.4 Hz, and 16 Hz)
3. Phase correction
4. Alpha-trimmed median stack (10%)
5. Windowing
6. Determination of resistance and error

Phase correction was applied to align the voltage time-series to the respective current time-series. As the underlying crosscorrelation could easily produce sign switches, we continued with the absolute values of the apparent resistivities. Step four stacks the voltage time-series into 16 s cycles. The signal plateaus were then partitioned into time windows for identification of polarization asymptotes. Error values were estimated considering the voltage variation within the windows, as well as the voltage variation among the windows. Respecting the wide range of signal quality found in the stacked SD-ERT data, we estimate the average ratio of effective signal to effective noise to be about 10, which yields an average S/N of about 20 dB. An example of representative field data is given in Figure 5.3.

The pseudosections of the four SD-ERT surveys are shown in Figure 5.4. They allow for a first qualitative assessment with the following major findings: First, the best S/N can be found for the surface-downhole readings (Figure 5.4, upper part). Second, apparent resistivities obtained by current injection at the inner circle (Figure 5.4, abscissa E01-E08) are, on average, slightly higher than apparent resistivities with current injection at the outer circle (Figure 5.4, abscissa E09-E16). Third, an increase in resistivity over time can be seen for the electrodes that are deployed near the CO_2 injector in Ktzi201. Fourth, the third repeat shows an increase in resistivity for the Ktzi202 electrodes 31-34. Fifth, Ktzi202 electrodes 38-45 show remarkably low values. Sixth, Ktzi200 electrode 11 yields high apparent resistivities, which appears inconsistent with the adjacent electrodes.

5.3.2 Quality assessment by means of contact resistance checks

Operation of the VERA and electrode arrays at similar depths raises two questions: (1) Did any mechanical damage occur during the installation and (2) What is the operational lifetime?

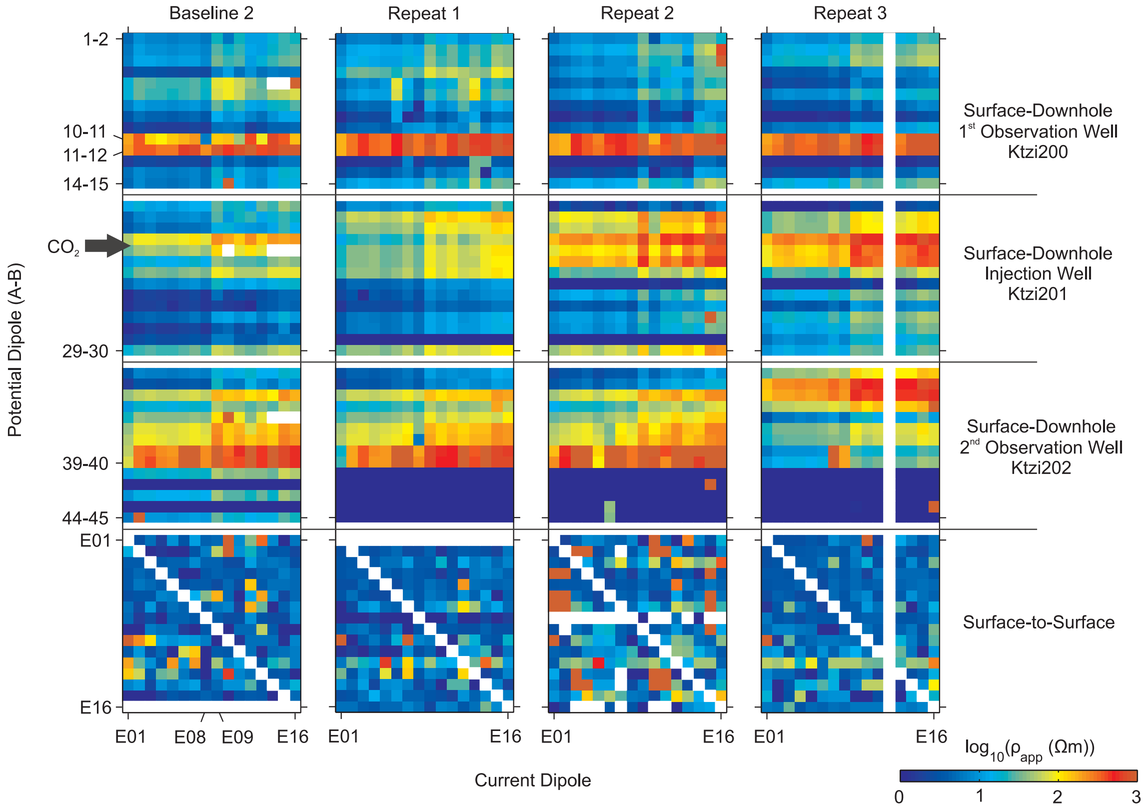

Figure 5.4: Pseudo-sections showing the apparent resistivities of the SD-ERT surveys. Abscissa shows the location of current injection at the surface dipoles E01-E16 (Figure 5.4). Ordinate shows the potential dipoles with the VERA electrodes 1-45 (Figure 5.2) and surface dipoles E01-E16.

The latter of these questions is determined by the reservoir conditions, which build an environment that is likely to cause metal corrosion and embrittlement of the nonmetallic cable elements, and is not yet conclusively assessable. To track the degradation of the subsurface electrodes, resistance checks were carried out before and during the CO_2 injection. These checks measure the resistances between adjacent electrodes and use them simultaneously for currents and voltages. Therefore, these checks are more sensitive to the contact resistances than to reservoir resistivity and serve here as an indicator of the condition of the electrodes and materials in close contact (Figure 5.5). Resistance checks were first performed on a daily basis shortly before the start of the CO_2 injection, and continued with about one measurement per week since September 2008.

Figure 5.4 shows the conspicuous behavior of electrodes 39-45. In the following, we put some emphasis on them because they are an example for technical influences found in the SD-ERT data. The pseudosections show very low values for electrodes 39-45 (Figure 5.4), which seems to be confirmed by the rather low values found in the resistance checks (Figure 5.5). During the operation of the VERA system, we observed small amounts of brine at the surface termination of the multiconductor cable. Further investigation showed that this brine originated from the cable strands of electrodes 39-45. We suppose that the brine has penetrated the cable through a weakness of the insulation and has been moved upward by the subsurface overpressure. Figure 5.4 shows this behavior to be present from the beginning of the resistance checks. We consider it possible that the cable insulation has been mechanically damaged during the installation. An abrasion might have opened a pathway for the brine to enter the cable strands, which is plausible because the strands for electrodes 39-45 are placed adjacently within the cable. This damage is further supposed to be located between electrodes 38 and 39, ultimately disconnecting the deeper electrodes (>39). Subsequently, this could have created a short circuit, which would explain the low resistivities observed in the SD-ERT data and resistance checks. In conclusion, we decided the readings taken at electrodes 39-45, and for similar reasons, electrode 11, to be excluded from further processing.

Aside from these defects, the resistance checks allow us to draw some remarkable conclusions regarding resistivity increases found in the SD-ERT data. First, contact resistances and SD-ERT apparent resistivities display a steady increase for electrodes close to the CO_2 injection point (compare Figure 5.4 and Figure 5.5 at the arrows indicating the CO_2 injection). Both observations, although they reflect different effects (electrode degradation as opposed to a change in formation properties), are likely to be a consequence of the electrodes near the injection point coming into contact with the CO_2. Secondly, we find an abrupt increase in apparent resistivity at the Ktzi202 electrodes 31-34 (Figure 5.4). This increase appears with the third SD-ERT repeat survey, whereas the previous surveys indicated lower values at a relatively good repeatability. This abruptness becomes clearer in the resistance checks, which narrows the occurrence to the time interval 18-25 March 2009. This agrees with the chemically detected CO_2 arrival at this well on 21 March 2009.

We have developed the following working hypothesis for this abrupt resistivity increase: Because there is no cementation in the interval above the filter screens of Ktzi202 (Figure 5.2), the arriving CO_2 displaced the brine in the annulus. This, in turn, caused the electrodes to lose contact with the formation, which the resistance checks indicate to have happened for electrodes 31-34 shortly before the third repeat survey. Further, we suppose the CO_2 uptake to have lasted a few weeks until having filled the annulus because the resistance checks stabilized at rather high levels within four to five measurement cycles (Figure 5.5).

5.3.3 ERT inversion

Given that the vertical spacing of the VERA electrodes is in the order of meters and the diameter of the outer electrode circle is in the order of kilometers, the volume to be inverted covers a range of scales. Thus, we required a nonequidistant parametrization to allow for efficient 3D inversions. To overcome these geometric constraints, we apply the triple-grid inversion technique (Günther et al., 2006) provided by the open-source software package BERT (boundless electrical resistivity tomography, www.resistivity.net). BERT combines a finite-element forward operator (Rücker et al., 2006) and a Gauss-Newton algorithm with inexact line search (Günther et al., 2006) and has been successfully applied in several case studies dealing with single-state, as well as time-lapse ERT data sets (e.g. Heincke et al., 2010; Coscia et al., 2011).

To define the inversion domain, we constructed a volume with a side length of 5 km and a depth of 2 km. This cube has then been populated with a parameter mesh of about 22,000 unstructured tetrahedral cells using the noncommercial mesh generator TetGen (Si, 2003). The resulting cell volumes were forced to be smallest near the electrodes and to coarsen toward the cube faces.

Inversion parameters have been determined successively by running inversions for which single pa-

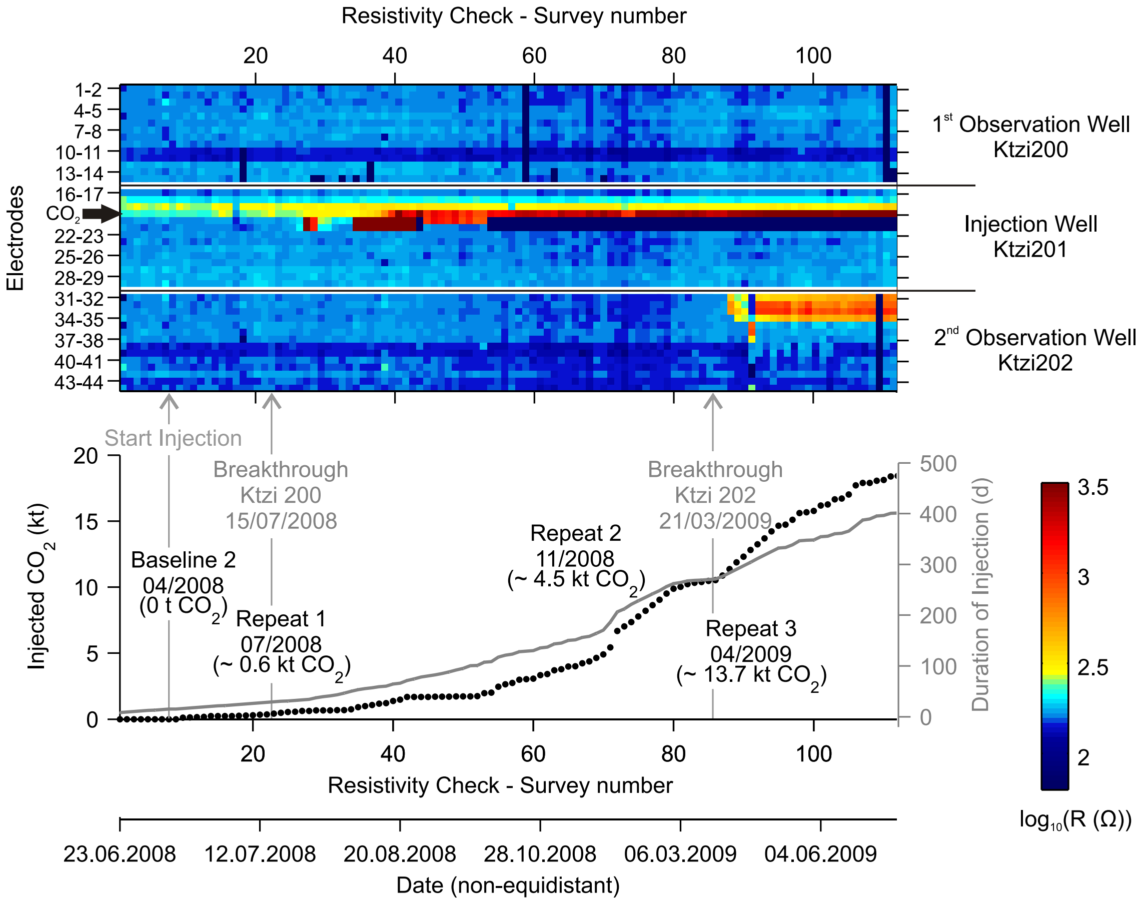

Figure 5.5: Resistance checks (upper plot) shown for the time line of injection (lower plot). Black dots in time line indicate the cumulative mass of injected CO_2 (left ordinate), grey line shows the duration of injection in days (right ordinate). The lower plot is parameterized by the index of the resistivity check, which leads to a non-equidistant axis for the dates. Specific choice of the colormap reveals that electrodes 11 and 39-45 are characterized by rather low resistances, presumably since the installation.

rameters were varied. From these, we ascertain that the choices of the regularization parameter and the vertical roughness gradient weight have the largest impact on the inversion result. Large regularization parameters have the tendency to produce oversmoothed inversion results with poor data fits. Inversion with lower regularization parameters produce better data fits by means of increased model roughness. Finally, too weak regularizations generate mainly spurious structures. To foster the choice, we ran additional inversion sequences with variant regularization. From these, we selected a realization for which the inversion achieved an acceptable error, produced a result that is consistent with the preinversion data, and showed inverted resistivities to be stable for a relatively wide range of realizations. Following these criteria, we selected the regularization parameter equal to 20. We further assessed the choice of the regularization parameter by means of an L-curve analysis (Hansen and O'Leary, 1993; Figure 5.6). The inversion program aims to minimize the

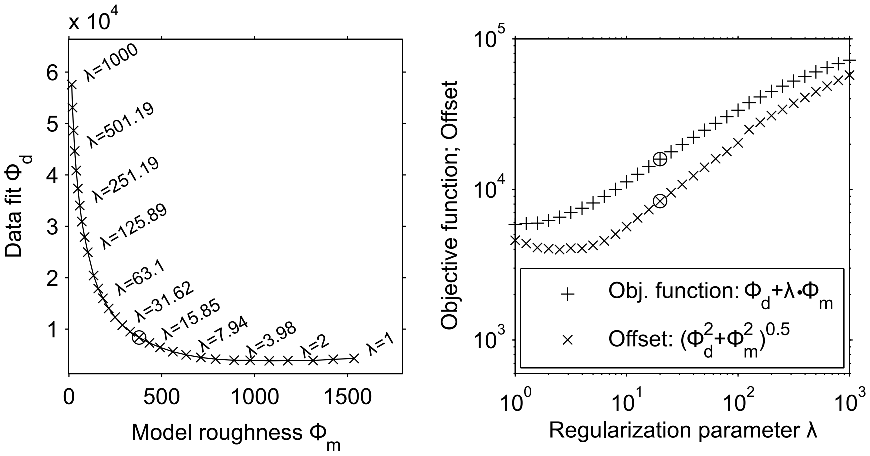

Figure 5.6: L-curve for the inversion of the second baseline dataset (left) and L-curve parameters parameterized by the regularization (right). Circles indicate the solution for a regularization parameter of 20.

objective function which considers the data misfit, Φ_d, and the model misfit, Φ_m (Günther et al., 2006). Contributions of both misfits to the objective function are balanced by the regularization parameter, λ. A commonly used L-curve criterion suggests the optimum regularization parameter to be found where the offset of the function $\Phi_d(\Phi_m)$ to the origin is minimal (e.g. Aster et al., 2005).

According to this criterion, we assess from Figure 5.6 a lower regularization parameter of about 2.5 to be justified as well. However, we retained a regularization parameter of 20 because that resulted in a better continuity in the time-lapse images (i.e., resistivity ratios). This, of course, leads to larger values for the objective function and χ^2 (final values are in the range of 4.7 to 7.8). Nevertheless, the relevant features in the resistivity images remain. The advantage of using stronger regularization is a better stability in the resistivity ratios. This is mainly due to the weakened impact of outliers, which can have a deteriorating impact when adverse perturbations occur in the numerators and denominators of the resistivity ratios. In our case, these low fits are partly attributed to the heterogeneous coverage in the inversion volume. Large parts of the inversion volume are being poorly covered by the acquisition geometry. At some distance to the array, we do not expect to find a meaningful resistivity image. This is reflected in the fact that the low-coverage parts of the inversion volume do not show significant resistivity changes over time, which is principally acceptable.

The weight for vertical roughness gradients allows, to some extent, the incorporation of knowledge about the degree of geologic stratification. It can be used to stimulate an anisotropic appearance of the resulting resistivity image Ellis and Oldenburg (e.g. 1994), which seems reasonable in view of the predominantly horizontal layering of the Ketzin reservoir. However, it will be shown later that the limited angle variation in the SD-ERT acquisition geometry causes a directional trend in the sensitivity patterns. In consequence, the sensitivity patterns already inherit an emphasis of lateral structures in the inverted images. Because a further enhancement of this effect was not intended, we have opted for an almost isotropic roughness gradient. Although the code offers the definition

Table 5.1: Parameters for mesh definition and inversion

Parameter	Setting	Remark
Mesh definition:		
Parameter mesh	5 km × 5 km × 2 km	Inversion domain
Secondary mesh	20 km × 20 km × 10 km	Forward modeling domain
Spatial groth rate of cells	1.12	BERT: Para3DQuality
Inversion:		
Regularization strength (λ)	20	
λ decrease	1	Constant regularization
Zweight	0.9	Almost isotropic
Lower/upper resistivity bound	0.1/2000 Ωm	

of different regions with separate inversion parameters, we concentrated on selecting a set of global inversion parameters with respect to the reservoir geology. Inversion parameters are summarized in Table 5.1 and corresponding resistivity sections are shown in Figure 5.7 from which we make the following observations:

- Baseline 2: The east-west plane indicates a lower resistivity above and below the storage reservoir (Figure 5.7a). The north-south plane shows high resistances for Ktzi202 (at electrode 37), possibly extending into the reservoir (Figure 5.7b and 5.7c).
- Repeat 1: Figure 5.7c shows, compared with the baseline image, a rather similar resistivity image with a slight resistivity decrease near the injector (Figure 5.7d).
- Repeat 2: A resistive structure appears centered at Ktzi201 near the injector (Figure 5.7g).
- Repeat 3: The resistive structure at Ktzi201 shows a more significant appearance (Figure 5.7j). A second strong resistivity increase appears at the upper electrodes of Ktzi202 (Figure 5.7k and 5.7l).

The model sensitivity, i.e., the Jacobi matrix containing the derivatives of the synthetic data with respect to changes in the model cell resistivities, was recalculated after each iteration, which was the most time consuming part of the inversion. The time-lapse procedure consists of taking the baseline resistivity inversion as the initial model for the subsequent repeats. The final baseline model was approached in five iterations, whereas the subsequent repeat models approached their final states after three to four iterations. As the number of iterations per repeat data set was not constant, we decided to keep the regularization fixed throughout the inversions. The initial model resistivity of the baseline was set to the median of the apparent resistivity of the field data, which is about 6.94 Ωm for the baseline data set.

We found that the incorporation of the data error, directly derived from the time-series, is not desirable for the temporal stability of the inversion results. After testing different error schemes, we decided to keep the data error as a threshold criterion for the individual readings. Unfortunately, due to the limited currents allowed for the borehole cables, it was not possible to realize reciprocal measurements, which could have been used for error estimation (e.g. Ramirez et al., 1996; LaBrecque et al., 2004). In consequence, we used an error estimation suggested by (Friedel, 2003). This error

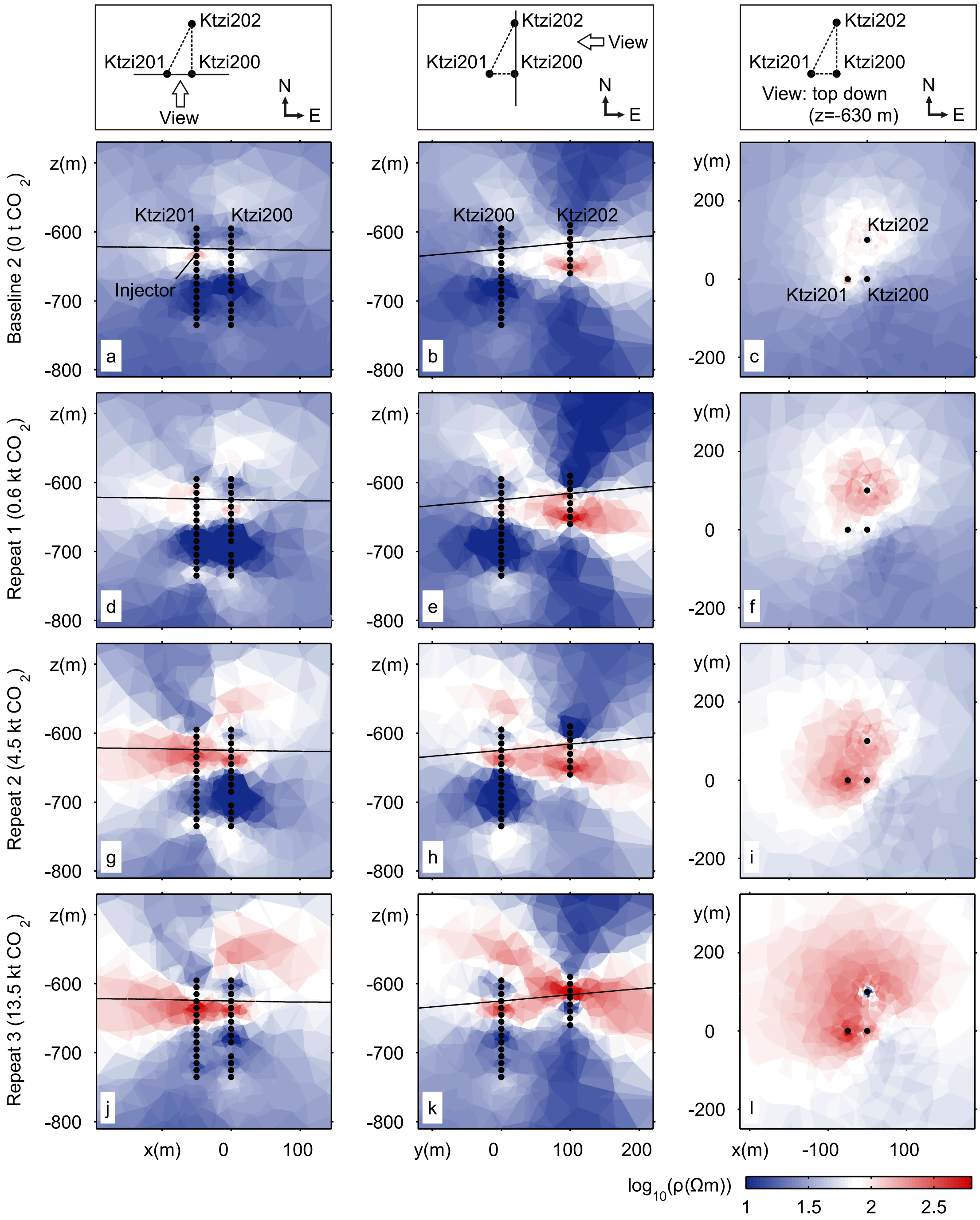

Figure 5.7: Inverted resistivity models for time-lapse SD-ERT datasets. The electrode next to the CO_2 injection is marked in (a). Black line shows the depth of top of the Stuttgart Formation as interpreted from seismic investigations (Juhlin et al., 2007). Coordinates are referenced to Ktzi200 and the ground surface. The main regions of resistivity increase are situated at the CO_2 injector (g and j) and in the upper part of Ktzi202 (k). The resistive zone at Ktzi202 is probably due to unsufficient contact of the respective electrodes to the formation (b, e, and h). Resistivity ratios for the observation plane Ktzi200/201 are given in Figure 5.11.

estimation is based on the minimum resolvable voltage U_{min}, which is to be known from equipment specifications and noise analysis of field data. Because the standard deviation usually increases as the measured voltage approaches U_{min}, readings become mainly random. This behavior is considered by an error drawn from the percentage ratio of the actual voltage and U_{min}, which is added to a percentage base-level error. Together with the data error drawn from the selective stacking and the electrode rejection based on the resistance checks, this estimated error is the third step in the data quality assessment.

5.4 Interpretation

The resistivity increase at the injector is the most notable feature in Figure 5.7. This increase is generally consistent with the resistance checks, except for the resistivity decrease in repeat 1, for which we cannot provide a reasonable explanation yet. To the east, the resistivity increase can be traced to reach out to the observation well Ktzi200 (Figure 5.7g and 5.7h). To the west of Ktzi201 we find this signature to smear out, which indicates that it is somewhat less resolved outside the VERA.

The second resistive structure, appearing with the third repeat at Ktzi202, reflects the uptake of CO_2 into the uncemented annulus (Figure 5.7k and 5.7l). Because the annulus is a feature that is clearly below the resolution limit of the SD-ERT, we find its image as a spurious signature of increased resistivity in the formation. Generally, the resistivity image is strongly affected by sensitivities that are related to the acquisition geometry. The typical sensitivity pattern of the SD-ERT arrangement is given in Figure 5.8a and appears as a tilted quadrupole with elongated cones. From this pattern, we find that the resolution is decreasing with distance to VERA electrodes, which makes imaging of thin-layered CO_2 migration at a distance of several electrode spacings unfeasible.

The data coverage is defined by the sum of the absolute sensitivities for all measurements (Figure 5.8b), and serves as a measure for the information content of the individual model cells. Due to the sparse surface-electrode arrangement, we can observe relatively poor coverages in the volume overlying the VERA. As the region around the VERA electrodes shows the best coverage, it should yield the best resolution in the inversion image.

5.4.1 Impact of large-scale heterogeneities and reservoir intercalations

By comparison of SD-ERT data with well-logged resistivities (Figure 5.2), we found two inconsistencies. First, SD-ERT resistivities (Figure 5.4) are, on average, one order of magnitude larger than logged resistivities. Second, the baseline SD-ERT (Figure 5.7a) shows the reservoir to be a zone of increased resistivity.

To understand these observations, we investigated a conceptual model comprising 15 electrodes situated in the subsurface and two current dipoles at the surface (Figure 5.9, left). The geometry was chosen to resemble the Ketzin SD-ERT setup with a single well. It further comprises the following elements: (a) a near-surface layer representing quaternary deposits, (b) a horizontal layer representing the K2 anhydrite, (c) a vertical layer embedding the well electrodes representing a simplified well completion, and (d) a layer of 2 m thickness representing a reservoir intercalation of cemented sandstone. The base model assumes a homogeneous resistivity of 2 Ωm for the background and all

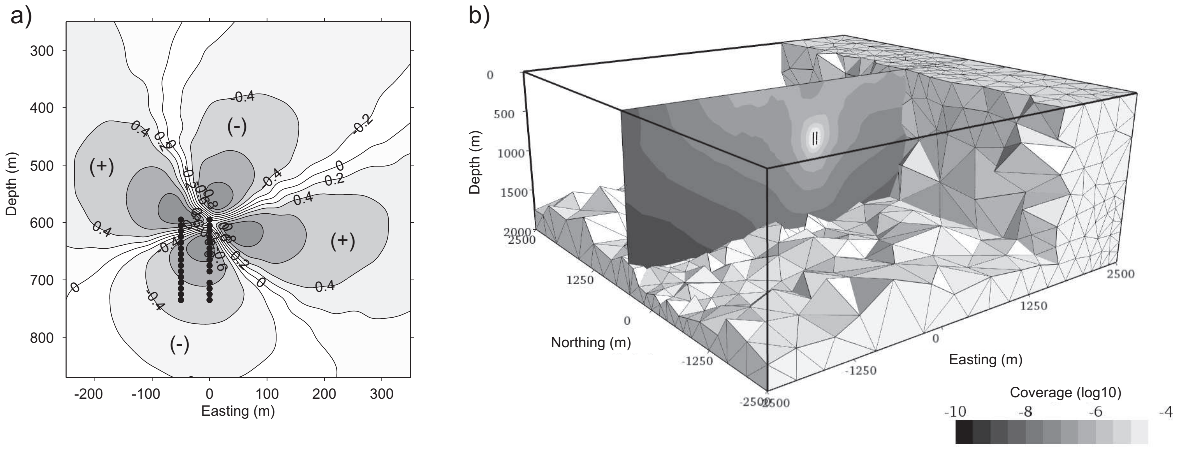

Figure 5.8: (a) Sensitivity pattern of a dipole-dipole SD-ERT measurement near the electrodes (black dots) of well Ktzi200 and Ktzi201. (b) Slice through the coverage volume embedded in the inversion mesh. The bright central part of the slice shows the highest coverage region near the VERA electrodes (black dots). Note that the average cell volumes decreases towards the VERA electrodes, to generate a low cell density at the boundary of the volume.

elements. Each of the subsequent resistivity modelings were conducted with one of the elements perturbed and compared against the results of the base model (Figure 5.9, right).

Model 1 investigates the impact of a near-surface layer that has its resistivity increased by a factor of 50. This factor was drawn from a short-spread resistivity survey, in which we found an average resistivity of about 100 Ωm up to a depth of 25 m. Corresponding synthetic apparent resistivities interestingly show a rather insignificant change. This lets us conclude that weathering-related moisture fluctuations in the near-surface might be of minor importance to the SD-ERT surveys, if they affect the surface dipoles equally. Model 2 incorporates a deeper layer that mimics the K2 anhydrites. It leads to a notable offset, shifting apparent resistivities toward smaller values. This offset seems to be increasing with decreasing distance between current injection and well head, and leads to a reduction of the apparent background resistivity by more than 50% in our model. The layer acts as a current barrier, which could be an explanation for the difference in SD-ERT resistivities with current injections performed at both circle radii.

The simplified well completion of model 3 assumes a homogeneous concrete column of 200 Ωm to be surrounding the electrodes. It leads to decreased resistivities at the top of the electrode array and slightly increased resistivities at the bottom. The effect is somewhat asymmetric with respect to the center of the downhole electrode arrangement and shows a magnitude of roughly -25%. However, the transferability of model 3 to the situation in Ketzin is limited due to the irregular completions of the Ketzin wells. We see a need for further investigation of completion-related effects following the approach of Doetsch et al. (2010). Effects of damages to the external coating of the steel casings, facilitating conductive coupling between the casing and the electrodes, need particular attention.

Model 4 incorporates a thin resistive layer between electrodes 4 and 5. This model addresses reservoir

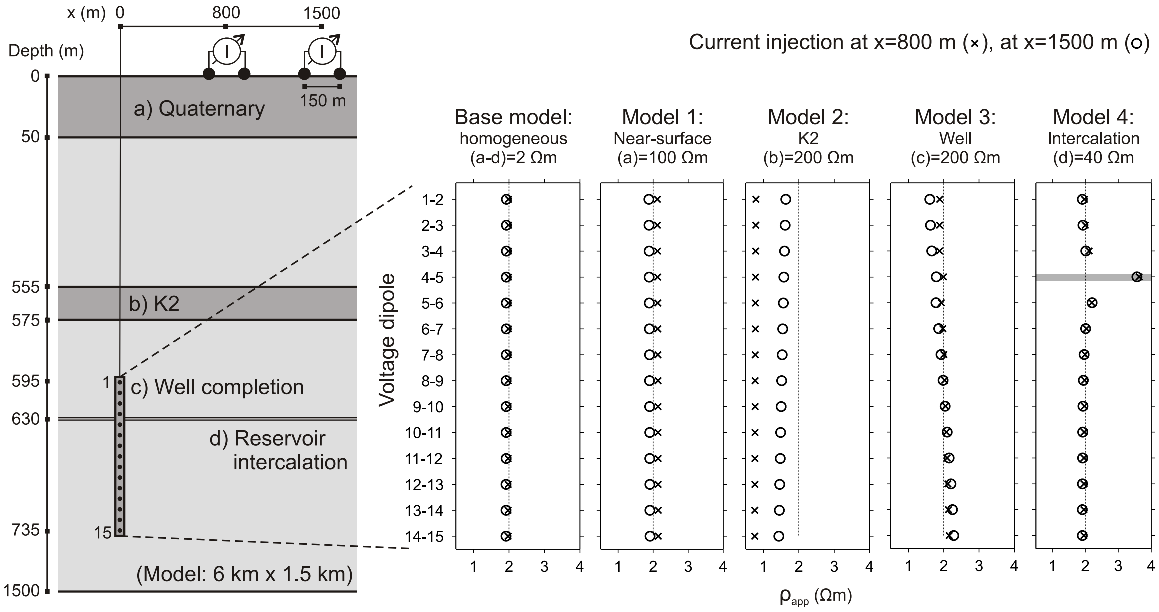

Figure 5.9: Left: Conceptual model comprising two current injections at the surface, 15 subsurface electrodes (black dots), and elements a-d used for resistivity modeling. Geometry is not drawn to scale. Right: Apparent resistivities from forward modeling. Gray bar in Model 4 shows the voltage dipole which measures across the intercalation at a depth of 630 m.

intercalations of cemented sandstone of which at least three are present within the reservoir at Ktzi201 (Figure 5.2). Cemented layers of the reservoir sandstone act not only as relatively resistive intervals in the resistivity logs (Figure 5.2), but are also low-permeability constraints to the fluid migration (Wiese et al., 2010). Apparent resistivities of model 4 show a strong but highly localized increase with a maximum effect on the background resistivity of nearly +100% at the voltage dipole measuring across the layer. This, in turn, leads to the reservoir being imaged as an apparently resistive zone.

Although these models describe implications of resistive structures that can realistically be expected in the geologic setting of the survey area, none of them can explain the consistently higher resistivity values compared to those found in the logs. We consider the likelihood that this observation is caused by the logging as rather low because the available logs are in good agreement, although being partly acquired by different logging operators. To evaluate potential technical reasons, we acquired additional SD-ERT data with different equipment, using a VIP10000 current transmitter (IRIS instruments) and Earth Data logger (GFZ Potsdam), but found a resistivity range that is consistent with our initial data. Thus, we consider it likely that the mismatch is a matter of the prospected scale and possibly anisotropy. There are, unfortunately, only a few references addressing the comparability of resistivity readings made on different spatial scales (e.g. Anderson et al., 1994; Jones, 1995; Aggelopoulos et al., 2005). However, it is widely accepted that there are scale-dependent effects involved when comparing data from well logs and surface-based surveys. In the end, it is important to note that time-lapse application of SD-ERT surveying has the potential to reduce effects of static background heterogeneities.

5.4.2 CO_2 saturation estimation

Several petrophysical experiments have investigated the interdependence of CO_2 saturation and electric resistivity for the sandstones of the Ketzin reservoir (e.g. Schütt et al., 2005; Fleury et al., 2010; Zemke et al., 2010). Kummerow and Spangenberg (2011) constituted a relation between resistivity increase and saturation of pure CO_2 for the sandstone of the Ketzin reservoir (Figure 5.10), which will be used below.

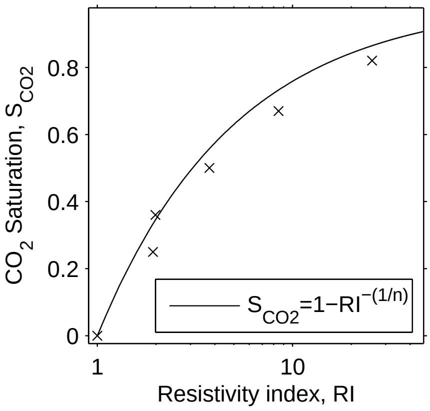

Figure 5.10: Resistivity index versus CO_2 saturation for the Ketzin reservoir sandstone modified after Kummerow and Spangenberg (2011). The solid line is plotted with n=1.62.

Although the quantitative impact of the interfering effects is uncertain, we observe relative resistivity changes that appear consistent with these laboratory results. Thus, we use them to estimate the CO_2 saturation and subsequently conduct a validation with CO_2 saturations drawn from well logging. We follow the approach of Nakatsuka et al. (2010) by using the resistivity index (RI), i.e., the ratio of repeat resistivity and baseline resistivity. This approach requires no explicit knowledge about Archie parameters except for the saturation index, n, which is reported from laboratory experiments under in situ conditions to be about 1.62 (Kummerow and Spangenberg, 2011). Resistivity indexes and CO_2 saturation estimates for the observation plane Ktzi200/Ktzi201 are given in Figure 5.11. The resistivity indexes given in Figure 5.11 show a dominant resistivity increase in the upper part of Ktzi201. This increase has a similar appearance as in Ktzi202 and, thus, might reflect problematic coupling conditions of the electrodes to the formation. Due to this similarity, we consider it likely that CO_2 penetrated into the well annulus of Ktzi201. We will return to this issue in the subsequent comparison with logging results. The third repeat interestingly shows this increase to diminish, and further, a notable resistivity increase in the sandstone interval. Corresponding CO_2 saturations range from up to 30% for the first repeat, 30-50% for the second repeat, to up to 70% for the third repeat.

5.4.3 Comparison with pulsed Neutron-Gamma logging

For a validation of the estimated CO_2 saturations, we compare them with results from time-lapse pulsed neutron-gamma (PNG) logging performed in the Ketzin wells. The PNG technique uses controlled neutron bursts that interact with the nuclei of the surrounding borehole and formation.

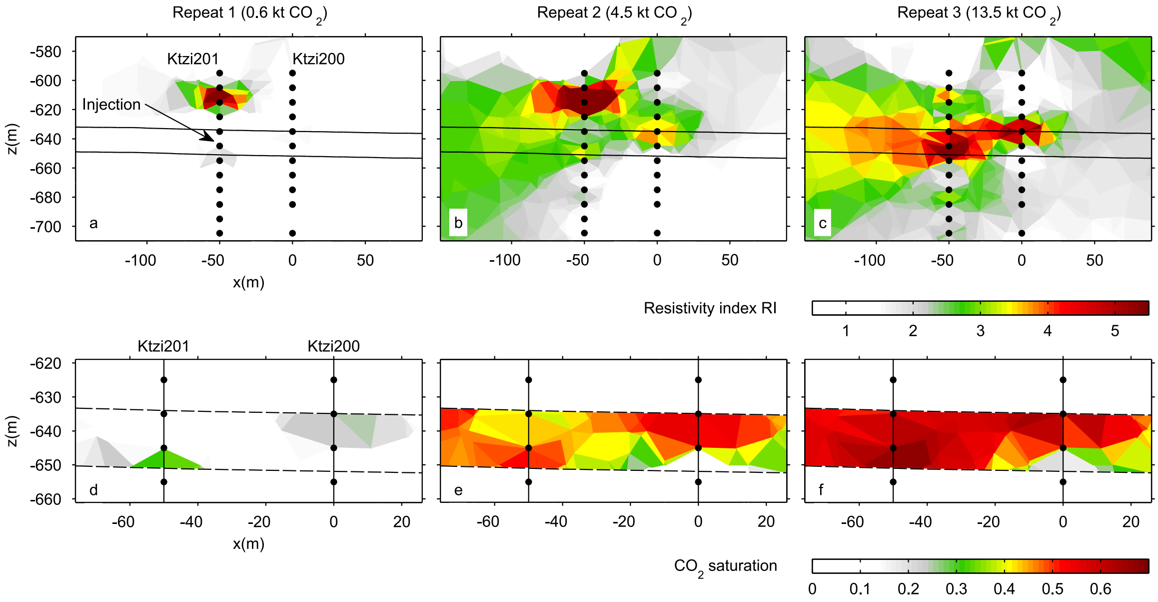

Figure 5.11: Resistivity index (top row) and estimated CO_2 saturation (bottom row) for the investigation plane Ktzi201/200. Dashed lines show the spatial extent of the reservoir sandstones schematically. CO_2 saturation estimation is constrained to the reservoir sandstones, for which the petrophysical relation given in Figure 5.10 was used.

After elastic and inelastic scattering, the neutrons are finally captured, mainly by hydrogen and chloride with a corresponding emission of gamma rays. The macroscopic capture cross section, SIGMA (Σ), is given in capture units (c.u.) and derives from the temporal decline of gamma rays. The high contrast of SIGMA between saline formation brine and gases makes the PNG technique well suited for detection of saturation changes during CO_2 injection in saline aquifers (Sakurai et al., 2005).

Baseline PNG logging was conducted on 9-10 June 2008, and several repeat logs were subsequently acquired. All of these logging runs were carried out with the Reservoir Saturation Tool (RST, Trademark of Schlumberger). For the purpose of this study, the second repeat run performed in June 2009 is evaluated because it is chronologically closest to the SD-ERT repeat 3. CO_2 saturations based on the PNG logs have been computed for a maximum scenario with standard environmental corrections and a minimum scenario using empirical corrections to consider the uncemented annuli. Details on the saturation calculations and corrections are given in Ivanova et al. (2012). Maximum and minimum scenario CO_2 saturations were averaged for a number of depth intervals that are compared against the CO_2 saturation estimates of the SD-ERT (Figure 5.12).

In the Ktzi201 and 200 wells (Figure 5.12), the main reservoir sandstone interval is separated by an intercalation of cemented sandstone at a depth of about 643 m (Norden et al., 2010). The intercalation is characterized by low porosities and low SIGMA values during the baseline RST run (Figure 5.12, iv and x), and separates the sandstone interval in an upper and a lower compartment (denoted as A/D and B/E, respectively, in Figure 5.12), both with a thickness of about 8-9 m.

For Ktzi201, PNG measurements yield CO_2 saturations of 61-82% in the upper compartment (A),

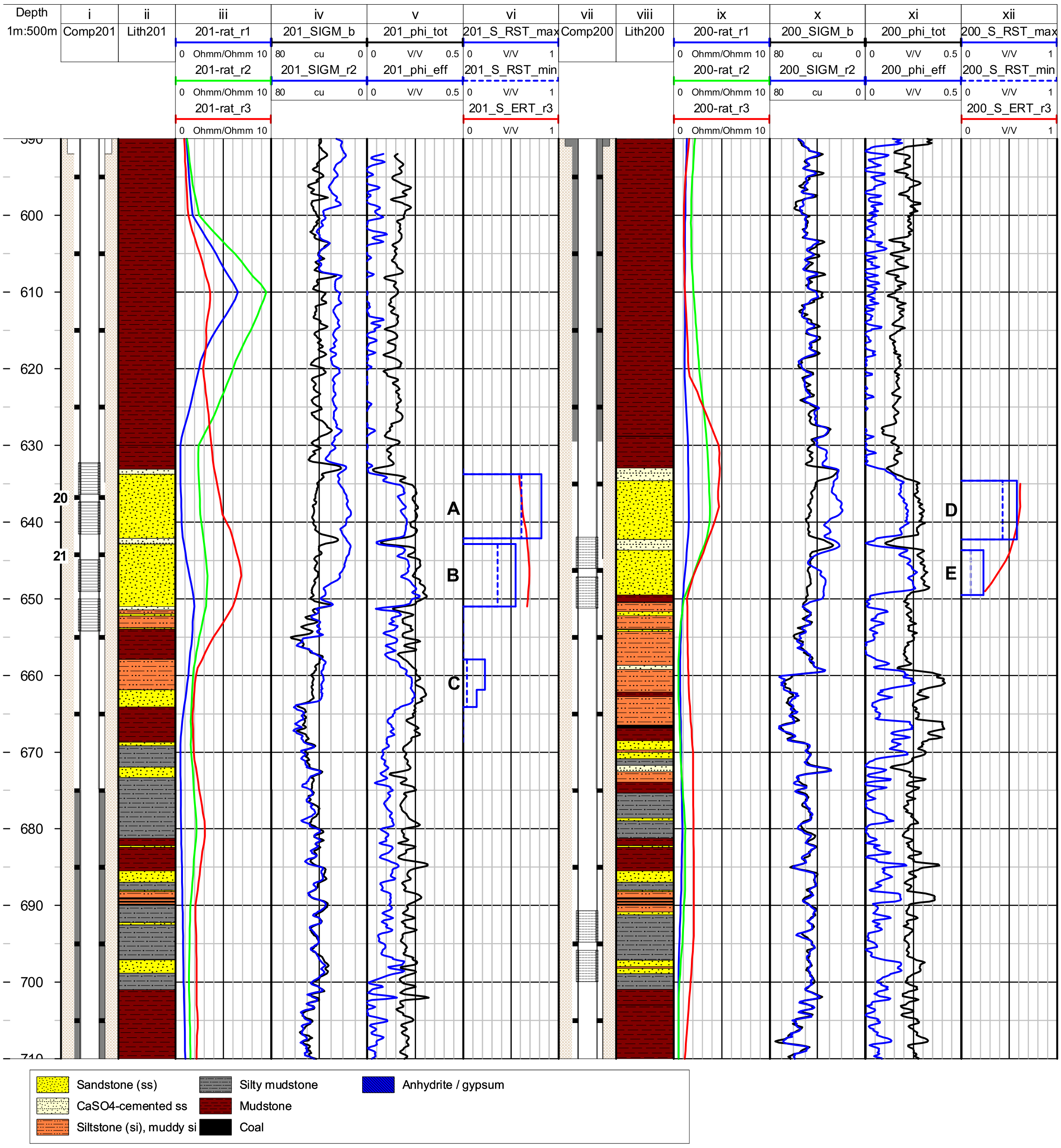

Figure 5.12: Comparison of CO_2 saturations derived from SD-ERT and PNG measurements for the injection well Ktzi201 (panel i-vi) and the observation well Ktzi200 (panel vii-xii). Panels show: Schematic well completion (i,vii), lithology after Förster et al. (2010) (ii,viii), Resistivity ratio of baseline and repeated SD-ERT surveys (rat_r1, rat_r2, rat_r3 in iii,ix), SIGMA logs from baseline (b) and second repeat (r2) PNG runs (SIGM_b, SIGM_r2 in iv, x), porosities after Norden et al. (2010) (v,xi), and minimum and maximum scenario CO_2 saturations from PNG runs (S_RST_min, S_RST_max in vi,xii) overlain with the CO_2 saturations from the third SD-ERT repeat (S_ERT_r3 in vi,xii). VERA electrodes are shown by black symbols in the schematic well completions.

which compares to the range of 60-70% estimated by the SD-ERT. In the lower compartment (B), PNG measurements yield CO_2 saturations in the range of 43-58%. Corresponding CO_2 saturations based on SD-ERT are in the range of about 70%. Comparing the saturations derived from both methods, the SD-ERT appears to result in an overestimation here. In general, the SD-ERT indicates a major saturation increase to be situated within the lower compartment in contrast to the PNG logs, which indicate most significant saturations to occur in the upper compartment. This discrepancy may be due to the individual depth positions of the two electrodes (electrode 20 at 635 m depth and electrode 21 at 645 m depth) in the reservoir (Figure 5.12). We find electrode 21 to be situated relatively centered within the sandstone reservoir. Compared to that, we find electrode 20 at a short distance below the caprock, which produces weaker resistivity ratios than an electrode that is centered in the sandstone interval. We suppose that this is the reason for the smaller CO_2 saturation in the upper sandstone compartment compared to the lower compartment. There is a deeper interval in Ktzi201 (C) for which the PNG measurements yield CO_2 saturations in the range of 4-23%. This interval is, however, not recognizable in the resistivity ratios. Because this can probably be attributed to the low thickness of this interval and the rather low CO_2 saturations at this depth, it gives some indication about the detection threshold provided by the SD-ERT.

In Figure 5.11, we observed a significant resistivity increase at Ktzi201 in the mudstone caprock at depths of about 600-630 m. The PNG SIGMA measurements show systematic offset of about 2.4-7 c.u. between the baseline and repeat measurements within the uncemented interval above the reservoir section of both wells (Ktzi201 and Ktzi202). This is interpreted as an effect related to a buoyancy-driven displacement of brine by CO_2 within these uncemented intervals of the well annuli because the otherwise required displacement within the mudstone caprock itself is physically not plausible at the given low effective porosities and permeabilities. The previous conclusions regarding the invasion of CO_2 into Ktzi201 and Ktzi202 are therefore confirmed by the PNG measurements.

For Ktzi200, we find PNG-based CO_2 saturations of 43-58% in the upper sandstone compartment (D) and 10-23% in the lower compartment (E), respectively. Although there is a reasonable match between the maximum values of the PNG logged CO_2 saturations and the saturations estimated from SD-ERT, we find the respective signature in the SD-ERT resistivity ratios to extend over a vertical distance of about 30 m (620-650 m). Under the assumption that the CO_2 in the upper compartment dominates the resistivity increase, the vertical extent of this resistivity increase might be an indicator for the relatively low vertical resolution. Accordingly, we estimate the SD-ERT to provide a vertical resolution of about three times the vertical electrode spacing. In contrast to that, vertical resolution and penetration depth of the PNG logs are in the order of a few decimeters. In consequence, it appears attractive to address future work on the calibration of ERT-based CO_2 saturations by the PNG measurements to gain saturation constraints at some distance to the wells.

5.5 Conclusions

This article presents the acquisition, inversion, and interpretation of the SD-ERT experiments that were conducted for monitoring of the Ketzin CO_2 storage pilot, Germany. We analyzed one baseline survey and three repeat surveys that were performed during the first year of site operation. Over the time of the three repeat surveys, the injected CO_2 amounted to 0.6 kt, 4.5 kt, and 13.5 kt, respectively. SD-ERT acquisitions were carried out in a dipole-dipole configuration with 16 current injections arranged on two concentric circles centered at the injection site. Current injections were performed at the surface with simultaneous voltage acquisition at the surface as well as downhole. Downhole voltages were measured using the VERA system, which provides 45 permanent electrodes within the injection well and two observation wells. Since the beginning of the CO_2 injection routine contact resistance checks are being carried out regularly to monitor the technical integrity of the VERA subsurface installations.

Inversion of the SD-ERT data was performed on an unstructured tetrahedral mesh, which was a crucial prerequisite for an efficient handling of the inverse problem. This applies in particular because the model, with a lateral extent of several kilometers, is required to incorporate the VERA electrodes that represent an arrangement on the 1-10 m scale. As of the second repeat survey, the inverted models image an increase in resistivity around the CO_2 injector. An analysis of the lateral distribution of the resistivity increase indicates a preferential CO_2 migration in a northwesterly direction. We find a clear impact of the sensitivity patterns and consequential coverage in the resistivity images. There is a gradual decrease in sensitivity outside the VERA volume, leading to a rather low-resolved resistivity image at some distance to the wells.

We further used the imaged resistivity changes to estimate CO_2 saturations by means of the resistivity index method. This estimation was based on an established petrophysical relation, the Archie model, which was calibrated with lab data acquired under representative in situ conditions from the Ketzin reservoir sandstone. For the third repeat survey, estimated CO_2 saturations showed values of up to 70% near the injector, which was confirmed by a comparison with CO_2 saturations obtained independently from PNG logging.

Our investigations revealed the following three key issues concerning the reliability of the imaged resistivities. (1) The SD-ERT data showed a moderate S/N. This was addressed by sequential application of a selective stacking approach to the voltage time-series, contact resistance checks, and incorporation of error weights in the inversion. (2) The Ketzin reservoir is characterized by a rather pronounced heterogeneity and features several thin highly resistive layers of cemented sandstone. Due to their subhorizontal orientation, they cause apparently high resistivities in the SD-ERT image of the reservoir. The effects of selected background structures on the inversion results have been tested systematically with simple models. Time-lapse imaging has the potential to largely reduce effects of such background heterogeneities. (3) Realization of the Ketzin well completions was determined by the operational constraints. For instance, perforation of well casings after installation was not permitted due to uncontrollable risks for permanently installed inhole sensors. Therefore, a staged cementation procedure was conducted to prevent clogging of the preperforated filter-screens. In consequence, the Ketzin wells comprise uncemented intervals that produced significant time-lapse signals in the SD-ERT data when swept with CO_2. Thus, it was possible to identify time-lapse signatures in Ktzi201 and Ktzi202, which can likely be explained by CO_2 occupying these parts of the annuli. For a more detailed interpretation of the situation in Ktzi201, a comparison with PNG logs proved to be useful since providing information about the near-wellbore conditions.

We consequently underline three important aspects for practical realizations of deep ERT monitoring projects with downhole electrodes: (1) implementation of well completions that provide minimal irregularity, and (2) use of robust materials and installation designs that resist the corrosive environment in brine and CO_2 saturated reservoirs over the lifetime of the monitoring project. (3) We recommend additional quality controls for the electrodes, such as the described resistance checks.

Beside these technical results, our study has shown that imaging of CO_2 at the Ketzin site is possible by means of repeated SD-ERT surveys with a satisfactory resolution and sensitivity. A detailed analysis of the SD-ERT data sets showed not only its capability of detecting CO_2, but also, to some extent, reliable quantification of CO_2 saturations. With respect to our rather sparse survey layout, we see perspective improvement by the deployment of additional current dipoles, increased current dipole spacings, surface-downhole current injections, and electrode installations in potentially deviated wells.

Due to the abundance of aspects for the crosswell ERT surveys, it was not possible to give a comparison with the SD-ERT already here. It is, however, worth noting that surface-downhole surveying is a particular option for situations where broad azimuth coverage is demanded or only single wells are available. The use of permanently installed downhole electrodes proved to be crucial to achieve sufficient coverage and resolution at the target reservoir. Furthermore, the VERA realization of such electrodes at the Ketzin site has proved to offer diverse opportunities for alternative geoelectric and electromagnetic surveys. In this regard, we see a promising perspective in the collaboration of frequently repeated crosshole ERT and periodical SD-ERT. Moreover, there is multiple potential for integration of SD-ERT results with other monitoring methods. In this context, we will address continuing investigations on a combined interpretation with the time-lapse seismic data acquired at the Ketzin site, as well as the incorporation of seismic structural constraints into the SD-ERT inversion.

Based on the presented outcomes and the practical experience gained at the Ketzin site, we consider SD-ERT as a promising method that can contribute to monitoring of CO_2 storages within a suite of geophysical methods. Finally, there is a potential for SD-ERT to be an easily applicable supplement to borehole ERT, which is also of interest for monitoring of other subsurface fluid migration processes that lead to sufficient resistivity changes.

Data access

The presented SD-ERT data can be retrieved from DOI:10.5880/GFZ.b103-12051.1 and further technical descriptions at Labitzke et al. (2012). Here, one will find the raw field data (voltage time-series), the preprocessed data (apparent resistivities), and the scripts that were used for processing and inversion of the data.

Acknowledgements

We express thanks to the landowners for permitting access to their properties. We are also grateful to the many people involved in the surveys, in particular Erik Danckwardt, Roland Hohberg, Martin Seidel, Günter Petzold, Marco Pohle, and René Voigt of Leipzig University. Kay Krüger (GFZ) is acknowledged for valuable technical comments and Birgit Schöbel (GFZ) for support in operational and logistic matters. Dat Vu-Hoang and Karl Schwab (Schlumberger) are acknowledged for their cooperation on the interpretation of the PNG logging data. We thank the reviewers (Oliver Kuras and two anonymous reviewers) for their constructive criticism that helped to improve this paper.

We would like to thank all partners of the Ketzin project for their continued support and contributions. The project CO_2SINK and its follow-up CO_2MAN receive their funding from the European

Commission (Sixth Framework Program, FP6), two German ministries — the Federal Ministry of Economics and Technology (COORETEC Program) and the Federal Ministry of Education and Research (GEOTECHNOLOGIEN Program) — as well as from industry partners. We acknowledge the COSMOS project for funding the VERA system. The first author would like to thank the GeoEn project (Grant 03G0671A/B/C), a national scientific initiative in the field of energy research.

6

Combined seismic and geoelectric investigations

Publication IV

Combination of seismic reflection and constrained resistivity inversion with an application to 4D imaging of the CO_2 storage, Ketzin, Germany

P. Bergmann[1], M. Ivandic[2], B. Norden[1], C. Rücker[3], D. Kiessling[4], S. Lüth[1], C. Schmidt-Hattenberger[1], and C. Juhlin[2]

Submitted to Geophysical Prospecting

Contents

---

[1] Helmholtz Centre Potsdam, GFZ German Research Centre for Geosciences, Centre for CO_2 Storage, Telegrafenberg, 14473 Potsdam, Germany

[2] Uppsala University, Department of Earth Sciences, Villavägen 16, 75236, Uppsala, Sweden

[3] Technical University Berlin, Department of Applied Geophysics, Ernst-Reuter-Platz 1, 10587 Berlin, Germany

[4] University of Leipzig, Institute of Geophysics and Geology, Talstaße 35, 04103 Leipzig, Germany

Abstract: Geophysical monitoring at the CO_2 pilot storage site Ketzin includes both time-lapse seismic and time-lapse geoelectric measurements. These measurements are well known to image geological structures differently, in particular for a variable saturation of CO_2. We present an integration of these methods by means of a structurally constrained inversion approach. Lithostructural constraints are interpreted from the seismic reflection data and implemented in the geoelectric inversion by a local regularisation, which allows inverted resistivities to behave discontinuously across boundaries. A tetrahedral finite-element parameterisation is used to closely follow the reservoir-caprock boundary as derived from the seismic reflection data. Thus, seismics and constrained resistivity inversion are arranged in a sequential workflow which is based on structural similarity.

This approach is evaluated using both a numerical example and a real data example. The latter is performed for the Ketzin datasets which include repeated 3D seismic surveys and repeated surface-downhole geoelectric surveys. Consistent with the synthetic example, an enhanced delineation of the resistivity image along the caprock-reservoir boundary is found using the constrained inversion. The time-lapse signature of the resistivity image is found to correlate well with that of the seismic investigations. In summary, the results confirm the relevance of the presented approach for an integrated geophysical monitoring of CO_2 storage sites.

6.1 Introduction

Imaging of subsurface fluid flow is a longstanding geophysical research task, in which CO_2 storage monitoring is a relatively recent application. It is well known that such monitoring can benefit greatly from a combination of different methods; in particular, if these methods complement each other with regard to imaging characteristics and, in our case, sensitivity to variable saturation of CO_2. For instance, geoelectrics provides a limited resolution compared to that of the seismic reflection method. Its key parameter, the electric resistivity, is mainly related to the presence and chemistry of fluids in the pore-space. On the other hand, the reflection seismic response of a rock is mainly related to the elastic parameters of the bulk matrix.

Honouring the demand for multi-method geophysical monitoring, present CO_2 storage sites generally practice broad monitoring activities. Moreover, available best-practice manuals consistently recommend multiple (geo-)physical parameters to be monitored (e.g. Chadwick et al., 2008; NETL, 2009), however, only few references are made in these manuals on how to proceed with the different parameters in combined manner.

In this context, the Ketzin project provides an experimental test site for the geological storage of CO_2 with a primary objective of evaluating geophysical methods and integrated monitoring procedures (Schilling et al., 2009; Giese et al., 2009). Consequently, this has led to a wide range of geophysical methods being performed at the Ketzin site. Asides from well logging, both seismic methods and electric resistivity tomography (ERT) have been extensively applied. So far, the most comprehensive view of CO_2 migration in the Ketzin reservoir is provided by the first repeat of the 3D seismic surveys which revealed a time-lapse signature in reflection amplitude near the reservoir formation (Lüth et al., 2011; Ivanova et al., 2012). Independently, a resistivity increase around the CO_2 injector had been proven by means of repeated surface-downhole electrical resistivity tomography (SD-ERT) surveys (Bergmann et al., 2012b).

Based on these data, we present a combination of reflection seismics and geoelectrics through a structural constrained inversion approach. For this purpose, structural constraints are implemented in the geoelectric inversion by a local regularisation, which allows inverted resistivities to behave discontinuously across prominent geological boundaries. In addition, a tetrahedral finite-element parameterisation is used to closely follow geometric structures interpreted from the seismic reflection data. Consequently, seismics and geoelectrics are arranged in a sequential workflow which is based on a structural similarity of their relevant petrophysical parameters.

In this paper we begin with an outline of the Ketzin project and describe the constrained inversion method. Subsequently, we perform a synthetic study to evaluate the imaging characteristics of the constrained inversion. We then proceed with the real datasets acquired at the Ketzin site and go into detail on the geologically-supported mesh construction, data inversion and interpretation. Finally, we discuss potential implications of our results for monitoring of CO_2 storage sites.

6.2 The Ketzin project

Since its operational inception in 2007, the Ketzin test site hosts an in-situ laboratory for CO_2 storage which is located near Berlin, Germany (Figure 6.1a). Initiated within the CO_2SINK project (duration 2004-2010) it is currently operated under the CO_2MAN project. The injection site is situated in the eastern part of the Roskow–Ketzin double anticline where the injection reservoir is at a depth of about 630–650 m. Sandstones within the Stuttgart Formation within the Triassic Keuper section comprise the storage reservoir. These sandstones consist of sandy channel-(string)-facies rocks with good reservoir properties alternating with muddy floodplain facies rocks of poor reservoir quality (Förster et al., 2006; Norden et al., 2010). The upper seal of the Stuttgart Formation is the Weser Formation, consisting mainly of mudstones and anhydrite (Beutler et al., 1999) with a total thickness of approximately 80 m (Norden et al., 2010). The high clay mineral content and the observed pore-space geometry make the Weser Formation a suitable seal for the CO_2 storage reservoir (Förster et al., 2007). The top of the Weser Formation contains a 10–20 m thick anhydrite layer, known as the Heldburg-Gips or K2 horizon, which constitutes a prominent seismic reflector in this area. Above are mudstones and carbonates of the Arnstadt Formation (Beutler and Nitsch, 2005) that exhibit similar sealing properties as the Weser Formation. In the shallower sandstones of the Hettangian and Sinemurian Groups natural gas had been stored at depths of 250–400 m until the year 2000. The seal to the former gas storage, the muddy sediments of the Pliensbachian Group, provides a second barrier to the deeper CO_2 storage. A third barrier consists of the Tertiary Rupelton, a clay about 80 m thick. The near-surface layers are mainly composed of Quaternary sands and tills which exhibit a relatively flat surface topography.

The injection well, CO2 Ktzi 201/2007, and the two additional observation wells, CO2 Ktzi 200/2007 and CO2 Ktzi 202/2007, were drilled in 2007 and penetrate through the storage reservoir to depths of 750–810 m. In the following we will abbreviate these wells with Ktzi201, Ktzi200, and Ktzi202, respectively. Since the 30th June 2008, CO_2 has been injected into the saline-water-bearing sandstone units via the Ktzi201 borehole. During the first year of injection a total amount of about 17.900 metric tons of food-grade CO_2 has been injected at a rate of about 45tons/d (Figure 6.1b). From gas-chemical monitoring the arrival of CO_2 at the Ktzi200 borehole (50 m away from the Ktzi201 well) was detected after the injection of about 530 tons of CO_2 on July 15th 2008. Arrival

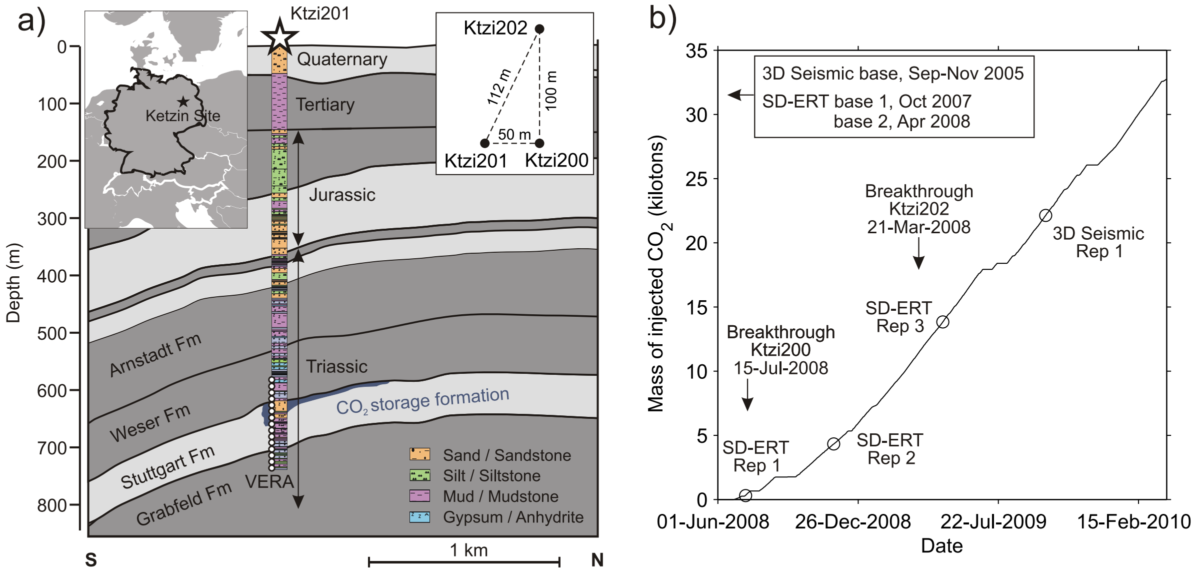

Figure 6.1: (a) Schematic block diagram of the Ketzin anticline showing the principal structural and stratigraphic features. Target reservoir horizon for CO_2 injection is the Upper Triassic Stuttgart Formation. Figure modified after (Förster et al., 2006). (b) Timeline of the CO_2 injection and monitoring activities at the Ketzin site during the CO_2INK project period.

at the second observation well (Ktzi202, 112 m distance to the Ktzi201 borehole) was detected on March 21st 2009 after about 11,000 tons of CO_2 had been injected (Zimmer et al., 2011; Martens et al., 2011). The heterogeneity of the channel-reservoir sandstones is likely to be responsible for the unexpected late CO_2 arrival time at the Ktzi202 borehole.

The maximum amount of CO_2 to be stored at the Ketzin research site is limited by legal regulations to 100,000 tons, which is considerably smaller than demanded for industrial scale projects (Martens et al., 2011). However, due to the relatively small amount of CO_2 injected, combined with the strongly heterogeneous storage reservoir, the site poses qualified conditions for testing of monitoring approaches.

6.3 Method

During recent years numerous studies have adressed the incorporation of a priori information into the inversion of geoelectric data in particular and potential field data in general. Methodical research in this field dates back several decades and is still ongoing (e.g. Pedersen, 1979; Pous et al., 1987; Backus, 1988; Portniaguine and Zhdanov, 1999; Gholami and Siahkoohi, 2009). Practical application, however, became relevant only in recent years, being triggered by the availability of improved acquisition instruments and computational capacities. Nowadays, the term constrained inversion is widely established and offers besides joint inversion and joint interpretation an opportunity for integration of different geophysical methods.

In this context, it has become common practice to support the inversion of magnetotelluric and gravity data with structural constraints obtained from seismic data (Favetto et al., 2007; Jegen et al., 2009). As an example using both seismic and geoelectric data, Saunders et al. (2005) presented an approach in which the ERT inversion is conditioned by means of a curvature-based regularisation obtained from seismic traveltime tomography. Alternatively, Olayinka and Yaramanci (2000b) presented an approach in which layers and bodies of equal resistivity are employed in the inversion. For our investigations, we follow an approach using a combination of ERT and seismics as reported by Günther et al. (2011). They implemented seismic structural information as fully decoupled constraints into the ERT inversion. However, there are also other methods which allow for efficient delineation of structures that can be used for constraint definition, such as ground penetrating radar (Doetsch et al., 2012). In summary, these examples consistently report improved delineations, which could not be achieved with the strict use of potential field methods only. It is interesting to note that our objective, monitoring of geological CO_2 storage sites, is characterized by a particular time-lapse component. For such monitoring, al Hagrey (2011b) stresses constrained inversion to be the sole option for achieving a satisfactory resolution with the ERT method.

In this study, the incorporation of structural information into the ERT inversion focuses on the local regularisation scheme proposed by Günther and Rücker (2006). Most commonly, the ERT inversion aims to minimize the objective function Φ as given in equation 6.1. It accounts for the data misfit Φ_d and model misfit Φ_m by least square norms. Further, $\mathbf{d}$ denotes the data vector, $\mathbf{f}$ the forward operator, $\mathbf{m}$ the modelled data, and $\mathbf{m}^0$ the starting or reference model. Contributions of Φ_d and Φ_m to the objective function are balanced by the regularisation parameter λ.

$$\Phi = \Phi_d + \lambda\Phi_m = \|\mathbf{d} - \mathbf{f}(\mathbf{m})\|_2^2 + \lambda \left\|\mathbf{m} - \mathbf{m}^0\right\|_2^2 \tag{6.1}$$

Günther and Rücker (2006) suggest a generalized regularisation for Φ_m by introducing a constraint weight matrix $\mathbf{W}_c$, model control matrix $\mathbf{W}_m$, and roughness matrix $\mathbf{C}$ which determines the strength of interdependence for neighbouring model cells.

$$\Phi_m = \left\|\mathbf{W}_m\mathbf{C}\mathbf{W}_c\left(\mathbf{m} - \mathbf{m}^0\right)\right\|_2^2 \tag{6.2}$$

In the case of an unconstrained inversion, the constraint matrix contains ones where non-zero elements indicate the connection between neighbouring cells (Figure 6.2). A down-weighting of the elements belonging to a connected segment of cell boundaries reduces the regularisation-imposed smoothness locally. This, in turn, gives the inversion more degrees of freedom to find an optimizing model. The term $\mathbf{W}_m\mathbf{C}\mathbf{W}_c$ then allows for local weighting of model cells and boundaries, retaining global regularisations in otherwise homogeneous areas. Throughout the paper we will use the constrained strength as a parameter to denote the factor that down-weights the respective elements of $\mathbf{C}$. We will refer to the approach given in equation 6.1 as unconstrained or regular inversion and the approach given in equation 6.2 as constrained inversion, respectively. In fact, it is possible to fully weight all elements of $\mathbf{W}_m\mathbf{C}\mathbf{W}_c$ in equation 6.2 such that an unconstrained inversion is realized (0% constraint strength).

This approach allows for an integration of structural information from unconnected, but structurally similar datasets, into the ERT inversion. Application to the Ketzin datasets is, therefore, based on the minimum-assumption that if a change in petrophysical characteristics (e.g. rock type, porosity,

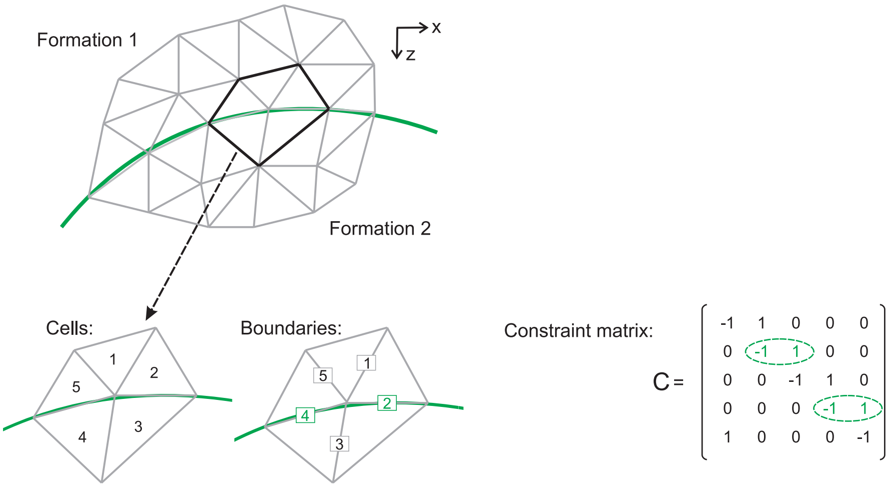

Figure 6.2: Simplified example for a compilation of the constraint matrix $\mathbf{C}$ on a subset of a tetrahedral parameterisation. A boundary (green line) separates two formations and has been incorporated into the parameterisation. The subset has five cells and five boundaries which define the elements of $\mathbf{C}$. Those elements of $\mathbf{C}$ that belong to the boundary are marked with dashed ellipses and would be down-weighted to realise the boundary as structural constraint.

pore-fill) constitutes a change in elastic properties, it is likely to do so for electric resistivity, and vice versa. The corresponding workflow is illustrated in Figure 6.3.

Inversions were performed with the open-source code BERT (www.resistivity.net), which uses the tetrahedral mesh technique of Rücker et al. (2006) for model parametrisation. This allows the incorporation of bended geological structures, which otherwise would be difficult to capture with blocky finite-difference parametrisations. Solution of the inverse problem within BERT is performed with the Gauß-Newton approach (Günther et al., 2006).

It is important to note that the workflow in Figure 6.3 is, despite the structural similarity, independent from any assumptions about petrophysical cross-relations between seismic and electric parameters. This is particularly crucial, since our imaging objective is characterized by a variable saturation of CO_2. In such a case the Biot-Gassmann model and Archie laws can be used for a first-order petrophysical description during fluid substitution. Comparison of both models shows, interestingly, a quite complementary behaviour in seismic and electric parameters when brine is replaced by CO_2 within the pore space. As an example from the Ketzin site, Figure 6.4 shows laboratory data for compressional wave velocity and resistivity with regard to saturation with gaseous CO_2. The Biot-Gassmann model predicts a drop in seismic velocity to occur for the first few percent of CO_2 saturation. This is due to the compressibility of the pore-space fluid which is significantly decreased even for small amounts of gas. In contrast, the Archie-based resistivity response shows for small CO_2 saturations rather constant values and a notable increase only at larger CO_2 saturation.

This discussion becomes more complicated for realistic scenarios in which clay-bearing sediments and patchy CO_2 saturation can occur. In the case of patchy saturation, the velocity-saturation relation behaves more linearly than for the homogeneous saturation described by the Biot-Gassman

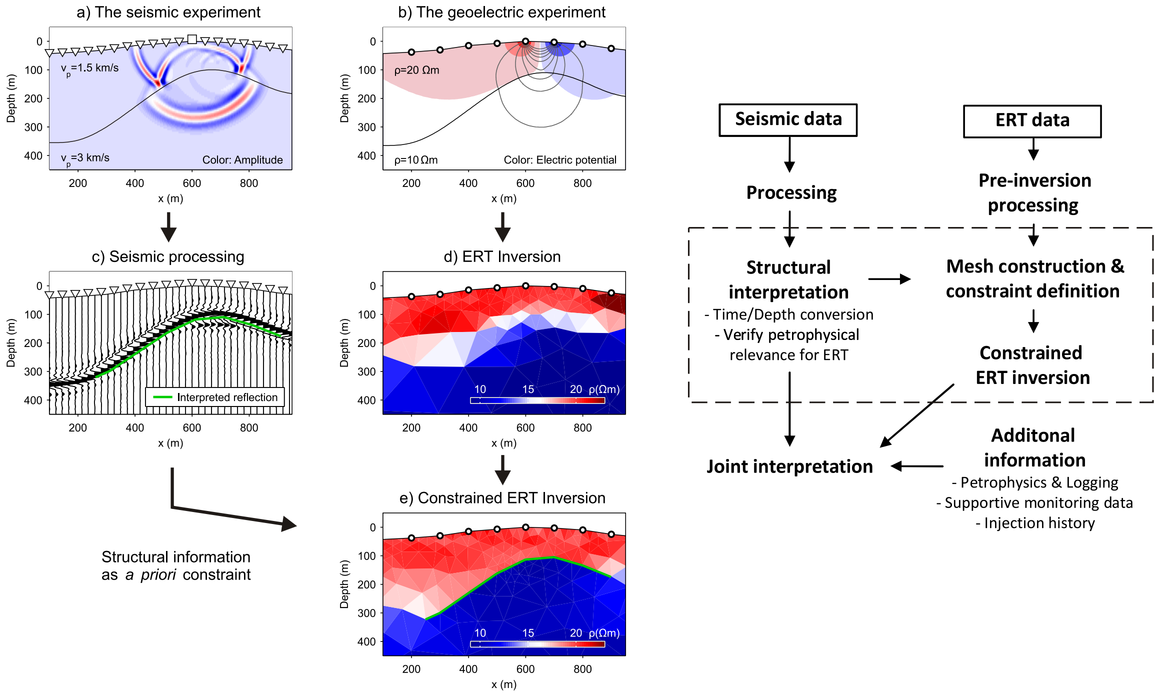

Figure 6.3: Illustration of the sequential workflow for the combined assessment of reflection seismic and geoelectric measurements by means of a constrained inversion. Left: Incorporation of structural information imaged by seismic reflection into the geoelectric inversion using a priori constraints. Right: Arrangement of the constrained inversion workflow (dashed box) within a conceivable monitoring procedure.

model (see also Kazemeini et al., 2010a). The investigations of Kummerow and Spangenberg (2011) indicate that the applicability of the patchy saturation model (resulting in a sensitivity over the complete range of CO_2 saturation), the Biot-Gassmann model (resulting in a sensitivity only at low CO_2 saturations) or mixtures of both may be also a matter of impurities in the injected CO_2 (Figure 6.4).

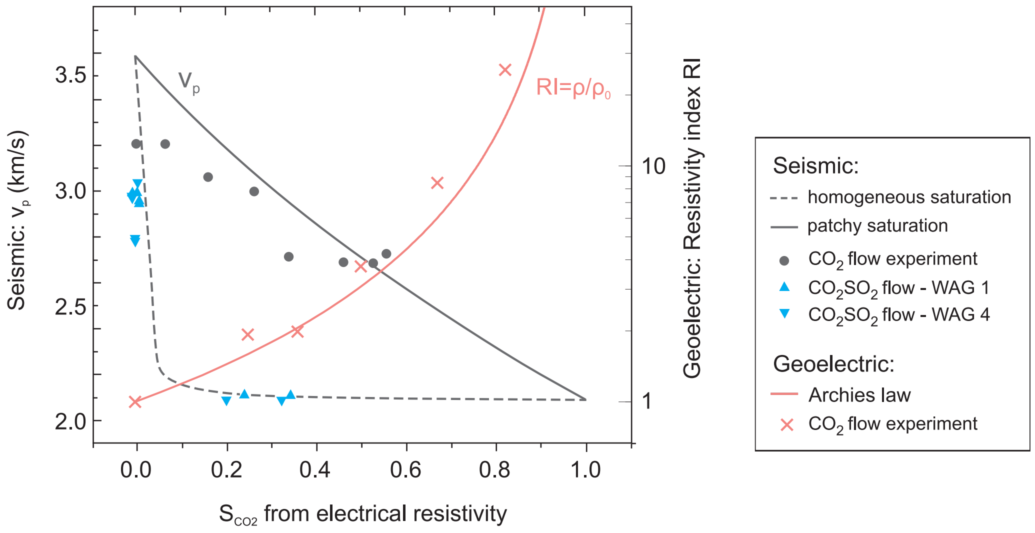

Figure 6.4: Seismic and geoelectric fluid substitution models for the Ketzin reservoir sandstone compiled and redrawn after Kummerow and Spangenberg (2011). Seismic p-wave velocity and electric resistivity index (RI) is given on the left and right axis, respectively. Note that RI, the ratio of repeat resistivity to baseline resistivity, is shown in a logarithmic scale. Illustrated results stem from flow-through experiments on Ketzin core samples performed under representative in-situ conditions of the Ketzin reservoir (p_{conf} = 15 MPa, p_{pore} = 7.5 MPa, and T = 40°C) in sequential cycles of water alternating gas (WAG). Further shown are the Biot-Gassmann data fit for pure CO_2 (solid black line), impure CO_2 (dashed line), resistivity with the Archie data fit (red line).

6.4 Synthetic example

We begin with a synthetic example in order to investigate the imaging characteristics of the constrained inversion. Therefore, we use a simple model which resembles the acquisition geometry of the SD-ERT at the Ketzin site. The forward model comprises the VERA electrodes representing the situation in Ktzi200 and Ktzi201 (Figure 6.5a). Within each well, 15 electrodes are placed in the depth range of 595-735 m (10 m vertical spacing). Electrode dipoles for electric current injection are located at the surface and voltage measurement is simulated for the surface dipoles as well as for the downhole electrodes. Voltage acquisitions with the downhole electrodes are conducted for each electrode to its lower neighbour. The CO_2 distribution has been modified after Bergmann et al. (2010b) in which fluid-flow simulations were used for crosshole ERT modelling. Modifications have been carried out since these studies covered a period of only 28 days, which was stipulated as twice the time span after which the CO_2 had been detected at Ktzi200. Because this period represents only an amount of about 1150 tons of CO_2 in the models, the respective distribution was scaled up to assure that a sufficient response would be visible in the surface-downhole inversions. A further modification was made for the resistivity-saturation relation. Based on preliminary laboratory data, Bergmann et al. (2010b) used a resistivity range which corresponds to a maximum saturation of 50% CO_2 in the forward models. More recently, Ivanova et al. (2012) reported Pulsed-Neutron-

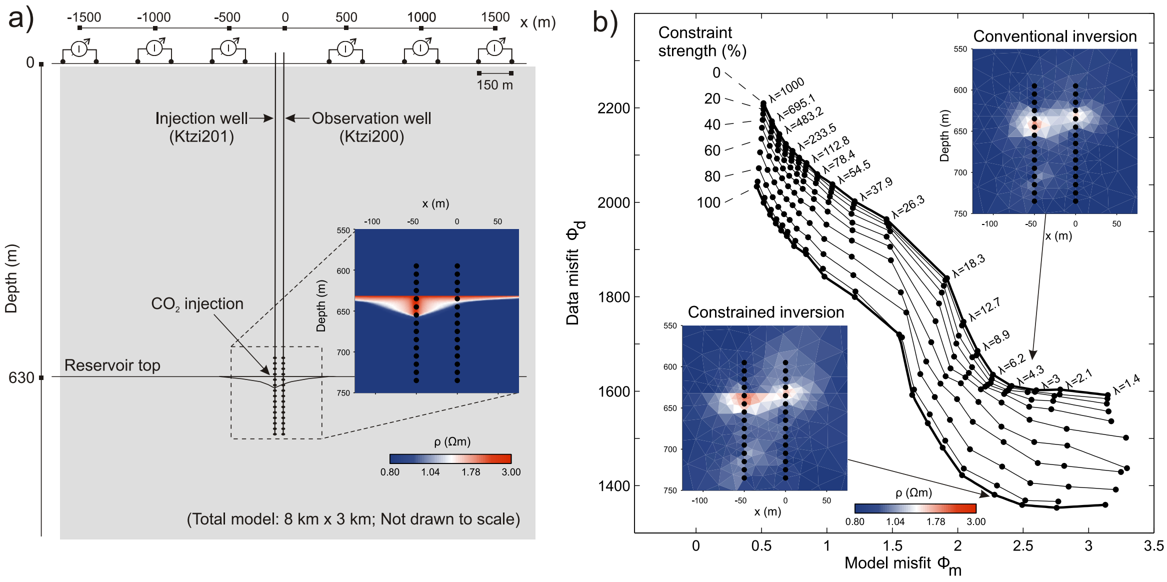

Figure 6.5: (a) Geometry of the synthetic model and (b) set of L-curves for variable regularisation and constraint strength (right). The two models indicated by the maximum-curvature criterion are shown. Note that an increase in constraint strength leads to a decrease in data misfit.

Gamma loggings that show peak saturations of up to 82% at Ktzi201. Hence, we extended the resistivity range in the forward model correspondingly, using a maximum resistivity of 5 Ωm.

We placed the variable constraint strengths along the virtual reservoir caprock boundary as it had been used in the fluid-flow simulations. Subsequently, inversions were carried out for a range of regularisations and constraint strengths, and then arranged into L-curves (Figure 6.5b). Over the entire range of constraint strengths, the quality of the reconstructed resistivities depends to a large extent on the selected regularisation. We make the generic observation that strong regularisations produce over-smoothed models with poor data fits and weaker regularisations rougher models with better data fits. According to the maximum-curvature criterion of Hansen and O'Leary (1993) we selected from the unconstrained inversions a regularisation close to 5. Within a range of regularisations around this value, the inverted models show that the true model can be reconstructed to some extent (Figure 6.5b). From visual inspection it can be found that the results of the constrained inversions represent the true model better than those of unconstrained inversions. However, both types of inversion image resistivities which are below the true resistivities. This observation confirms the findings of al Hagrey (2011b) and is associated to the underestimation of resistivity contrasts in linearized resistivity tomography (Loke and Barker, 1995). The better resolved resistivity contrast along the reservoir top is the most notable feature in the constrained inversion models. It appears that the constrained inversion allows the models to relax towards a stronger gradient along the reservoir-caprock boundary. In principle, the constraint strength determines the steepness of the gradient and Figure 6.5b shows that an increase in constraint strength shifts the L-curves towards lower data misfits.

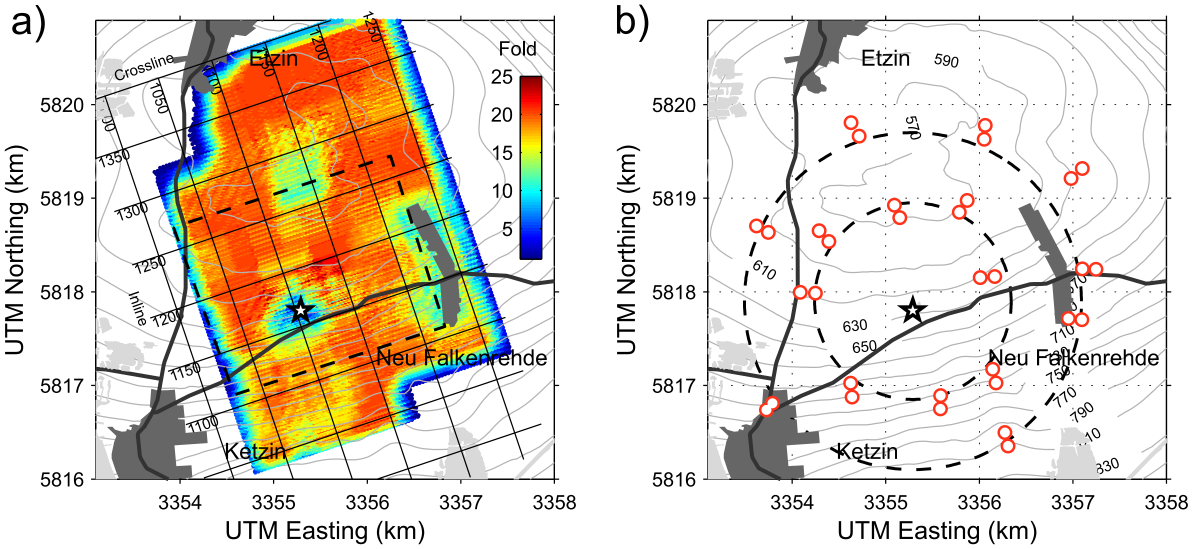

Figure 6.6: (a) Acquisition geometry of the 3D seismic surveys and (b) 3D SD-ERT surveys. The depicted seismic fold represents the fold of the baseline seismic survey. The dashed box indicates the extent of the first repeat survey. SD-ERT surveys comprise also VERA downhole measurements in the three Ketzin wells (Figure 6.1). Grey isolines indicate approximate depth of the storage formation (Top Stuttgart Formation).

6.5 Ketzin data example

A wide range of time-lapse seismic methods was initiated at the Ketzin site (Lüth et al., 2011). These methods comprise 3D (Juhlin et al., 2007; Ivanova et al., 2012), pseudo (or sparse)-3D (Ivandic et al., 2012), and 2D (Bergmann et al., 2011) data acquisition. Additionally, vertical seismic profilings (VSP), moving source profilings (MSP), and crosswell seismic surveys have been performed (Yang et al., 2010; Götz et al., 2011). There is also a number of further studies which focus on the processing and interpretation of these datasets, e.g. for geologic characterisation (Yordkayhun et al., 2009b; Kazemeini et al., 2009, 2010b) or time-lapse imaging (Kashubin et al., 2011; Zhang et al., 2012).

The baseline 3D seismic survey was carried out in 2005 and covered an area of approximately 12 km^2, including the area around the injection location and the strongly faulted anticline crest (Juhlin et al., 2007)(Figure 6.6a). An accelerated weight-drop was used for activation of about 7500 source points. The survey was realized in a template geometry with a bin size of 12 m × 12 m and a nominal fold of 25. This fold could, however, not be achieved at several locations due to infrastructure obstacles. In 2009, after injection of about 22 kilotons of CO$_2$, a 3D subset of approximately 7 km^2 was repeated around the injection location. Time-lapse processing of both surveys imaged a decrease in reflectivity for the CO$_2$ storage formation. After a preliminary assessment of this reflectivity change by Bergmann et al. (2010a), a subsequent interpretation and CO$_2$ mass quantification was performed by Ivanova et al. (2012).

Geoelectric activities comprise measurements of SD-ERT in 2D and 3D setups, as well as crosshole

ERT (Kiessling et al., 2010). The 3D surface-downhole ERT surveys have been performed with 16 current dipoles deployed on two circles concentrically arranged around the injection site (Figure 6.6b). Electrical current injections were performed with up to 11 A at a voltage of up to 3.3 kV. These large-scale geoelectrical measurements were adapted to the demand of high-resolution monitoring of the storage reservoir by a joint operation with a vertical electrical resistivity array (VERA) which is permanently installed in the Ketzin wells (Schmidt-Hattenberger et al., 2011). Additional surface-downhole data acquisition surveys were realized near the reservoir target by a combination of surface surveys and voltage measurements with the VERA. The SD-ERT surveys imaged a resistivity increase at the injector, which is consistent with observations from crosshole geoelectric measurements (Schmidt-Hattenberger et al., 2012). Based on this resistivity increase Bergmann et al. (2012b) estimated CO_2 saturations in the vicinity of the wells, for which they found some agreement with the corresponding estimates from Pulsed-Neutron-Gamma logging. They, however, note that the SD-ERT images are influenced by various uncertainties. Despite a general difficulty to quantify these, they elaborate on the impact of the irregular well completions and a shift in magnitude for the apparent resistivities compared to those from well logging. Although this shift is suspected to be associated with the difference in scale for both types of resistivity measurements, it is presently not well understood. Compared to the 3D seismic geometry, the SD-ERT surveys comprise a very sparse acquisition geometry with a spatial illumination, as will be shown later, that is rather focused on the volume surrounding the borehole electrodes. Due to its relatively short preparation times and lower acquisition efforts, it was possible to perform SD-ERT surveys at a denser frequency than the seismic surveys and to align them partly to the arrival times of CO_2 at the monitoring wells (Figure 6.1b). In this paper, we will focus on the comparison of the third SD-ERT repeat survey with the 3D repeat seismic survey (time distance to the 3D repeat seismic survey: $\sim$6 months, difference in injected CO_2: $\sim$8300 tons).

6.5.1 Mesh construction and constraint definition based on geologic interpretation

The 3D seismic baseline survey together with available borehole data form the base for the structural and geological interpretation of the Ketzin site. The seismic data processed by Juhlin et al. (2007) included a single zero-phase filter after stacking of the seismic data. Hence, the used 3D seismic data are rather mixed phase. A depth-conversion of the data was made using the smoothed stacking velocities after Juhlin et al. (2007). For the structural interpretation of the new 3D seismic, the seismic data were analysed together with available legacy data by using the commercial software package (Petrel 2010$^{\mathrm{TM}}$) (Figure 6.7a). In order to optimize the structural interpretation, horizon markers from 52 wells were used to relate seismic data to geological boundaries for horizons of the post-Weser formation (Kling, 2011). Below the prominent K2 reflector, the Ketzin wells are the only direct source available for linking geophysics to geology. Here, synthetic seismograms and modelled seismic data guided the interpretation as the Top Stuttgart does not appear as a persistent reflector. Thus, the synthetic seismogram at the Ktzi200 borehole does not correlate with a coherent reflection at the top and base of the Stuttgart Formation determined on the cores. Lithologically, the boundaries between the Stuttgart Formation and the deeper Grabfeld Formation and the overlying Weser Formation, respectively, are heterogeneous. The channel bodies could cut deep into the underlying Grabfeld Formation and thus produce sharp lithologically contrasts of porous sandstones next to playa-type mudstones. The Ketzin boreholes show, however, a smooth transition from muddy to more silty and sandy rocks (Figure 6.7b). The base of the Stuttgart Formation at the Ketzin wells was assigned based on core and logging data to the occurrence of the first strata of silty mudstone or siltstone above the mudstone carbonate-dominated Grabfeld Formation, whereas the Top of the Stuttgart Formation was defined as the occurrence of the last siltstone/sandstone strata below the mudstone sulphate rocks of the Weser Formation (Förster et al., 2010). Due to the smooth lithological transitions between the formations, the seismic reflectivity of the boundaries of the Stuttgart Formation are non-persistent. Therefore, a "Near Top" and "Near Base" Stuttgart horizon was created by shifting the K2 reflector to match it with the stratigraphic well data of the Ketzin boreholes (Ktzi200-Ktzi202). Although it is expected that the thickness of the Stuttgart Formation will show some variation due to the erosive character of locally present basal sand channels, the Near Top Stuttgart horizon reflects a proper estimate of the uppermost depth level of possible sandstone occurence within the Stuttgart Formation. Faults were interpreted on horizon slices and 2D intersections at the top of the Ketzin anticline (the Central Graben Fault Zone, CGFZ; Juhlin et al., 2007) and could be traced down to below the Stuttgart Formation occasionally, showing a displacement of up to 30 m. Due to their distance to the injection site (and the spatial resolution of the geoelectric monitoring data) these faults were not considered in this study.

In order to avoid misinterpretation in the constrained inversion workflow shown in Figure 6.8, it is necessary to evaluate whether a structure interpreted from the seismic reflection data has sufficient petrophysical relevance for ERT imaging. The mainly anhydritic K2 layer, for instance, separates two mudstone dominated formations and produces a pronounced seismic reflection. In the ERT, however, it will not be feasible to resolve such a thin layer without adjacent electrodes.

The Top Stuttgart itself produces only a poor response in both the seismic reflection and the ERT (Juhlin et al., 2007; Schmidt-Hattenberger et al., 2011). There is, however, a change from permeable reservoir sandstones of the fluvial facies to impermeable playa-mudstones of the Weser Formation (Figure 6.7). Thus, the petrophysical relevance of the reservoir-caprock boundary is more of implicit character, which becomes considerable as a barrier for the fluid migration. The interpreted Near Top Stuttgart horizon is therefore understood as the upper boundary for the possible occurence of reservoir rock and can be used as a constraint for the ERT imaging. In the next step the interpreted Near Top Stuttgart horizon was used to construct the inversion domain. Therefore, a cube has been created with a side length of 5 km and a depth of 1.5 km. Within this cube, the Near Top Stuttgart horizon had been placed as a piecewise linear complex such that it separates the cube into two regions. For a reduction of numerical boundary effects in the forward computations, the cube was extended to a side length of 20 km and a depth of 10 km. Further, mixed type boundary conditions were applied at the bottom and side faces, as well as Neumann conditions (no current flow) at the surface (Rücker et al., 2006). This extended cube defined then the domain in which forward computations were carried out to determine the sensitivity kernels (Jacobian matrix). Parametrisation of both domains was done with the TetGen mesh generator (Si, 2003) using unstructured tetrahedral cells. The cube was populated with about 17,000 cells, arranged such that they incorporate the Near Top Stuttgart horizon (Figure 6.8c). Cell volumes were

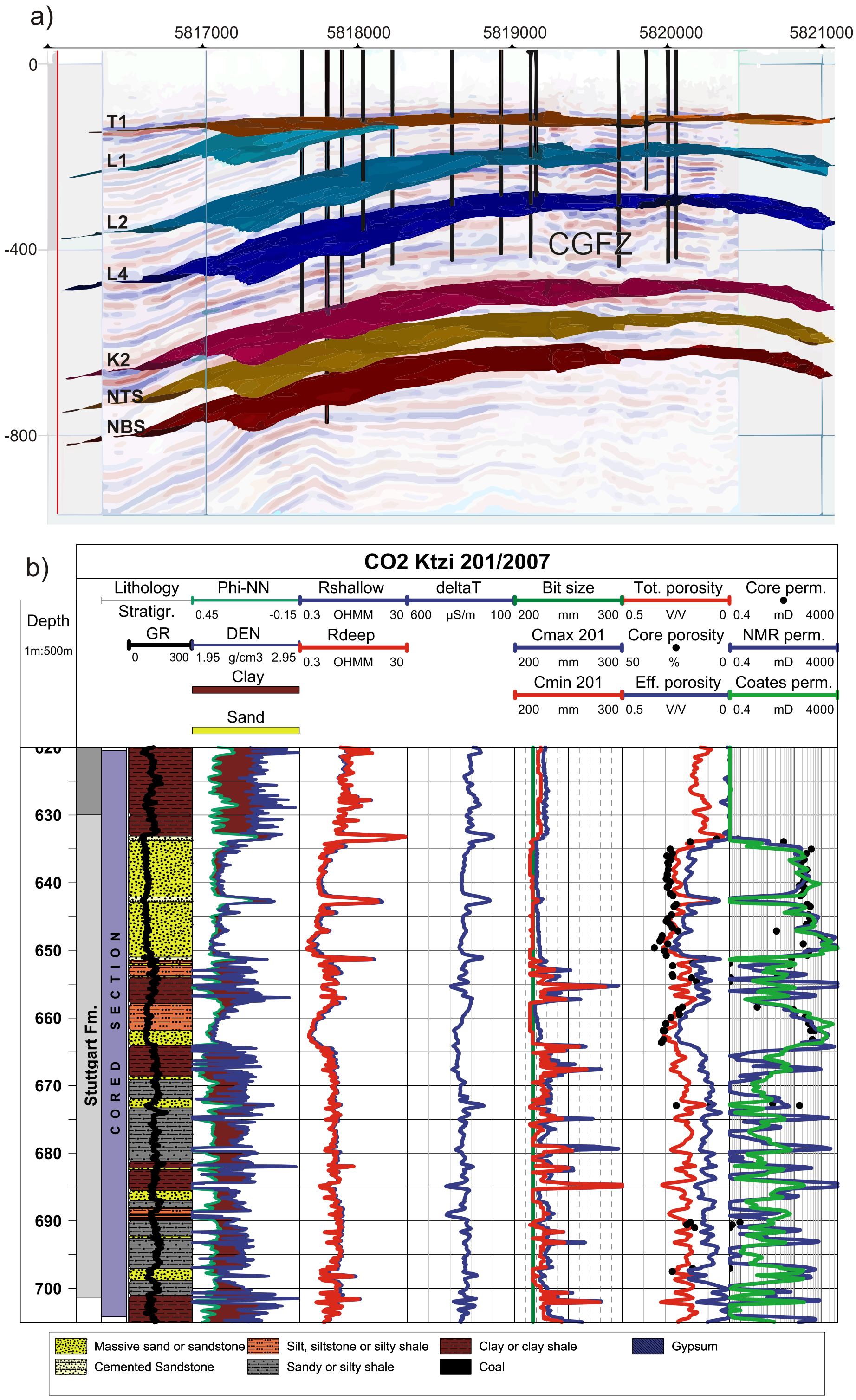

Figure 6.7: (a) Block view of one depth converted seismic line (crossline 1095) together with interpreted horizons (T1, base Tertiary; L1, base Toarcian; L4, base Hettangian; K2, top Weser; NTS, near top Stuttgart; NBS, near base Stuttgart) and well paths used for the seismic-to-well tie. View direction is from east; CGFZ indicates the Central Graben Fault Zone at the top of the anticlinal structure. (b) Core-log analysis of the injection well Ktzi201 modified, showing also different determined permeabilities (after Norden et al., 2010).

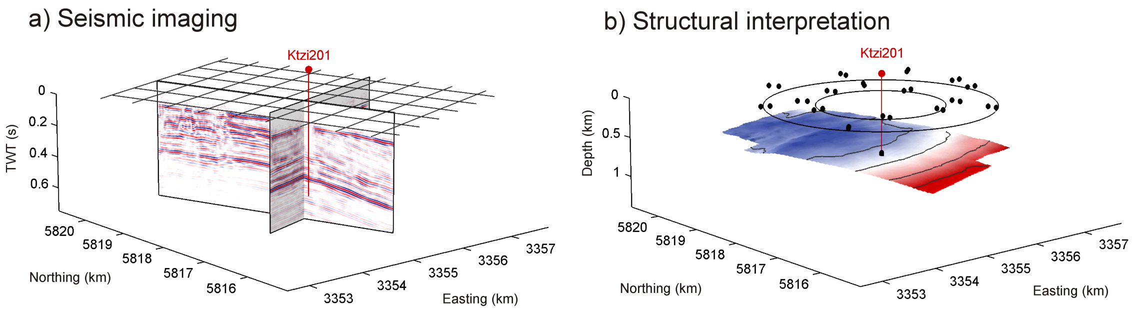
a) Seismic imaging

b) Structural interpretation

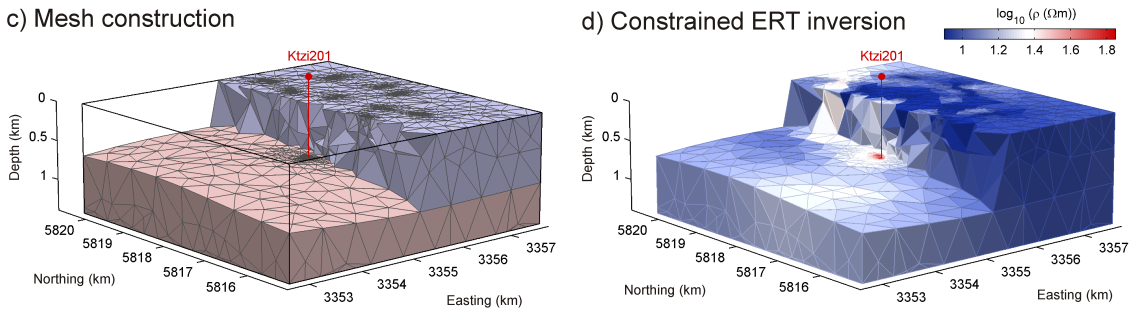
c) Mesh construction

d) Constrained ERT inversion

Figure 6.8: Realisation of the constrained inversion workflow for the Ketzin SD-ERT data: (a) seismic imaging and (b) interpretation of the Near Top Stuttgart horizon with depth conversion. (c) Construction of the inversion mesh and (d) ERT inversion. The spatial extent of the baseline seismic survey is indicated by the black lines in subplot (a). The extent of the SD-ERT surveys is indicated in subplot (b), respectively. Subplot (c) shows the refinement of the mesh cells towards the downhole electrodes in the centre of the model. Note that subplots (b)-(d) are shown with vertical exaggerated depth axes.

forced to be smallest near the electrodes and to coarsen towards the cube faces where sensitivities are lowest. According to the triple mesh technique of Günther et al. (2006), two refinements were implemented on the basis of this mesh. Actual forward computations were carried out on a secondary field mesh as the first refinement (about 187,000 cells). In order to avoid boundary effects, this mesh was extended laterally beyond the parameter mesh. The second refinement generates the primary field mesh on which electric potentials are computed for a constant conductivity model. Computation of the primary potentials was performed once prior to the inversion in order to avoid singularities near the electrodes (Rücker et al., 2006).

6.5.2 Inversion

To assure a better comparison of results from conventional inversion and constrained inversions the same mesh was used, but with varying constraint strength across the inserted Near Top Stuttgart horizon. Special attention was paid to prevent mesh specific effects by performing several inversions with different mesh settings. In these we found some variability with regard to the cell density, due to the regularisation in the inversion code being parameterized by the cell faces. Thus, a chosen

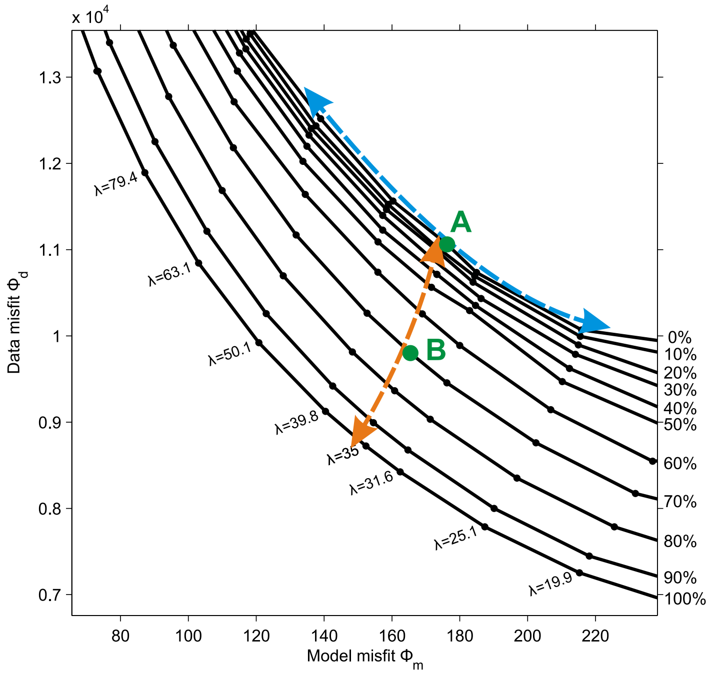

Figure 6.9: Set of L-curves for the inversion of the baseline data. Numbers on the right of the graph represent the constraint strength. The blue curve indicates the search for an optimum regularisation. The orange curve indicates the subsequent search for a constraint strength. Points (A) and (B) represent the models shown in Figure 6.10.

regularisation cannot be freely transferred to meshes of different cell density. The incorporation of the constraint surface requires auxiliary grid points, which leads to a finer grid around wells. In consequence, we reassessed for our new mesh the regularisation parameter selected by Bergmann et al. (2012b) for regular inversions.

Therefore, a number of constrained and unconstrained inversions was performed with varying regularisation (Figure 6.9). From these we selected a preliminary regularisation to be in the range 25-50. Within this range we carried out a refined search from which we selected a regularisation equal to 35. We then inverted for varying constraint strengths at a constant regularisation, from which we selected a constraint strength equal to 70%. A full constraint strength was not chosen due to the observation that the time-lapse inversions tended to bias the resistivity ratios for very high constraint strengths. Figure 6.10 shows the resistivity models that were selected from Figure 6.9.

Each data point in Figure 6.9 represents the time-lapse inverson of the different datasets in which the re-computations of the sensitivities were the most time consuming component. Baseline sub-inversions started from a model with a homogeneous resistivity that was set equal to the median of the apparent resistivities in the baseline data (about 6.5 Ωm). Sub-inversions of the repeat data were then initialized with the models obtained from the baseline data.

By variation of the regularisation we found different regularisation parameters to be optimal for the individual time-lapse data sets. This is caused by a variable signal-to-noise ratio (SNR) and

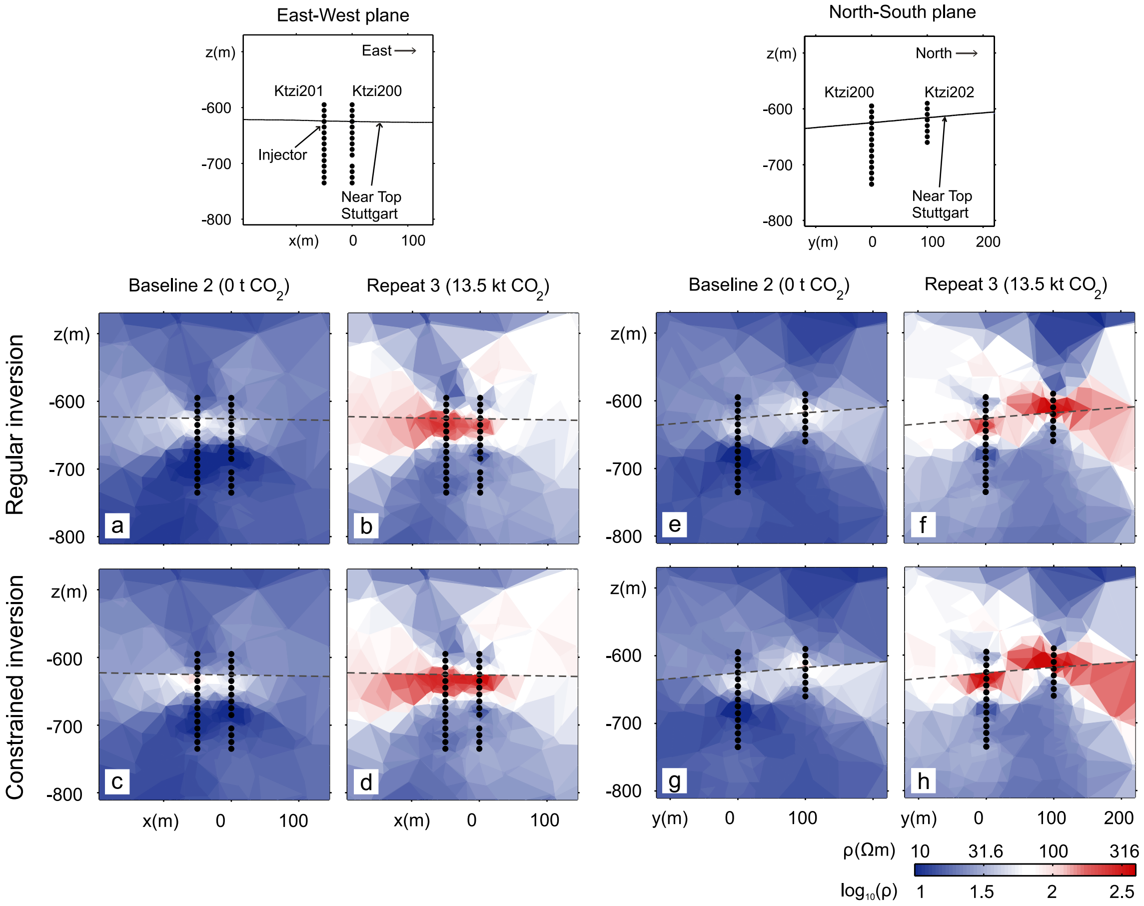

Figure 6.10: Resistivity models from regular inversion (top row, point A in Figure 6.9) and constrained inversion (bottom row, point B in Figure 6.9) for a constraint strength of 70%. Subplots (a)-(d) show the East-West plane, subplots (e)-(h) show the North-South plane, correspondingly.

resulted also in the fact that inversions of the repeat time steps did not terminate within a constant number of iterations. For our selected regularisation, for instance, the final baseline model was approached after five iterations, whereas the subsequent repeat models were approached after 3-4 iterations. This was also the reason for keeping the regularisation constant throughout the iterations, instead of using an annealing regularisation. It is important to note that the BERT code allows inversion parameters (e.g. regularisation or resistivity boundaries) to vary within different regions of the inversion domain. However, we used everywhere the same parameters to avoid intrusive intervention into the models.

6.6 Interpretation and comparison with seismic data

In the following, the interpretation of Figure 6.10 will be based on the interpretations made by Bergmann et al. (2012b) from unconstrained inversions. We hereby focus on the impact of the

Table 6.1: Estimated interpretation depths based on the coverage of the Ketzin SD-ERT acquisition geometry (Figure 6.11). The lateral investigation depth denotes the radius around the downhole electrode array in which a certain type of interpretation can be performed.

Coverage (log10)	Type of admissible interpretation	Max. radial investigation depth
cov>-3.5	Quantitative interpretation	40 m
-3.5>cov>-4.5	Qualitative interpretation	80 m
-4.5>cov>-6	Directional trends only	∼200 m

constraint on the inverted resistivities, which is best-studied for two regions.

First, we consider the region at Ktzi201 around the CO_2 injection location. The regular inversion of the first repeat survey shows a resistive signature that reaches out to Ktzi200 (Figure 6.10b). Comparing this to the constrained inversion (Figure 6.10d), we find a signature with a higher resistivity and a better delineated resistivity contrast along the reservoir-caprock boundary, which seems consistent with the findings from the previously presented synthetic study. Above the reservoir, this contrast leads to generally lower resistivities compared with those of the regular inversion. This is also observed in the resistive coverage-related region above Ktzi200, which is notably reduced in the constrained inversion (compare subplot b and d in Figure 6.10).

Next, we consider the region near the upper VERA electrodes in Ktzi202 (Figure 6.10f,h). Unlike the relatively steady resistivity increase near the CO_2 injector, this feature was caused by an abrupt resistivity increase that occurred between the second and third SD-ERT repeat surveys (Bergmann et al., 2012b). This increase was due to an uncemented segment in the well annulus of Ktzi202, which is present in a depth interval that covers a lower section of the Weser Formation and an upper section of the Stuttgart Formation. At the time when the CO_2 swept into the uncemented annulus, the corresponding VERA electrodes lost contact to the formation. Since the diameter of the annulus is clearly below the resolution of the SD-ERT, the inversion spuriously images this feature as a highly-resistive zone within the caprock formation. The constrained inversion largely confirms this image, but shows some extrapolation of the resistivity contrast into the low-coverage region to the North (Figure 6.10h). This behaviour is to a lesser degree already present in the regular inversions and, in fact, raises the question about the extent of the region that can be reliably interpreted. For the target depth under investigation, Figure 6.11a shows that the region with useful coverage is confined around the VERA electrodes. We conclude, that for a quantitative interpretation the radial distance to the VERA electrodes may be in the order of a few tens of meters. In addition, an extended radius of some more tens of meters may be used only for qualitative interpretations. Table 1 gives investigation depths for different types of interpretations that may be carried out. It is important to note that these values refer to the acquisition geometry of the Ketzin SD-ERT and are meant as a rough guideline for the interpretation of the models.

Due to the above reasoning we concentrate on the wellbore surroundings for the comparison of the SD-ERT results and the seismic sections (Figure 6.12). Time-lapse processing of the seismic data consisted of the following four steps (Ivanova et al., 2012): The first step, time and phase shift, attempts to correct for static time shifts that occur between seismic traces, most likely due to near surface velocity variations that are not completely corrected by the pre-stack statics. In the second step, a shaping filter was used to match the phase and amplitude spectra of the wavelet from one

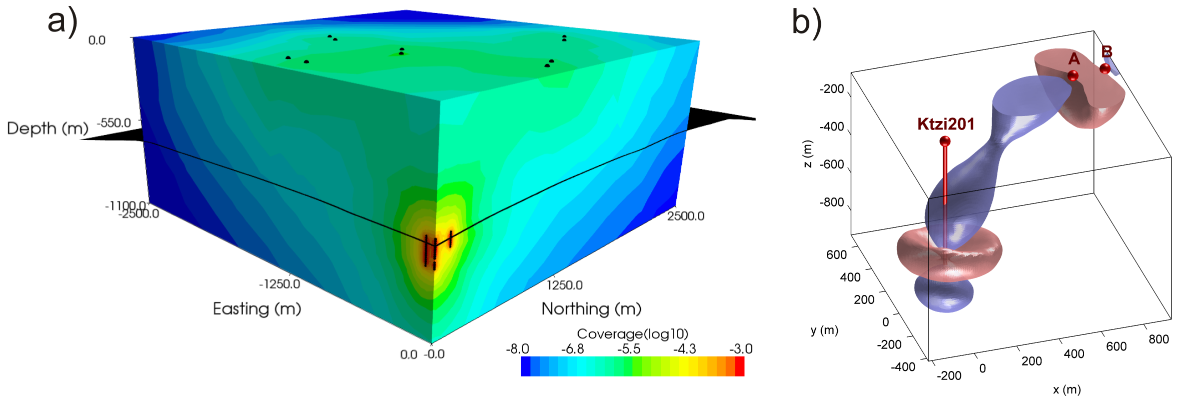

Figure 6.11: (a) Coverage pattern resulting from the sum of the absolute sensitivities. Black dots indicate the electrodes used for the measurement (current injection at the surface, voltage acquisition downhole). The black surface shows the Near Top Stuttgart horizon. Note that sufficient coverage for the target of interest is merely present around the well electrodes. (b) Sensitivity pattern of a single SD-ERT measurement. Reddish iso-surfaces enclose the regions with a coverage greater than 0.2 and blue iso-surfaces enclose the regions with a coverage lower than -0.2. Electrodes for current injection are indicated by A and B. The voltage electrodes are located in Ktzi201 at a depth of 675 m and 685 m, respectively.

volume to the other. The next calibration step was the application of time variant shifts, which were performed in order to remove shifts at all times, and, therefore, also to correct for injection induced timing-delays below the reservoir. Finally, a cross-normalisation process was applied to the monitor data to correct for amplitude scaling differences between traces.

Because the reservoir top has a lower acoustic impedance than the caprock (e.g. Kazemeini et al., 2010a), the boundary between the two is characterised by a negative seismic reflection coefficient. Flooding with CO_2 causes a further decrease of the reflection coefficient due to a decrease in the reservoir impedance. On the basis of the 3D seismic data, Yang (2012) estimated a value of -0.1 for the pre-injection reflection coefficient and a value of -0.24 for the reflection coefficent at the time of the first repeat 3D seismic survey.

Figure 6.12 shows that the seismic and geoelectric signature generally correlate well. This is particularly interesting since the resistivity image of Figure 6.12a does not reveal any of the structural detail visible in the seismic image. In fact, the SD-ERT provides here a poor structural image which we attribute to (1) the sparseness of the applied SD-ERT acquisition geometry, (2) a generally lower capability to resolve layers by ERT compared with that of the seismic reflection method, and (3) the absence of notable resistivity contrasts for the investigated geology, as it consists mainly of low-resistive mudstones and brine-bearing sandstones.

Another interesting aspect that can be studied from Figure 6.12 is the different spatial resolutions provided by both methods. Yang (2012) report a dominant frequency of about 50 Hz and Kazemeini et al. (2010a) an average p-wave velocity of 2765 m/s for the brine saturated reservoir sandstone, corresponding to a tuning thickness of about 14 m. From a comparison with the Pulsed-Neutron-Gamma logs, Bergmann et al. (2012b) estimated the vertical resolution of the SD-ERT to be about

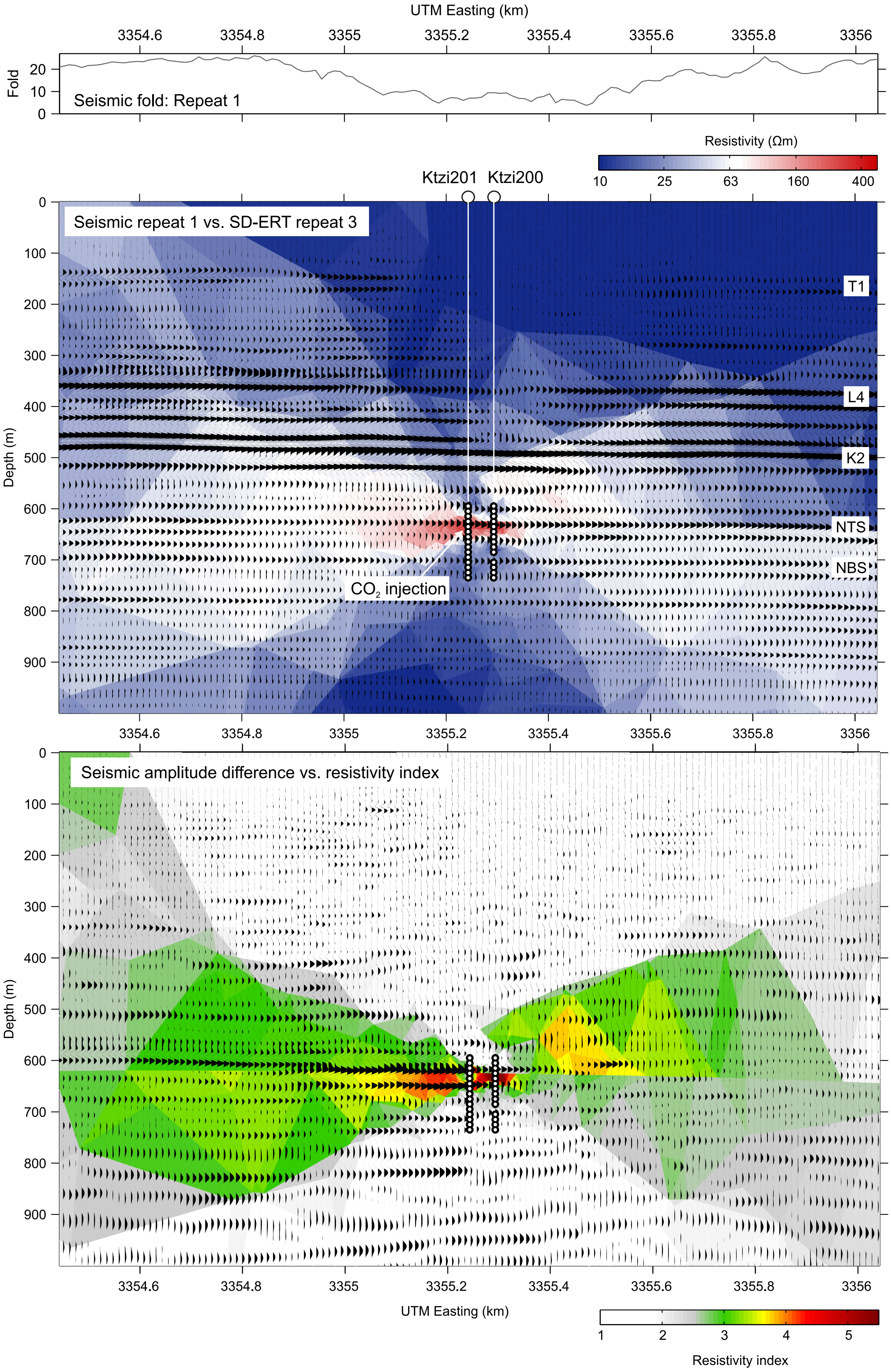

Figure 6.12: Composite illustration of ERT and depth-converted seismic for the East-West section crossing the Ktzi201 and Ktzi200. Top: Baseline models (T1, base Tertiary; K2, top Weser; NTS, near top Stuttgart; NBS, near base Stuttgart). Bottom: Depth-conversion with the smoothed velocity field that was used for conversion of the time-interpreted horizons into the depth domain. Due to an inability to perform seismic data acquisition at the injection site, the seismic fold in the centre of the sections is reduced. Seismic data after Ivanova et al. (2012).

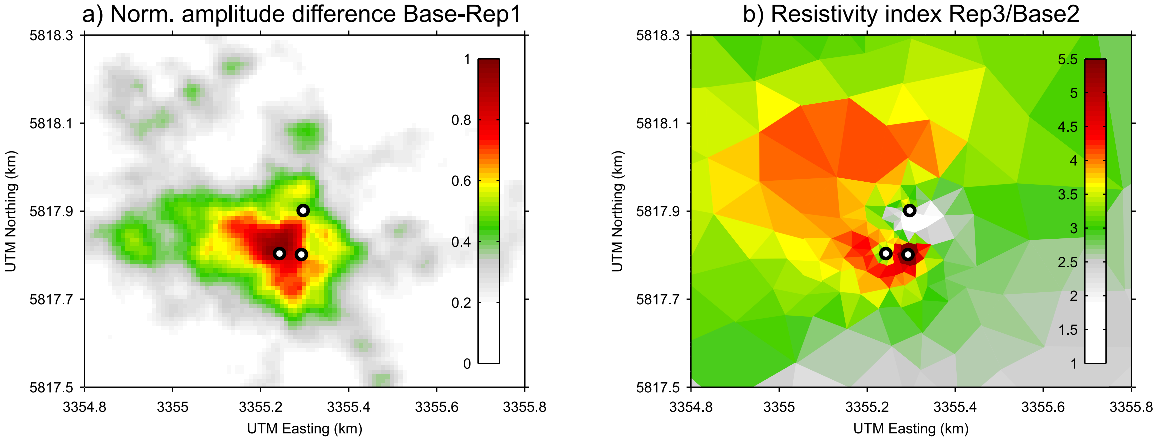

Figure 6.13: Comparison of time-lapse responses along the Near Top Stuttgart horizon. (a) Amplitude difference of the 3D seismic surveys (after Ivanova et al., 2012). (b) Resistivity index (ratio of repeat 3 and baseline 2) for the constrained inversion.

2-3 electrode spacings, i.e. about 20-30 m for the VERA system. They note that this resolution is just present near the VERA electrodes and decreases with increasing distance to the wells. In contrast to surface seismic methods, which provide a laterally uniform fold, the lateral SD-ERT coverage is limited. VSP also provides limited lateral coverage around the wells and may be considered as a seismic analogue to the SD-ERT method.

The lateral characteristics of the images can be investigated in more detail in Figure 6.13, which shows the seismic and geoelectric time-lapse signature along the Near Top Stuttgart horizon. The seismic amplitude anomaly has an extent of about 250 m in N-S direction and about 350 m in W-E direction with a tendency of higher amplitudes towards the West. In comparison, the resistivity signature shows a much larger extent with a gradual decrease away from the wells. This is due to the sensitivity patterns of the SD-ERT measurements for which an example is shown in Figure 6.11b. Since voltage acquisitions of our SD-ERT data are restricted to vertically arranged pairs of voltage electrodes of the VERA, the positive sensitivities that cover the reservoir show only a limited angle variation. Therefore, it seems impossible to map the extent of the entire CO_2 distribution on the basis of the SD-ERT data, due to limits in the radial penetration depth around the wells. However, the asymmetrical shape of the resistivity anomaly suggests preferential CO_2 migration towards the NW (Figure 6.13b), although a more northerly direction would be expected from the dip direction of the anticline. This is in fair agreement with the migration direction indicated by the time-lapse seismic signature (Figure 6.13a).

Both the reflection seismic and SD-ERT methods support the idea of a dominantly horizontal CO_2 migration, that is within the reservoir. However, the CO_2 distribution itself seems to be in large parts a sub-wavelength feature to both methods, which introduces some uncertainty in a quantitative analysis of the images CO_2. Therefore, future investigations are intended to test the suitability of the presented models for a more sophisticated joint interpretation. In this context we make reference to the approaches of Paasche et al. (2006) and Muñoz et al. (2010), but alternative schemes are conceivable as well. Since resistivity is rather insensitive towards pressure changes, the SD-ERT models might be helpful for discriminating pressure effects from saturation effects in the seismic data.

When considering CO_2 storage on an industrial scale, the planned storage depths are greater than that of the storage reservoir of the Ketzin project. The main practical challenge for SD-ERT at those depths will be the availability of permanent downhole electrode arrays, such as the VERA. At present, there are only a few reports on the installation and achievable operational lifetime of such electrode arrays (Kleef et al., 2001; Bryant et al., 2001; Schmidt-Hattenberger et al., 2011), whereby it is important to realize that brine-CO_2 prevailing conditions place special requirements for some array components. In this connection, further experience gained on the electrode arrays at the Cranfield SECARB project, USA, (Carrigan et al., 2009) and the planned CIUDEN Hontomin project, Spain, (Ledo et al., 2011) will be highly relevant since these projects deal with CO_2 storage at depths of about 3100 m and 1400 m, respectively. The ERT investigations at these sites could easily adopt the combined methodology presented here since the monitoring at both sites also includes time-lapse seismic investigations. In this respect, it is important that the presented approach is not restricted to surface-downhole measurements, but can be applied to arbitrary ERT geometries for which lithostructural information is available.

6.7 Conclusions

The primary objective of this study was twofold. First, we investigated potential benefits of incorporating seismic structural information into geoelectric imaging through a constrained inversion approach. For this, we assumed a structural similarity for seismic parameters and resistivity and used a local regularisation of the inverse ERT problem. We demonstrated this approach with a synthetic study on a model that included some of the elements featured at the Ketzin pilot site, Germany. Here, we found that the incorporation of prior structural information enabled a better delineated resistivity image, which could not be achieved with only the geoelectric data.

Secondly, we applied this approach for time-lapse imaging of the CO_2 that is stored in the Ketzin site, Germany. Based on the interpretation of the seismic data, the geometry of the reservoir-caprock boundary was mapped and inserted as structural a priori information in the constrained resistivity inversion. This real data example demonstrates that the approach is capable of combining both methods despite their different acquisition geometries and resulting illumination variations of the imaging target. In our case, the surface-downhole geoelectric measurements provide an image that is rather focused around the downhole electrodes, whereas the surface seismic surveys yield a laterally more continuous image. Since the structure is used as link, no cross-relation between seismic parameters and resistivity is assumed, whereby the approach preserves the method-related sensitivities to variable saturation of CO_2. This is an important point for investigations that are oriented towards quantification of CO_2 saturations, for which the respective petrophysical relations are unknown or only loosely connected. For an estimation of CO_2 saturations, the use of a constrained inversion is in advantage over joint inversions since no petrophysical cross-relations or shared gradients for coupling of the inverted images are used.

Respecting the differences in imaging characteristics of both methods, the presented models image the injected CO_2 consistently and show the potential for further joint interpretations. In summary, the presented structure-based combination of seismics and geoelectrics proves to be a valuable approach for an integrated geophysical monitoring of CO_2 storage site. Beyond this example, the presented approach seems to be promising for monitoring of other subsurface processes that trigger changes in elastic and electric parameters.

Acknowledgements

The authors thank all partners of the Ketzin project for their continued support and contributions. This work is part of the on-going research project CO_2MAN (www.co2ketzin.de) funded from the Federal Ministry of Education and Research within the GEOTECHNOLOGIEN Program (grant 03G0760A) and from industry partners. Peter Bergmann would like to acknowledge the GeoEn project (grant 03G0671A/B/C), a national scientific initiative in the field of energy research. Tim Labitzke is acknowledged for support in technical and logistical matters.

7

Summary & Conclusions

It is well known that seismic reflection and electrical resistivity tomography (ERT) image the subsurface differently. This is due to the different physical principles that are inherent in both methods. Electric current flow, for instance, is mainly sensitive to the presence and chemistry of pore-space fluids, whereas seismic wave propagation is mainly sensitive to the rock matrix properties. As another example, the coverage of the ERT image is high where electric current density is high, i.e. near the electrodes. On the other hand, the seismic fold usually increases with depth, and reaches maximum at some distance to the surface datum. Even though this behavior renders it difficult to combine both methods, such a combination is nonetheless desirable in order to gain a comprehensive subsurface image. In recognition of potential benefits that can be achieved through the combination of both methods, it was the overall aim of this dissertation (1) to combine the processings of seismic and geoelectric data, and (2) to apply this combination to the monitoring of the Ketzin site.

The investigations presented in this dissertation started with a review of existing approaches for the combination of both methods. Herein it was found that these approaches range from joint interpretations, which are not capable of to combine both methods already in the processing phase, to joint inversions, which are most often based on intrusive assumptions about petrophysical cross-relations. In this study, a constrained inversion workflow was selected in which structural information is the key link. This workflow was investigated through a numerical case study as well as a real data application, both of which were carried out in the framework of the Ketzin site monitoring. Overall, this dissertation first presented the seismic and geoelectric studies separately, in order continue with their combination in the final part. Accordingly, the studies presented in this dissertation did not strictly focus on the constrained inversion approach, but also reflected their embedding into the broader context of the geophysical monitoring activities at the Ketzin site.

7.1 Synthetic investigations

Chapter 3 presented a synthetic study in which forward modellings were performed as a support for the geoelectrical and seismic experiments carried out at the Ketzin site. Within these modellings, time-dependent CO_2 distributions were used as obtained from multiphase fluid-flow simulations. Additional constraints on the reservoir properties were deduced from well logs and the structural interpretation of the baseline 3D seismic data. In the first part of this study, resistivity data were modelled for three crosshole ERT configurations that are applied at the Ketzin site. These modellings were performed on the basis of fluid flow simulations for three different reservoir permeabilities. The modelled data showed that sufficient time-lapse responses occur with variable emphasis regarding the individual electrode configurations and reservoir permeabilities. Measurements from Dipole-Dipole cross (DDc) configurations, for example showed the most promising response for low-permeable reservoirs in which buoyancy driven upward migration of the CO_2 dominates. Highly permeable reservoirs, in which lateral CO_2 migration beneath the reservoir-caprock boundary dominates, would give preference to electrode configurations of Bipole-Bipole (BB) type. However, it is important to note that these findings were made with negligence of environmental noise, which plays an eminent role for the quality of a time-lapse image, as the subsequent real data processings showed.

In the second part of this study, a synthetic time-lapse seismic experiment has been carried out for a baseline and repeat model. Herein, the latter of both incorporated a local velocity and density perturbation due to a hypothetic CO_2 plume. The associated time-lapse signature observed in the difference stack indicated that the lateral extent of the CO_2 plume may be accurately detectable. The thickness of the CO_2 plume was only expressed as a change in the waveform coda. Given the used frequencies, this waveform change was found to be below the vertical resolution limit. It was however still within the detection limit if we assume the absence of significant environmental noise. By means of this study it was realized that fluid-flow simulations can yield valuable constraints for synthetic monitoring studies. However, if we take into consideration the real monitoring results that became available later, the presented synthetic results seem to be oversimplified and too optimistic. Due a large number of uncertainties in the model setup and the abundance of effects deteriorating the response in the real data, time-lapse modelling may be one of the most difficult tasks undertaken in this PhD project. Since there is a general demand for reliable feasibility prediction of time-lapse geophysical projects prior to field activities, this issue deserves additional attention. In conclusion, it seems sensible to incorporate realistic noise and establish statistical frameworks in order to deal with the given sets of uncertain input model parameters.

7.2 Seismic investigations

Chapter 4 presented the processing of the 2D seismic data that have been acquired within the baseline (2005) survey and first repeat (2009) survey at the Ketzin site. These surveys aimed to image the injected CO_2 and to allow for comparison with other monitoring methods, in particular with the 3D seismic surveys. A time-lapse interpretation of the processed 2D data showed that no CO_2 related time-lapse signature is observable where the 2D lines allowed for imaging of the reservoir. This finding was further supported by the time-lapse results of the 3D surveys which imaged a reflectivity change that is centred at the injection well but does not reach the sections monitored by the 2D lines. Additionally, an AVO analysis was conducted which gave some indication for an injection-induced pressure change in the reservoir but confirmed that the CO_2 had not migrated as far as the 2D lines. In the following course of the thesis, the 3D seismic results were therefore used as the main basis for further time-lapse interpretations. A comparison of the 2D and 3D results showed that both image the subsurface with local differences due to the different acquisition geometries and source types used.

One of the major difficulties encountered during the processing of the 2D seismic data were the changes in near-surface velocities that resulted from different weathering conditions during the survey periods. These velocity changes deteriorated the time-lapse image and could only imperfectly be resolved by refraction static corrections. In order to improve the pre-stack cross-alignment of both time-lapse data sets, a surface-consistent static correction was proposed and tested. This approach proved to display less time-lapse noise in the difference stacks and to be less labour-consuming, since error-prone first break picking is only necessary once for the baseline data. Moreover, the decomposed source and receiver solutions of the pre-stack static corrections allowed for an interpretation of changes in the near-surface velocities. The long wavelength component of the solutions indicated, that near-surface velocities at the repeat survey were larger than for the baseline baseline survey, which is consistent with water level observations at the surface.

Although not reported in the thesis it is important to note that this approach was, due to the positive experiences with the 2D data, subsequently extended to the 3D data (Bergmann et al., 2012a). There it consistently yielded a reduction of the noise level in the difference stack. Interestingly, the decomposed 3D solution further shows a remarkable correlation with the pattern in the first break differences and with the difference in cumulative precipitation maps reported by Kashubin et al. (2011).

7.3 Geoelectric investigations

Chapter 5 presented the acquisition, inversion, and interpretation of the surface-downhole electrical resistivity tomography (SD-ERT) experiments that were carried out at the Ketzin site. One baseline survey and three repeat surveys, which were performed during the first year of site operation, have been analyzed. SD-ERT acquisitions were performed with current injections at the surface and voltage acquisition using surface electrodes as well as permanent downhole electrodes. Originally adapted from near-surface hydrogeophysical investigations, these experiments represent so far a unique approach for CO_2 storage monitoring. Several accompanying investigations involved weekly measured resistance checks, the degradation of the subsurface installation, and the impact of the irregular completions of the Ketzin wells. The last point showed that it is highly recommendable to design the completion of wells, in which permanent electrode arrays are installed, as uniform as possible. In our case, the second observation well of the Ketzin wells comprised an uncemented interval, which produced a spurious time-lapse signal in the SD-ERT data when swept with CO_2. Although clearly identifiable, this signal led to an unfortunate reduction of the monitored region.

Besides this effect it was possible to image a long-term resistivity increase that is attributed to the injected CO_2. An inversion and interpretation of the resistivity data indicated a preferential CO_2 migration that follows the structural trend of the caprock, i.e. in northerly direction. However, the resistivity image is characterized by the sensitivity pattern of the SD-ERT acquisitions, which results in a gradual decrease in sensitivity with increasing radial distance to the wells. An estimation of CO_2 saturations on the basis of the resistivity changes was therefore only permitted in a limited region around the wells. Nevertheless, these estimates showed CO_2 saturations of up to 70% near the injector, which matched the range of CO_2 saturations independently obtained from pulsed

Neutron-Gamma logging.

In the context of a future improvement of the SD-ERT technique it appears promising to investigate additional acquisition setups in order to enhance the S/N of the acquired data and to enlarge the monitored region. With respect to the rather sparse SD-ERT acquisition geometry at the Ketzin site, a perspective improvement seems achievable by the deployment of additional current dipoles, increased current dipole spacings, and surface-downhole current injections.

7.4 Combined seismic and geoelectric investigations

Chapter 6 presented the combination of both methods by means of structural constraints that are incorporated into the ERT inversion. Through an adaptive reduction of the regularization, such constraints allow the inverted resistivity model to render contrasts at locations where prominent lithostructural boundaries are present. The combination proposed in this dissertation used seismic structure information in order to enhance the structuredness of the ERT image, and hereby tackled one of the traditional weaknesses of the ERT method. Consequently, a workflow was established in which (1) the constraint geometry is deduced from a structural interpretation of the seismic data, (2) the petrophysical relevance of the constraint is examined by well logs, and (3) the constraint is used for a local regularization of the inverse ERT problem.

In a first step, this approach was tested by a numerical case study. This study was based on a model which captured the main geometrical features of the SD-ERT measurements presented in Chapter 5 as well as a CO_2 distribution that was adapted from the fluid-flow simulations presented in Chapter 3. Similar to the flow boundary used in the fluid-flow simulations, the ERT inversions implemented the constraint along the reservoir-caprock-boundary. Forward modelled resistivity data were inverted for variable regularizations and variable constraint strengths. From these it was found that an increase in constraint strength leads to a decrease in data misfit. The reason for this is the buildup of a resistivity contrast which would otherwise be suppressed by the rather smoothness-seeking regularization of a regular inversion.

Based on these outcomes, the workflow was extended to the real data, i.e. the combination of the 3D time-lapse seismic and SD-ERT data acquired at the Ketzin site. Special attention was paid herein to evaluate the petrophysical relevance of the reservoir-caprock-boundary. Although it represents a significant lithological change from brine-bearing sandstones in the reservoir to clayey mudstones in the caprock, well log analyses and surface geophysical data indicated that the associated changes in elastic parameters and resistivity are relatively low. Nevertheless, the reservoir-caprock-boundary is likewise representing a striking change in porosity and permeability, which entails a constraint for the fluid migration and motivated its incorporation into the ERT inversion. Generally, the models obtained from the constrained inversions confirmed the interpretations that were made from the regular inversions with regard to the CO_2 migration. However, a detailed comparison showed that these interpretations could have been made from the constrained inversions in a clearer and more straightforward sense.

The Ketzin data example yielded the important finding that it was possible to join both methods despite their unequal degree of reservoir illumination. For instance, unlike to the SD-ERT, the seismic time-lapse model allowed for an interpretation of the lateral extent of the CO_2 plume.

Respecting such differences in imaging characteristics, an interpretation of the models showed that (1) the time-lapse signatures of both methods collocate and that (2) they support the idea of a dominantly subhorizontal CO_2 migration.

7.5 Recommendations

The presented constrained inversion workflow was found to be a very valuable approach for the combination of seismic and geoelectric data. It is based on a structural similarity of seismic and geoelectric parameters, i.e. a change in elastic impedance is expected to occur together with a change in resistivity and vice versa. Therefore, this approach is fortunately devoid of any specific assumption about a petrophysical cross-relation, whereby it preserves the method-related sensitivities to variable saturation of CO_2. Practical demonstration for the Ketzin datasets showed that the workflow has a potential for an integrated geophysical monitoring of CO_2 storages. Beyond this, it is significant also for the monitoring of other subsurface processes, which trigger changes in elastic parameters and resistivity.

Besides the above given perspectives, three additional aspects are relevant in order to follow up the presented investigations. First, for a further development of the workflow it seems worthwhile to incorporate a locally variable constraint strength, which might be related to the reflection strength in the seismic stack. For example, a cell interface derived from a segment of strong seismic reflectivity might be assigned to a correspondingly high constraint strength. This would make it possible to investigate the introduction of seismic attribute-based information, rather than the sheer structural information, in the ERT inversion.

Secondly, the time-lapse inversion strategy followed in this thesis was based on the propagation of the baseline resistivity model as starting model for the subsequent time-steps. Although this is a rather simple and established strategy, there are a number of alternative strategies for the time-lapse ERT inversion. These strategies range from the inversion of resistivity ratios to simultaneous schemes in which closeness constraints are applied to the individual time-steps. Although all of them are associated to certain advantages and disadvantages (for a discussion see Hayley et al., 2011), they should be considered for a further processing of the Ketzin SD-ERT data.

Thirdly, any geophysical monitoring aims to deliver information that calibrates the geological model used in reservoir simulations. Important constraints for such a model are the presence of hydraulic barriers, preferential flow-paths, and the actual distribution of the CO_2. Based on an updated (or calibrated) reservoir simulation, one can perform geophysical modellings similar to those presented in Chapter 2. A cross-validation of synthetic and real geophysical data can then be used to test the plausibility of the updated geological model. The geophysical models established in this dissertation can serve as real data for such a validation, particularly so because complementary geophysical methods have already been joined during the processing stage.

Bibliography

Aggelopoulos, C., Klepetsanis, P., Theodoropoulou, M., Pomoni, K., and Tsakiroglou, C.: Large-scale effects on resistivity index of porous media, Journal of contaminant hydrology, 77, 299–323, 2005.

Aki, K. and Richards, P.: Quantitative Seismology, University Science Books, 1980.

al Hagrey, S.: 2D Optimisation of electrode arrays for borehole surveys, in: Near-Surface 15th European Meeting of the EAGE, Dublin, Ireland, p. 5, 2009.

al Hagrey, S.: 2D Optimized Electrode Arrays for Borehole Resistivity Tomography and CO_2 Sequestration Modelling, Pure and Applied Geophysics, pp. 1–10, 2011a.

al Hagrey, S.: CO_2 plume modeling in deep saline reservoirs by 2D ERT in boreholes, The Leading Edge, 30, 24–33, 2011b.

Anderson, B., Bryant, I., Lülig, M., Spies, B., and Helbig, K.: Oilfield anisotropy: Its origins and electrical characteristics, Oilfield Review, 6, 48–56, 1994.

Archie, G.: The Electrical Resistivity Log as an Aid in Determining Some Reservoir Characteristics, Transactions of the American Institute of Mining, Metallurgical and Petroleum Engineers, 146, 54, 1942.

Arts, R., Eiken, O., Chadwick, A., Zweigel, P., Van Der Meer, L., and Zinszner, B.: Monitoring of CO_2 injected at Sleipner using time-lapse seismic data, Energy, 29, 1383–1392, 2004.

Arts, R., Meekes, J., Brouwer, J., van der Werf, M., Noorlandt, R., Paap, B., Visser, W., Vandeweijer, V., Lüth, S., and Giese, R.: Results of a monitoring pilot with a permanent buried multicomponent seismic array at Ketzin, Energy Procedia, 4, 3588–3595, 2011.

Aster, R., Borchers, B., and Thurber, C.: Parameter estimation and inverse problems, Burlington, Massachusetts; Elsevier Academic Press, 2005.

Asveth, P.: in: Petroleum Geology, edited by Bjørlykke, K., chap. 18 - Exploration Rock Physics, Springer Verlag, 2009.

Bachrach, R., Dvorkin, J., and Nur, A.: High-resolution shallow-seismic experiments in sand, Part II: Velocities in shallow unconsolidated sand, Geophysics, 63, 1234–1240, 1998.

Backus, G.: Comparing hard and soft prior bounds in geophysical inverse problems, Geophysical Journal, 94, 249–261, 1988.

Bakke, N. and Ursin, B.: Thin-bed AVO effects, Geophysical Prospecting, 46, 571–587, 1998.

Barbier, M., Bondon, P., Mellinger, R., and Viallix, J.: Mini-SOSIE for land seismology, Geophysical Prospecting, 24, 518–527, 1976.

Bergmann, P., Giese, R., Götz, J., Ivanova, A., Juhlin, C., Juhojuntti, N., Kashubin, A., Lüth, S., Yang, C., and Zhang, F.: Preliminary results from a repeat 3D seismic survey at the CO_2SINK injection site, Ketzin, Germany, 72nd Annual EAGE Conference, Barcelona, p. 4, 2010a.

Bergmann, P., Lengler, U., Schmidt-Hattenberger, C., Giese, R., and Norden, B.: Modelling the geoelectric and seismic reservoir response caused by carbon dioxide injection based on multiphase flow simulation: Results from the CO_2SINK project, Chemie der Erde – Geochemistry, 70, supplement 3, 173–183, 2010b.

Bergmann, P., Yang, C., Lüth, S., Juhlin, C., and Cosma, C.: Time-lapse processing of 2D seismic profiles with testing of static correction methods at the CO_2 injection site Ketzin (Germany), Journal of Applied Geophysics, 75, 124–139, 2011.

Bergmann, P., Kashubin, A., Ivandic, M., Juhlin, C., Lüth, S., Ivanova, A., Lundberg, E., and Zhang, F.: Cross-correlation time-lapse static corrections vs. refraction static corrections on 4D land seismic CO_2 monitoring at Ketzin, Germany, 82st SEG Annual International Meeting, p. 4, 2012a.

Bergmann, P., Schmidt-Hattenberger, C., Kiessling, D., Rücker, C., Labitzke, T., Henninges, J., Baumann, G., and Schütt, H.: Surface-downhole electrical resistivity tomography applied to monitoring of CO_2 storage at Ketzin, Germany, Geophysics, 77, B253–B267, 2012b.

Berryman, J. and Milton, G.: Exact results for generalized Gassmann's equations in composite porous media with two constituents, Geophysics, 56, 1950–1960, 1991.

Beutler, G. and Nitsch, E.: in: Paläographischer Überblick, Stratigraphie von Deutschland IV, edited by Beutler, G., chap. Keuper, Cour. Forsch.-Inst. Senckenberg 253, 2005.

Beutler, G., Hauschke, N., and Nitsch, E.: Faziesentwicklung des Keupers im Germanischen Becken, in: Trias, eine ganz andere Welt, edited by Hauschke, N. and Wilde, V., Verlag Dr. Friedrich Pfeil, München, 1999.

Biondi, B.: Three dimensional seismic imaging, 14, Society of Exploration Geophysicists, 2006.

Bortfeld, R.: Approximations to the reflection and transmission coefficients of plane longitudinal and transverse waves, Geophysical Prospecting, 9, 485–502, 1961.

Brunner, I., Friedel, S., Jacobs, F., and Danckwardt, E.: Investigation of a tertiary maar structure using three-dimensional resistivity imaging, Geophysical Journal International, 136, 771–780, 1999.

Bryant, I., Chen, M., Raghuraman, B., Raw, I., Delhomme, J., Chouzenoux, C., Pohl, D., Manin, Y., Rioufol, E., Oddie, G., Swager, D., and Smith, J.: Utility and reliability of cemented resistivity arrays in monitoring waterflood of the Mansfield Sandstone, Indiana, USA, in: SPE Annual Technical Conference and Exhibition, New Orleans, Louisiana, DOI:10.2118/71710-MS, 2001.

Butler, D. and Knight, R.: Electrical conductivity of steam-flooded, clay-bearing geologic materials, Geophysics, 63, 1137–1149, 1998.

Carcione, J., Ursin, B., and Nordskag, J.: Cross-property relations between electrical conductivity and the seismic velocity of rocks, Geophysics, 72, E193–E204, 2007.

Carrigan, C., Ramirez, A., Newmark, R., Aines, R., and Friedmann, S.: Application of ERT for tracking CO_2 plume growth and movement at the SECARB Cranfield site, in: 8th Annual Conference on Carbon Capture & Sequestration, Pittsburgh, PA, United States, 2009.

Cassiani, G., Bruno, V., Villa, A., Fusi, N., and Binley, A.: A saline trace test monitored via time-lapse surface electrical resistivity tomography, Journal of Applied Geophysics, 59, 244–259, 2006.

Castagna, J.: Offset-dependent reflectivity: Theory and practice of AVO analysis, 8, SEG, 1993.

Chadwick, A., Arts, R., Bernstone, C., May, F., Thibeau, S., and Zweigel, P.: Best practice for the storage of CO_2 in saline aquifers - observations and guidelines from the SACS and CO_2STORE projects, URL `http://nora.nerc.ac.uk/2959/`, 2008.

Chadwick, R., Arts, R., and Eiken, O.: 4D seismic quantification of a growing CO_2 plume at Sleipner, North Sea, Geological Society, London, Petroleum Geology Conference series, 6, 1385–1399, 2005.

Christensen, N., Sherlock, D., and Dodds, K.: Monitoring CO_2 injection with cross-hole electrical resistivity tomography, Exploration Geophysics, 37, 44–49, 2006.

Christiansen, A., Auken, E., Foged, N., and Sørensen, K.: Mutually and laterally constrained inversion of CVES and TEM data: A case study, Near Surface Geophysics, 5, 115–124, 2007.

Clément, R., Descloitres, M., Günther, T., Oxarango, L., Morra, C., Laurent, J., and Gourc, J.: Improvement of electrical resistivity tomography for leachate injection monitoring, Waste management, 30, 452–464, 2010.

Coggon, J.: Electromagnetic and electrical modeling by the finite–element method, Geophysics, 36, 132, 1971.

Coscia, I., Greenhalgh, S., Linde, N., Doetsch, J., Marescot, L., Günther, T., Vogt, T., and Green, A.: 3D crosshole ERT for aquifer characterization and monitoring of infiltrating river water, Geophysics, 76, G49–G59, 2011.

Cosma, C. and Enescu, N.: Characterization of fractured rock in the vicinity of tunnels by the swept impact seismic technique, International Journal of Rock Mechanics and Mining Sciences, 38, 815–821, 2001.

Cox, M.: Static corrections for seismic reflection surveys, SEG, Tulsa, OK, 1999.

Daily, W., Ramirez, A., Binley, A., and LeBrecque, D.: Electrical resistance tomography, The Leading Edge, 23, 438–442, 2004.

de Witte, L.: A study of electric log interpretation methods in shaly formations, Transactions of the AIME, 204, 103–110, 1955.

Deregowski, S.: What is DMO, First Break, 4, 7–24, 1986.

Doetsch, J., Coscia, I., Greenhalgh, S., Linde, N., Green, A., and Günther, T.: The borehole-fluid effect in electrical resistivity imaging, Geophysics, 75, F107, 2010.

Doetsch, J., Linde, N., Pessognelli, M., Green, A., and Günther, T.: Constraining 3-D electrical resistance tomography with GPR reflection data for improved aquifer characterization, Journal of Applied Geophysics, 78, 68–76, 2012.

Domes, F.: The influence of overburden on quantitive time-lapse seismic interpretation, Ph.D. thesis, Heriot-Watt University, Edinburgh, 2010.

Eberhart-Phillips, D., Han, D., and Zoback, M.: Empirical relationships among seismic velocity, effective pressure, porosity, and clay content in sandstone, Geophysics, 54, 82–89, 1989.

EC: European Council – Communication on community strategy on climate change, Council conclusions, p. Document number 8518/96, URL `http://ue.eu.int/ueDocs/cms_Data/docs/pressData/en/envir/011a0006.htm`, 1996.

EC: European Council – Presidency conclusions, URL `http://www.consilium.europa.eu/uedocs/cms_data/docs/pressdata/en/ec/84335.pdf`, 2005.

EC: European Comission – Energy roadmap 2050, URL `http://ec.europa.eu/energy/publications/doc/2012_energy_roadmap_2050_en.pdf`, 2009a.

EC: European Comission – Directive 2009/31/EC on the geological storage of carbon dioxide in selected European jurisdictions – the United Kingdom, Germany, Poland, Romania, Spain and Norway, 2009b.

EEA: European Environment Agency (EEA), URL `http://ec.europa.eu/energy/publications/doc/statistics/ext_CO2_emissions_by_sector.pdf;http://ec.europa.eu/energy/publications/doc/statistics/part_4_energy_pocket_book_2010.pdf`, 2009.

Ellis, R. and Oldenburg, D.: Applied geophysical inversion, Geophysical Journal International, 116, 5–11, 1994.

Engelmann, M., Lippmann, P., Zemke, J., and Zenner, M.: Eignungsnachweis für die Speicherung geringer Mengen CO_2 am Standort Ketzin CO_2SINK, Untergrundspeicher- und Geotechnologie-Systeme GmbH, 2008.

Favetto, A., Pomposiello, C., Booker, J., and Rossello, E.: Magnetotelluric inversion constrained by seismic data in the Tucumán Basin (Andean Foothills, 27° S, NW Argentina), Journal of Geophysical Research, 112, 12, 2007.

Fleury, M. and Deschamps, H.: Electrical conductivity and viscosity of aqueous NaCl solutions with dissolved CO_2, Journal of Chemical & Engineering Data, 53, 2505–2509, 2008.

Fleury, M., Gautier, S., Gland, N., Boulin, P., Norden, B., and Schmidt-Hattenberger, C.: Petrophysical measurements for CO_2 storage: Application to the Ketzin site., in: International Symposium of the Society of Core Analysts, Halifax, Nova Scotia, Canada, 4–7 October 2010, SCA2010-06, 12 p., 2010.

Förster, A., Norden, B., Zinck-Jørgensen, K., Frykman, P., Kulenkampff, J., Spangenberg, E., Erzinger, J., Zimmer, M., Kopp, J., Borm, G., Juhlin, C., Cosma, C., and Suzanne, H.: Baseline characterization of the CO_2SINK geological storage site at Ketzin, Germany, Environmental Geosciences, 13, 145–161, 2006.

Förster, A., Springer, N., Beutler, G., Luckert, J., Norden, B., and Lindgren, H.: The mudstone-dominated caprock system of the CO_2-storage site at Ketzin, Germany, in: Proceedings of the 2007 AAPG Annual Convention and Exhibition, Long Beach, USA, 2007.

Förster, A., Giese, R., Juhlin, C., Norden, B., Springer, N., and group, C.: The geology of the CO_2SINK site: From regional scale to laboratory scale, Energy Procedia, 1, 2911–2918, 2009.

Förster, A., Schöner, R., Förster, H., Norden, B., Blaschke, A., Luckert, J., Beutler, G., Gaupp, R., and Rhede, D.: Reservoir characterization of a CO_2 storage aquifer: The upper triassic Stuttgart Formation in the Northeast German Basin, Marine and Petroleum Geology, 27, 2156–2172, 2010.

Foster, D., Keys, R., and Lane, F.: Interpretation of AVO anomalies, Geophysics, 75, 75A3–75A13, 2010.

Friedel, S.: Resolution, stability and efficiency of resistivity tomography estimated from a generalized inverse approach, Geophysical Journal International, 153, 305–316, 2003.

Frohlich, R. and Parke, C.: The electrical resistivity of the vadose zone-field survey, Ground water, 27, 524–530, 1989.

Gallardo, L. and Meju, M.: Joint two-dimensional DC resistivity and seismic travel time inversion with cross-gradients constraints, Journal of Geophysical Research, 109, B03 311, 2004.

Gallardo, L. and Meju, M.: Joint two-dimensional cross-gradient imaging of magnetotelluric and seismic traveltime data for structural and lithological classification, Geophysical Journal International, 169, 1261–1272, 2007.

Gassmann, F.: Über die Elastizität poröser Medien, Vierteljahresschrift der Naturforschenden Gesellschaft Zürich, 96, 1–24, 1951.

Gelchinsky, B.: The common reflecting element (CRE) method (non-uniform asymmetric multifold system), Exploration Geophysics, 19, 71–75, 1988.

Gelchinsky, B., Berkovitch, A., and Keydar, S.: Multifocusing homeomorphic imaging: Part 2. Multifold data set and multifocusing, Journal of Applied Geophysics, 42, 243–260, 1999.

Gholami, A. and Siahkoohi, H.: Simultaneous constraining of model and data smoothness for regularization of geophysical inverse problems, Geophysical Journal International, 176, 151–163, 2009.

Giese, R., Henninges, J., Lüth, S., Morozova, D., Schmidt-Hattenberger, C., Würdemann, H., Zimmer, M., Cosma, C., and Juhlin, C.: Monitoring at the CO_2SINK site: A concept integrating geophysics, geochemistry and microbiology, Energy Procedia, 1, 2251–2259, 2009.

Girard, J., Coppo, N., Rohmer, J., Bourgeois, B., Naudet, V., and Schmidt-Hattenberger, C.: Time-lapse CSEM monitoring of the Ketzin (Germany) CO_2 injection using 2 MAM configuration, Energy Procedia, 4, 3322–3329, 2011.

Gochioco, L.: Tuning effect and interference reflections from thin beds and coal seams, Geophysics, 56, 1288–1295, 1991.

Gosselet, A. and Singh, S.: 2D Full wave form inversion in time-lapse mode: CO_2 quantification at Sleipner, 70th EAGE Conference and Exhibition, p. 5, 2008.

Götz, J., Giese, R., Lüth, S., Schmidt-Hattenberger, C., Juhlin, C., and Cosma, C.: Borehole seismic monitoring of CO_2 storage within a saline aquifer at Ketzin, Germany, EAGE Borehole Geophysics Workshop, 16-19 January 2011, Istanbul, Turkey, EarthDoc-47183, p. 5, 2011.

Greenpeace: False Hope: Why carbon capture and storage won't save the climate, Greenpeace International, URL `http://www.greenpeace.org/usa/Global/usa/report/2008/5/false-hope-why-carbon-capture.pdf`, 2008.

Guéguen, Y. and Palciauskas, V.: Introduction to the physics of rocks, Princeton University Press, New Jersey, 1994.

Günther, T. and Rücker, C.: A general approach for introducing information into inversion and examples from DC resistivity inversion, EAGE Near Surface Geophysics Workshop. 4–6 September 2006, Helsinki, Finland, p. 5, 2006.

Günther, T., Rücker, C., and Spitzer, K.: Three-dimensional modelling and inversion of DC resistivity data incorporating topography II: Inversion, Geophysical Journal International, 166, 506–517, 2006.

Günther, T., Schaumann, G., Musmann, P., and Grinat, M.: Imaging of a fault zone by a large-scale DC resistivity experiment and seismic structural information, EAGE Near Surface, Leicester, UK, 12-14 September 2011, p. 5, 2011.

Guy, E., Radzevicius, S., and Conroy, J.: Computer programs for application of equations describing elastic and electromagnetic wave scattering from planar interfaces, Computers & Geosciences, 29, 569–575, 2003.

Haber, E. and Oldenburg, D.: Joint inversion: A structural approach, Inverse Problems, 13, 63–77, 1997.

Han, M., Youssef, S., Rosenberg, E., Fleury, M., and Levitz, P.: Deviation from Archie's law in partially saturated porous media: Wetting film versus disconnectedness of the conducting phase, Physical Review E, 79, 031 127, 2009.

Han, T., Best, A., Sothcott, J., and MacGregor, L.: Joint elastic–electrical properties of reservoir sandstones and their relationships with petrophysical parameters, Geophysical Prospecting, 59, 518–535, 2011.

Hansen, P. and O'Leary, D.: The use of the L-curve in the regularization of discrete ill-posed problems, SIAM Journal on Scientific Computing, 14, 1487, 1993.

Haszeldine, R.: Carbon capture and storage: How green can black be?, Science, 325, 1647–1652, 2009.

Hayley, K., Pidlisecky, A., and Bentley, L.: Simultaneous time-lapse electrical resistivity inversion, Journal of Applied Geophysics, 75, 401–411, 2011.

Heincke, B., Günther, T., Dalsegg, E., Rønning, J., Ganerød, G., and Elvebakk, H.: Combined three-dimensional electric and seismic tomography study on the Åknes rockslide in Western Norway, Journal of Applied Geophysics, 70, 292–306, 2010.

Hill, R.: Elastic properties of reinforced solids: Some theoretical principles, Journal of the Mechanics and Physics of Solids, 11, 357–372, 1963.

Hoversten, G. and Gasperikova, E.: Non-seismic geophysical approaches to monitoring, in: Carbon dioxide capture for storage in deep geologic formations – Results from the CO_2 capture project, Volume 2: Geologic storage of carbon dioxide with monitoring and verification, edited by Benson, S., pp. 1071–1112, Elsevier Science, 2005.

IEA: International Energy Agency - Energy technology perspectives 2010, p. 20, 2010a.

IEA: International Energy Agency - World energy outlook 2010, p. 738, 2010b.

IPCC: Intergovernmental Panel on Climate Change – Special report on carbon dioxide capture and storage, IPCC Cambridge, England, 2005.

IPCC: Intergovernmental Panel on Climate Change – Climate Change 2007: Synthesis Report, p. 104, IPCC, Geneva, Switzerland, 2007.

Ivandic, M., Yang, C., Lüth, S., Cosma, C., and Juhlin, C.: Time-lapse analysis of sparse 3D seismic data from the CO_2 storage pilot site at Ketzin, Germany, Journal of Applied Geophysics, 84, 14–28, 2012.

Ivanova, A., Kashubin, A., Juhojuntti, N., Kummerow, J., Henninges, J., Juhlin, C., Lüth, S., and Ivandic, M.: Monitoring and volumetric estimation of injected CO_2 using 4D seismic, petrophysical data, core measurements and well logging: A case study at Ketzin, Germany, Geophysical Prospecting, 60, 957–973, 2012.

Ivanova, A., Kashubin, A., Juhonjuntti, N., Kummerow, J., Henninges, J., Juhlin, C., and Lüth, S.: Time-Lapse analysis of 3D seismic data from the CO_2 injection site, Ketzin, Germany (published as Ivanova et al., 2012), Geophysical Prospecting, submitted.

Jackson, D.: Interpretation of inaccurate, insufficient and inconsistent data, Geophysical Journal of the Royal Astronomical Society, 28, 97–109, 1972.

Jäger, R., Mann, J., Höcht, G., and Hubral, P.: Common-reflection-surface stack: Image and attributes, Geophysics, 66, 97–109, 2001.

Jegen, M., Hobbs, R., Tarits, P., and Chave, A.: Joint inversion of marine magnetotelluric and gravity data incorporating seismic constraints: Preliminary results of sub-basalt imaging off the Faroe Shelf, Earth and Planetary Science Letters, 282, 47–55, 2009.

Jones, J.: Scale-dependent resistivity measurements of Oracle granite, Geophysical Research Letters, 22, 1453–1456, 1995.

Juhlin, C. and Young, R.: Implications of thin layers for amplitude variation with offset (AVO) studies, Geophysics, 58, 1200, 1993.

Juhlin, C., Giese, R., Zinck-Jørgensen, K., Cosma, C., Kazemeini, H., Juhojuntti, N., Lüth, S., Norden, B., and Förster, A.: 3D baseline seismics at Ketzin, Germany: The CO_2SINK project, Geophysics, 72, B121–B132, 2007.

Kashubin, A., Juhlin, C., Malehmir, A., Lüth, S., Ivanova, A., and Juhojuntti, N.: A footprint of rainfall on land seismic data repeatability at the CO_2 storage pilot site, Ketzin, Germany, 81st SEG Annual International Meeting, p. 4, 2011.

Kazemeini, S., Juhlin, C., Zinck-Jørgensen, K., and Norden, B.: Application of the continuous wavelet transform on seismic data for mapping of channel deposits and gas detection at the CO_2SINK site, Ketzin, Germany, Geophysical Prospecting, 57, 111–123, 2009.

Kazemeini, S., Juhlin, C., and Fomel, S.: Monitoring CO_2 response on surface seismic data; a rock physics and seismic modeling feasibility study at the CO_2 sequestration site, Ketzin, Germany, Journal of Applied Geophysics, 71, 109–124, 2010a.

Kazemeini, S., Yang, C., Juhlin, C., Fomel, S., and Cosma, C.: Enhancing seismic data resolution using the prestack blueing technique: An example from the Ketzin injection site, Germany, Geophysics, 75, V101–V110, 2010b.

Kearey, P., Brooks, M., and Hill, I.: An introduction to geophysical exploration, Wiley-Blackwell, 2002.

Kelly, K., Ward, R., Treitel, S., and Alford, R.: Synthetic seismograms: A finite-difference approach, Geophysics, 41, 2–27, 1976.

Kemna, A., Kulessa, B., and Vereecken, H.: Imaging and characterisation of subsurface solute transport using electrical resistivity tomography (ERT) and equivalent transport models, Journal of Hydrology, 267, 125–146, 2002.

Kiessling, D., Schmidt-Hattenberger, C., Schuett, H., Schilling, F., Krüger, K., Schöbel, B., Danckwardt, E., and Kummerow, J.: Geoelectrical methods for monitoring geological CO_2 storage: First results from cross-hole and surface-downhole measurements from the CO_2SINK test site at Ketzin (Germany), International Journal of Greenhouse Gas Control, 4, 816–826, 2010.

Kim, H., Song, Y., and Lee, K.: Inequality constraint in least-squares inversion of geophysical data, Earth Planets and Space, 51, 255–260, 1999.

Kirsch, R.: in: Groundwater geophysics, edited by Kirsch, R., chap. 1 – Petrophysical properties of permeable and low-permeable rocks, Springer, 2006.

Kleef, R., Hakvoort, R., Bhushan, V., Al-Khodhori, S., Boom, W., Bruin, C., Babour, K., Chouzenoux, C., Delhomme, J., Manin, Y., Pohl, D., Rioufol, E., Charara, M., and Harb, R.: Water flood monitoring in an Oman carbonate reservoir using a downhole permanent electrode array, in: SPE Middle East Oil Show, 17-20 March 2001, Bahrain, DOI: 10.2118/68078-MS, 2001.

Kling, C.: Structural interpretation and application of spectral decomposition for facies analysis of three-dimensional reflection seismic data at the Ketzin CO_2 storage site, Master's thesis, Technical University Berlin, Institute of Applied Geosciences, FG Exploration Geology, 2011.

Koglin, I., Mann, J., and Heilmann, Z.: CRS-stack-based residual static correction, Geophysical prospecting, 54, 697–707, 2006.

Kragh, E. and Christie, P.: Seismic repeatability, normalized RMS, and predictability, The Leading Edge, 21, 640–647, 2002.

Kummerow, J. and Spangenberg, E.: Experimental evaluation of the impact of the interactions of CO_2-SO_2, brine, and reservoir rock on petrophysical properties: A case study from the Ketzin test site, Germany, Geochemistry Geophysics Geosystems, 12, Q05 010, 2011.

Labitzke, T., Bergmann, P., Kiessling, D., and Schmidt-Hattenberger, C.: 3D Surface-downhole electrical resistivity tomography data sets of the Ketzin CO_2 storage pilot from the CO_2SINK project phase, GFZ/Scientifc technical report – Data 10/05, DOI:10.2312/GFZ.b103-12051, 2012.

LaBrecque, D. and Yang, X.: Difference inversion of ERT data: A fast inversion method for 3-D in situ monitoring, Journal of Environmental & Engineering Geophysics, 6, 83–89, 2001.

LaBrecque, D., Heath, G., Sharpe, R., and Versteeg, R.: Autonomous monitoring of fluid movement using 3-D electrical resistivity tomography, Journal of Environmental & Engineering Geophysics, 9, 167–176, 2004.

Landrø, M.: Discrimination between pressure and fluid saturation changes from time-lapse seismic data, Geophysics, 66, 836–844, 2001.

Landrø, M., Solheim, O., Hilde, E., Ekren, B., and Stronen, L.: The Gullfaks 4D seismic study, Petroleum Geoscience, 5, 213–226, 1999.

Lange, G.: Gleichstromgeoelektrik, in: Handbuch zur Erkundung des Untergrundes von Deponien und Altlasten. Band 3: Geophysik, edited by Knödel, K., Krummel, H., and Lange, G., Springer, Berlin, 1997.

Lawton, D.: Computation of refraction static corrections using first-break traveltime differences, Geophysics, 54, 1289–1296, 1989.

Lay, T. and Wallace, T.: Modern global seismology, vol. 58, Academic Press, 1995.

Ledo, J., Queralt, P., Marcuello, A., Ogaya, X., Escalas, M., Piõa, P., Bosch, D., and Vilamajó, E.: Review of EM Methods Applied for the Characterization and Monitoring of the Hontomin (Spain) CO_2 Storage Pilot Plant, in: 1st Sustainable Earth Sciences Conference & Exhibition – Technologies for Sustainable Use of the Deep Sub-surface, 8-11 November 2011, Valencia, Spain, EarthDoc-55542, 2011.

Lee, M.: Connectivity equation and shaly-sand correction for electrical resistivity, U.S. Geological Survey Scientific investigators Report 2011-5005, 2011.

Lines, L., Schultz, A., and Treitel, S.: Cooperative inversion of geophysical data, Geophysics, 53, 8, 1988.

Liu, Y. and Schmitt, D.: Amplitude and AVO responses of a single thin bed, Geophysics, 68, 1161–1168, 2003.

Loke, M. and Barker, R.: Least-squares deconvolution of apparent resistivity pseudosections, Geophysics, 60, 1682–1690, 1995.

Lumley, D.: Time-lapse seismic reservoir monitoring, Geophysics, 66, 50–53, 2001.

Lüth, S., Bergmann, P., Cosma, C., Enescu, N., Giese, R., Götz, J., Ivanova, A., Juhlin, C., Kashubin, A., and Yang, C.: Time-lapse seismic surface and down-hole measurements for monitoring CO_2 storage in the CO_2SINK project (Ketzin, Germany), Energy Procedia, 4, 3435–3442, 2011.

Martens, S., Liebscher, A., Möller, F., Würdemann, H., Schilling, F., and Kühn, M.: Progress report on the first European on-shore CO_2 storage site at Ketzin (Germany) – Second year of injection, Energy Procedia, 4, 3246–3253, 2011.

Mavko, G. and Mukerji, T.: Bounds on low-frequency seismic velocities in partially saturated rocks, Geophysics, 63, 918–924, 1998.

Mavko, G., Mukerji, T., and Dvorkin, J.: The rock physics handbook: Tools for seismic analysis of porous media, Cambridge University Press, 2003.

Mayne, W.: Common reflection point horizontal data stacking techniques, Geophysics, 27, 927–938, 1962.

McGillivray, P. and Oldenburg, D.: Methods for calculating Fréchet derivatives and sensitivities for the non-linear inverse problem: A comparative study, Geophysical Prospecting, 38, 499–524, 1990.

Meissner, R. and Meixner, E.: Deformation of seismic wavelets by thin layers and layered boundaries, Geophysical Prospecting, 17, 1–27, 1969.

Meju, M., Gallardo, L., and Mohamed, A.: Evidence for correlation of electrical resistivity and seismic velocity in heterogeneous near-surface materials, Geophysical Research Letters, 30, 26–1, 2003.

Michael, K., Golab, A., Shulakova, V., Ennis-King, J., Allinson, G., Sharma, S., and Aiken, T.: Geological storage of CO_2 in saline aquifers – A review of the experience from existing storage operations, International Journal of Greenhouse Gas Control, 4, 659–667, 2010.

Mukerji, T., Mavko, G., and Gomez, C.: Cross-property rock physics relations for estimating low-frequency seismic impedance trends from electromagnetic resistivity data, The Leading Edge, 28, 94–97, 2009.

Muñoz, G., Bauer, K., Moeck, I., Schulze, A., and Ritter, O.: Exploring the Groß Schönebeck (Germany) geothermal site using a statistical joint interpretation of magnetotelluric and seismic tomography models, Geothermics, 39, 35–45, 2010.

Nakatsuka, Y., Xue, Z., Garcia, H., and Matsuoka, T.: Experimental study on CO_2 monitoring and quantification of stored CO_2 in saline formations using resistivity measurements, International Journal of Greenhouse Gas Control, 4, 209–216, 2010.

NETL: Best practices for: Monitoring, verification, and accounting of CO_2 stored in deep geologic formations. NETL – US DOE National Energy Technology Laboratory, p. 132, URL `http://www.netl.doe.gov/technologies/carbon_seq/refshelf/MVA_Document.pdf`, 2009.

Nimmer, R., Osiensky, J., Binley, A., Sprenke, K., and Williams, B.: Electrical resistivity imaging of conductive plume dilution in fractured rock, Hydrogeology Journal, 15, 877–890, 2007.

Norden, B., Förster, A., Vu-Hoang, D., Marcelis, F., Springer, N., and Le Nir, I.: Lithological and petrophysical core-log interpretation in CO_2SINK, the European CO_2 onshore research storage and verification project, in: SPE Asia Pacific Oil and Gas Conference and Exhibition, 2008.

Norden, B., Förster, A., Vu-Hoang, D., Marcelis, F., Springer, N., and Le Nir, I.: Lithological and petrophysical core-log interpretation in CO_2SINK, the European CO_2 onshore research storage and verification project, SPE Reservoir Evaluation & Engineering, 13, 179–192, 2010.

OECD: Organisation for Economic Co-operation and Development – Energy: The next fifty years, p. 160, 1999.

Olayinka, A. and Yaramanci, U.: Assessment of the reliability of 2D inversion of apparent resistivity data, Geophysical Prospecting, 48, 293–316, 2000a.

Olayinka, A. and Yaramanci, U.: Use of block inversion in the 2-D interpretation of apparent resistivity data and its comparison with smooth inversion, Journal of Applied Geophysics, 45, 63–81, 2000b.

Paasche, H., Tronicke, J., Holliger, K., Green, A., and Maurer, H.: Integration of diverse physical-property models: Subsurface zonation and petrophysical parameter estimation based on fuzzy C-means cluster analyses, Geophysics, 71, H33, 2006.

Paasche, H., Tronicke, J., and Dietrich, P.: Automated integration of partially colocated models: Subsurface zonation using a modified fuzzy C-means cluster analysis algorithm, Geophysics, 75, P11, 2010.

Palmer, D.: Non-uniqueness with refraction inversion – A syncline model study, Geophysical Prospecting, 58, 203–218, 2010.

Park, C., Miller, R., Steeples, D., and Black, R.: Swept impact seismic technique (SIST), Geophysics, 61, 1789–1803, 1996.

Parthasarathy, C. and Hathaway, A.: A comparison of tetrahedron quality measures, Finite Elements in Analysis and Design, 15, 255–261, 1994.

Pedersen, L.: Constrained Inversion of Potential Field Data, Geophysical Prospecting, 27, 726–748, 1979.

Pelton, J.: Near-surface seismology: Surface-based methods, in: Investigations in Geophysics No.13, Near-surface geophysics., edited by Butler, D., SEG Tulsa, Oklahoma, USA, 2005.

Pevzner, R., Shulakova, V., Kepic, A., and Urosevic, M.: Repeatability analysis of land time-lapse seismic data: CO_2CRC Otway pilot project case study, Geophysical Prospecting, 59, 66–77, 2011.

Pidlisecky, A. and Knight, R.: FW2_5D: A MATLAB 2.5-D electrical resistivity modeling code, Computers & Geosciences, 34, 1645–1654, 2008.

Portniaguine, O. and Zhdanov, M.: Focusing geophysical inversion images, Geophysics, 64, 874–887, 1999.

Poupon, A., Loy, M., and Tixier, M.: A contribution to electrical log interpretation in shaly sands, Journal of Petroleum Technology, 6, 27–34, 1954.

Pous, J., Marcuello, A., and Queralt, P.: Resistivity inversion with a priori information, Geophysical Prospecting, 35, 590–603, 1987.

Prevedel, B., Wohlgemuth, L., Legarth, B., Henninges, J., Schütt, H., Schmidt-Hattenberger, C., Norden, B., Förster, A., and Hurter, S.: The CO_2SINK boreholes for geological CO_2-storage testing, Energy Procedia, 1, 2087–2094, 2009.

Pridmore, D., Hohmann, G., Ward, S., and Sill, W.: An investigation of finite-element modeling for electrical and electromagnetic data in three dimensions, Geophysics, 46, 1009, 1981.

Pruess, K., Oldenburg, C., and Moridis, G.: TOUGH2 user guide, Version 2.0, Report LBNL-43134, Lawrence Berkeley National Laboratory, Berkeley, California, 1999.

Ramirez, A., Daily, W., LaBrecque, D., Owen, E., and Chesnut, D.: Monitoring an underground steam injection process using electrical resistance tomography, Water Resources Research, 29, 73–87, 1993.

Ramirez, A., Daily, W., Binley, A., LaBrecque, D., and Roelant, D.: Detection of leaks in underground storage tanks using electrical resistance methods, Journal of Environmental & Engineering Geophysics, 1, 189–203, 1996.

Ramirez, A., Newmark, R., and Daily, W.: Monitoring carbon dioxide floods using electrical resistance tomography (ERT): Sensitivity studies, Journal of Environmental & Engineering Geophysics, 8, 187, 2003.

Rhoades, J., Manteghi, N., Shouse, P., and Alves, W.: Soil electrical conductivity and soil salinity: New formulations and calibrations, Soil Science Society of America Journal, 53, 433–439, 1989.

Rickett, J. and Lumley, D.: Cross-equalization data processing for time-lapse seismic reservoir monitoring: A case study from the Gulf of Mexico, Geophysics, 66, 1015–1025, 2001.

Ronen, J. and Claerbout, J.: Surface-consistent residual statics estimation by stack-power maximization, Geophysics, 50, 2759–2767, 1985.

Ross, C.: Effective AVO crossplot modeling: A tutorial, Geophysics, 65, 700, 2000.

Ross, C. and Kinman, D.: Nonbright-spot AVO; Two examples, Geophysics, 60, 1398, 1995.

Rücker, C., Günther, T., and Spitzer, K.: Three-dimensional modelling and inversion of DC resistivity data incorporating topography I: Modelling, Geophysical Journal International, 166, 495–505, 2006.

Sakurai, S., Ramakrishnan, T., Boyd, A., Mueller, N., and Hovorka, S.: Monitoring saturation changes for CO_2 sequestration: Petrophysical support of the Frio brine pilot experiment, in: 46th Annual Logging Symposium Transactions, Society of Petrophysicists and Well Log Analysts, New Orleans, Louisiana., 2005.

Saunders, J., Herwanger, J., Pain, C., Worthington, M., and De Oliveira, C.: Constrained resistivity inversion using seismic data, Geophysical Journal International, 160, 785–796, 2005.

Schilling, F., Borm, G., Würdemann, H., Möller, F., and Kühn, M.: Status report on the first European on-shore CO_2 storage site at Ketzin (Germany), Energy Procedia, 1, 2029–2035, 2009.

Schmidt-Hattenberger, C., Bergmann, P., Kießling, D., Krüger, K., Rücker, C., Schütt, H., and Ketzin Group: Application of a Vertical Electrical Resistivity Array (VERA) for monitoring CO_2 migration at the Ketzin site: First performance evaluation, Energy Procedia, 4, 3363–3370, 2011.

Schmidt-Hattenberger, C., Bergmann, P., Labitzke, T., Schröder, S., Krüger, K., Rücker, C., and Schütt, H.: A modular geoelectrical monitoring system as part of the surveillance concept in CO_2 storage projects, Energy Procedia, 23, 400–407, 2012.

Schütt, H., Wigand, M., and Spangenberg, E.: Geophysical and geochemical effects of supercritical CO_2 on sandstones, in: Carbon dioxide capture for storage in deep geologic formations – Results from the CO_2 capture project, Volume 2: Geologic storage of carbon dioxide with monitoring and verification, edited by Benson, S., Elsevier Science, London, 2005.

Schütze, C. and Flechsig, C.: Structural investigation of an active hydrothermal system beneath the Long Valley Caldera, California, using DC-resistivity imaging methods, Zeitschrift für Geologische Wissenschaften, 30, 119–129, 2002.

Scriba, H.: Computation of the electric potential in three-dimensional structures, Geophysical Prospecting, 29, 790–802, 1981.

Sheriff, R.: Encyclopedic dictionary of applied geophysics, vol. 13, SEG, 2002.

Sheriff, R. and Geldart, L.: Exploration seismology, Cambridge University Press, 1995.

Shewchuk, J.: Triangle: A two-dimensional quality mesh generator and Delaunay triangulator, URL `http://www.cs.cmu.edu/%7Equake/triangle.html`, 1995.

Shuey, R.: A simplification of the Zoeppritz equations, Geophysics, 50, 609–614, 1985.

Si, H.: TetGen: A 3D delaunay tetrahedral mesh generator, Technical Report 4, Weierstrass Institute for Applied Analysis and Stochastics, WIAS, Berlin, http://tetgen.berlios.de, 2003.

Si, H.: Adaptive tetrahedral mesh generation by constrained Delaunay refinement, International Journal for Numerical Methods in Engineering, 75, 856–880, 2008.

Sifuentes, W., Giddins, M., and Blunt, M.: Modeling CO_2 storage in aquifers: Assessing the key contributors to uncertainty, Proceedings of Offshore Europe, SPE 123582, p. 13, 2009.

Slater, L., Binley, A., Daily, W., and Johnson, R.: Cross-hole electrical imaging of a controlled saline tracer injection, Journal of Applied Geophysics, 44, 85–102, 2000.

Spitzer, K.: A 3-D finite-difference algorithm for DC resistivity modelling using conjugate gradient methods, Geophysical Journal International, 123, 903–914, 1995.

Spitzer, K.: The three-dimensional DC sensitivity for surface and subsurface sources, Geophysical Journal International, 134, 736–746, 1998.

Storz, H., Storz, W., and Jacobs, F.: Electrical resistivity tomography to investigate geological structures of the earth's upper crust, Geophysical Prospecting, 48, 455–472, 2000.

Streich, R., Becken, M., Matzander, U., and Ritter, O.: Strategies for land-based controlled-source electromagnetic surveying in high-noise regions, The Leading Edge, 30, 1174–1181, 2011.

Telford, W., Geldart, L., and Sheriff, R.: Applied geophysics, Cambridge University Press, 1990.

Tikhonov, A. N.: Solution of incorrectly formulated problems and the regularization method, Soviet Mathematical Doklady, vol. 4, 1963.

Todd, T. and Simmons, G.: Effect of pore pressure on the velocity of compressional waves in low-porosity rocks, Journal of Geophysical Research, 77, 3731–3743, 1972.

Vasco, D.: Regularization and trade-off associated with nonlinear geophysical inverse problems: Penalty homotopies, Inverse problems, 14, 1033–1052, 1998.

Verdon, J. and Campman, X.: The feasibility of imaging the CO_2 plume at CO_2SINK using 4D seismics, in: 72nd EAGE Annual Meeting, Barcelona, 2010.

Virieux, J. and Operto, S.: An overview of full-waveform inversion in exploration geophysics, Geophysics, 74, WCC1–WCC26, 2009.

Vogel, C.: Non-convergence of the L-curve regularization parameter selection method, Inverse problems, 12, 535, 1996.

Vozoff, K. and Jupp, D. L. B.: Joint inversion of geophysical data, Geophysical Journal, Royal Astronomical Society, 42, 977–991, 1975.

Wang, Y.: Approximations to the Zoeppritz equations and their use in AVO analysis, Geophysics, 64, 1920, 1999.

Wang, Z.: Fundamentals of seismic rock physics, Geophysics, 66, 398–412, 2001.

Waxman, M. and Smits, L.: Electrical conductivities in oil-bearing shaly sands, SPE Journal, 8, 107–122, 1968.

Waxman, M. and Thomas, E.: Electrical conductivities in shaly sands – I. The relation between hydrocarbon saturation and resistivity Index; II. The temperature coefficient of electrical conductivity, Journal of Petroleum Technology, 26, 213–225, 1974.

White, D.: Monitoring CO_2 storage during EOR at the Weyburn–Midale Field, The Leading Edge, 28, 838–842, 2009.

Widess, M.: How thin is a thin bed?, Geophysics, 38, 1176, 1973.

Wiese, B., Böhner, J., Enachescu, C., Würdemann, H., and Zimmermann, G.: Hydraulic characterisation of the Stuttgart Formation at the pilot test site for CO_2 storage, Ketzin, Germany, International Journal of Greenhouse Gas Control, 4, 960–971, 2010.

Wisen, R. and Christiansen, A.: Laterally and mutually constrained inversion of surface wave seismic data and resistivity data, Journal of Environmental & Engineering Geophysics, 10, 251, 2005.

Worthington, P.: The evolution of shaly-sand concepts in reservoir evaluation: The Log Analyst, 1985.

Wu, X.: A 3-D finite-element algorithm for DC resistivity modelling using the shifted incomplete Cholesky conjugate gradient method, Geophysical Journal International, 154, 947–956, 2003.

Würdemann, H., Möller, F., Kühn, M., Heidug, W., Christensen, N., Borm, G., and Schilling, F.: CO_2SINK – From site characterisation and risk assessment to monitoring and verification: One year of operational experience with the field laboratory for CO_2 storage at Ketzin, Germany, International Journal of Greenhouse Gas Control, 4, 938–951, 2010.

Xue, Z., Kim, J., Mito, S., Kitamura, K., and Matsuoka, T.: Detecting and monitoring CO_2 with p-wave velocity and resistivity from both laboratory and field scales, in: SPE International Conference on CO_2 Capture, Storage, and Utilization, San Diego, CA, USA, SPE 126885, 2009.

Yang, C.: Time-lapse analysis of borehole and surface seismic data, and reservoir characterization of the Ketzin CO_2 storage site, Germany, Ph.D. thesis, Acta Universitatis Upsaliensis. Digital Comprehensive Summaries of Uppsala Dissertations from the Faculty of Science and Technology, ISSN 1651-6214; 887, 2012.

Yang, C., Juhlin, C., Enescu, N., Cosma, C., and Lüth, S.: Moving source profile data processing, modelling and comparison with 3D surface seismic data at the CO_2SINK project site, Ketzin, Germany, Near Surface Geophysics, 8, 601–610, 2010.

Yang, C., Juhlin, C., Ivanova, A., and Fan, W.: AVO attributes analysis of time-lapse 3D surface seismic data from CO_2SINK project site, Ketzin, Germany., EGU General Assembly, Vienna, Austria, pp. EGU2011–265, 2011.

Yi, M., Kim, J., and Chung, S.: Enhancing the resolving power of least-squares inversion with active constraint balancing, Geophysics, 68, 931–941, 2003.

Yilmaz, Ö.: Seismic data analysis, Society of Exploration Geophysicists, 2001.

Yordkayhun, S., Juhlin, C., Giese, R., and Cosma, C.: Shallow velocity-depth model using first arrival traveltime inversion at the CO_2SINK site, Ketzin, Germany, Journal of Applied Geophysics, 63, 68–79, 2007.

Yordkayhun, S., Ivanova, A., Giese, R., Juhlin, C., and Cosma, C.: Comparison of surface seismic sources at the CO_2SINK site, Ketzin, Germany, Geophysical Prospecting, 57, 125–139, 2009a.

Yordkayhun, S., Juhlin, C., and Norden, B.: 3D seismic reflection surveying at the CO_2SINK project site, Ketzin, Germany: A study for extracting shallow subsurface information, Near Surface Geophysics, 7, 75–91, 2009b.

Zemke, K., Liebscher, A., and Wandrey, M.: Petrophysical analysis to investigate the effects of carbon dioxide storage in a subsurface saline aquifer at Ketzin, Germany CO_2SINK, International Journal of Greenhouse Gas Control, 4, 990–999, 2010.

Zhang, F., Juhlin, C., Cosma, C., Tryggvason, A., and Pratt, R.: Cross-well seismic waveform tomography for monitoring CO_2 injection: A case study from the Ketzin Site, Germany, Geophysical Journal International, 1, 629–646, 2012.

Zhang, Y. and Schmitt, D.: A case study: QC analysis of time-lapse seismic monitoring in a heavy oil reservoir, CSEG National Convention 2004, URL `www.cseg.ca/conventions/abstracts/2004/2004abstracts/119S0226-Zhang_Y_QC_Analysis_Timelapse.pdf`, 2004.

Zhdanov, M.: Geophysical inverse theory and regularization problems, vol. 36, Elsevier Science Ltd., 2002.

Zimmer, M., Erzinger, J., and Kujawa, C.: The gas membrane sensor (GMS): A new method for gas measurements in deep boreholes applied at the CO_2SINK site, International Journal of Greenhouse Gas Control, 5, 995–1001, 2011.

Zöppritz, K.: Erdbebenwellen VIIIb, über Reflexion und Durchgang seismischer Wellen durch Unstetigkeitsflächen, Göttinger Nachrichten, 1, 66–84, 1919.

Acknowledgements

Working in the Ketzin project meant collaboration with a lot of people across several disciplines. Therefore, I would like to thank everybody with whom I puzzled together and who allowed me to accomplish this thesis. I am particularly grateful to:

- Prof. Dr. Wolfgang Rabbel (University of Kiel) for accepting to be the first examiner. Although timing constraints somehow hindered collaboration at larger depth, I am grateful for always being interested, some fruitful discussions, and the pleasant atmosphere in Kiel.
- Prof. Dr. Christopher Juhlin (Uppsala University) for accepting to be the second reviewer. I thank Chris for his curiosity on the ERT investigations at the Ketzin site, valuable corrections of my English, and a very constructive collaboration.
- I thank Prof. Dr. Charlotte Krawczyk (LIAG) and Prof. Dr.Christian Berndt (GEOMAR) for their willingness to join the defence committee as opponents.
- Dr. Cornelia Schmidt-Hattenberger (GFZ Potsdam) for numerous discussions and an always heartily atmosphere. It was your support and supervision, which made the work on this PhD project entirely enjoyable.
- A big thanks goes to the geophysical CO_2 storage monitoring group of the GFZ: Dr. Stefan Lüth, Dr. Rüdiger Giese, Julia Götz, Alexandra Ivanova, Dana Kiessling, Magda Gil, Tim Labitzke, Stefan Schröder, Dr. Michaela Bock. Special thanks owe to Tim for helping me significantly with the preparation of the SD-ERT data. Marcus Möller and Florian Wagner provided a very pleasant atmosphere in our office and I wish them all the best for their PhD theses.
- I thank Dr. Can Yang, Dr. Monika Ivandic, Dr. Artem Kashubin, and Fengjiao Zhang from the Uppsala seismic group for the close collaboration and some funny times.
- Particular thanks are due to Dr. Carsten Rücker (TU Berlin) and Dr. Thomas Günther (LIAG). Their BERT code plays an important role in this thesis. Moreover, it was Carsten's continuous interest and support regarding meshing and ERT inversion of the Ketzin datasets which made an impact on this thesis.
- Although a complete list can clearly not be given here, I thank the many people being engaged in the survey crews. With regard to the seismic surveys, I would like to acknowledge Hans (Hasse) Palm, Dr. Sverker Olson, and Prof. Dr. Alireeza Malehmir. With regard to the geoelectric surveys, I would like to acknowledge Günther Petzold, Rene Voigt, and Roland Hohberg. From student helper to field veteran, please know that I enjoyed to be in the field with you and that the later processing of the acquired data created a lot of nice moments.
- I further enjoyed working and being together with the colleagues of the Centre for CO_2 at the GFZ. Especially, I am thankful for the great company of Dr. Marco De Lucia, Gunther Baumann, Sebastian Fischer, Dr. Thomas Kempka, Benjamin and Natalie Nakaten, Jenny Meistring, Cornelia Loch, and Prof. Dr. Dr. Michael Kühn. As the history of the

CO_2SINK project ranges back beyond my PhD project, I'm grateful to those who made hands-on reasearch at the Ketzin site possible.

- Some people teach one how to analyse and tackle problems. In this respect, I owe special gratitude to Dr. Manfred Degutsch (University of Münster) and Christoph Witte (DMT Essen) with whom I was allowed to work before starting on the Ketzin project. Thanks for very instructive and enjoyable times which have teached me many things that gave benefit to this PhD project.
- I thank the GeoEn project (Grant 03G0671A/B/C), a national scientific initiative in the field of energy research, for granting financial support of this PhD project.
- Without my parents, Marita and Hans-Georg, this work would not have been possible. This is not only due to my mere physical existence, but also due to their love and support throughout my entire life. Therefore, I dedicate this work to them and am, for similar reasons, indepted to Barbara, her deceased husband Manfred, Tina, Tim, and Michael.
- Last, and most importantly, I'm deeply thankful to my beloved Eva and our son Jannes for their love.

Erklärung

Hiermit erkläre ich, dass diese Disseration – abgesehen von den angegebenen Mitarbeiten – nach Inhalt und Form meine eigene Arbeit ist. Die Arbeit ist weder ganz noch zum Teil einer anderen Stelle im Rahmen eines Prüfungsverfahrens vorgelegt und unter Einhaltung der Regeln guter wissenschaftlicher Praxis entstanden.

....
Peter Bergmann
Potsdam, 20.12.2012
